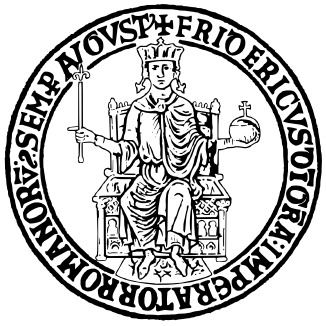

University of Naples Federico II
Department of Industrial Engineering
- Mechanic and Energetic Section -

Ph.D. School in Industrial Engineering - XXXVI Cycle

Advancing Sustainable Transportation: A Comprehensive Study on Alternative Fuels, Powertrain Technologies, and Energy Management Strategies

Doctoral Thesis

Ph.D. School Coordinator
Prof. Michele Grassi

Tutor
Prof. Fabio Bozza
Prof. Vincenzo De Bellis

Ph.D. Candidate
Marco Piras

Ph.D. Thesis

Advancing Sustainable Transportation: A Comprehensive Study on Alternative Fuels, Powertrain Technologies, and Energy Management Strategies

Written by: Mr. Marco Piras
Supervised by: Prof. Fabio Bozza
Prof. Vincenzo De Bellis

Reviewing board:

Prof. Marco Sorrentino
Prof. Christoph Hametner

Napoli, October 2023

Abstract

To mitigate the impacts of global warming, the effects of which are evident in our daily lives, major countries around the world are pushing for new and more stringent regulations that affect the transportation sector, responsible for a significant portion of CO_2 emissions in the atmosphere. It is within this context that industries and researchers are pushing the boundaries of knowledge to discover technological solutions for the environmental and political challenges that arise periodically. This PhD thesis aims to introduce the reader to some of these solutions, demonstrating that the transportation sector can be transformed towards carbon neutrality through various approaches operating at different stages of decarbonization. Four main layers of decarbonization are identified.

It is widely acknowledged that the most commonly used propulsion system for our vehicles today is the internal combustion engine (ICE), which is simultaneously identified as a major source of gaseous CO_2. However, it is important to note that the source of pollutants lies in the fuel, rather than the engine itself. Therefore, the first step in achieving carbon neutrality involves addressing the nature of the fuel, which can either be burned in an ICE or chemically converted in fuel cells. Currently, biofuels and e-fuels, with a strong focus on hydrogen, are subjects of extensive research and testing.

The second layer of decarbonization involves optimizing the propulsion system that converts the chemical energy from fuel (or stored in a battery) into mechanical power for propulsion. This PhD thesis primarily focuses on ICEs and fuel cells. Concerning ICE-powered vehicles, a critical challenge is managing the existing vehicle fleet until it reaches the end of its life while minimizing its environmental impact. In this context, it is crucial to enhance and convert existing ICEs. One potential technical solution is water injection. A numerical study conducted during this PhD work demonstrated the benefits of applying this strategy to a gasoline spark ignition engine, highlighting advantages in terms of both efficiency and performance with the implementation of an appropriate control strategy. Hydrogen-fueled engines are another important area of research. They have the potential to reduce CO_2 tailpipe emissions from ICEs to nearly zero; however, they still present technological challenges. During this doctoral research, a phenomenological 1D model of a hydrogen-fueled engine was developed and validated, showing satisfactory agreement with experimental data. Consequently, this model serves as a valuable tool for a comprehensive understanding of hydrogen engines. Fuel cell vehicles are progressively gaining a larger market share and can unquestionably serve as a practical alternative to ICE-powered vehicles. The fourth chapter provides a comprehensive overview of fuel cell systems, including a discussion of various

widely adopted technologies. Following this, a detailed description of the fuel cell system model utilized in the development of a Fuel Cell Hybrid Electric Vehicle (FCHEV) model is presented.

The third layer of decarbonization pertains to the vehicles themselves. Optimizing the powertrain is imperative, and hybrid vehicles have effectively demonstrated that by amalgamating various technologies (such as ICEs, batteries, fuel cells, supercapacitors, etc.), the full potential of each component can be unlocked. When these components operate in isolation, they may not achieve the same level of performance.

However, the growing complexity of powertrains necessitates a suitable energy management system, which constitutes the fourth and final decarbonization layer investigated in this PhD study. After a concise review of the literature, this doctoral research introduces an expansion of the ETESS (Efficient Thermal-Electric Skipping Strategy). This expansion aims to enhance energy management in Plug-in Hybrid Electric Vehicles (PHEVs) equipped with small-sized engines. The core concept underlying this approach revolves around the alternative utilization of both the thermal engine and electric motor to fulfill the power requirements for propulsion. In recent years, the rapid advancements in artificial intelligence and computer technologies have led to the increasing adoption of learning algorithms within the field of Energy Management Strategies, positioning it as a burgeoning and highly esteemed research area. As a result, during the last part of this PhD work, an EMS enhanced by the incorporation of neural networks has been developed and tested for a heavy-duty FCHEV.

"Plus Ultra"
Cit.
"All Might, My Hero Academia."

Acknowledgements
Ringraziamenti

Contents

List of Figures

List of Tables

Nomenclature

Acronyms

A-ECMS	Adaptive-ECMS
A-ETESS	Adaptive-ETESS
AECC	Association for Emission Control by Catalyst
AFC	Alkaline Fuel Cells
AI	Artificial Intelligence
ANN-ECMS	Artificial Neural Network ECMS
ANN	Artificial Neural Network
ATDC	After TDC
BDC	Bottom dead center
BEV	Battery electric vehicle
BMEP	Brake mean effective pressure
BoP	Balance of plant
BSFC	Brake Specific Fuel Consumption
BTDC	Before TDC
CA10	Crank angle at 10% mass fraction burned
CA25	Crank angle at 25% mass fraction burned
CA50	Crank angle at 50% mass fraction burned
CA75	Crank angle at 75% mass fraction burned
CA90	Crank angle at 90% mass fraction burned
CAD	Crank angle degree
CAI	Controlled auto ignition
CB	Charge Blended

CCS	Carbon capture and storage
CCV	Cycle to cycle variability
CD	Charge Depleting
CFD	Computational Fluid Dynamics
CI	Compression ignition
CS	Charge Sustaining
DI	Direct injection
DMFC	Direct Methanol Fuel Cells
DP	Dynamic Programming
ECMS	Equivalent Consumption Minimization Strategy
ECU	Engine control unit
EF	Equivalence Factor
EGR	Exhaust Gas Re-circulation
EIVC	Early intake valve closure
EMS	Energy management strategy
EOL	End Of Life
EREV	Extended range electric vehicle
ETESS	Efficient Thermal/Electric Skipping Strategy
EVC	Exhaust valve closure
EVO	Exhaust vale opening
EV	Electric vehicle
FAME	Fatty acid methyl esters
FCHEV	Fuel cell hybrid electric vehicle
FCS	Fuel cell system
FCV	Fuel cell vehicle
FC	Fuel cell
FHEV	Full-hybrid electric vehicle
GHG	Greenhouse gas
GIE	Gross indicated efficiency
H_2	Hydrogen
HCCI	Homogeneous charge compression ignition
HEV	Hybrid electric vehicle
HiL	Hardware in the Loop
HRR	Heat Release Rate
HVO	Hydrotreated Vegetable Oil

ICEV	Internal combustion engine vehicle
ICE	Internal combustion engine
IMEP	Indicated mean effective pressure
ISFC	Indicated specific fuel consumption
IVC	Intake valve closing
IVO	Intake valve opening
KLSA	Knock limited spark advance
LHV	Low heating value
LPG	Liquid petroleum gas
LSTM	Long-Short Term Memory
MBT	Maximum brake torque
MCFC	Molten Carbonate Fuel Cells
MEA	Membrane electrode assembly
MHEV	Mild-hybrid electric vehicle
ML	Machine Learning
NG	Natural gas
NN	Neural network
OECD	Organization for Economic Cooperation and Development
OME	Oxymethylene ethers
P-ECMS	Predictive-ECMS
PAFC	Phosphoric Acid Fuel Cells
PCCI	Premixed charge compression ignition
PEM	Proton exchange membrane
PFI	Port fuel injection
PHEV	Plugin hybrid electric vehicle
PiL	Processor in the Loop
PMP	Pontryagin Minimum Principle
PM	Particulate matter
RBS	Rule-Based Strategy
RCCI	Reactivity controlled compression ignition
RL	Reinforcement Learning
RMSE	Root Mean Square Error
RNN	Recurrent Neural Network
rpm	Engine speed
S-ECMS	Standard ECMS

SACI	Spark-assisted compression ignition
SAE	Society of Automotive Engineers
SA	Spark advance
SCC	Stratified charge combustion
SI	Spark ignition
SoC	State of charge
SOFC	Solid Oxide Fuel Cells
TDC	Top dead center
TEN	Trans European Network
VCR	Variable compression ratio
VVA	Variable valve actuation
VVL	Variable valve lift
VVT	Variable valve timing
WI	Water injection
ZEV	Zero-emission vehicle

Greek symbols

α	Charge transfer coefficient
Δ	Variation
δ_L	Laminar flame thickness
ϵ	Dissipation rate
η	Efficiency (general)
λ	Air-fuel ratio
λ	Co-state
ω	Rotational speed
ϕ	Equivalence ratio
ρ	Density
ρ_b	Burned gases density
ρ_u	Unburned gases density
Ξ	Wrinkling factor

Latin symbols

$\dot{m}$	Mass flow rate
$\dot{m}_f$	Fuel mass flow rate
A_f	Frontal area
B	Bore

C	Mass transport loss coefficient
C_d	Drag coefficient
$c_{fdm}, c_{fd0}, c_{pkk}$	Tuning constants in the turbulence model
c_{roll}	Rolling resistance coefficient
$c_{trans}, c_{wkr}, x_{wc}$	Tuning constants in the fractal combustion model
CO	Carbon monoxide
CO_2	Carbon dioxide
d	derivative
D_3	Fractal dimension
Da	Damkohler number
E_{batt}	Battery energy
F	Faraday constant
G	Gibbs free energy
g	Gravity acceleration
H	Hentalpy
H	Piston position referred to cylinder head
H_f	Forecasting horizon
HC	Hydrocarbons
i	Current
i_0	Exchange current density
i_l	Limiting current density
J	Performance index
K	Mean flow kinetic energy
k	Turbulent kinetic energy
K_T	Tumble kinetic energy
k_{pen}	Adaptive function
k_p	Proportional gain
Ka	Karlovitz number
L_t	Integral length scale
L_{min}, L_{max}	Minimum / maximum flame front wrinkling scale
m	Mass (general)
m_b	Burned mass
N_2	Nitrogen
NO	Nitrogen monoxide
NO_x	Nitrogen oxides

O_2	Oxygen
P	Power
p	Pressure (general)
P_{batt}	Battery power
p_{cath}	Cathode pressure
P_{el}	Electrical power
P_{FCS}	Fuel cell system power
P_{trac}	Traction power
R	Universal gas constant
r_f	Flame radius
r_T	Tumble radius
R_{ohm}	Ohmic resistance
Re	Reynolds number
RH	Relative humidity
S	Entropy
s	Equivalence factor
$S\hat{o}C$	Predicted SoC
S_F	Laminar adiabatic freely propagating flame speed
S_L	Laminar flame speed
S_T	Turbulent flame speed
Sc	Schmidt number
T	Temperature (general)
T	Torque
T	Tumble
t	time (general)
t_0	Initial time
T_{cath}	Cathode temperature
t_f	Final time
u'	Turbulent intensity
U_f	Mean flow velocity
U_T	Tumble flow velocity
V	Cylinder volume
V	Voltage
V_{act}	Activation losses
V_C	Concentration losses

V_{OC}	Open circuit voltage
V_{ohm}	Ohmic losses
X_b	Burned mass fraction

Chapter 1

Introduction

1.1 Context

Despite a slight setback due to the COVID-19 pandemic, the global demand for energy continues to rise, driven by both population growth and economic development, particularly in emerging countries that are not members of the OECD [1] (Figure 1.1).

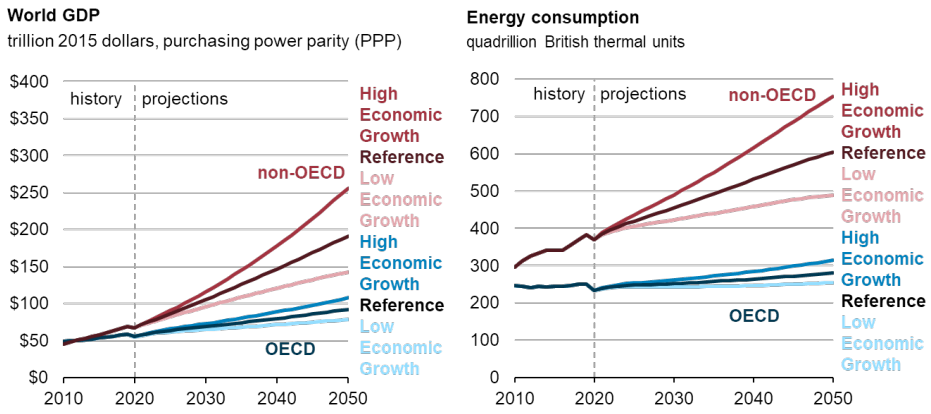

Figure 1.1: Hystory and projections of world GDP (left), energy consumption (right). Source [2].

Focusing on the transportation sector, it can observed that in 2020 it accounted for 17% of global greenhouse gas (GHG) emissions, with road

transport contributing 12% of that (Figure 1.2).

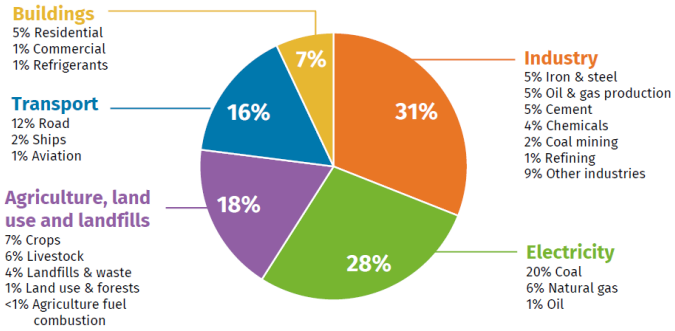

Figure 1.2: Global GHG emissions by sector in 2020. Source [3]

If this data is now combined with future projections on energy consumption in the transportation sector, it becomes evident to the reader that there is a need to effectively reduce emissions from this sector. Going into further detail, Figure 1.3 shows that a projection until 2050 indicates almost unchanged energy consumption in the transportation sector for OECD countries compared to the values recorded in 2010 (+5%). On the other hand, it will more than double (+111%) for non-OECD countries, primarily driven by African and Asian countries, surpassing OECD countries' consumption by 53%. It is important to keep these data in mind to understand in which part of the world and to what extent the energy consumption of the transportation sector will be shifted.

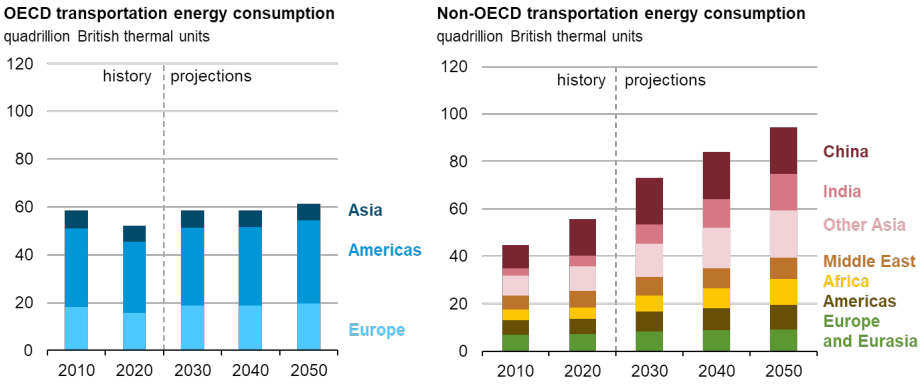

Figure 1.3: Hystory and projections of transportation energy consumption: OECD (left), no-OECD (right). Source [2]

Figure 1.4 presents, within the same forecasting horizon, the trend of light-duty vehicle stock for both OECD and non-OECD countries. In the case of OECD countries, there is an increasingly noticeable decline in the adoption of diesel-powered vehicles, while the use of gasoline-powered engines is expected to remain relatively constant. At the same time, the adoption of plug-in hybrid and electric vehicles is projected to steadily increase. The same does not apply to non-OECD countries. While there is still an expected growth in the adoption of electric and plug-in hybrid vehicles in this case, there is an even greater diffusion of vehicles equipped with gasoline and diesel engines.

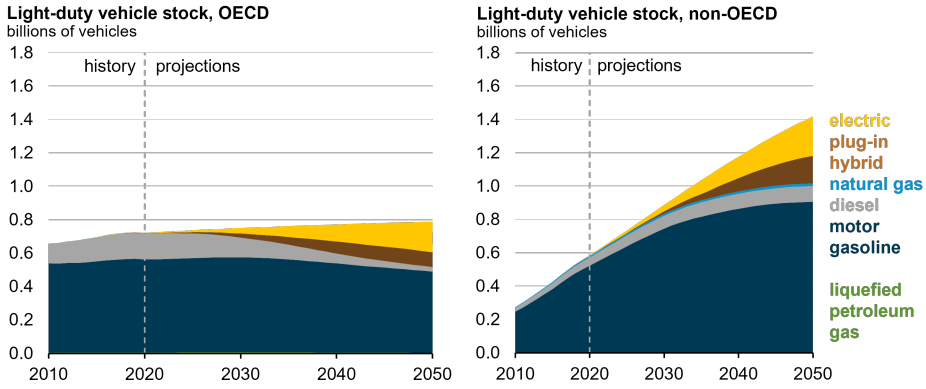

Figure 1.4: Hystory and projections of light-duty vehicle stock: OECD (left), no-OECD (right). Source [2]

An undeniable conclusion that can be drawn from the data just analyzed is that the use of electric power in the transportation sector is destined to grow even further. However, it is appropriate to pose a question to the reader: "Is the electrification of transportation always the right path for an 'effective reduction' of GHG emissions?". Figure 1.5 could help to find an answer displaying the share of net electricity generation for four different regions: USA, Europe, India, and Africa. In all cases, an increasing contribution of renewable sources (solar, wind, and hydroelectric) is expected, but accompanied by a varying contribution of a highly polluting source: coal. India, a country expected to experience significant growth in energy demand from the transportation sector (Figure 1.3), will see approximately 20% of its electricity generated from coal combustion. Lower percentages are projected for the United States and Africa, although they will still have a significant contribution from natural gas, which is a fossil fuel source of GHG emissions (methane itself is a potent greenhouse gas). In Europe, on the other hand, a generation share of over 70% from

renewable sources is projected by 2050.

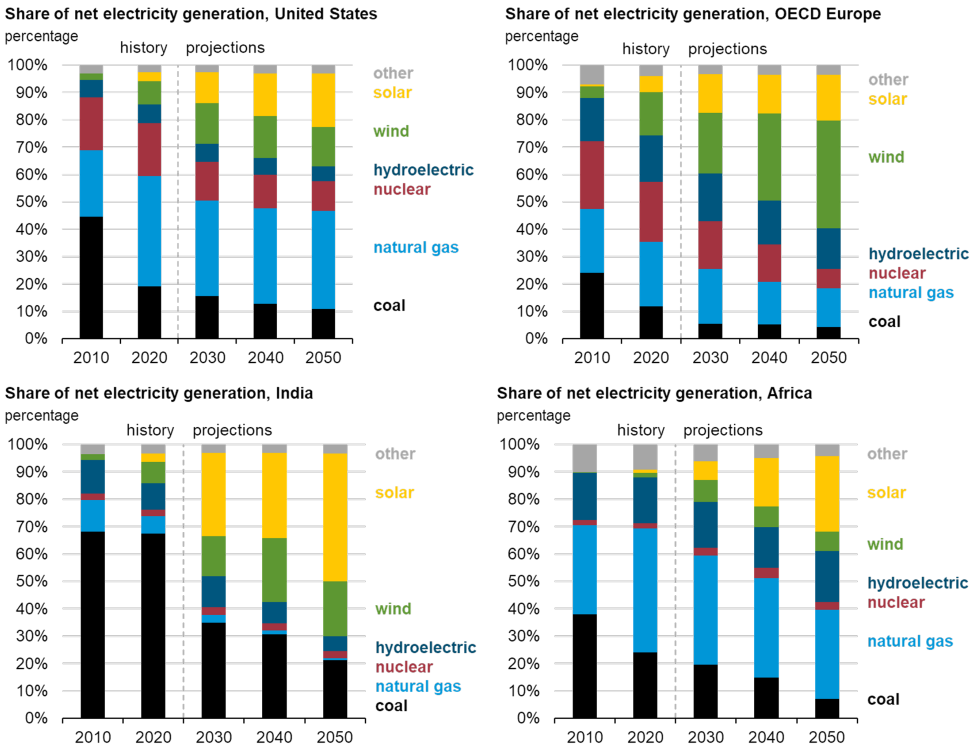

Figure 1.5: Hystory and projections of share net-electricity generation in different countries. Source [4]

This prediction is a consequence of the fact that Europe is paying great attention to the issue of climate change. In November 2019, the European Parliament declared a climate emergency, urging the Commission to ensure that all proposals align with the objective of limiting global warming below 1.5°C and significantly reducing greenhouse gas emissions. Subsequently, the European Commission presented the European Green Deal, a road map to achieve climate neutrality in Europe by 2050 [5]. On June 24, 2021, the Parliament approved the European Climate Law, which legally binds the objective of reducing emissions by 55% by 2030 and achieving climate neutrality by 2050. This will enable the EU to move closer to the goal of achieving net-negative emissions post-2050 while reaffirming its leadership in the global fight against climate change. In this context, the new Euro 7 regulations for the transportation sector are under examination. Euro 7 will regulate emissions from tyres and

brakes for the first time worldwide. To support electrification, the proposal also includes a new procedure and limits for the battery durability. The European Union also proposed a ban of internal combustion engines for new sold vehicles starting from 2035. However, there have been several opponents. Among them, the Association for Emission Control by Catalyst (AECC) has published its key messages for achieving the planned 55% reduction in emissions outlined in the Green Deal. These include [6]:

- "The EU zero-emissions transport objectives can best be achieved by the contribution of all available powertrain technologies, hybrid ICE, BEV, FCEV, etc."
- "Emission control technologies fully operating in combination with drop-in sustainable renewable fuels enable ultra-low pollutant emissions contributing towards net-zero CO2 emissions."
- "The target of sustainable renewable fuels is currently not aligned with the overall European Green Deal ambition. Higher targets which take account of the contribution of hybrids using sustainable renewable fuels are needed."
- "Sustainable renewable fuels should be integrated as an additional path within the Zero Emission Vehicles (ZEV) definition. It is the use of fossil fuels that should be banned, rather than the use of internal combustion engines."

Germany has also expressed its displeasure, stating that e-fuels represent a valid pathway towards decarbonization. In the end, with effect from 2035, the EU and Germany came to an agreement on March 25 in 2023 to scale down plans to outlaw all combustion-engine cars. ICE models may be sold and registered in the EU after the 2035 deadline as long as they exclusively use fuels that are carbon-neutral [7].

Among the various pathways to achieve the goals of the Green Deal, Europe also recognizes the importance of hydrogen and has published the Hydrogen Roadmap [8]. The roadmap focuses on several key points:

- Hydrogen technology development: The roadmap emphasizes the need for investment in research and development of hydrogen technologies, including production systems, storage, distribution, and utilization in industrial and transportation sectors.
- Hydrogen infrastructure: Establishing a robust hydrogen infrastructure is highlighted as a crucial step. This includes the development of production

facilities, refueling stations, and distribution networks to facilitate the widespread adoption of hydrogen as a clean fuel.

- Applications of hydrogen: The roadmap explores various applications of hydrogen across energy, transportation, industry, and buildings sectors. It underscores the potential of green hydrogen (produced from renewable sources) in achieving decarbonization objectives.

- International cooperation: The roadmap emphasizes the importance of international cooperation to develop common norms, standards, and regulations for hydrogen. This aims to create a global market for clean hydrogen, fostering the transition to a low-carbon economy.

Moreover, focusing on transports, for buses, trucks, trains, ships, big cars, and commercial vehicles, hydrogen is recognized as the most potential decarbonization solution for four reasons. Hydrogen provides a route to complete decarbonization, whilst other solutions can only serve as a stopgap. Second, because to its better energy density per unit mass, hydrogen has a significant amount of power for long distances and large payloads. Finally, while originally a barrier, hydrogen infrastructure has many advantages over fast charging, including quicker refueling, more adaptable load, less space required, and comparable investment prices. Last but not least, hydrogen is the ideal fuel for ships, trains, and aviation, and hydrogen-based synthetic fuels can decarbonize other modes of transportation including air travel. Considering the advantages associated with using hydrogen rather than heavy battery packs, Battery Electric Vehicles (BEVs) are recognized as the optimal solution for small passenger cars (Figure 1.6).

To summarize, the analysis conducted so far can lead to the following conclusions:

- A growth in global energy demand for the transportation sector is projected, primarily driven by countries with emerging economies where the adoption of ICE-powered vehicles is increasing. Although these countries are expected to generate electricity increasingly from renewable sources, the contribution of fossil fuels will still be significant.

- The European Union is strongly pushing for extensive electrification. BEVs and FCHEVs are gaining an increasingly larger market share. This drive is accompanied by a strong policy towards energy generation from renewable sources.

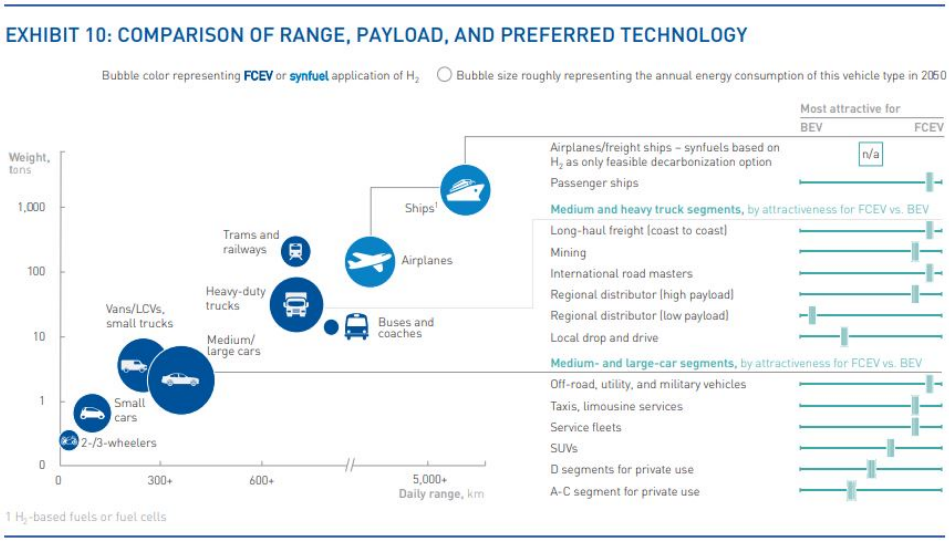

Figure 1.6: Comparison of payload, range and preferred technology bewteen FCHEV and BEV. Source [8]

- E-fuels have been recognized by the European Union as a potential pathway towards decarbonization. They also offer the possibility to reduce the environmental impact of the existing vehicle fleet, for which the optimization of ICEs is of utmost importance. Indeed, the disposal of existing vehicles will need to be gradual to avoid causing environmental damage due to the disposal process.

The decarbonization of the transportation sector is both necessary and urgent. This imperative is embedded within a vast and intricate global landscape that, unfortunately, does not offer a single silver bullet solution. Consequently, it is essential that, depending on the specific context, diverse approaches are pursued, all with the shared objective of reducing and ultimately eliminating the environmental impact of our transportation systems.

1.2 Objectives

The primary objective of this thesis is to investigate current and future solutions for decarbonizing the transportation sector across multiple scales. The research begins by studying the fuels used within engines and fuel cells, focusing on their

decarbonization potential. These systems are then integrated into vehicles, where energy management optimization takes place. By examining the interplay between fuels, powertrain technologies, and vehicle energy management, this study aims to showcase the diverse levels at which decarbonization can be achieved. Starting from the fuel level, progressing to the powertrain, and finally to the vehicle as a whole, a comprehensive approach to decarbonization is explored.

The following partial objectives must be accomplished in order for this overall goal to be realized:

- Development and optimization of a virtual model of an internal combustion engine capable of replicating the effects caused by the implementation and utilization of technologies and fuels for the reduction of CO_2 emissions. For this purpose, the GT-Suite software has been used and integrated with customized routines.
- Development and optimization of a virtual model for a plug-in hybrid vehicle.
- Optimization of an existing model of a heavy-duty FCHEV.
- Development of suitable energy management strategies (EMS) for controlling the two studied vehicles. This has involved the integration of artificial intelligence techniques to maximize the performance of the strategies.

1.3 General outlines

This introduction (**chapter 1**), which provides a general overview of the thesis, is the first of the seven chapters that make up the thesis. This is a list of each chapter's primary contents:

Chapter 2 details the literature review of alternative fuels for reducing GHG emissions. Biofuels and e-fuels are considered, with a particular emphasis on hydrogen, including discussions on its production, storage, and distribution.

In **chapter 3**, the operating principles of internal combustion engines are discussed. The description of the developed virtual model is preceded by a brief literature review on combustion models. Two applications of the model are then presented. The first one focuses on the study of water injection in a spark-ignition port fuel injection engine to increase power and efficiency. A correlation for calculating the laminar flame speed, taking into account the effects of water presence, is provided. The second application involves the validation of the model for a hydrogen engine. A new correlation for the laminar flame speed is developed based on chemical kinetics calculations. The thermal

diffusion effects causing hydrogen flame instability are considered. Finally, a numerical-experimental comparison is presented for different indicated mean effective pressure (IMEP) and air-fuel ratios.

Chapter 4 provides an overview of fuel cell systems, including a discussion of various widely adopted technologies. It also includes a literature analysis of key fuel cell models, followed by a detailed description of the model used for developing the FCHEV model discussed in the subsequent chapter.

Chapter 5 provides a description and analysis of the primary powertrain technologies. The main focus is directed towards hybrid vehicles equipped with internal combustion engines and fuel cell vehicles, which are the key subjects of study in this thesis. Additionally, an examination of BEVs is conducted, highlighting their respective pros and cons. Furthermore, detailed descriptions are provided for the two vehicle models under investigation, laying the foundation for the subsequent chapter's elucidation of their associated control strategies.

The first part of **Chapter 6** provides a comprehensive description of the main EMSs for hybrid vehicles. The study then proceeds to present the results of the investigation on the Efficient Thermal/Electric Skipping Strategy (ETESS), which has been appropriately extended to accommodate the operation of the previously discussed plug-in hybrid vehicle. Furthermore, a concise introduction to neural networks and artificial intelligence sets the stage for a literature review on AI-driven EMS. Lastly, the study encompasses the development and examination of a predictive control strategy for the heavy-duty FCHEV, utilizing the model discussed in the preceding chapter.

The most important outcomes of this study's work and the key conclusions are finally summarized in **chapter 7**. The expertise and knowledge gained during the production of this thesis are also used to suggest some recommendations for future directions.

References

[1] *OECD.org - OECD*. URL: `https://www.oecd.org/` (visited on 06/21/2023).

[2] *International Energy Outlook - U.S. Energy Information Administration (EIA)*. URL: `https://www.eia.gov/outlooks/ieo/index.php` (visited on 06/21/2023).

[3] *Global Greenhouse Gas Emissions: 1990-2020 and Preliminary 2021 Estimates*. Rhodium Group. URL: `https://rhg.com/research/global-greenhouse-gas-emissions-2021/` (visited on 06/21/2023).

[4] *Short-Term Energy Outlook - U.S. Energy Information Administration (EIA)*. URL: https://www.eia.gov/outlooks/steo/data.php (visited on 06/21/2023).

[5] *European Green Deal*. 2022. URL: https://www.consilium.europa.eu/en/policies/green-deal/ (visited on 06/21/2023).

[6] *AECC key messages on Fit for 5*. AECC. URL: https://www.aecc.eu/aecc-key-messages-on-fit-for-55/ (visited on 06/21/2023).

[7] *Europe steps back from 2035 ICE ban*. URL: https://www.sae.org/news/2023/03/european-ice-ban (visited on 06/21/2023).

[8] Cells, {and} Fuel and Undertaking, Hydrogen 2 Joint. *Hydrogen roadmap Europe : a sustainable pathway for the European energy transition*. Publications Office, 2019. DOI: doi/10.2843/341510.

Chapter 2

Greening Transportation: Examining Alternative Fuels for Pollutant Emissions Reduction

Currently, the predominant source of energy for transportation is derived from liquid fuels obtained from fossil sources, accounting for over 95% [1]. However, the future need not be limited to this scenario, as alternative options are available. Sustainable fuels that can power internal combustion engines can be produced through various methods, offering lower carbon content compared to fossil fuels or achieving carbon neutrality, and in some cases, even carbon negativity. While certain fuels necessitate engine modifications, many can be used with existing engines, potentially allowing for the utilization of carbon-neutral fuels without the need for vehicle replacements.

Notably, oil refiners believe that achieving widespread use of carbon-neutral fuels within the proposed time-frames is feasible. A report by FuelsEurope, the European oil refiners association, outlines an approach that involves the utilization of biofuels, hydrotreated vegetable oil (HVO), fuels derived from lignocellulosic residues and waste, e-fuels, and carbon capture and storage to accomplish decarbonization targets by 2050 [2]. Although oil refiners naturally prioritize solutions involving their assets, the fact that they perceive such a transition as achievable, and present a viable pathway is noteworthy. A key advantage of many carbon-neutral fuels is their compatibility with

existing engines, allowing for the decarbonization of transportation without necessitating the purchase of new vehicles. This approach holds significant global implications, particularly in regions where electricity infrastructure is not yet well-established.

The age of vehicles varies worldwide, with an average vehicle age of 12 years in the USA [3], 11 years in Europe [4] and 5 years in China [5]. Unless substantial global subsidies for fleet renewal are implemented, many of the current new vehicles are likely to remain in operation until the 2040s. Therefore, achieving transportation decarbonization necessitates the adoption of low-carbon fuels compatible with the existing vehicle fleet.

In addition to economic incentives, this approach offers the advantage of avoiding carbon emissions associated with the manufacturing of new vehicles. Carbon-neutral fuels can be categorized into two main types: biofuels and e-fuels. These labels encompass a diverse range of hydrocarbon components, analogous to the variation observed in gasoline and diesel fuels, which consist of various chemical mixtures. Biofuels are derived from recent biomass sources, where solar energy plays a substantial role in fuel production. On the other hand, e-fuels primarily rely on renewable electricity as their main energy input. Furthermore, e-fuels often incorporate CO_2 obtained through direct air capture or from sources such as power station exhaust. It is important to note that the classification of a fuel as a biofuel or e-fuel is based on its production method rather than its performance in vehicles.

2.1 Biofuels

Biofuels hold significant potential for the decarbonization of future mobility. Biofuels are defined as fuels made from recent biomass, with the biomass source being any organic material. Theoretically, a fuel produced from biomaterial, such as plants that absorb CO_2 from the atmosphere, can achieve carbon neutrality as long as any harvested biomaterial used to create the fuel is replanted. However, in practice, the situation is not as straightforward.

There are carbon emissions associated with land use, and concerns arise regarding food supply, particularly in an unpredictable world where food security is not guaranteed. It must be ensured that biofuel crops do not displace crops necessary for food production. Additionally, the CO_2 emissions associated with biofuel production and transportation must be taken into account. Despite these challenges, biofuels have the potential to be a cost-effective solution for reducing CO_2 emissions from transportation [6, 7].

Similarly to the two main liquid fossil fuels used in transportation (gasoline and diesel), biofuels can be categorized into two groups: biogasoline and

biodiesel. In terms of combustion, biofuels and oxygenate fuels behave no differently from "conventional" hydrocarbons. However, certain properties, such as freezing point, may vary.

2.1.1 Biogasoline

Ethanol (C_2H_5OH) is a widely utilized biofuel component in gasoline fuels. Presently, bioethanol is predominantly produced through the fermentation of sugars obtained from various crops such as cassava, corn, hemp, potato, and sugarcane. Fermentation, a well-established industrial process, is followed by distillation to eliminate water content. For instance, the overall chemical equation for glucose fermentation is:

$$C_6H_{12}O_6 \rightarrow 2C_2H_5OH + 2CO_2$$

It is worth noting that this process generates CO_2. However, as the only gaseous by-product of the reaction, it can be captured. The crops mentioned earlier, as well as the method employed to produce bioethanol, rely on agricultural crops. Nevertheless, such feedstocks may not be the most suitable choice since they could be more effectively utilized for food production. These biofuels are referred to as first-generation biofuels. However, since 2013, commercial plants have successfully produced ethanol from cellulosic sources.

Cellulosic ethanol can be derived from any feed source containing cellulose, which represents the fibrous and typically non-edible part of a plant. This can include wood or any plant matteror waste.

There are two primary processes for the production of cellulosic ethanol:

1. A three-step process involving hydrolysis to break down the cellulosic material, followed by enzymatic conversion of cellulose into simple sugars, and finally fermentation and distillation, as in the conventional method.

2. Gasification, which employs partial combustion to convert the cellulosic material into gaseous carbon monoxide and hydrogen. These gases are subsequently subjected to fermentation and distillation, following the same procedure as before.

These second-generation bioethanol approaches exhibit significant promise and will play a crucial role in the development of sustainable fuels. In addition to these cellulosic approaches, bioethanol can also be produced from municipal solid waste, such as household trash and rubbish.

2.1.2 Biodiesel

Biodiesel is predominantly produced through the process of transesterification. Transesterification involves three steps: the removal of water and impurities from the feedstock, a catalyzed reaction between the lipids (fats/oils) and ethanol to generate fatty acid methyl esters (FAMEs) and glycerol, and finally the purification and removal of glycerol. The feedstocks used in this process can encompass various common waste products, such as used oils (soybean oil, vegetable oil, Jatropha, sunflower oil, and palm oil), animal fats, algae, sewage, and even used coffee grounds. The resulting group of oxygenate hydrocarbons produced from this process is referred to as FAMEs.

In comparison to bioethanol, biodiesels are frequently considered "drop-in" fuels that can be used without modifications (at least at low blend levels with fossil diesel) in many older vehicles. However, modern diesel engines equipped with high-pressure fuel systems (up to 3000 bar) have limitations on the amount of biodiesel they can accommodate due to concerns about fuel separation or even freezing (at high pressure rather than low temperature). Today, biodiesel blends are commonly used in various vehicles, including cars, trains, ships, and even aircraft.

2.2 E-Fuels/Synthetic fuels

An alternative approach to decarbonize transportation involves the utilization of fuels derived from CO_2 using electricity, commonly known as "e-fuels" [8]. E-fuels, also referred to as power-to-liquid (P2L) fuels, e-gasoline, and renewable synthetic fuels derive their names from the fact that electricity serves as the energy carrier for their production. By employing catalysts to split CO_2 into its constituent components, liquid fuel can be directly synthesized from CO_2. The CO_2 can be sourced from CO_2-rich exhaust emissions (e.g., from a power plant) or extracted directly from the atmosphere. If the manufacturing process, albeit energy-intensive, utilizes renewable energy, the resulting fuel becomes CO_2 neutral since any CO_2 emitted during combustion has been extracted from the atmosphere during its production [9].

An example pathway for a basic e-fuel is composed by:

1. Electrolysis of water to generate hydrogen:

$$2H_2O \rightarrow 2H_2 + O_2.$$

2. The reverse water-gas shift reaction (opposite to the process used for hydrogen production from coal). In this step, carbon monoxide (CO)

is produced by combining CO_2 and a portion of the hydrogen obtained from electrolysis:

$$CO_2 + H_2 \rightarrow CO + H_2O.$$

3. A hydrogenation process of some kind. This final step involves utilizing the CO generated in the second step, along with the remaining hydrogen from the first step, to produce an e-fuel (e.g., methanol) with water as a byproduct. The reaction takes place over a catalyst at high temperatures, requiring energy input:

$$CO + 2H_2 \rightarrow CH_3OH + H_2O.$$

This particular e-fuel pathway necessitates both energy and catalysts, resulting in the production of methanol (CH_3OH). Methanol can be used directly as a fuel or serve as a base for producing other fuels. Alternatively, instead of producing methanol, the third step mentioned above can be replaced with hydrocarbon synthesis from syngas (a mixture of carbon monoxide and hydrogen) via the Fischer-Tropsch process. The Fischer-Tropsch process theoretically enables the production of any hydrocarbon:

$$(2n + 1)H_n + CO \rightarrow C_nH_{2n+2} + nH_2O.$$

These long-chain, saturated hydrocarbons resemble fossil fuels and can be seamlessly integrated ("dropped-in") into existing vehicles without complications [10]. However, as the carbon number in the hydrocarbon increases, the synthesis process becomes increasingly energy-intensive and expensive. Although fuels with higher carbon numbers may have advantages in certain applications (e.g., aviation due to their higher energy density), the energy and cost implications must be considered.

While theoretically, any hydrocarbon fuel can be manufactured using the aforementioned processes, the current focus primarily revolves around oxymethylene ethers (OMEs), octanol (as a diesel substitute), and methanol (as a gasoline substitute) due to their cost-effectiveness. However, as this field rapidly develops, the focus may shift in the future.

Apart from the pathway described above, other e-fuel manufacturing routes exist. These include direct electrochemical conversion, where CO_2 is directly converted into fuel; non-thermal plasma, where high-voltage electrons convert CO_2 directly into fuel; direct bio-electrochemical conversion, where microorganisms on a biocathode convert CO_2 directly into fuel; and indirect bio-electrochemical conversion, where biocatalysts convert CO_2 and hydrogen

into methane or liquid fuels. However, these alternative methods are still in the early stages of development compared to the established approach discussed earlier, which presents lower risks.

Germany has emerged as a global leader in e-fuel initiatives, with pilot projects like Sunfire Synlink already producing fuels. Several German studies suggest that e-fuels, especially those imported from the Middle East and North Africa region, will play a crucial role in achieving carbon neutrality in Germany, particularly in freight transportation and aviation. However, this perspective is subject to ongoing debates [11]. The MENA region is well-suited for e-fuel production, and synthesis costs are expected to drop below 1 euro per liter of diesel equivalent by 2030 due to abundant solar energy and consequently low electricity costs [12].

One challenge shared by many renewable energy sources in e-fuel synthesis is the intermittent nature of energy production. This poses a significant economic challenge for large-scale chemical plants required for e-fuel production, as they are extremely costly. While e-fuels provide a potential pathway to achieve carbon-neutral mobility, it remains uncertain whether they represent the most economically and energetically efficient solution, especially considering the limited supply of renewable electricity. Unlike biofuels, e-fuels do not require arable land and can potentially be produced in regions with abundant renewable energy sources. Nonetheless, the energy-intensive manufacturing process and high costs remain significant hurdles that need to be addressed for widespread adoption. According to Billig et al. [42], it is suggested that e-fuels will be allocated for high-value applications where the energy density of liquid hydrocarbons is crucial, such as long-distance road transportation or aviation [48]. Irrespective of the specific application, the majority of studies concur that e-fuels are indispensable in achieving the EU climate targets within the transport sector.

2.3 Hydrogen

In recent times, the adoption of hydrogen as the primary fuel in the transportation industry has emerged as a crucial approach for accomplishing the decarbonization goals set for 95% of the transport sector by 2050 to limit the average global temperature increase below 2°C with respect to 1990 levels. Even though hydrogen is not the only path to decarbonization, it is considered an essential option among a set of other technologies [13]. In fact, it implies several advantages that can be summarized in:

- Hydrogen production can be carried out using a wide range of energy

resources.

- Hydrogen is the cleanest choice available, producing just water when used in fuel cells or combustion processes.
- Hydrogen can be used in a variety of ways to meet energy needs, including hydrogen fuel cell cars, homes, energy carriers, and systems that provide both heat and electricity.
- Using clean fuels like hydrogen or ammonia for maritime operations, off-grid offshore wind energy can play a significant part in decarbonizing the maritime sector.
- Hydrogen serves as an ideal energy carrier and can be utilized as a storage medium for surplus energy.
- Unlike carbon-based fuels hydrogen does not emit CO_2 emissions during its use.

In the following, the aspects related to its production, distribution and storage are described and analyzed.

2.3.1 Hydrogen Production

The production of hydrogen can be categorized into four main types: green, purple, grey and blue. Green hydrogen is produced using renewable energy sources, while purple hydrogen relies on nuclear energy. Blue hydrogen involves coal gasification or natural gas combined with carbon capture and storage (CCS) methods. Although the process of producing grey hydrogen (steam methane reforming), which has a high CO_2 intensity, is now the most popular, green hydrogen can also be produced using renewable electricity. When fueled by renewable energy sources, electrolysis, a common method that uses electrical current to divide water into oxygen and hydrogen, can produce hydrogen with no direct CO_2 emissions. The Cost of producing hydrogen, particularly green hydrogen, is a significant barrier. To put it in perspective, for every unit of energy generated, steam reforming-based production is approximately three times more expensive than using natural gas. Similarly, electrolysis, which relies on electricity priced at 5 cents per kilowatt-hour (kWh), is almost twice as costly as natural gas-based production. However, a recent report by Renewable World Energy suggests that in the United States, wind energy can be sold at an historically low rate of 2.5 cents per kWh, significantly reducing the cost of electricity to less than a quarter of that for natural gas-based hydrogen production [14].

2.3.2 Hydrogen Storage

Efficient hydrogen storage is essential to address the intermittent nature of renewable energy sources and ensure a reliable fuel supply. Hydrogen can be stored in various forms, including as a gas, liquid, or solid, depending on the chosen method. When it comes to gas storage, hydrogen can be compressed into cylinders or containers made of materials such as steel, aluminum, or reinforced plastic-carbon fiber composites. Another option is storing gaseous hydrogen in underground cavities. These storage methods are feasible since hydrogen can withstand high pressures of up to 700 bar. Gas storage offers advantages such as low cost, simplicity, and fast charging and discharging processes. However, it's important to note that the volume density of hydrogen in its gaseous state is not directly proportional to storage pressure, meaning that higher pressure doesn't always result in increased storage capacity [15].

Compared to its gaseous form, liquid hydrogen storage has the benefit of having more energy per unit of volume. To keep the temperature at or below -253°C, however, specific storage containers are needed due to the substance's extremely low boiling point (-252.8°C). Due to its reliance on an insulated system and exact temperature control, this method is normally suggested for short-term storage. Cryo-compressed hydrogen storage, an alternative strategy, reduces boil-off losses linked to conventional cryogenic technologies while boosting the storage capacity from 70 g/l at 1 bar to 87 g/l at 240 bar [16].

Through chemisorption or physisorption, hydrogen molecules are grouped with other substances or hydrates for solid-state storage. In the process of chemisorption, hydrogen atoms react and integrate into the crystal structure of solid materials to produce metal hydrates. On the other hand, physisorption entails bonding hydrogen molecules to the material's surface. The ability to store more hydrogen in a smaller space is a benefit of solid-state storage. However, the choice of this option should take into account the unique uses of hydrogen, since it may provide difficulties with cost, regeneration, and transportation, depending on the strategy and material chosen [17].

Hydrogen is being used more frequently to produce electricity and as the main fuel for automobiles because of its adaptability and minimal negative effects on the environment. As a result, transportable storage systems were created for this use. However, not all hydrogen storage methods are equally useful. This method is difficult to apply, for instance, because liquid hydrogen must be kept below its boiling point, and it is also less efficient. Similar drawbacks apply to solid-state mobile storage devices, including high material prices, security worries, stability problems, and operating stresses. On the other hand, compressed hydrogen storage devices have been used in the transportation

industry with success. These systems allow for fast recharging in less than 10 minutes, function at room temperature, and offer a positive gravimetric energy value of 120 MJ/kg, which is nearly four times that of gasoline. The viability of compressed gas as a suitable option for incorporating hydrogen in vehicles has been emphasized by the Society of Automotive Engineers (SAE) through the development of the SAE J2600 standard [18].

2.3.3 Hydrogen Distribution

The transportation of hydrogen relies on the chosen storage method. Hydrogen gas can be conveyed via pipelines or tube trailers. Pipelines entail high costs, with construction expenses reaching approximately 80,000 USD per 100 meters [19]. Consequently, pipeline transportation of hydrogen is economically feasible only when handling large quantities. Conversely, transportation via tube trailers offers a more affordable alternative, albeit with an inherent risk of explosion [20]. This approach is better suited for small-scale hydrogen transportation. Thus, pipelines are typically employed to convey hydrogen in proximity to petrochemical complexes, where significant hydrogen production occurs. Tube trailers, on the other hand, are commonly used when transporting hydrogen to remote areas.

Liquefied hydrogen, such as liquid hydrogen or ammonia can be transported using tanker lorries, even within urban environments, owing to their excellent safety profile. However, establishing liquefaction facilities necessitates substantial investment, and energy efficiency tends to be relatively low. Ammonia, serving as a hydrogen transportation medium, liquefies at -33°C, offering enhanced energy efficiency [21]. Additionally, hydrogen transportation in the form of ammonia provides several advantages, including the utilization of existing ammonia infrastructure for storage and transportation purposes. Nevertheless, the dehydrogenation technology required to extract hydrogen from ammonia is still in the developmental stage, warranting further advancements [22].

Hydrogen refueling stations can be supplied with hydrogen through centralized (off-site) or localized (on-site) methods. In the centralized approach, hydrogen is generated in a specific area and then transported to the refueling station using pipelines or tube trailers. Although hydrogen production costs are relatively low, transportation costs can be significant [19, 20]. Conversely, the local supply method involves producing hydrogen directly at the refueling station through processes like reforming liquid petroleum gas (LPG) or natural gas (NG), or via water electrolysis. If the refueling station is located far from the hydrogen production site, this method can help reduce transportation costs. However, it comes with a higher installation cost due to the need for hydrogen production facilities at the refueling station [19, 20].

Hydrogen distribution and refueling processes must also consider safety aspects as a crucial factor. To gain wider acceptance within communities, it is important to address the prevention and mitigation of hydrogen-related hazards, as well as effectively managing incidents when they occur. The unique characteristics of hydrogen pose challenges in terms of safety. These include its susceptibility to leakage, low ignition energy, and a wide range of fuel-to-oxygen ratios for combustion. One notable feature of hydrogen is its high auto-ignition temperature, which is the temperature at which the fuel ignites without the need for an external ignition source (500 °C) [23]. Despite its broad flammability range, the auto-ignition temperature of hydrogen remains relatively consistent, even at higher oxygen concentrations and pressures [24]. While a high auto-ignition temperature is generally seen as safer, it is essential to note that the initial energy required to ignite hydrogen is exceptionally low compared to other fuels. Furthermore, hydrogen exhibits an extremely low rate of electro-conductivity, meaning that both the flow and agitation of hydrogen can potentially generate an electrostatic charge, leading to spark formation in both liquid and gaseous states. Therefore, it is crucial to eliminate potential ignition and heat sources (such as static electricity, hot objects, open flames, and electrical equipment) and ensure proper grounding of hydrogen-related devices.

2.4 Summary and conclusions

Along this chapter, the main alternatives to traditional fossil fuels have been discussed. Sustainable fuels capable of powering vehicles can be produced through various methods, offering lower carbon content compared to fossil fuels or even achieving carbon neutrality, and in some cases, carbon negativity. Biofuels, such as ethanol and biodiesel, are derived from renewable sources like crops or waste materials. These fuels can be blended with conventional gasoline and diesel or used in dedicated vehicles. Additionally, advanced biofuels produced from non-food feedstocks, such as algae or cellulosic materials, offer even greater emissions reductions and land-use efficiency. Furthermore, the concept of e-fuels emerges as a promising solution. E-fuels are produced by capturing and utilizing carbon dioxide emissions from industrial processes or directly from the atmosphere. Renewable electricity is used to convert carbon dioxide and water into synthetic hydrocarbon fuels like methane, methanol, or even sustainable aviation fuels. Hydrogen also represents an alternative fuel for reducing pollutant emissions in the transportation sector, offering numerous advantages, including its high versatility and functioning as an energy buffer. All the mentioned fuels share the common characteristic that their adoption

requires supportive policies and investments in research, development, and infrastructure. Governments, industries, and stakeholders must collaborate to create an enabling environment for the production, distribution, and use of these fuels. It is crucial to incentivize the scaling up of sustainable fuel production and deployment, as they have the potential to play a vital role in decarbonizing the transportation sector and achieving a more sustainable future.

References

[1] Kalghatgi, Gautam. "Is it really the end of internal combustion engines and petroleum in transport?" In: *Applied Energy* 225 (2018), pp. 965–974. DOI: 10.1016/j.apenergy.2018.05.076.

[2] FuelsEurope. *Clean Fuels for All*.

[3] *The average age of cars on America's roads went up again, report says*. CNET. URL: https://www.cnet.com/roadshow/news/average-vehicle-age-increase-america/ (visited on 06/08/2023).

[4] *Average age of the EU vehicle fleet, by country*. ACEA - European Automobile Manufacturers' Association. 2023. URL: https://www.acea.auto/figure/average-age-of-eu-vehicle-fleet-by-country/ (visited on 06/08/2023).

[5] *The boom of China's automotive aftermarket is imminent*. Ipsos. 2016. URL: https://www.ipsos.com/en/boom-chinas-automotive-aftermarket-imminent (visited on 06/08/2023).

[6] Leitner, Walter, Klankermayer, Jürgen, Pischinger, Stefan, Pitsch, Heinz, and Kohse-Höinghaus, Katharina. "Advanced Biofuels and Beyond: Chemistry Solutions for Propulsion and Production". In: *Angewandte Chemie International Edition* 56.20 (2017). _eprint: https://onlinelibrary.wiley.com/doi/pdf/10. pp. 5412–5452. DOI: 10.1002/anie.201607257.

[7] Mendiara, T. et al. "Negative CO2 emissions through the use of biofuels in chemical looping technology: A review". In: *Applied Energy* 232 (2018), pp. 657–684. DOI: 10.1016/j.apenergy.2018.09.201.

[8] Artz, Jens et al. "Sustainable Conversion of Carbon Dioxide: An Integrated Review of Catalysis and Life Cycle Assessment". In: *Chemical Reviews* 118.2 (2018). Publisher: American Chemical Society, pp. 434–504. DOI: 10.1021/acs.chemrev.7b00435.

[9] Hombach, Laura E. et al. "Economic and environmental assessment of current (2015) and future (2030) use of E-fuels in light-duty vehicles in Germany". In: *Journal of Cleaner Production* 207 (2019), pp. 153–162. DOI: 10.1016/j.jclepro.2018.09.261.

[10] Marketing, F. E. V. *Almost CO2-neutral Mobility | FEV Corporate Magazine*. URL: https://magazine.fev.com/en/almost-co2-neutral-mobility/ (visited on 06/08/2023).

[11] *Berlin and Brussels should realise that e-fuels for trucks are a bad, expensive bet*. www.euractiv.com. Section: Transport. 2019. URL: https://www.euractiv.com/section/transport/opinion/berlin-and-brussels-should-realise-that-e-fuels-for-trucks-are-a-bad-expensive-bet/ (visited on 06/08/2023).

[12] Marketing, F. E. V. *Carbon-neutral transport – the role of synthetic fuel | FEV Corporate Magazine*. URL: https://magazine.fev.com/en/carbon-neutral-transport-the-role-of-synthetic-fuel/ (visited on 06/08/2023).

[13] Cells, {and} Fuel and Undertaking, Hydrogen 2 Joint. *Hydrogen roadmap Europe : a sustainable pathway for the European energy transition*. Publications Office, 2019. DOI: doi/10.2843/341510.

[14] Burger, Andrew. *US Wind Energy Selling At Record Low Price of 2.5 Cents per kWh*. Renewable Energy World. 2015. URL: https://www.renewableenergyworld.com/wind-power/us-wind-energy-selling-at-record-low-price-of-2-5-cents-per-kwh/ (visited on 06/12/2023).

[15] Abe, J. O., Popoola, A. P. I., Ajenifuja, E., and Popoola, O. M. "Hydrogen energy, economy and storage: Review and recommendation". In: *International Journal of Hydrogen Energy* 44.29 (2019), pp. 15072–15086. DOI: 10.1016/j.ijhydene.2019.04.068.

[16] Edalati, Kaveh et al. "Design and synthesis of a magnesium alloy for room temperature hydrogen storage". In: *Acta Materialia* 149 (2018), pp. 88–96. DOI: 10.1016/j.actamat.2018.02.033.

[17] Langmi, Henrietta W., Engelbrecht, Nicolaas, Modisha, Phillimon M., and Bessarabov, Dmitri. "Chapter 13 - Hydrogen storage". In: *Electrochemical Power Sources: Fundamentals, Systems, and Applications*. Ed. by Tom Smolinka and Jurgen Garche. Elsevier, 2022, pp. 455–486. DOI: 10.1016/B978-0-12-819424-9.00006-9.

[18] *J2600_201211: Compressed Hydrogen Surface Vehicle Fueling Connection Devices - SAE International*. URL: https://www.sae.org/standards/content/j2600_201211/ (visited on 06/10/2023).

[19] Korean Energy Economics Institute. *Energy focus*. 2019.

[20] International Energy Agency. *Technology roadmap: hydrogen and fuel cells*. 2015.

[21] Staffell, I. et al. *The role of hydrogen and fuel cells in the future energy systems*. 2017.

[22] Intralink. *The hydrogen economy South Korea, market intelligence report*. 2021.

[23] *Basic Hydrogen Properties | Hydrogen Tools*. URL: https://h2tools.org/hyarc/hydrogen-data/basic-hydrogen-properties (visited on 06/09/2023).

[24] Mazloomi, Kaveh and Gomes, Chandima. "Hydrogen as an energy carrier: Prospects and challenges". In: *Renewable and Sustainable Energy Reviews* 16.5 (2012), pp. 3024–3033. DOI: 10.1016/j.rser.2012.02.028.

Chapter 3

From Pistons to Power: Understanding Internal Combustion Engines

Internal combustion engines have long been the historical powertrain of the transportation sector. These engines revolutionized the way we move by converting the energy released from the combustion of fuel into mechanical work. The development of the first internal combustion engine can be traced back to the late 19th century, with pioneers such as Nikolaus Otto and Rudolf Diesel making significant contributions. Since then, internal combustion engines have powered various modes of transportation, from automobiles to airplanes, shaping the modern world's mobility. Despite advancements in electric technologies, chapter 1 highlighted the continued prevalence of internal combustion engines in the transportation sector, while acknowledging the environmental concerns associated with them. This has led to the exploration of new engine technologies and alternative solutions, which will be discussed in this chapter that aims to present some of the possibilities for reducing the environmental impact of internal combustion engines. To achieve this goal, it is essential to first explain the fundamentals and operating principles of internal combustion engines, followed by an exploration of the currently utilized and emerging technologies for engine optimization. Subsequently, the development and construction of the quasi-dimensional model used in the PhD thesis to investigate two different applications of innovative engines, namely water injection and pure hydrogen fueling, are described. The results of these studies are reported in the second

part of this chapter.

3.1 Fundamentals of Internal Combustion Engines

In this section, the discussion is mainly focused on spark-ignition engine because it serves as the primary propulsion system for the majority of today's cars [1]. The four-stroke cycle is represented in Figure 3.1. To complete the sequence of events that result in one power stroke, each cylinder of the engine necessitates four strokes of its piston, equivalent to two complete revolutions of the crankshaft.

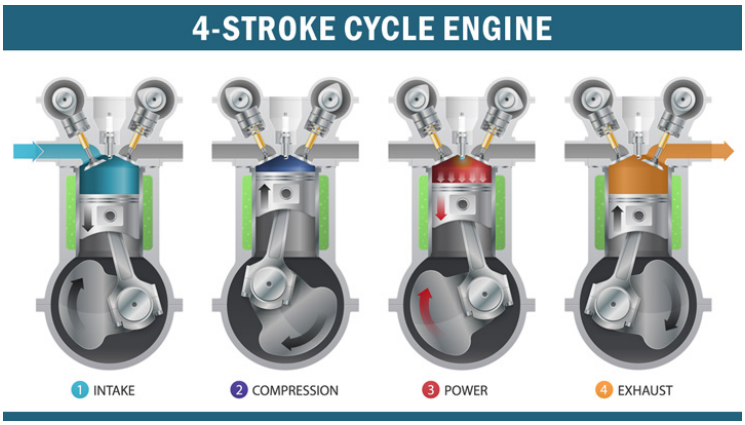

Figure 3.1: Four-stroke SI engine cycle. Source [2].

The operational phases of the engine can be described as follows:

1. **Intake phase**: To inhale air into the combustion chamber, the piston depresses as it moves from the Top Dead Center (TDC) to the Bottom Dead Center (BDC) of the cylinder. The intake valve is typically opened 10–40 CAD before the Top Dead Center (BTDC) and then closed 30–50 CAD after the Bottom Dead Center (ABDC), with the main goal being to maximize the air mass introduced to achieve a high volumetric efficiency.

2. **Compression phase**: This represents the closed valve phase, which occurs when both the intake and exhaust valves are sealed shut. During this phase, the piston moves from BDC to TDC, compressing the fuel-air mixture and elevating the pressure and temperature within the combustion chamber. As the piston approaches TDC, the mixture ignites either spontaneously or through the ignition of a spark plug, resulting in a rapid increase of pressure and temperature.

3. **Expansion phase**: It begins after the compression stroke has finished. With the goal of converting the heat emitted from the chemical energy stored in the fuel into mechanical work, the piston travels from the TDC to the BDC. At the moment the exhaust valve (EVO) opens, this period comes to a close.

4. **Exhaust phase**: The two sub-phases of the exhaust phase are spontaneous exhaust (from EVO to BDC) and forced exhaust (from BDC to EVC). The burned gases can naturally escape from the cylinder into the exhaust pipes because the cylinder pressure is initially higher than the exhaust manifold pressure. The exhaust gases are then expelled from the cylinder by the volume reduction when the piston advances from BDC to TDC. The engine cycle restarts as soon as the intake valves open.

Controlling the air/fuel mixture input into the cylinder is essential to achieve the optimum load level and ensure effective combustion. The design of the intake pipes, the throttle valve, and, if necessary, the existence of a turbocharging system are some of the variables that affect how the air flow is regulated. Port Fuel Injection (PFI) and Direct Injection (DI) are the two ways to carry out fuel injection. While DI distributes gasoline directly into the cylinder at a higher pressure, PFI injects fuel into the intake port at a lower pressure. DI systems improve fuel diffusion and vaporization due to the higher injection pressure. However, it should be noted that compared to PFI, DI systems may result in increased particulate matter (PM) when fuel comes into contact with the cylinder walls [3]. For a beneficial effect on the combustion process, heat transfer, and air/fuel mixing, the flow motion inside the cylinder must be optimized. Three different flow patterns, tumble, swirl, and squish, can be produced by adjusting intake port design, valve geometry, and combustion chamber form. The combustion rate and charge mixing are intended to be improved by these flow patterns. An electric discharge across the spark plug, normally timed before the TDC, causes combustion to occur once the full air/fuel mixture has been fed into the combustion chamber and the valves have been sealed. From the spark plug, a turbulent flame spreads outward, filling the chamber before going out as it comes into touch with the cylinder walls. The combustion process normally lasts 40 to 60 crank angle degrees (CADs), which causes the in-cylinder pressure to rise quickly. Following the expansion phase, the cylinder releases exhaust gases during the exhaust phase in order to get ready to take in a fresh charge for the following cycle. Depending on the particular engine architecture, it may be possible to modify engine control parameters like Spark Advance (SA), valve timing, throttle position, or air/fuel ratio to reach the desired load. It's crucial to remember that even in the

absence of adjustments to these control variables, two successive engine cycles are never the same. Cycle to Cycle Variation (CCV) is a result of changes in the local flow motion, turbulence levels, and mixture homogeneity, particularly close to the spark plug. CCV introduces variations in the rate of heat release, which affect the amount of usable work produced by each combustion event as well as fuel use and pollutants. The development of the best engine control systems is challenging due to the stochastic and unpredictable character of CCV.

3.1.1 Internal cylinder flow and turbulence development

The gas motion inside the cylinder plays a crucial role in governing the combustion process of SI engines. It not only influences the heat transfer within the engine but also affects the turbulence characteristics of the flow. The flow motion within the cylinder is primarily influenced by the intake process, which controls the initial in-cylinder flow. As the compression stroke begins, the gas motion undergoes significant modifications. In the following, the key aspects of gas motion inside the cylinder, which are influenced by the flows entering and exiting through valves or ports, as well as the motion of the piston and the cylinder/piston geometry, are described. As the piston descends from the TDC to the BDC during the intake phase, air is forced into the cylinder and a pressure differential is created between the intake manifold and the combustion chamber. An annular conical jet with axial and radial velocities greater than the mean piston speed is created in the cylinder as a result of the intake valve opening. The principal cause of turbulence motion is the separation of the jet from the valve heads and seats, which results in shear layers with enormous velocity gradients. Recirculation zones are produced by this procedure close to the cylinder wall and head, as well as beneath the valve head. Then, the jets interact with the cylinder wall generating large-scale rotating flow, which brings in the cylinder fluid kinetic energy and shears. Thus, the main factors contributing to obtain the proper flow motion are the design of the intake valves, port geometries, and shape of the combustion chamber.

These factors contribute to the turbulence of the charge motions entering the engine cylinder. When comparing the rates of transfer and mixing in turbulent flows to those caused by molecular diffusion, the former is many times higher. This "turbulent diffusion" results from the small-scale variations in the flow field and boosts the momentum, heat, and mass transfer rates, which are crucial for the successful operation of SI engines. Dissipative fluxes characterize all turbulence. This is because the fluid is deformed by the viscous shear stresses, which improve internal energy at the expense of turbulent kinetic energy. Energy is necessary for the turbulence creation process; in fact, if this

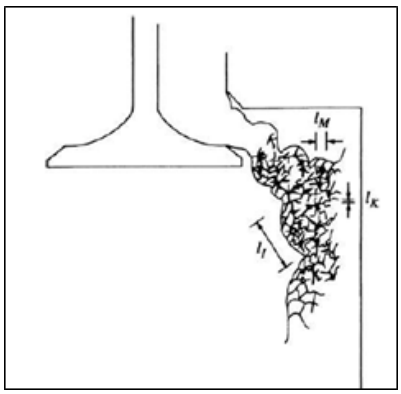

Figure 3.2: Schematic of jet created by the flow through the intake valve indicating its turbulent structure [4]

is lacking, the turbulence degrades. Shear in the mean flow structures is thus a typical source of energy for the turbulent velocity fluctuation. In particular, turbulence is three-dimensional, rotating, and characterized by significant fluctuating vorticity. In the case of an engine cylinder, the flow is unstable and may show significant cycle-to-cycle changes. It is composed of turbulent shear layers, recirculating zones, and boundary layers. Both large-scale and small-scale turbulent motions are crucial elements influencing the overall flow behavior in this situation.

It is important to note that because the flow pattern into the cylinder changes throughout the engine cycle, applying these turbulence principles to the subject of engines is challenging. Additionally, the mean flow might significantly alter from one cycle to the next. As a result, turbulent fluctuations about the mean flow of a given cycle occur along with cycle-to-cycle variations in the mean or bulk flow at any instant in the cycle. Since turbulent flow is erratic or random, statistical approaches are frequently used to define this phenomenon [4]. The decomposition of the velocity components in the mean values and their turbulent components in this situation is the conventional method for flow characterisation.

There are various length scales that describe various elements of the behavior of turbulent flows. The system boundaries set a size limit on the greatest eddies in the flow, whereas molecular diffusion controls the size of the smallest eddies. The schematization of a jet entering the cylinder from the intake valve in Figure 3.2 provides a qualitative illustration of the three basic length scales. Large eddies in the conical jet flow between the valve and seat are to blame for the majority of the turbulence production. Integral length scale l_t is used

to measure the biggest scales in turbulent flow. A spectrum of smaller-sized eddies is placed over this scale, fed by the ongoing disintegration of bigger eddies. These tiniest structures are where turbulence energy is dissipated. The kinetic energy is converted into thermal energy at the Kolmogorov scale l_k by the action of molecular viscosity. The microscale (Taylor microscale) l_M is the final scale that defines a turbulent flow. It is described by coupling the turbulence intensity to the varying strain rate of the turbulent flow field.

Moving to the in-cylinder flow patterns, the swirl effect refers to the organized rotational movement of the air-fuel mixture around the cylinder axis in an internal combustion engine. It is achieved by introducing the intake flow into the cylinder with an initial angular momentum along the cylinder axis. Typically, the swirl motion generated during the intake phase persists throughout the compression, combustion, and expansion phases, although it gradually diminishes due to frictional losses during the engine cycle. The degree of swirl can be controlled depending on the design of the combustion chamber. For instance, the rotational motion created during the intake phase significantly increases during compression in engines with bowl-in-piston combustion chambers. Diesel engines and some engines with stratified charges frequently use swirl to speed up the mixing of the injected fuel and air charge. In order to speed up combustion, it is also used in spark-ignition engines. The pre-combustion chamber holes in pre-chamber engines are oriented correctly during compression to produce the swirl there as well.

By encouraging quicker burn rates, the tumble effect is used in SI engines to improve the combustion process. The rotation of the air-fuel mixture around an axis that is perpendicular to the cylinder axis is referred to as tumble. It is frequently noticed in combustion chambers with pent-roofs that have four valves with slanted valve stems. In order to create tumble, the intake ports are placed so that the incoming airflow passes through the area above the valve head and valve seat, causing the air to move transversely. The flow moves downhill near the liner on the opposite side of the intake valves as the piston descends. The flow then changes its direction along the piston crown, flows up the liner, and completes its rotation. The transverse flow velocity beyond the valve is higher due to the uneven distribution of the intake-valve open area, which results in more kinetic energy being stored within this tumbling flow. It is significant to note that uneven use of the valve open area increases flow resistance at the intake valve and lowers volumetric efficiency of the engine. The ascending piston compresses the tumble flow during the compression phase, causing it to fragment into smaller vortices and produce turbulent kinetic energy. Following the spark ignition event, the combustion rate is increased in part by this turbulent energy. Even though it may reduce engine breathing

capacity at higher loads and speeds, the tumble phenomena is largely used in SI engines to generate faster burn rates, notably for better part-load operating conditions.

3.1.2 Turbulent combustion

The quick release of chemical energy from the fuel during the combustion process results in high-pressure, high-temperature burnt gases that exert force on the piston. This mechanism is important to the operation of ICEs. Combustion must happen quickly compared to the length of the entire cycle in order to convert energy effectively. The interplay between the growth of the flame and turbulent flow has a significant impact on the combustion process. The spark plug's electric discharge is what starts the flame, and the flow field is created during the intake phase and changed during the compression stroke. The evolution of the flame is depicted in Figure 3.3 in a 2D depiction, which was acquired via digital imaging in an optically accessible single-cylinder PFI engine [5]. The pictures illustrate various crank angles and show significant stages of combustion. The spark ignites at 3 degrees BTDC, and the first visible flame appears at 2 degrees ATDC, at first taking on an almost round shape. Early flame development is the term for this initial stage, when laminar conditions are predominantly used for flame propagation. At around 6 degrees ATDC, the flame form starts to change as the combustion advances as a result of the interaction with turbulent flow, producing wrinkles and corrugations on the flame surface. The turbulent flame propagation phase begins as a result of this interaction, which increases the burning rate. Once the flame reaches the cylinder walls at about 16 degrees ATDC, combustion is complete and the flame enters the flame termination phase.

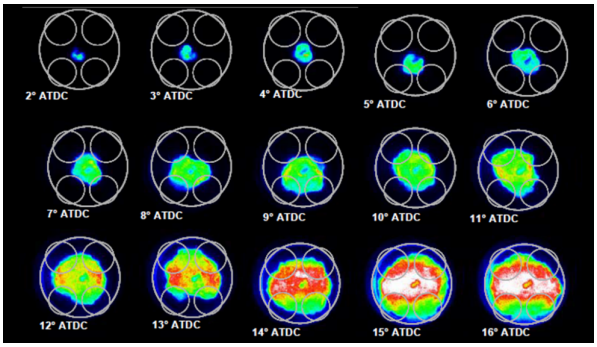

Figure 3.3: UV-visible digital images of the flame propagation, SA= 3 CAD [5]

Three crucial factors influencing the combustion process in ICEs are the spark advance, laminar flame speed, and turbulent flow within the cylinder. The SA plays a vital role in achieving optimal performance and maximum brake torque (MBT). An excessively early ignition could lead to increased pressure during the compression stroke, resulting in reduced expansion work. Conversely, a highly delayed spark timing causes a late pressure peak during the expansion stroke, leading to a decrease in available work. The ideal SA is determined by maximizing the cycle area and available work. In a conventional SI engine, the SA is typically set to achieve 50% mass fraction burned (CA50) around 7-8 CAD ATDC [4]. However, if abnormal combustion occurs, such as knock, the SA may be adjusted to a delayed value relative to the MBT to mitigate the phenomenon.

As described before, after the spark event, a smooth quasi-laminar flame develops between the spark plug electrodes, characterized by a reduced thickness (δ_L) and a laminar flame speed (S_L). Experimental studies have been conducted to determine the laminar flame speed, resulting in various correlations proposed for different air-fuel blends [6–8]. Early formulations, such as the power law formula, neglected cross-influences between pressure and temperature, while newer formulations considered these factors [7]. However, due to limitations in experimental testing, alternative models based on reaction kinetics calculations have been developed to improve accuracy under engine-like conditions [9, 10]. The selection of surrogate fuels and the composition of the fuel blend also have a significant impact on laminar flame speed predictions. Experimental data show that laminar flame speed peaks near stoichiometric or slightly rich air-fuel mixtures. The laminar flame speed decreases with increasing pressure, and the presence of EGR significantly reduces it. In conventional SI gasoline engines, a maximum laminar flame speed of approximately 1 m/s is typically observed. To ensure complete combustion within the combustion chamber, turbulent flow generation is necessary to enhance the combustion velocity.

A flow in which the motion of the particles fluctuates erratically in space and time with significant velocity field fluctuations is what defines turbulence as a three-dimensional phenomenon. As a result, the flow is uneven, rotating, diffusive, and composed of eddies of varying sizes. The so-called turbulent energy cascade mechanism, which involves the interaction of the vortices to produce an energy transfer from the larger eddies to the smaller ones, takes place during the engine cycle. In this regard, a distinctive time scale for macro- and micro-vortices may be defined, and it is as follows:

Integral length scale (L_t): This scale quantifies the largest structures in the turbulent flow, characterized by low frequency and large fluctuations. It is obtained by integrating the autocorrelation coefficient of the fluctuating

velocity between adjacent points in the flow. The equation for calculating L_t is:

$$L_t = \int_0^\infty R_x dx$$

where $R_x = \frac{1}{N_m - 1} \sum_{i=1}^{N_m} \frac{u(x_0)u(x+x_0)}{u'(x_0)u'(x+x_0)}$, and N_m represents the number of measurements.

Taylor length scale (L_M): This scale relates the fluctuating strain rate of the turbulent flow field to the turbulence intensity. The equation for L_M is:

$$\frac{\partial u}{\partial x} \approx \frac{u'}{L_M}$$

Kolmogorov length scale (L_k): This scale corresponds to the smallest scale of turbulent motion, where kinetic energy dissipates into thermal energy through molecular viscosity. The equation for L_k is:

$$L_k = \left(\frac{\nu^3}{\epsilon} \right)^{\frac{3}{4}}$$

Depending on the interaction between the flame and the turbulent flow field, various combustion regimes can arise, each characterized by specific flame evolution and shape. These regimes are classified based on a comparison of characteristic lengths, speeds, and times. Table 3.1.2 summarizes the characteristic speed, length, and time scales of turbulent combustion.

Scale	Speed	Length	Time
Chemistry	S_L	δ_L	$\tau_L = \frac{\delta_L}{S_L}$
Kolmogorov	u_k	L_k	$\tau_k = \frac{L_k}{u_k}$
Integral	u'	L_t	$\tau_t = \frac{L_t}{u'}$

Table 3.1: Characteristics of speed, length, and time scales in turbulent combustion.

These comparisons can be represented in the Borghi diagram, as depicted in Figure 3.1.2. The diagram helps define possible combustion regimes in premixed turbulent flames. Three dimensionless numbers are introduced for this purpose: Reynolds number (Re), Damköhler number (Da), Karlovitz number (Ka). The Reynolds number represents the ratio between inertial forces associated with turbulent flow motion and viscous forces. A fully developed turbulent flow occurs when Re is large, indicating the dominance of inertia over viscosity. The

relationship between flame thickness and laminar flame speed ($\delta_L = \frac{\nu}{S_L}$) can be derived using Re:

$$Re = \frac{u'^2 L_t}{\nu} \quad \Rightarrow \quad \frac{u'}{S_L} = Re \left(\frac{L_t}{\delta_L}\right)^{-1}$$

The Damköhler number represents the ratio between the turbulence characteristic time of the macro-vortices and the chemical kinetics characteristics time. The relationship between flame thickness and laminar flame speed can be derived using Da:

$$Da = \frac{\tau_t}{\tau_L} = \frac{\frac{L_t}{u'}}{\frac{\delta_L}{S_L}} \quad \Rightarrow \quad \frac{u'}{S_L} = Da^{-1} \frac{L_t}{\delta_L}$$

the Karlovitz number defines the ratio between the characteristic time of the chemistry and the characteristic time of the micro-vortices. The flame thickness is smaller than the Kolmogorov scale when Ka is less than 1, and the chemical time scale is shorter than any turbulent scale. This suggests that the chemical processes taking on within the flame front are unaffected by turbulence. The reactive zone of the flame is penetrated by turbulent eddies when Ka rises above unity. Using Ka, it is possible to determine the connection between flame thickness, Kolmogorov scale, and laminar flame speed:

$$Ka = \frac{\tau_L}{\tau_k} = \frac{\frac{\delta_L}{S_L}}{\frac{L_k}{u_k}} = \left(\frac{\delta_L}{L_k}\right)^2 \quad \Rightarrow \quad \frac{u'}{S_L} = Ka^{\frac{2}{3}} \left(\frac{L_t}{\delta_L}\right)^{\frac{2}{3}}$$

Five distinct combustion regime zones can be found in the Borghi diagram by equating the aforementioned numbers to one. Laminar flame speed is greater in the wrinkled flamelets zone than turbulence intensity, indicating that the flame front is not corrugated by turbulence. Furthermore, the presence of turbulence has little impact on chemical kinetics because Ka is less than 1. The combustion regime changes to the corrugated flamelets area as the turbulence intensity rises and surpasses the laminar speed.

3.1.3 Knock phenomena

In SI-ICE, the knock phenomenon is a substantial abnormal combustion occurrence. When the end gas auto-ignites, it is characterized by the occurrence of noise that is transferred through the engine structure. As a result, there is an abrupt release of heat, and pressure waves spread throughout the combustion chamber. For a variety of reasons, it is best to avoid the knock phenomenon. First of all, it results in less work being available due to the pressure oscillations'

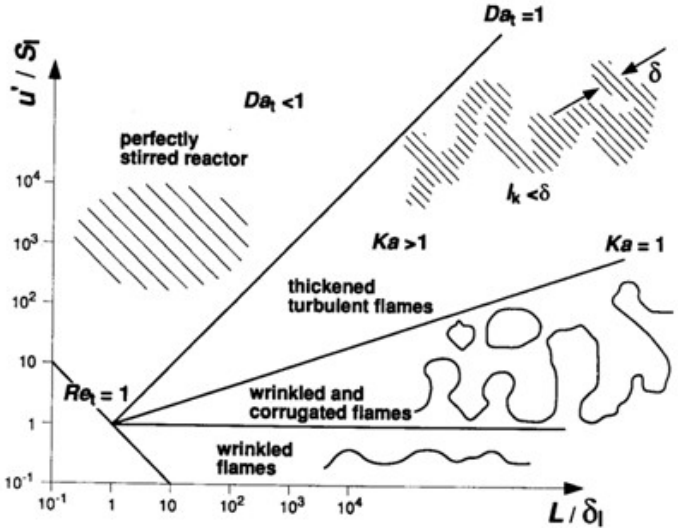

Figure 3.4: Borghi diagram and turbulent premixed combustion regimes [11].

promotion of heat transfer, which increases thermal losses. Second, the lubricant layer surrounding the cylinder may be removed if there are pressure wave reflections. Moreover, heavy knocking can cause irreversible damage to the cylinder. During severe knock, excessive heat is transferred to the combustion walls, causing overheating of the cylinder head and piston. The elevated temperature further intensifies the occurrence of knock, making the phenomenon even more severe. Without proper control, this can lead to engine failure in a short period of time. The pressure waves induced by knock create non-uniform pressure distribution, leading to variations in pressure values depending on the location of the transducer within the cylinder. To measure and quantify knock intensity, different methods have been proposed in the literature [12]. One widely adopted approach involves analyzing in-cylinder pressure signals using a flush-mounted pressure transducer in the combustion chamber. The collected pressure data is then processed using a band-pass filter in the range of 4-20 kHz. The low cut-off frequency filters out regular combustion noise, while the high cut-off frequency eliminates signal disturbances caused by sensor resonances. The pressure trace is taken by a pressure transducer to measure the knock, and a specific crank angle window around the combustion phase is chosen (often 30–60 CAD). As a result, the IMPO is the integral of the filtered pressure and it is the region below the pressure oscillation, whereas the MAPO is the maximum amplitude of oscillation of the filtered pressure cycle in the given crank angle window. Additionally, to acquire the averaged

values, the MAPO and IMPO readings are usually averaged across hundreds of consecutive cycles. The Dimensionless Knock Indicator, another knock index, is the ratio of the IMPO and MAPO multiplied by the base of a rectangle with the MAPO as its height and the crank angle duration of the oscillation as its base. The knock indices are frequently used to track and stop the knock event. For instance, in a Dual Fuel engine, the strength of the knock is decreased by altering the pilot quantity and timing, whereas in SI engines, the knock is avoided by adjusting the spark time.

3.1.4 State of art technologies

While internal combustion engines have a long history dating back over a century, ongoing research continues to focus on enhancing their efficiency and reducing pollutant emissions. In particular, significant efforts have been made in the past decade to explore various approaches for improving the efficiency of SI ICEs. This section provides a more detailed description of some of the technologies that have been developed and adopted over time. These technologies are examined in greater detail to highlight their advancements and applications.

Variable valve actuation

Variable valve actuation (VVA) is a technology utilized in ICE to provide greater control and flexibility over the engine's valve timing and lift. By adjusting the opening and closing of the intake and exhaust valves, VVA enables precise regulation of the engine's air-fuel mixture, combustion process, and exhaust gas flow. This technology allows for optimized engine performance, improved fuel efficiency, and reduced emissions. VVA systems can employ various mechanisms, such as hydraulic, electro-mechanical, or camshaft phasing, to dynamically adjust valve timing and lift based on engine speed, load, and operating conditions. By adapting the valve operation to suit specific driving requirements, VVA contributes to enhancing overall engine efficiency and performance. There are two main types of VVA systems: Variable Valve Timing (VVT) and Variable Valve Lift (VVL). While the VVT system rigidly shifts the intake valve profile to accomplish early closure, the VVA system also modifies the valve lift to retain the same Intake Valve Opening (IVO) time. At partial load, an early intake valve closure (EIVC) approach is typically applied to lessen pumping losses. Additionally, by lowering the effective compression ratio, increasing the Intake Valve Closing (IVC) timing can help with knock reduction. Even under extremely low loads, these techniques suffer from reduced in-cylinder turbulence, and at fully opened throttle angles, they

produce unwanted gas-dynamic noise. It's important to remember that with a VVA system, the aforementioned benefits can be obtained while still preserving the typical exhaust valve event because the IVO is unaffected. For a VVT system, on the other hand, altering the exhaust event might be required to prevent scavenging problems brought on by greater valve overlap as a result of the development of IVO. The EGR level needs to be carefully watched in scenarios when the VVT system solely affects the intake side.

Variable compression ratio

Modifying the geometrical compression ratio of an engine can offer advantages in terms of fuel consumption across various load and speed conditions. Typically, the compression ratio of SI ICE is limited at high load conditions due to increased knock susceptibility. However, in other operating conditions, such as mid/low loads, a higher compression ratio is desirable to enhance thermodynamic efficiency. The concept of Variable Compression Ratio (VCR) aims to automatically adjust the compression ratio based on engine load and speed. Despite the potential benefits, this technology is constrained by its cost and mechanical complexity [13].

External EGR and dedicated EGR

Exhaust Gas Recirculation (EGR) is an emission control technique employed in ICEs to reduce the formation of NO_x emissions. EGR works by redirecting a portion of the exhaust gases back into the engine's intake system, where they are mixed with the incoming fresh air-fuel mixture. The purpose of EGR is to lower the combustion temperature and limit the production of NO_x, which is formed when high temperatures combine nitrogen and oxygen from the air during combustion [14]. By introducing exhaust gases into the combustion chamber, the EGR process dilutes the oxygen concentration, leading to lower combustion temperatures and reduced NO_x formation. EGR systems can be implemented using various methods. One common approach is through the use of an EGR valve, which controls the flow of exhaust gases entering the intake manifold. The EGR valve opens and closes based on engine load, speed, and other operating parameters, allowing precise control over the amount of recirculated exhaust gases. Benefits of EGR include improved fuel efficiency, reduced emissions, and compliance with stringent emission standards. By lowering NO_x emissions, EGR helps to mitigate air pollution and promote environmental sustainability. Additionally, EGR can contribute to smoother engine operation and reduced knock tendencies in certain operating conditions. However, EGR implementation requires careful calibration to strike a balance between emission

reduction and maintaining optimal engine performance. Proper integration with other engine control systems, such as turbocharging and combustion timing, is crucial to ensure the desired benefits without compromising overall engine efficiency and drivability. Advancements in EGR technology have been made, including the use of cooled EGR, where the recirculated exhaust gases are cooled before entering the intake system. This further enhances the effectiveness of EGR in reducing emissions and optimizing combustion.

Dedicated EGR (DEGR) is an unconventional concept developed at the Southwest Research Institute in Texas. In DEGR, one cylinder in a multi-cylinder engine deliberately runs rich with excess fuel, while the exhaust from that cylinder is directed into the remaining cylinders, which operate stoichiometrically or lean, if desired. The rich cylinder produces a mixture of CO and hydrogen known as syngas, which, together with CO_2 in the EGR, acts to suppress knock, enhance burn rate, and enable higher EGR utilization. This approach allows the engine to operate at higher compression ratios, leading to improved efficiency and reduced emissions across various operating conditions [15].

Dynamic skyp firing

Dynamic skip firing technology is an innovative approach to optimize engine efficiency and reducing fuel consumption. This technology selectively deactivates specific cylinders in an engine during low-load or light-demand operating conditions, allowing them to "skip" combustion cycles. By dynamically varying which cylinders are active and which are deactivated, the engine can operate in a more efficient manner, reducing pumping losses and improving overall fuel economy [16]. The engine control system intelligently manages the firing sequence, ensuring smooth operation and maintaining desired performance levels. Dynamic skip firing technology offers the potential for significant fuel savings without sacrificing power output, making it an attractive solution for enhancing the efficiency of internal combustion engines in various applications. However, the implementation of dynamic skip firing must address noise, vibration, and harshness issues, which can limit the claimed advantages.

Water injection

Water injection used in various engines has recently received a lot of attention as a promising method to increase fuel efficiency and meet stricter emissions regulations by lowering the in-cylinder and exhaust temperature, mitigating combustion knock, improving combustion phasing, and reducing NOx emissions. Water vaporizes with a significant cooling impact on the charge air because to

its high latent heat of vaporization. Moreover, the water vapor functions during the combustion process as a diluent, reducing NO_x emissions and preventing knock reactions in a manner similar to that of the cooled EGR gas. The use of water cooling in ICEs is not new, and the first effective use of WI to decrease combustion knock dates from the beginning of the 1930s. Similar uses of WI in high output aviation engine operating were made during the Second World War [17], and more research on other engine types continued throughout the 1980s [18]. Interest in this technique has grown with the widespread adoption of modern downsized engines, which are highly susceptible to knock. There are several potential sites that may be used as the WI points to inject water into the cylinder, each having its own benefits and drawbacks, especially when used with various types of ICEs. Depending on the locations and techniques for injection, common WI implementations may be divided into three groups:

- A single point WI, either front of or after the compressor or post charge air cooler.
- Multiple-point WI into the intake port or runner.
- Use a separate injector or the same injector as the gasoline to directly inject WI into the cylinder.

Water should initially evaporate after being injected, having a substantial impact on the engine's intake, compression, and subsequent combustion processes. The fresh charge may have a relative humidity of at or close to 100% for boosted engines with a effective charge air cooler [19]. If this is the case, water injected into the intake runner or port won't evaporate. Liquid water will instead enter and evaporate during the compression stroke, when the temperature and pressure within the cylinder rise,

Ultra-lean combustion

In recent years, automotive manufacturers have been exploring innovative architectures for SI engines, incorporating unconventional combustion concepts to achieve significant advantages across the entire engine operating range. The introduction of the Real Driving Cycle for vehicle homologation has necessitated the development of high-efficiency engines for most operating conditions. Of particular interest are combustion systems that operate with very lean air/fuel mixtures, as they offer the potential to simultaneously reduce raw NO_x emissions and fuel consumption. The lower combustion temperatures associated with lean conditions contribute to NO_x reduction. Additionally, lean combustion benefits from higher specific heat ratios, reduced heat losses, and improved

knock resistance. However, traditional flame-propagation-based SI engines have limitations in working with a high level of excess air, which hampers the true potential of lean combustion. Lean conditions lead to reduced laminar flame speeds, resulting in undesirable cyclic variability, misfires, and increased HC-CO formation [4, 20]. To overcome these limitations, various solutions have been explored in the literature. Stratified lean combustion has been investigated for many years, aiming to achieve a near-stoichiometric air/fuel ratio at the spark plug using strategies such as wall-guided, flow-guided, or spray-guided approaches [21, 22]. In order to address the challenges associated with the extremely low flame speed in lean conditions, alternative flameless combustion concepts have been proposed, including Homogeneous Charge Compression Ignition (HCCI) [23]. However, HCCI faces difficulties in controlling ignition timing, limited power output, and weak cold-start capability. Variants of HCCI, such as Spark-Assisted Compression Ignition (SACI) proposed in [24], have been explored. SACI promotes controlled auto-ignition of lean or diluted unburned mixtures through spark-initiated flame propagation.The concept of Premixed Charge Compression Ignition (PCCI) addresses the limitations of HCCI by combining it with Controlled Auto-Ignition (CAI). In PCCI, the homogeneous background mixture is ignited by an additional injection of the same fuel near the top of the piston stroke. This approach offers some of the benefits of HCCI while minimizing control and operating range challenges [25]. Another variation, Reactivity Controlled Compression Ignition (RCCI), takes a similar approach but utilizes two different fuels optimized for increased knock resistance and reduced ignition delay. Although RCCI aims to achieve the high efficiencies of HCCI with fewer operating restrictions and better combustion control, it does introduce additional complexity and cost due to the requirement of dual fuel injection systems [26, 27]. A practical solution for implementing ultra-lean combustion is the utilization of a Pre-Chamber ignition system. This system features a small volume connected to the main chamber through small orifices, housing the spark plug. In this configuration, the combustion process initiates at the spark plug and propagates into the main chamber through multiple turbulent jets of hot gas ejected from the pre-chamber. These jets enhance turbulence in the cylinder charge, enabling ignition and stable flame propagation even under extremely lean mixtures [28, 29]. The main challenges faced by these engine architectures revolve around precise control of combustion development and related emission formation. Consequently, more complex after-treatment systems are required, offering alternatives to traditional three-way catalysts. An additional approach that has been investigated to increase the reactivity in lean combustion involves introducing a small amount of hydrogen into the air/fuel mixture. This can

effectively extend the lean limit of combustion. The higher laminar flame speed of hydrogen supports ignition and flame propagation, resulting in reduced cyclic variability and fluctuations. Additionally, the presence of hydrogen improves resistance to auto-ignition, leading to increased efficiency through improved combustion timing and higher compression ratios. Furthermore, the addition of hydrogen helps reduce CO and HC emissions [30], and under certain conditions, it can also mitigate NO_x formation by optimizing the trade-off between the air/fuel ratio and maximum cylinder temperature. In recent years, there has been significant development in the field of pure hydrogen engines. These engines utilize hydrogen as the primary fuel source, offering unique advantages in terms of emissions reduction and energy efficiency. Given the significance of this topic, a separate section of the thesis is dedicated to explore hydrogen engines in detail.

Hydrogen fueled engine

Like most fuels, hydrogen needs the right amount of oxygen and a certain amount of ignition energy to burn. However, under combustion circumstances, hydrogen is more flammable and reactive. An engine that burns hydrogen as fuel functions similarly to a traditional internal combustion engine in terms of energy conversion. When the fuel mixture is ignited it burns and expands in the combustion chamber, pushing the piston as a result. This expansion is turned into mechanical work by the crankshaft, which is coupled through the crank linkage, converting chemical energy into external mechanical energy. A hydrogen engine functions essentially in the same way as a conventional internal combustion engine. Traditional fossil fuels are simply replaced with hydrogen in this scenario. However, because hydrogen has different properties from gasoline or diesel, the engine needs to be modified in order for it to run through its typical working cycle [31–33]. The benefits of using hydrogen as fuel were discussed in the previous chapter (2.3). It has also been noted that an increased concentration of hydrogen in internal combustion engines causes a noticable decrease in volumetric efficiency for direct injections, as stated in [34]. Investigation into how the spark ignition advance angle affected this issue revealed that a modest delay in ignition helps achieve higher efficiency, reduce the risk of detonation, improve cold start performance, and lower NO_x emissions. The formation of NO_x can be linked to the cylinder's intake of nitrogen together with air, which subsequently undergoes oxidation at high temperatures and in the presence of plenty of oxygen. Reducing the in-cylinder temperature is an efficient way to reduce NO_x emissions because the elevated temperature considerably encourages their production. The consequences of various hydrogen injection techniques have been researched in the literature.

PFI's main distinction from manifold injection is that fuel with PFI is injected into the intake tract, whereas with manifold injection, fuel is injected into the intake manifold that corresponds to each cylinder. Low injection pressure, stability, and time for adequate fuel and air mixing are all benefits of PFI. However, it has limitations like poor delivery efficiency, erratic fuel control, and difficulty overcoming the risks of backfiring and low hydrogen bulk density's effects on engine performance. Manifold injection, on the other hand, differs from PFI in that it uses the same number of injectors as the number of cylinders even though it is also an out-of-cylinder injection. This feature sets it apart from PFI because it allows fine control of the fuel injection parameters for each cylinder. In a study by Cheolwoong et al. [35], they used a hydrogen injector in place of the fuel injector of a port fuel injection gasoline engine. They noticed that a higher hydrogen volume ratio led to a smaller mixture intake volume, which in turn resulted in a lower torque output. Backfire became a difficult problem, especially at greater speeds. Jianbing et al. [36] examined the causes of backfires occurring in port fuel injection engines and suggested corresponding control strategies. They included a backfire schematic diagram in 3.1.4 (a). They proposed installing a wire mesh flame arrestor in the intake manifold, as shown in Figure 3.1.4 (b), to solve this problem. Without impairing regular engine running, this flame arrestor efficiently collects a large quantity of heat from a mild flame. According to a research, using direct injection in combination with the right injection technique can significantly reduce the risk of backfire and improve volumetric efficiency. For more information, see [37]. The injection pressure is increased to make this improvement, which gives a clear advantage over PFI systems. Internal combustion engines' dynamic performance is directly impacted by combustion, which is an essential part of their operation. Creating effective, reliable, and simple to use combustion methods is crucial for optimizing the engine system and achieving high-quality combustion. One such technology is stratified charge combustion (SCC), which permits lean combustion by establishing a gradient in the fuel concentration, with higher fuel concentration close to the spark plug and leaner mixture farther from it. This configuration makes it easier to ignite a locally rich combination, and it relies on flame spread to ignite the far lean mixture. The effectiveness and stability of SCC can be impacted by a variety of circumstances because it is a complicated process. A sophisticated combustion strategy known as the colorless distributed combustion (CDC) method was introduced by Mustaf et al. [38]. With this approach, the flame temperature is controlled by lowering the reaction rate, leading to extremely low NO_x emissions, a larger flame range, and a more even temperature distribution. The CDC technique successfully reduces the high temperature and NOx emissions brought on by

hydrogen-rich circumstances, allowing the hydrogen-rich combustion range to be extended. Hydrogen can also be used as fuel in RCCI engines, according to [39]. Both lean combustion and hydrogen-rich combustion are unconventional strategies that require specific hydrogen concentrations during operation but represent two contrasting approaches. Lean combustion, particularly suitable for hydrogen-fueled engines, offers advantages such as reduced fuel consumption and pollutant emissions. It is important to note that lean premixed hydrogen flames exhibit thermodiffusive instability. This phenomenon arises from the fuel's high mobility, resulting in localized acceleration and thinning of the flame. By excluding the influences of turbulent, acoustic, and buoyancy effects, lean premixed hydrogen flames exhibit two notable instabilities: the Darrieus-Landau instability and the thermodiffusive instability. The former arises as a consequence of the density decrease resulting from heat release across the flame, while the latter originates from an imbalance between thermal and molecular diffusion. Extensive experimental observations have provided evidence for the existence of these instabilities [40, 41]. The occurrence of thermodiffusive instability can be understood by examining the Lewis number of the reactants, which represents the ratio between the thermal diffusivity and the molecular diffusivity of the chemical species. When the molecular diffusion is higher than the thermal diffusivity ($Le < 1$), the flame front exhibits acceleration in regions where it is convex towards the fresh gases. This leads to an increase in the local flame speed , resulting in a thinner flame front and higher temperature compared to the reference laminar flame, which is assumed to be one-dimensional, steady, and unstretched. Conversely, when the flame front is convex towards the burnt gases, the flame velocity decreases compared to the reference laminar flame speed, causing the flame to thicken and the temperature to decrease. This creates an unstable condition where the flame front becomes wrinkled, leading to an increase in flame speed and the formation of chaotic burning cells. These cells are separated by regions of near extinction, resulting in what is commonly referred to as cellular burning or self-turbulent propagation regime. Since the study discussed in Chapter 3.3.2 focuses on the modeling of a hydrogen-fueled engine, a more detailed analysis of hydrogen flame instability is presented in Chapter 3.3.2.

3.1.5 Pollutant emission

Since the development of the technologies previously described stems from the need to maximize performance and reduce pollutant emissions, this paragraph briefly outlines the fundamental concepts related to the formation of the main pollutants produced by internal combustion engines. Nitrogen oxides (NO and trace amounts of NO_2; together known as NO_x), CO, and unreacted or

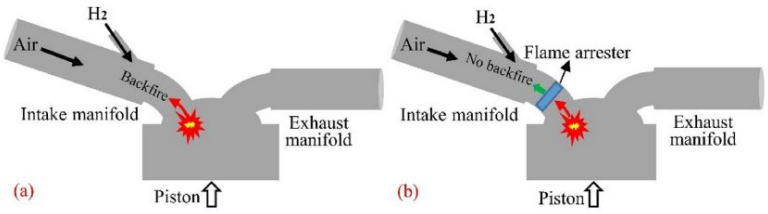

Figure 3.5: Schematic diagram of: (a) Backfire phenomenon and (b) The role of the flame arrester [42].

partially reacted fuel hydrocarbons are all present in the exhaust gases from SI engines. The concentrations of these pollutants vary depending on the operating environment and engine configuration. To reduce non-exhaust hydrocarbon emissions, methods including blowby gas recirculation and vapor-absorbing carbon canisters are used. Particulate emissions have increased significantly, even for SI engines, due to the increasing use of DI engines. NO_x exhaust emissions from diesel engines are comparable to those from SI engines, although CO emissions are lower. Diesel engines emit considerable amounts of hydrocarbons, but they do so at a lesser rate than SI engines. Additionally, diesel engines produce significant amounts of particulate pollutants, with 0.2–0.5% of the fuel mass released as tiny particles mostly made up of soot and other hydrocarbon substances. Exhaust gas concentrations of pollutants depart from chemical equilibrium. To comprehend the creation and elimination of pollutants, a thorough understanding of combustion chemistry is required. The production and oxidation processes of CO, organic molecules, and particulates are strongly related to the primary fuel combustion process. Although the synthesis and oxidation of nitrogen oxides and sulfur oxides happen independently from the burning of fuel, they are nonetheless connected because they happen in the same atmosphere as combustion. Exhaust gas treatment systems include equipment like catalytic converters—which include oxidizing catalysts for HC and CO, reducing catalysts for NOx, and three-way catalysts for all three pollutants—and particle traps or filters to minimize emissions. For the simultaneous removal of CO, HC, and NOx from SI engine exhausts, three-way catalysts are effective, although they call for stoichiometric combustion conditions. The main pollutants released by lean-burn CI engines are NOx and particulates. Oxidizing catalysts are frequently employed to lower HC emissions and stop them from adhering to soot particles. The operating temperature, exhaust gas flow rate, and compatibility between catalyst size and chemical conversion requirements are only a few of the variables that affect how effective these

exhaust catalysts, including three-way and oxidizing catalysts, are. A coordinated design of the catalyst and engine systems, often incorporating sensors and feedback loops, is necessary. Catalyst warm-up is crucial, as the surface temperature should reach around 300°C for optimal effectiveness

3.2 Simulation of internal combustion engines

3.2.1 Literature review

Evaluation of various technologies and integrated solutions is essential in the light of the complicated and difficult situation facing internal combustion engines. New combustion modes, turbocharging and after-treatment technologies, alternative fuels, and hybrid electric vehicles are included in this. With little support from experiments, simulation codes have emerged as a crucial instrument in this evaluation, enabling the analysis and comparison of technical solutions. These simulation tools provide accurate findings and allow for the optimization of different technologies through virtual engine development, resulting in more efficient procedures and shorter engine design times. Different methods, grouped into four main categories: 0D, 1D, quasi-dimensional, and 3D, are used to model ICE. The degree of approximation utilized differs across approaches. By assuming time-dependent thermodynamic properties and ignoring spatial dependencies, the 0D model simplifies the engine. It offers a rapid picture of in-cylinder operations, but because it cannot account for pressure wave propagation in pipes, it cannot estimate volumetric efficiency. By calculating unsteady flow equations in the pipes while taking uniform properties along each pipe section into account, the 1D technique gets around this restriction. For the purpose of analyzing, enhancing, and calibrating engine performance, 0D refined models combined with 1D models enable precise and effective predictions of engine behavior. A thorough description of thermo-fluid dynamics in intricate 3D geometries is provided by the 3D approach, which is based on the integration of Navier Stokes equations. However, it needs a lot of computing work and is usually applied to particular engine parts that operate in constrained environments. A mix of 0D and 1D models have been used in this PhD research. Phenomenological 0D sub-models are employed to mimic in-cylinder processes, while a 1D method is used to represent the flow inside the intake and exhaust pipes. A 0D turbulence sub-model's development and validation have also been supported by the use of 3D models' results.

Combustion modeling for SI engines

In the literature, several 0D combustion models have been proposed with the objective of accurately predicting the heat release rate. These models consider factors such as the combustion chamber geometry, turbulent intensity, and the effects of EGR. Notably, each model is characterized by a set of calibrating constants, which significantly influence the predictive capability of the model.

Accordingly to the eddy burn up approach, the combustion process can be divided into two stages. Firstly, the fresh gases, characterized by a density ρ_u, are entrained into the flame front at a velocity equal to the sum of a laminar component (S_L) and a turbulent component (S_T). This process can be mathematically represented as:

$$\frac{dm_{ent}}{dt} = \rho_u A_L (\frac{S_L}{S_T}) \tag{3.1}$$

Secondly, the entrained mass undergoes combustion within a characteristic time τ_b. This can be described by the following equation:

$$\frac{dm_\mathrm{b}}{dt} = \frac{m_{ent} - m_b}{\tau_\mathrm{b}} \tag{3.2}$$

In this approach, the physical model does not explicitly describe the flame-wall interaction that occurs at the end of combustion. However, a simple exponential term [4] can be introduced to account for this phenomenon. The time from the beginning of combustion (τ_start) to the point when the flame reaches the wall (τ_wall) can be used as:

$$\frac{dm_\mathrm{b}}{dt} = \frac{m_{ent} - m_b}{\tau_\mathrm{b}} exp(C_{tw} \frac{t_{wall} - t}{\tau_b}) \tag{3.3}$$

The characteristic burn time τ_b is defined as the ratio of the integral length scale and the laminar flame speed. To adapt the model to different operating points of the engine being simulated, an adjusting coefficient C_{tb} is introduced.

$$\tau_b = C_{\tau b} \frac{L_t}{S_L} \tag{3.4}$$

The turbulent flame speed can be modeled as reported in [43], which builds upon the work of Zimont [44]. This expression effectively captures the behavior of freely propagating flames and the early development of the flame kernel through an exponential term:

$$S_T = Da^{0.25} A_{st} u' \sqrt{1 + \frac{\tau_t}{t}[exp(\frac{-t}{\tau_t}) - 1]} \tag{3.5}$$

Here, the relation incorporates a calibrating coefficient A_{st} and the Damköhler number (Da). The characteristic eddy turnover time τ_t is determined by the ratio of the integral length scale and the turbulence intensity, multiplied by a coefficient $C_{\tau t}$.

$$\tau_t = C_{\tau t} \frac{L_t}{u'} \tag{3.6}$$

In the Flame Surface Density (FSD) model, the calculation of the wrinkling factor (defined as the ratio between the turbulent and the laminar flame area $\frac{A_T}{A_L}$) is based on a 0D differential equation [45]:

$$\frac{1}{\Xi}\frac{d\Xi}{dt} = \Gamma \left(\frac{u'}{S_L}\frac{L_t}{\delta_L} \right) \frac{u'}{L_t} \left(\frac{\Xi_{equ} - \Xi}{\Xi_{equ} - 1} \right) - \frac{2\rho_u}{R_f \rho_b} (\Xi - 1) S_L \tag{3.7}$$

This equation is derived from reducing a 3D CFD equation for flame surface density [46]. The reduction process is explained in detail in [47]. The first term on the right-hand side of the equation represents the wrinkling of the flame due to turbulent scales, while the second term accounts for the thermal expansion of the spherical flame, which reduces the turbulent wrinkling of the flame front [48]. The turbulent term incorporates the efficiency function of the turbulent flow (Γ) and the equilibrium wrinkling factor (Ξ_{equ}).

$$\Xi_{equ} = 1 + 2\frac{u'}{S_L}\sqrt{\frac{C\Gamma}{S_c}} \tag{3.8}$$

The inclusion of the efficiency function in this model considers the laminar flame speed (S_L) and the laminar flame thickness (δ_L), as well as the influence of all turbulent scales. Meneveau and Poinsot [49] originally determined the efficiency function numerically using Direct Numerical Simulation (DNS) and combining flame/vortex interaction with multi-fractal theories, as in [50, 51]. The strain rate of the flame front, caused by a pair of counter-rotating vortices, is integrated for all turbulent scales, assuming that each scale independently affects the wrinkling of the flame front. A fitting process is performed to obtain the final expression for Γ. The specific expression used can be found in [49, 52]. The presence of the efficiency function in this model is based on the following assumptions [52]:

- There is no single turbulent scale that controls flame wrinkling. A wide range of turbulent scales, from Kolmogorov to integral scales, contribute to flame wrinkling.
- The characteristics of the laminar flame, such as thickness (δ_L) and speed (S_L), must be taken into account to accurately model flame wrinkling.

$$\log_{10}(\Gamma) = -\frac{1}{s+0.4}\exp(-s-0.4)+(1-\exp(-s+0.4))\left(\sigma_1\left(\frac{u'}{S_L}\right)s-0.11\right) \tag{3.9}$$

$$s = \log_{10}\left(\frac{L_t}{\delta_L}\right) \quad \text{and} \quad \sigma_1 = \frac{2}{3}\left(1-\frac{1}{2}\exp\left(-\left(\frac{u'}{S_L}\right)^{1/3}\right)\right) \tag{3.10}$$

The equilibrium wrinkling factor (Ξ_{equ}) is determined analytically through the steady one-dimensional flame density equation [53]. It includes the calibration coefficient (C) of the combustion model and is influenced by the Schmidt number (S_c), which is dependent on the fuel used.

Since the combustion model used in the context of this thesis is based on the fractal approach, a specific paragraph is dedicated to it to provide a more detailed discussion later on.

3.2.2 Internal combustion engine model development

In this section, the main sub-models that constitute the complete simulation platform for ICEs, used during the PhD studies, are explored. In particular, the description of the turbulence model is followed by the discussion of the fractal combustion model, and finally, the detonation and heat exchange models.

Turbulence model

The turbulence model deeply expalined in [54] is here briefly recalled. The main variables involved are the tumble angular momentum, T, mean flow kinetic energy, K, and turbulent kinetic energy, k. They can be calculated as:

$$k = \frac{3}{2}u' \tag{3.11}$$

$$K = \frac{1}{2}U_{fK}^2 \tag{3.12}$$

$$T = U_T r_T \tag{3.13}$$

where U_{fk} is the mean velocity of air and fuel flow, u' the turbulence intensity and U_T and r_T are the tumble velocity and radius respectively. An inscribed circle in the combustion chamber can be schematized as the tumble radius. The K-k-T model is used to define the main turbulence variables, according to the system of equations:

$$\begin{cases} \frac{dmk}{dt} = (\dot{m}k)_{inc} - (\dot{m}k)_{out} + \frac{2}{3}\frac{\dot{\rho}}{\rho}(-mv_t\frac{\dot{\rho}}{\rho} + mk) + P - m\varepsilon \quad \text{(I)} \\ \frac{dmK}{dt} = (\dot{m}K)_{inc} - (\dot{m}K)_{out} - f_d\frac{mK}{\tau_T} + mK\frac{\dot{\rho}}{\rho} - P \quad \text{(II)} \\ \frac{dmT}{dt} = (\dot{m}T)_{inc} - (\dot{m}T)_{out} - f_d\frac{mT}{\tau_T} \quad \text{(III)} \end{cases} \tag{3.14}$$

The entering and outgoing flow via the valves are represented by the first two terms of the equations; the decay brought on by the shear stresses is defined by the third term of the last two equations. The dimensionless parameter f_d is defined by the following equation:

$$f_d = c_{fd0} + c_{fdm}\left[\max\left(\frac{B}{H}, 1\right), -1\right] \tag{3.15}$$

Thus, the tuning constants cfd_0 and cfd_m are used to define the decay function. More specifically, cfd_0 defines the dissipation of the tumble as well as the kinetic energy dissipation brought on by the viscous forces, whereas cfd_m defines the decay brought on by the collapse of the tumble vortex as the piston approaches the TDC. Since the instability worsens as the height gets smaller in relation to the bore, this multiplier is only dependent on that ratio. It is important to note that the time scale known as t_T is the tumble characteristic time scale and is defined as:

$$\tau_T = r_T/u' \tag{3.16}$$

Moreover, the K equation presents two additional terms: $mK\frac{\dot{\rho}}{\rho}$ which represents the compressibility term and P, which is the production term related to the energy cascade mechanism Since the energy is extracted from the mean flow field and transferred to the turbulent flow field, the term P is an additive term in the k equation and a subtractive term in the K equation. It can be defined as:

$$P = c_{pKk}\frac{m(K - K_T)}{t_T} \tag{3.17}$$

Where K_T is the tumble kinetic energy and c_{pKk} is a tuning constant. The difference $(K - K_T)$ represents the unorganized kinetic energy in the tumble motion, that indicates the energy transferred from the mean flow field to the turbulent one. The convective terms in equation 3.14 are modeled, for both forward and reverse flow (f and b subscripts, respectively), according to:

$$(\dot{m}k)_{inc} = 0 \tag{3.18}$$

$$(\dot{m}k)_{out} = k(\dot{m}_{inb} - \dot{m}_{exf}) \tag{3.19}$$

$$(\dot{m}K)_{inc} = \frac{1}{2}\left[\dot{m}_{\text{inf}}(c_{\text{Kin0}}v_{\text{Kinf}})^2 + \dot{m}_{\text{exf}}v_{\text{Kexf}}^2 + \dot{m}_{\text{exb}}v_{\text{Kexb}}^2\right] \tag{3.20}$$

$$(\dot{m}K)_{out} = K(\dot{m}_{inf} - \dot{m}_{exf}) \tag{3.21}$$

$$(\dot{m}T)_{inc} = r_t\left(\dot{m}_{\text{inf}}c_{T_{\text{in0}}}v_{T_{\text{inf}}} - \dot{m}_{\text{exf}}v_{\text{Texf}} - \dot{m}_{\text{exb}}v_{\text{Texb}}\right) \tag{3.22}$$

$$(\dot{m}T)_{out} = 2T(\dot{m}_{inb} - \dot{m}_{exf}) \tag{3.23}$$

where v_K and v_T are the mean flow and tumble velocity respectively. Finally, in the k equation the term ϵ represents the dissipation of the turbulent flow. It can be evaluated as:

$$\epsilon = c_\mu^{3/4}\frac{k^{3/2}}{L_t} \tag{3.24}$$

L_t is the integral length scale defined through S-shaped functions and c_μ is a tuning constant to adjust the dissipation rate.

Combustion model

The initial version of the fractal combustion model was proposed several years ago [55]. This model is based on the combustion characteristics observed in the most common combustion regime found in a conventional SI engine, known as the wrinkled-corrugated flamelet zone, as shown in Figure 3.1.2 [56]. In this regime, the flame front has a larger surface area, A_T, compared to the laminar area, A_L, due to its interaction with turbulence, u'. Although the flame still propagates locally at a laminar speed, S_L, the burn rate is enhanced by the turbulence effect. This process is illustrated in Figure 3.6. The increase in flame surface area is incorporated into the model using the principles of fractal geometry. Experimental evidence has shown that a wrinkled flame front exhibits fractal behavior, demonstrating self-similarity in its basic structure [56–59]. This allows for the correlation of the extent of the turbulent flame front with the laminar flame front based on turbulence characteristics such as speed, time, and length scales [55].

Based on the aforementioned assumptions, the burn rate can be expressed as a function of the wrinkling factor, Ξ, defined as the ratio between the turbulent flame area (A_T) and the laminar flame area (A_L):

$$\left(\frac{dm_b}{dt}\right)_{\text{fractal}} = \rho_u A_T S_L = \rho_u A_L S_L\left(\frac{A_T}{A_L}\right) = \rho_u A_L S_L \Xi \tag{3.11}$$

$$\Xi = \left(\frac{L_{\max}}{L_{\min}}\right)^{D_3-2} \tag{3.12}$$

The wrinkling factor, Ξ, can be estimated using the expression provided in [60], which depends on the fractal dimension, D_3, and the maximum and

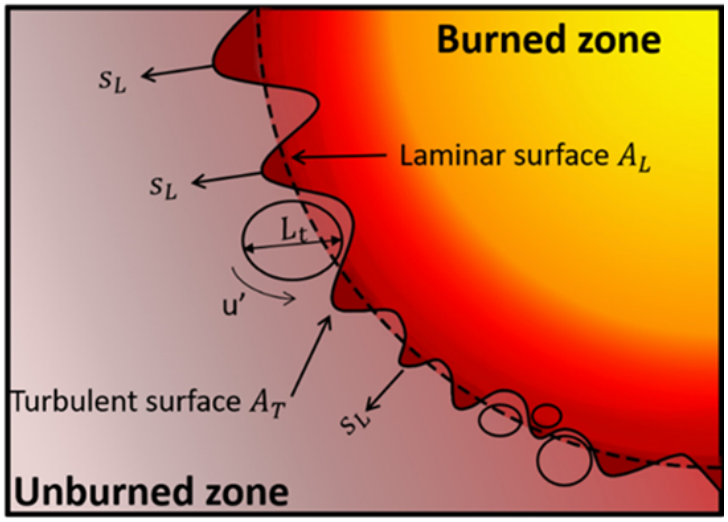

Figure 3.6: Schematic of the fractal combustion model.

minimum flame wrinkling scales, $L_{\max}$ and $L_{\min}$. D_3 is a function of turbulence intensity, u', and laminar flame speed, S_L, as correlated in [59] by the following equation (3.13):

$$D_3 = \frac{2.35u' + 2.00S_L}{u' + S_L} \tag{3.13}$$

Considering the wrinkling scales, $L_{\max}$ is associated with a macroscopic characteristic dimension of the flame front, proportional to the flame radius (r_f), multiplied by the tuning constant c_{wrk} (wrinkling multiplier):

$$L_{\max} = c_{\text{wrk}} r_f \tag{3.14}$$

On the other hand, $L_{\min}$ is assumed to be equal to the size of the smallest turbulent eddies [56], expressed by the Kolmogorov length scale, L_k:

$$L_{\min} = L_k \tag{3.15}$$

The model described above applies to a fully developed and freely expanding turbulent flame. However, modifications to the model are required to account for the early flame development and combustion completion. During the initial stages of combustion, as mentioned earlier, the flame front exhibits laminar propagation rather than turbulence-induced corrugation. Thus, the transition from laminar to turbulent combustion can be modeled by progressively

increasing the fractal dimension, D_3, according to equations (3.16) and (3.17):

$$D_3 = \frac{D_{3,\max} u' + D_{3,\min} S_L}{u' + S_L} \tag{3.16}$$

$$D_{3,\min} = 2.00; D_{3,\min} = 2.00(1 - w_{\text{trans}}) + 2.35 w_{\text{trans}} \tag{3.17}$$

The wrinkling evolution depends on the variable w_{trans}, as defined in equation (3.18), which is a function of a characteristic time scale, t_{trans}, and a model tuning constant, c_{trans} (transition multiplier). The characteristic time scale is determined using the turbulence kinetic energy, k, and its dissipation rate, ε:

$$w_{\text{trans}} = \int \frac{dt}{c_{\text{trans}} t_{\text{trans}}}; t_{\text{trans}} = \frac{k}{\varepsilon} \tag{3.18}$$

Furthermore, when the flame front interacts with the combustion chamber walls, the burning rate is further modified. Although a detailed description of flame-wall interaction is challenging with a quasi-dimensional model, it can be assumed that flame front wrinkling near the walls is reduced, resulting in a slower burning rate. Therefore, the overall burning rate can be expressed as a weighted average of the fractal burning rate and a laminar wall combustion, as shown in equations (3.19) and (3.20):

$$\left(\frac{dm_b}{dt}\right) = (1 - w_{\text{wall}}) \left(\frac{dm_b}{dt}\right)_{\text{fractal}} + w_{\text{wall}} \left(\frac{dm_b}{dt}\right)_{\text{wall}} \tag{3.19}$$

$$\left(\frac{dm_b}{dt}\right)_{\text{wall}} = \rho_u A_L S_L \tag{3.20}$$

Here, the variable w_{wall} describes the transition from turbulent to wall combustion, according to equation (3.21). It represents the ratio between the area wetted by the flame front on the piston, head, and cylinder (A_w) and the total flame front area (A_{tot}). This ratio is multiplied by the mass fraction of burned gas, x_b, raised to an exponent amplified by the tuning constant x_{wc} (wall combustion multiplier):

$$w_{\text{wall}} = \frac{A_w}{A_{\text{tot}}} x_b^{10 x_{\text{wc}}} \tag{3.21}$$

The laminar flame area, A_L, is evaluated using a tabulated approach to reduce computational time. The flame area table is read during runtime based on the current piston position and the burned gas volume. The table is calculated offline using an automated procedure that determines the intersections

between an "ideal" spherically smoothed flame front, centered on the spark plug, and the surfaces of the piston, head, and cylinder.

To complete the combustion model, it is necessary to evaluate the laminar flame speed. Since, within this thesis, the engine model has been applied for a study on the effects of water injection and a study on hydrogen combustion, the different correlations developed for laminar flame speed are reported and explained in their respective sections (3.3).

Knock model and heat transfer model

Another important aspect to consider during the engine calibration on the test bench is the determination of the KLSA to prevent abnormal combustion events. Therefore, in order to perform numerical calibration, a knock model needs to be integrated with the combustion model.

In a 0D framework, the knock phenomenon is commonly represented by simulating the auto-ignition (AI) process in the unburned mixture. Accurately describing the complex AI processes requires solving detailed chemical kinetic schemes, which involve hundreds of species and thousands of reactions [61]. However, this approach is computationally expensive. Alternatively, a simplified model based on empirical formulations of auto-ignition delay [62] can be utilized. One limitation of this approach is that it may not accurately capture the AI process when boundary conditions (initial pressure and temperature) and mixture compositions (air/inert/fuel ratios) fall outside the ranges considered during correlation development. Additionally, it may have limited capability to predict the chemical effects resulting from advanced knock suppression strategies such as EGR or water injection.

To strike a balance between accuracy and complexity, a tabulated approach [63] has been adopted to evaluate the AI. This approach involves solving chemical reactions offline in a constant-pressure (CP) or constant-volume (CV) reactor to generate a table of AI times, τ_{AI}, based on discrete values of pressure, temperature, equivalence ratio, and residual content. In the engine model, the knock event is triggered when the integral of AI time, as expressed in equation 3.25, exceeds a predefined threshold level.

$$\int \frac{dt}{\tau_{AI}} \tag{3.25}$$

To introduce a safety margin, a tunable threshold level, set below unity, is employed. As mentioned earlier, the AI table is generated through offline solutions of a kinetic scheme by varying the pressure, temperature, and air/fuel ratio of the unburned reactants in a constant-pressure reactor. In this study, two different kinetic schemes have been employed, depending on the type of

engine and fuel considered. For the gasoline SI engines in which water injection has been realized, the kinetic scheme developed by Liu et al. [64], which includes 5 elements, 56 species, and 168 reactions, was utilized. On the other hand, the AI table for the hydrogen engine has been generated by the kinetic scheme developed by Konnov [65], which includes 5 elements, 15 species, and 75 reactions was utilized.

A relevant attention is also posed to the modeling of in-cylinder heat transfer due to its impact on the knock onset and the engine performance. Heat transfer phenomena are also modeled for the exhaust sub-system to provide a reliable prediction of gas temperature at the engine exhaust. Inside the cylinders, the sole convective mechanism is considered. To this aim, the Woschni sub-model [66] is implemented in the 1D code to reproduce the in-cylinder gas-to-wall heat transfer.

3.3 Engine model applications

As previously mentioned, during this PhD work, the simulation platform described in the previous section has been applied for two different analyses: water injection in a gasoline PFI engine and the study of a hydrogen-powered engine. In this section, their outcomes are described in detail.

3.3.1 Water injection to improve fuel consumption and torque in a small displacement PFI spark-ignition engine

Engine description and experiments

Table 3.3.1 presents the main characteristics of the engine that was tested in this activity, while Figure 3.7 shows a simple schematic of the engine setup. The engine used in the experiment is a downsized two-cylinder SI engine that is connected to a waste-gated turbocharger. Gasoline is supplied to the engine via port injectors that are located upstream of the valves in the intake pipes. The engine features a conventional pent-roof head combustion chamber with 4 valves (2 intake and 2 exhaust), a centered spark-plug, and a standard ignition system. The commercial engine was modified to accommodate the water injection operations. In order to deliver the water amounts through a secondary injection system that pressurizes the fluid in the rail up to 4 bar, two low-pressure injectors are fitted along the intake runners upstream of the fuel injectors. One low pressure injector is installed for each cylinder. The aforementioned engine is set up on a test stand at the STEMS-CNR Lab in Naples, which is suitably fitted with sensors to measure the key parameters.

In specifically, both cylinders are fitted with piezo-quartz pressure sensors (with an accuracy of 0.1%) to monitor the instantaneous pressure traces throughout 270 cycles. Piezo-resistive low pressure indicated sensors are used to collect the instantaneous pressure data at the intake plenum and turbine inlet. Thermocouples are used to measure the temperature of the intake and exhaust gases. With the help of a LabView program, it is possible to switch from the engine control unit (ECU) provided by the manufacturer to a prototype driver that was "in-house developed" for the management of the timing of both gasoline and water injection. A TIT control is specifically achieved by adjusting the amount of injected gasoline, while the amount of injected water is tuned to achieve the ideal water/fuel (W/F) ratio. Experimental evidence from earlier tests on the engine under investigation suggests that there is an imbalance in the A/F ratio between the cylinders, with Cyl #2 receiving a larger amount of fuel injection (a richer A/F ratio) [67]. In this study, specialized experimental investigations have been performed to validate the numerical model for this engine while it is operated with WI operation.

Table 3.2: Main engine characteristics and performance in dry operations

Model	Downsized Turbocharged PFI Engine
Number of Cylinders	2
Layout	4 valves per cylinder
Displacement, cm^3	875.4
Bore/Stroke, mm	80.5/86
Connecting rod length, mm	136.85
Compression ratio, -	10
Maximum Brake Torque, Nm	147@2000 rpm
Maximum Brake Power, kW	64@5500 rpm

A group of 10 operational points were chosen for the validation. They are distinguished by medium/high loads (IMEP from 13.1 to 17.5 bar), various speeds (from 2160 to 5000 rpm), and A/F and W/F ratios, as shown in Table 3.3. The air-fuel mixture is rich in accordance with the strategy typically used in boosted SI engines to reduce the tendency for knocking as well as the temperature at the exhaust, and each control parameter is specified by the usual ECU calibration when the engine is just operated with gasoline (dry operations).

The W/F ratio ranges from 0.07 to 0.3. Spark timing is externally advanced at each required W/F mass fraction until knock develops or the maximum permitted value of in-cylinder peak pressure (85 bar) is reached. When incipient knock is confirmed, the engine block-mounted knock sensor triggers a recovery

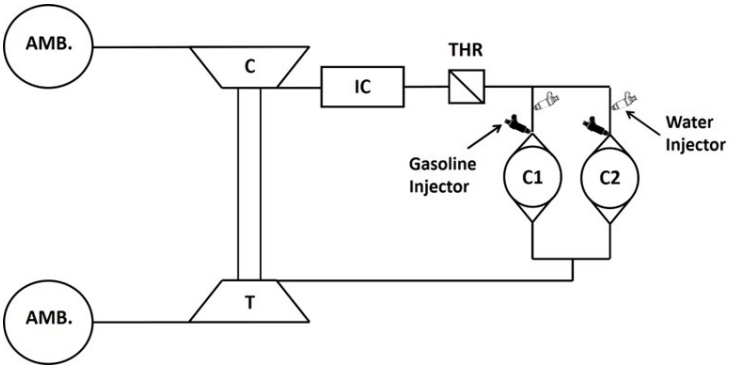

Figure 3.7: Schematic of the engine: T: Turbine; C: Compressor; AMB: ambient; IC: Intercooler; THR: Throttle valve; C1 and C2: engine cylinders. Source: [68]

Table 3.3: Test Case

Test Case	Engine Speed, rpm	IMEP, bar	W/F, -	Spark, CAD BFTDC	MFB50 Cyl #2, CAD AFTDC	A/F
1	2160	13.1	0.3	-6.5	27	14.6
2	2160	13.8	0.07	-6.5	26	14.2
3	2500	17.2	0.2	-11	20	14.3
4	2500	17.4	0.2	-7	25	13.5
5	2500	17.5	0.3	-12	19	13.8
6	3500	16.3	0.1	-12	18	12.9
7	3500	16.7	0.2	-20	9	14.9
8	4000	16.7	0.2	-20	9	14.7
9	5000	16.8	0.2	-13.5	22	12.3
10	5000	17.3	0.3	-14.5	23	12.6

mode that shuts off the fuel injection and power output. A new KLSA is discovered in this manner. Main engine parameters, such as torque/power, fuel flow rate, the relative A/F ratio, intake and exhaust pressures and temperatures, and in-cylinder pressure signals, are collected at the test bench during the tests. The conventional ECU also keeps track of a number of variables to ensure the regular operation of the engine and the turbocharger group and prevent excessive thermo-mechanical stresses. In order to maintain the integrity of the intake manifold, the functionality of port injectors, and to prevent the compressor surging at low engine speeds, the boost pressure is automatically adjusted acting on the waste-gate valve regulation (max boost pressure of

2.4 bar). The maximum in-cylinder pressure peak is limited to 85 bar, the maximum turbocharger speed is 255000 rpm, and the maximum turbine inlet temperature (TIT) for turbine thermal safety must be less than 950°C. The cycle-to-cycle variability are increased by water, but the CoVIMEP is still within an acceptable range of 2-4% for all the measured points.

Numerical approaches and model validation

The engine model is built using 1D commercial code (GT-Power). Using standard items from the software library, intake and exhaust flows are solved. Advanced "in house-developed" sub-models for the description of in-cylinder processes described in chapter 3.2, as well as correlations for the laminar flame speed and for water evaporation based on physical principles, are integrated into the 1D code in the form of user-routines. Spray evolution and liquid wall film formation on the intake ports are neglected.

The laminar flame speed, (S_L in equation 3.11), explicitly considers the water content in the unburned mixture and it has been developed in [69]. It is expressed by:

$$S_L = S_{L0} \left(\frac{T}{T_{ref}} \right)^{\alpha} \left(\frac{p}{p_{ref}} \right)^{\beta} (1 - \kappa x_r)^{\gamma} (1 - \chi x_w)^{\delta} \tag{3.26}$$

where x_r and x_w are the EGR and water mass fraction respectively. Details about the coefficients that provide the best fitting of the flame speed data can be found in [69]. The proposed correlation is able to separately evaluates the effects of water addition from those of other diluents on LFS variations. In fact, compared to the EGR, the presence of water in the combustion chamber generally results in a greater reduction in flame speed. This effect is illustrated in Figure 3.8.

A very small average fitting error of only about 2%, which is a remarkable ability to reproduce the kinetic LFS calculations given the numerous independent variables, their wide ranges of variation, and the various fuel compositions, is another significant aspect of the developed chemical-based LFS correlation. Additionally, LFS correlation showed to successfully extend the LFS predictions even for pressure and temperature levels far outside of its validity range (up to 120 bar of pressure and 1000 K of unburned temperature). In the end, this enables accurate simulation of the LFS values corresponding to common high-load engine conditions.
The evaporation process of the injected liquid water is an essential aspect considered in the model, as it plays a significant role in reducing the knock tendency at medium-high loads. In line with the experimental engine config-

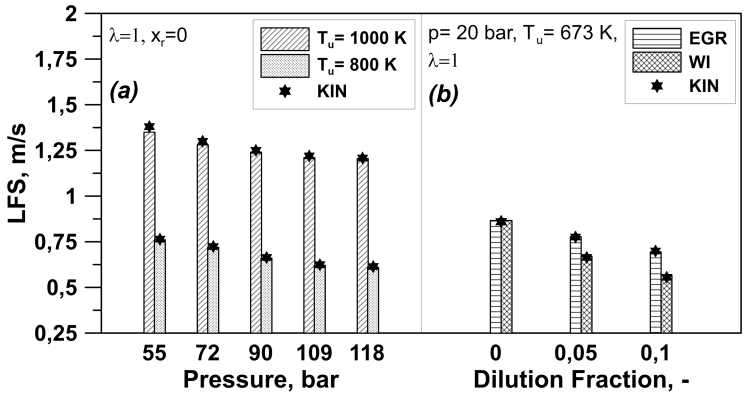

Figure 3.8: LFS under engine-like conditions (a); LFS vs Dilution fraction xr (b). (Dilution fraction is defined as the ratio of diluents to total mass). Source: [68]

uration, the liquid water is introduced through port injectors located along the intake runners. While some evaporation of the liquid water occurs within the intake pipes downstream of the injector positions, the majority of the evaporation takes place inside the engine cylinders. This is primarily due to the increasing gas temperatures during the compression stroke.

In the utilized 1D model, the evaporation of liquid water inside the engine cylinders is modeled using an evaporation rate (ER_w) determined by Equation 3.27. This equation represents a semi-empirical correlation that resembles the evaporation rate formulation implemented in the GT-Power code for liquid fuel.

$$ER_w = \frac{4.16 n_{ref}}{CA_{50}} \left(\frac{T}{T_{ref}}\right)^m \left(\frac{p}{p_{ref}}\right)^l \tag{3.27}$$

where CA_{50} is the 50% of the evaporation duration (in crank angle degrees), T is the mean in-cylinder gas temperature and T_{ref} its reference value; n is the engine speed in rpm and $nref$ the corresponding reference level; m and l are the exponents of temperature and speed ratios, respectively, and they are treated as two tuning constants. In the above correlation, the reference temperature is set at 600K, while the reference speed is equal to 4000 rpm. The evaporation of water inside the engine cylinders initiates during the intake phase and continues throughout the compression stroke until the spark event. The heat associated with the in-cylinder water evaporation is subtracted from both the working gas and the cylinder/piston walls. Since there are no direct measurements available to determine the exact distribution of heat between

the walls and the gas for each individual cylinder, a simple and reasonable assumption is made in this study. It assumes an equal and balanced heat distribution strategy, with 50% allocated to the walls and 50% to the gas.

The experimentally operated engine control parameters are imposed as input variables in the simulation for the validation under WI operations. The 1D model specifically defines the spark advance, valves actuation, and A/F ratio for each cylinder. Additionally, the waste-gate valve opening is controlled by a PID controller to replicate the experimental engine air flow rate for the load levels under consideration, while the throttle valve is set to be fully open. To replicate the experimental W/F ratio, port injectors inject measured amounts of liquid water. Following the tuning of the turbulence, combustion, and heat transfer sub-models, validation results are attained.

In the following figures 3.9-3.15, the numerical and experimental assessments of various performance parameters, combustion indicators, in-cylinder pressure traces, and burn rates are presented. These assessments are accompanied by the average error analysis. The reliability of the developed modeling approach in reproducing the experimental results is demonstrated using the ten operating conditions listed in Table 3.3. The error bars in the figures represent the standard deviations of measurements over 270 consecutive engine cycles.

Figure 3.9 specifically focuses on the comparison of the numerical and experimental results for the IMEP. The model shows a satisfactory prediction of the indicated load, with an average percent error of 2.5%.

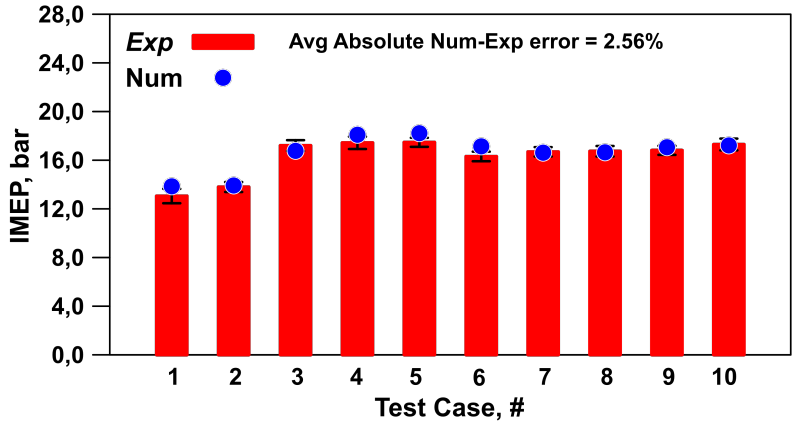

Figure 3.9: Experimental/numerical IMEP comparison under WI operation at different speed/load points and W/F ratios. Source: [68]

For combustion phasing (MFB_{50}) and in-cylinder pressure peaks of reference

Cylinder #2, Figures 3.10-3.11 provide the numerical/experimental comparison. The reproduction of combustion phasing exhibits an average error of 2.1%. However, a slightly higher error of 6.6% is observed for in-cylinder pressure peaks, which can be partly attributed to the inherent cycle-to-cycle variations in pressure. The numerically identified MFB_{50} levels and in-cylinder pressure peaks mostly fall within the corresponding experimental error band. Similar results were obtained for Cylinder #1.

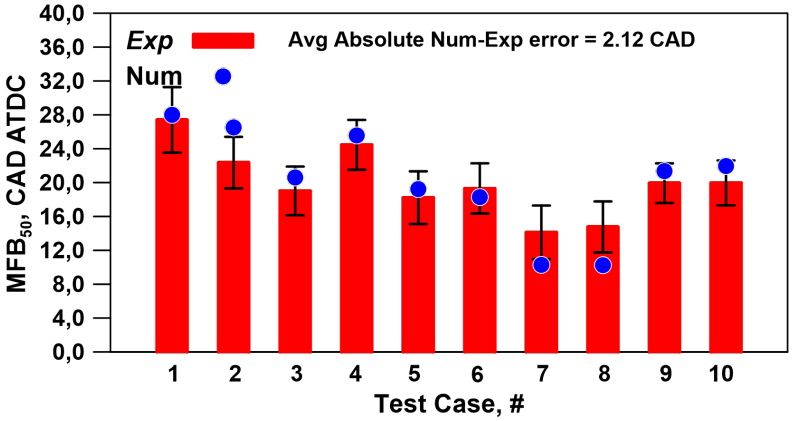

Figure 3.10: Experimental/numerical MFB_{50} comparison under WI operation at different speed/load points and W/F ratios. Source: [68]

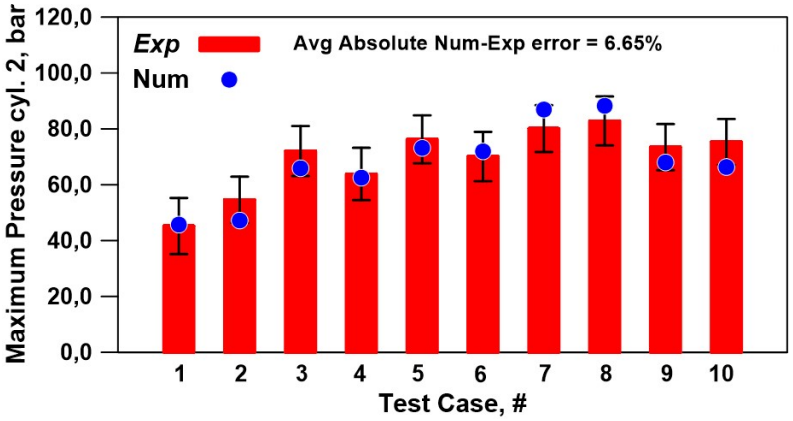

Figure 3.11: Experimental/numerical in-cylinder pressure peak comparison for Cyl#2 under WI operation at different speed/load points and W/F ratios. Source: [68]

Figure 3.12 presents the experimental/numerical assessment of indicated specific fuel consumption (ISFC). The model demonstrates an acceptable average error of approximately 4%, indicating its ability to accurately capture the combined effects of in-cylinder flow, combustion, and heat transfer characteristics.

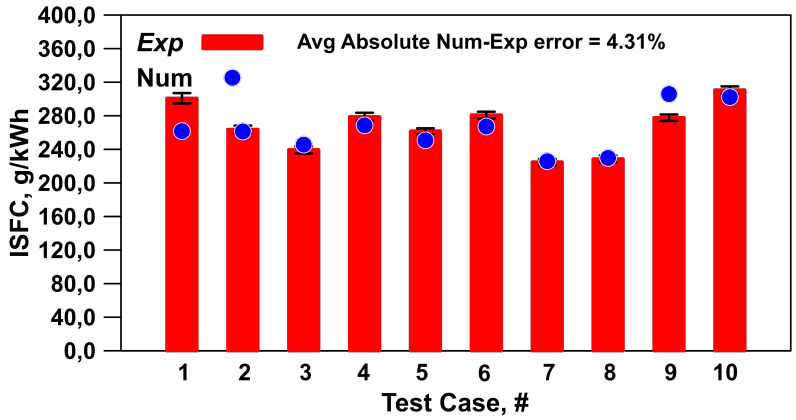

Figure 3.12: Experimental/numerical ISFC comparison under WI operation at different speed/load points and W/F ratios. Source: [68]

Furthermore, Figure 3.13 shows the comparison between numerical and experimental values for TIT, exhibiting an average error of 3.3%. This result confirms the advanced combustion modeling and the accurate representation of heat transfer in cylinders and exhaust ducts.

In summary, the numerical predictions for the discussed performance variables at the considered WI points fall within the allowable error band of ±5%.

To further demonstrate the reliability of the combustion model in capturing the influence of water injection on combustion characteristics, a comparison is made between the numerical in-cylinder pressure traces and burn rates and the corresponding experimental data for two cylinders. This analysis is presented in Figure 3.14 and Figure 3.15.

Figure 3.14 illustrates the results for a specific operating condition characterized by low speed, load, and W/F ratio (2160 rpm @ 13.8 bar, W/F = 0.07, A/F = 14.2). On the other hand, Figure 3.15 showcases the outcomes for a different operating condition with high speed, load, and W/F ratio (5000 rpm @ 17.3 bar, W/F = 0.3, A/F = 12.6).

The combustion model demonstrates its capability to accurately replicate the evolution of in-cylinder pressure and burn rates in both cylinders, spanning

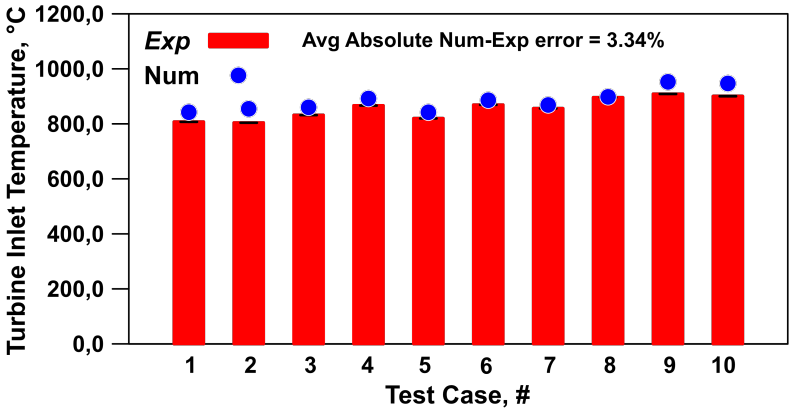

Figure 3.13: Experimental/numerical TIT comparison under WI operation at different speed/load points and W/F ratios. Source: [68]

across a wide range of rotational speeds, loads, and A/F ratios. This ability indicates the model's effectiveness in capturing the significant variations associated with different operating conditions. Additionally, the model maintains its accuracy even when simulating pressure cycles and burn rates at high W/F ratios, successfully reproducing the slower burn rate resulting from the increased water content (as observed in Figure 3.15). Moreover, the model appropriately responds to changes in the A/F ratio for both cylinders. This highlights the model's capability to account for variations in the A/F ratio and accurately capture their impact on combustion characteristics.

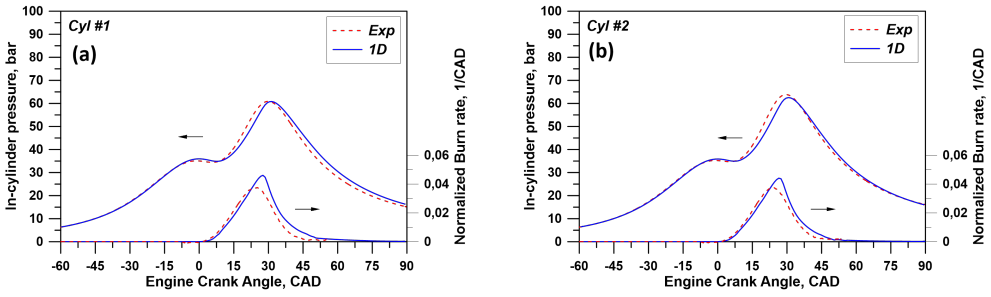

Figure 3.14: Numerical/Experimental comparison of in-cylinder pressure traces and burn rate profiles for the test case #2 2160rpm@13.8bar W/F=0.07 A/F=14.2: (a) Cyl#1, (b) Cyl#2. Source: [68]

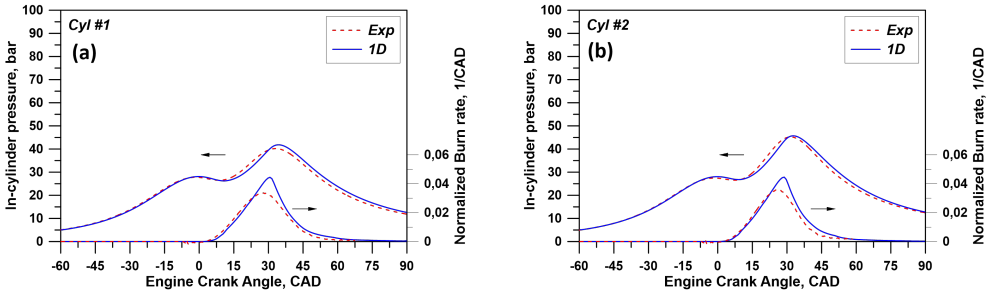

Figure 3.15: Experimental/Numerical comparison of in-cylinder pressure traces and burn rate profiles for the test case #10 5000rpm@17.3bar W/F=0.3 A/F=12.6: (a) Cyl#1, (b) Cyl#2. Source: [68]

Virtual engine re-calibration under WI

After demonstrating the capabilities of the developed 1D engine model in accurately reproducing experimental data, the validated model is utilized to conduct numerical engine calibrations at full load across the entire engine speed range, under both dry and WI conditions. To begin, a preliminary analysis under dry operation, referred to as the "Base" case, is performed. Similar to the experimental campaign, several operational constraints are taken into account to ensure the engine's safety and the integrity of its components. The engine control parameters are determined while adhering to constraints such as the maximum boost pressure (2.4 bar), turbocharger speed (255000 rpm), and turbine inlet temperature (950 °C). To fully exploit the benefits of water injection, the maximum allowable in-cylinder pressure is increased from its original value of 85 bar to a new limit of 100 bar. This adjustment aligns with the design of modern spark-ignition engine architectures [70]. During these calibrations, a fully open throttle valve is maintained, while the waste-gate opening is automatically controlled to achieve the desired load level at each speed within the maximum boost constraints. For knock-free operation, the SA is adjusted to set the MFB_{50} at 8 CAD AFTDC. Conversely, in the event of knock, the SA is automatically delayed to operate the engine at a knock borderline corresponding to a specified numerical knock index threshold, set at 0.95.

Additionally, gasoline injection is regulated by an additional PID controller, which enriches the A/F ratio to prevent exceeding the maximum allowable turbine inlet temperature. This controller specifies a stoichiometric A/F ratio when the turbine inlet temperature is below the related constraint.

Regarding the WI operations, a control logic for the injected water quantity needs to be defined. The maximum W/F ratio is extended to a limit of W/F = 0.5, surpassing the value of W/F = 0.3 selected during the experimental campaign. This new limit aligns with values reported in the literature [71, 72] and the developed model can accurately capture the in-cylinder phenomena even with a high water content.

In the first calibration strategy, named "Calibration A," the objective is to minimize the BSFC. This is achieved by selecting the maximum amount of injected water (W/F ratio = 0.5) while maintaining the Base full-load BMEP profile. By doing so, the lowest knock tendency is expected, enabling the selection of the highest A/F ratio (stoichiometric) and optimal combustion phasing at each speed, thereby identifying the lowest BSFC.

The second strategy, referred to as "Calibration B," aims to achieve a higher full load curve by imposing a stoichiometric A/F ratio and implementing different speed-related constraints:

- At low speeds (1500 rpm and 1800 rpm), a maximum W/F ratio of 0.5 is expected to be needed, and the waste-gate opening is automatically adjusted to match the allowable surge limit of the compressor. This choice maximizes the engine's torque output, thanks to the increased expansion work induced by water injection.

- In the medium speed range (from 1800 rpm up to 3600 rpm), the waste-gate opening is regulated to maintain an almost constant target BMEP of approximately 22 bar. The minimum amount of water is determined automatically to achieve a TIT level within the specified limit.

- At higher speeds, specifically from 3600 rpm to 5500 rpm, the selected maximum W/F ratio is insufficient to comply with the TIT constraint. In this case, additional adjustment of the waste-gate opening is applied to reduce the load until the TIT constraint is satisfied.

In summary, "Calibration B" represents a trade-off between improving BSFC and enhancing brake torque, aiming to achieve better overall performance compared to "Calibration A" while reducing the mean water consumption. The numerical results of the conducted virtual calibrations (Base, Calibration A, and Calibration B) are presented in the following.

A preliminary analysis compares the "Base" strategy with the "Calibration A" strategy, focusing on a selected set of engine performance variables. The assessment of these variables is presented through Figures 3.16 to 3.21. Figure 3.16 demonstrates the impact of water injection on improved combustion

phasing under full load conditions. Calibration A enables a significant advance in combustion phasing at each speed, particularly evident at low to medium speeds, with a maximum advance of approximately 12 CAD at 2100 rpm. It should be noted that even with the maximum water injection set, the engine does not operate at the MBT across the entire speed range.

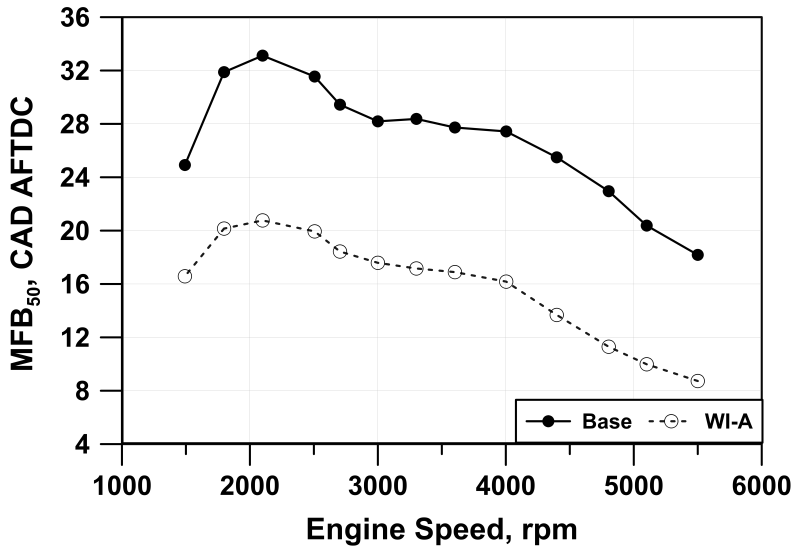

Figure 3.16: MFB_{50} vs engine speed for Base Calibration and WI-related Calibration A. Source: [68]

The advancement in combustion phasing achieved by Calibration A leads to higher in-cylinder pressure peaks compared to the Base Calibration levels, as shown in Figure 3.17. However, the adopted maximum in-cylinder pressure limit is never approached, indicating that all injected water is effectively utilized to mitigate knock occurrence and optimize the combustion process. The original design of the engine cylinders, which allows for a pressure peak of 85 bar, would limit the advancement in combustion phasing for speed points above 2700 rpm, thereby penalizing the thermal efficiency increase induced by water injection.

The delayed SA in the Base Calibration also results in increased TIT, reaching its maximum value in most of the speed range, as depicted in 3.18. Consequently, the in-cylinder air/fuel mixture needs to be progressively enriched above 2100 rpm, reaching a minimum A/F ratio of 11.3 at 4400 rpm. The injection of liquid water exerts both direct and indirect effects on TIT. The direct effect is associated with the vaporization heat of the injected water, which helps decrease the in-cylinder gas temperature. Additionally, the indirect effect of improved combustion phasing (Figure 3.16) enables further TIT reduction,

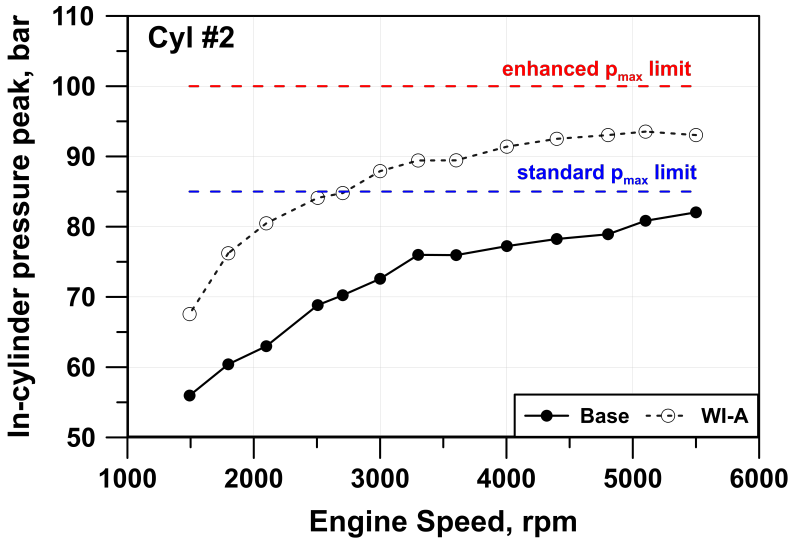

Figure 3.17: Pressure peak of Cyl#2 vs engine speed for Base Calibration and WI-related Calibration A. Source: [68]

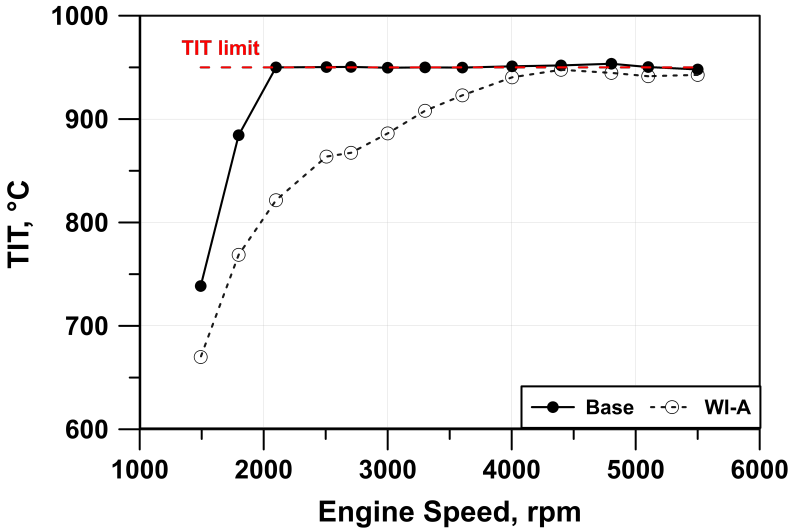

Figure 3.18: TIT vs engine speed for Base Calibration and WI-related Calibration A. Source: [68]

ensuring stoichiometric A/F ratio operation throughout.

The impact of water injection on combustion duration (MFB 10-90) is

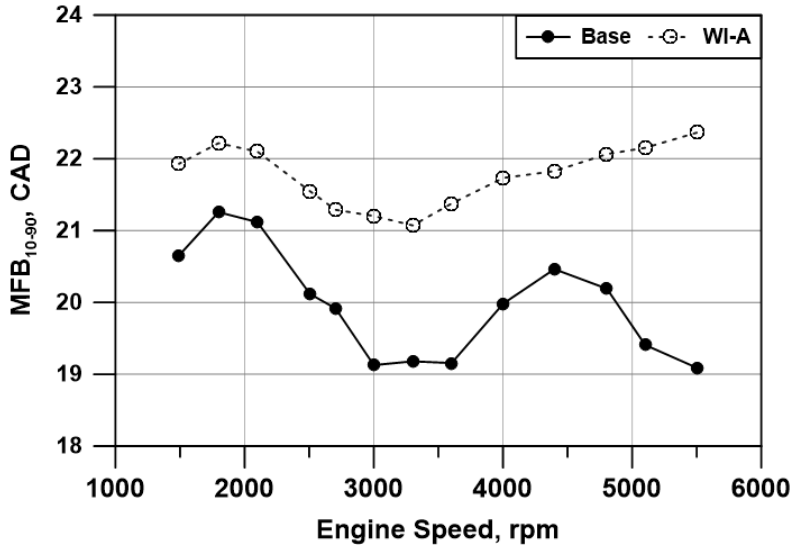

Figure 3.19: Combustion duration (MFB10-90) vs engine speed for Base Calibration and WI-related Calibration A. Source: [68]

shown in Figure 3.19. Despite the counteracting effect of optimized combustion phasing (Figure 3.16), water injection primarily contributes to lengthening the combustion duration.

Another notable effect of water injection is the modification of engine-turbocharging matching. Figure 3.20 demonstrates that Calibration A with water injection leads to a lower boost pressure demand at each speed. The presence of water vapor in the cylinders allows for greater expansion work and improved efficiency, resulting from increased knock resistance and stoichiometric operation. These effects tend to reduce the air flow rate. It is worth noting that Calibration A remains well below the maximum allowable peak boost pressure of 2.4 bar, providing the opportunity to explore alternative water injection strategies aimed at maximizing torque while maintaining compliance with constraints.

One of the main advantages of the considered water injection Calibration is its impact on BSFC. As anticipated, the combined effects of the aforementioned phenomena and compliance with engine operating constraints result in lower BSFC values compared to dry operation. At low speeds and up to 2100 rpm, the BSFC benefits are primarily derived from the optimization of combustion phasing induced by water injection (Figure 3.16), yielding approximately 13.8% improvement. Moving into the medium/high-speed range, even greater BSFC advantages are achieved due to both combustion phasing advancement and the

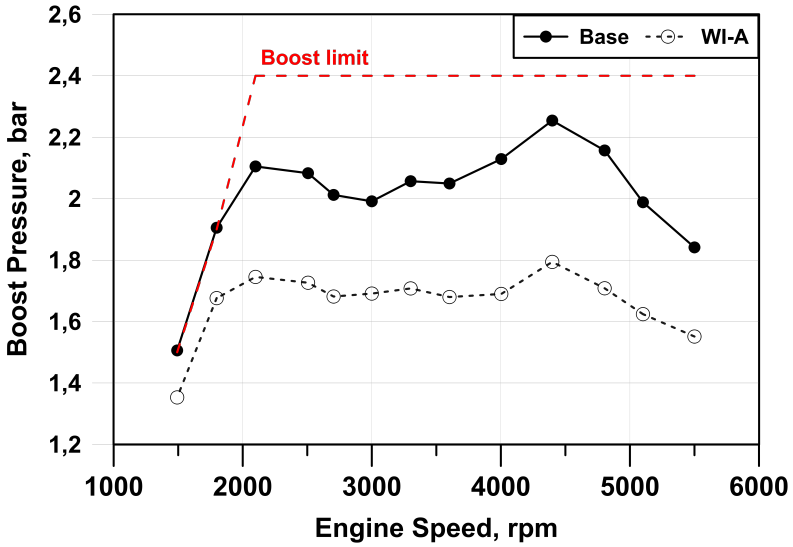

Figure 3.20: Boost pressure vs engine speed for Base Calibration and WI-related Calibration A. Source: [68]

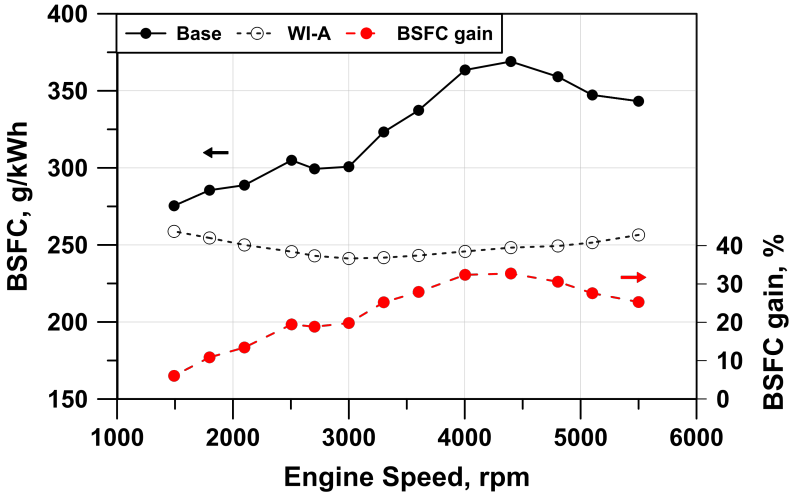

Figure 3.21: BSFC vs engine speed for Base Calibration and WI-related Calibration A. Source: [68]

suppression of A/F mixture enrichment. Figure 3.21 illustrates the maximum benefit realized at 4400 rpm, corresponding to a 32% gain in BSFC.

The second virtual engine calibration, referred to as Calibration B, intro-

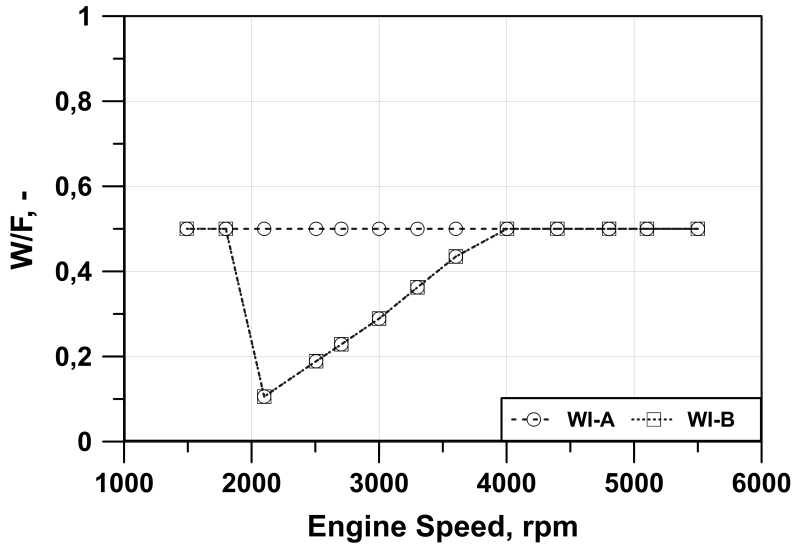

Figure 3.22: W/F vs engine speed for Calibration A and Calibration B. Source: [68]

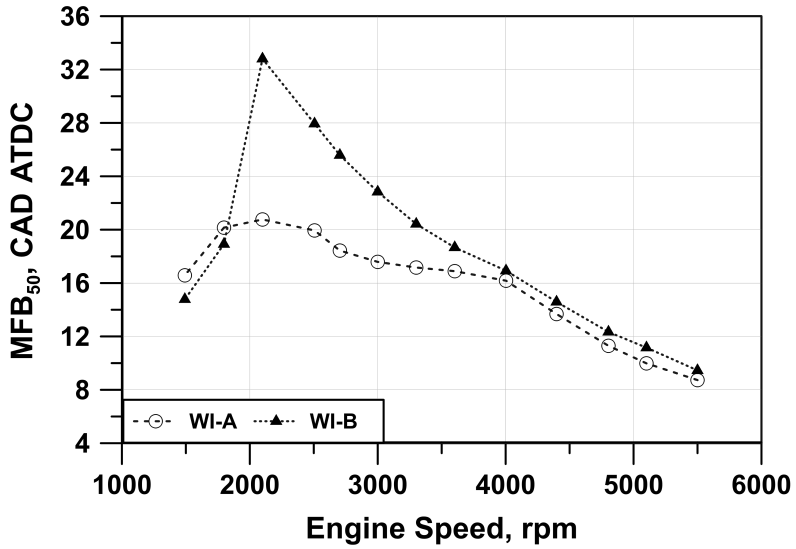

Figure 3.23: MFB_{50} vs engine speed for Calibrations A and B. Source: [68]

duces an innovative WI strategy that simultaneously enhances engine torque and efficiency. This calibration achieves a new full load curve while maintaining stoichiometric operation, adhering to the TIT constraint, and considering

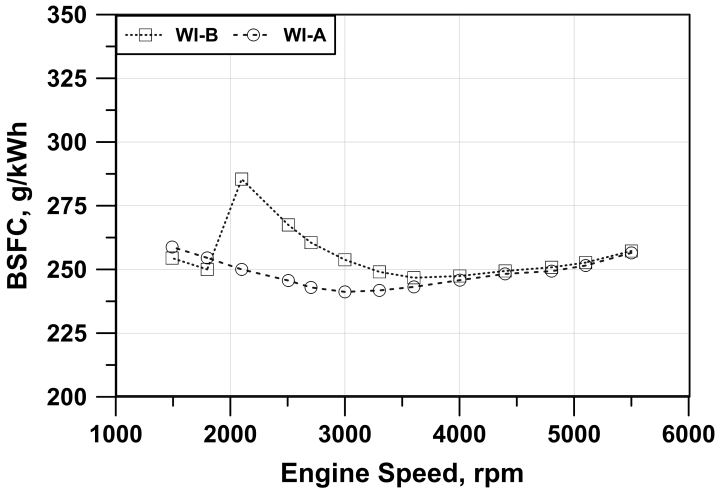

Figure 3.24: BSFC vs engine speed for Calibration A and Calibration B. Source: [68]

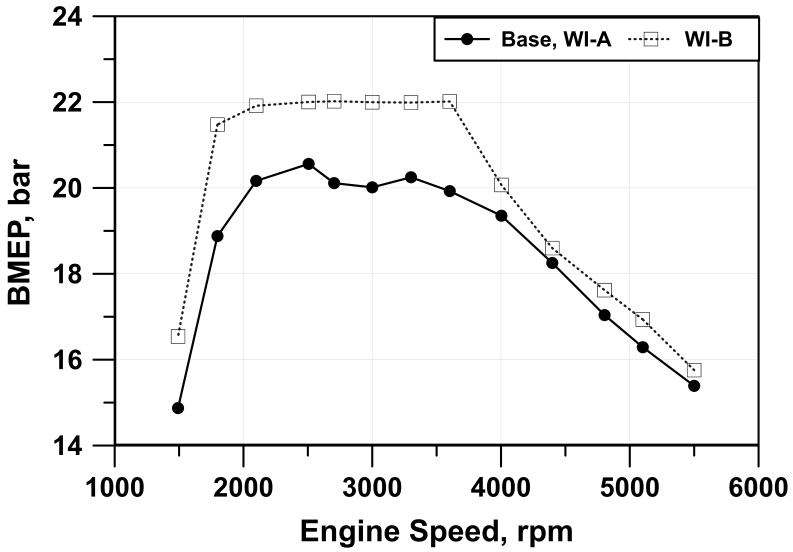

Figure 3.25: Comparison of Full Load-BMEP curves between Base calibration and WI-related Calibration B. Source: [68]

surge limits. By minimizing water consumption, Calibration B aims to reduce water-induced corrosion and the required water tank volume. Figures 3.22 to 3.25 provide a direct comparison between Calibration A and Calibration B.

Figure 3.22 illustrates the minimum required W/F ratio at each speed, with maximum values achieved at low speeds for torque increase and high speeds for TIT control. Figure 3.23 compares the MFB_{50} between Calibration A and Calibration B. In the medium speed range, the reduced W/F ratio in Calibration B leads to a slight delay in combustion phasing. Although a higher W/F ratio could optimize combustion phasing, the automatic controller of Calibration B selects the minimum water quantity to meet the TIT limit. This calibration choice serves as a compromise between fuel and water consumption, effectively reducing the water demand while keeping TIT below the 950°C limit.

Regarding BSFC, Figure 3.24 demonstrates slightly higher values in the medium speed range for Calibration B, with a maximum penalty of approximately 35g/kWh at 2100 rpm. Figure 3.25 presents the maximum BMEP as a function of engine speed for both calibration strategies. Calibration B enables an increase in maximum BMEP of up to 22 bar from 2100 rpm to 3600 rpm, with a peak torque enhancement of 13.8% at 1800 rpm.

3.3.2 Hydrogen fueled single cylinder research engine

Engine details and experimental tests

The calibration of the combustion model utilized experimental measurements obtained from tests conducted at the Instituto Universitario de Motores Térmicos (CMT) in Valencia (Spain), on a single-cylinder spark ignition research engine equipped with a gaseous PFI system. Table 3.3.2 summarizes the main characteristics of the engine.

Table 3.4: Engine Characteristics

Engine Characteristics	
Engine Type	4 stroke, 4 valves, port fuel injection
Number of cylinders	1
Displaced volume [cm^3]	454.2
Stroke [mm]	86
Bore [mm]	82
Compression ratio	10.7:1

Figure 3.26 illustrates the configuration of the test cell, highlighting the locations for pressure and temperature measurements, fuel injection, and other control and measuring devices. In-cylinder pressure was recorded using a Kistler piezoelectric transducer, while piezoresistive pressure sensors were employed for average flow pressures. Air mass flow was measured using a volumetric airflow

meter from Kromschroeder, while hydrogen mass flow was registered using a Bronkhorst F-113AC-1M0-AAD-55-V flow meter. Relevant emissions from the combustion process were monitored using a HORIBA MEXA-7600EGR gas analyzer. The engine's operating conditions were set using auxiliary systems, including an external compressor and air conditioning system for controlling intake pressure and temperature. Additionally, a knife-gate valve was utilized to simulate the desired exhaust backpressure. Table 3.3.2 provides a summary of the instrumentation used and the accuracy of certain relevant devices.

Table 3.5: Variable measured and devices used

Variable measured	Device	Manufacturer/model	Accuracy
In-cylinder pressure	Piezoelectric transducer	Kistler / 6125C	±1.25 bar
Intake/exhaust pressure	Piezoresistive transducers	Kistler / 4045A	±25 mbar
Temperature in flow pipes	Thermocouple	TC direct / type K	±2.5 °C
Crank angle, engine speed	Encoder	AVL / 365	±0.03 CAD
NOx, O2, CO2	Gas analyzer	HORIBA / MEXA 7600 DEGR	4%
Hydrogen mass flow	Fuel balances	Bronkhorst / F-113AC	±0.5%
Air mass flow	Air flow meter	Kromschroeder / RVG-G65	±1%

The hydrogen used in the experiments was stored in pressurized tanks and supplied to a pressure discharge control system before being fed into the injector. The injector used in this case is a Zavoli JET Injector designed for gaseous fuels, with a maximum working pressure of 4.5 bar, a working temperature range of -40 °C to 120 °C, and a discharge nozzle diameter of 3 mm. Further details regarding the fuel properties are provided in Table 3.6.

To ensure the stability of indicated parameters such as IMEP, Heat Release Rate (HRR), and combustion phasing, the test facility is equipped with an online combustion diagnostic software called INDICOM. Cycle-to-cycle variability is evaluated using the coefficient of variance of IMEP (CoV_{IMEP}), and steady-state operation of the engine is achieved when the CoV_{IMEP} is below 5%. Each operating condition is measured at least three times, with 250 cycles recorded each time to ensure sufficient data for averaging and subsequent thermodynamic analysis. For additional details regarding the test facility equipment and testing methodology, reference can be made to previous works [73].

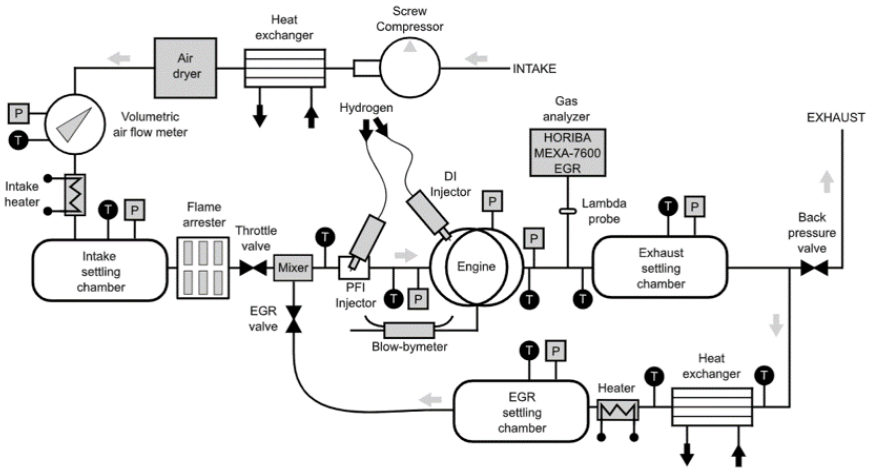

Figure 3.26: Test cell diagram

Table 3.6: Hydrogen properties

Formula	H2
Autoignition temperature [K]	858
Mass diffusivity in air [cm^2/s]	0.61
Cetane number [-]	55.7
RON [-]	130
MON [-]	62-64
Lower heating value [MJ/kg]	119.9
Purity [%]	99.9

The experimental measurements employed in this study to feed the numerical model cover a range of operating conditions. These conditions encompass IMEP values ranging from 5 to 11 bar, lambda values ranging from 1.4 to 4, and spark timings ranging from -36 to 0 CAD aTDC, as summarized in Table 3.7. The engine speed was fixed at 1500rpm. The inclusion of these diverse conditions ensures the versatility and adaptability of the combustion model in effectively capturing the tendencies and effects of the analyzed external parameters in this study.

Numerical approaches

The engine model employed in this study utilizes the 1D commercial software GT-Power. The intake and exhaust flows are computed using standard

Table 3.7: Case study parameters

Case	IMEP (bar)	λ (-)	ST (aTDC)
1	4.74	1.4	-2
2	4.87	1.6	-4.2
3	4.97	1.8	-8
4	5.06	2	-12.2
6	5.13	2.2	-16.2
6	5.13	2.4	-20
7	5.20	2.6	-20
8	5.22	2.8	-24.2
9	5.24	3	-28.2
10	5.25	3.2	-30.2
11	5.22	3.4	-32
12	5.17	3.6	-30
13	5.08	3.8	-36.2
14	4.80	4	-36.2
15	8.47	2.4	-24.2
16	8.46	2.6	-26
17	8.65	2.8	-28.2
18	8.71	3	-32
19	8.69	3.2	-34.2
20	8.60	3.4	-36.2
21	11.22	2.6	-30.2

components from the software library. To capture the intricate in-cylinder processes discussed in Chapter 3.2, custom sub-models developed in-house are incorporated into the 1D code. These sub-models are designed to accurately describe the relevant phenomena. The experimentally operated engine control parameters are imposed as input variables in the simulation. The 1D model specifically defines the spark advance to match the experimental center of combustion (CA50), valves actuation, and A/F ratio. Additionally, user-routines containing correlations for laminar flame speed and flame instabilities effects are integrated into the software to enhance its predictive capabilities.

Hydrogen laminar flame speed modeling

During the course of this research, a new correlation for hydrogen laminar flame speed has been developed by fitting the results of a chemical kinetics solver (CANTERA) applied to 1D planar laminar flames. The Konnov mechanism [65], including 5 elements, 15 species, and 75 reactions is utilized to perform

the CANTERA calculations. They are performed for several values of pressure, p, temperature, T, equivalence ratio, ϕ, and exhaust gas mass fraction, x_r, in the following ranges:

- Pressure: 1-120 bar
- Temperature: 600-850 K
- Equivalence ratio: 0.25-1
- Exhaust gas mass fraction: 0-0.25

The composition of the residual gas is established in each condition as the equilibrium composition of the combustion products. The S_L correlation is expressed as:

$$S_L = a\left(a_1\phi^3 + a_2\phi^2 - a_3\phi^3 - a_4\right)\left(\frac{T}{T_{ref}}\right)^b \left(\frac{p}{p_{ref}}\right)^{\left(b_1\phi^3 - b_2\phi^2 + b_3\phi^3 - b_4\right)} e^{cx_r} \tag{3.28}$$

The values of the correlation constants that provide the best fitting of the S_L data are listed in Table 3.8

Table 3.8: Coefficients and reference conditions for S_L correlation

Coefficients	
a	16.693
a1	35.265
a2	-85.431
a3	-72.679
a4	11.973
b	3.289
b1	0.722
b2	2.776
b3	3.767
b4	2.198
c	3.901
Reference conditions	
T, K	300
p, bar	1

The coefficient of regression is 0.99 and the regression plot is shown in Figure 3.27

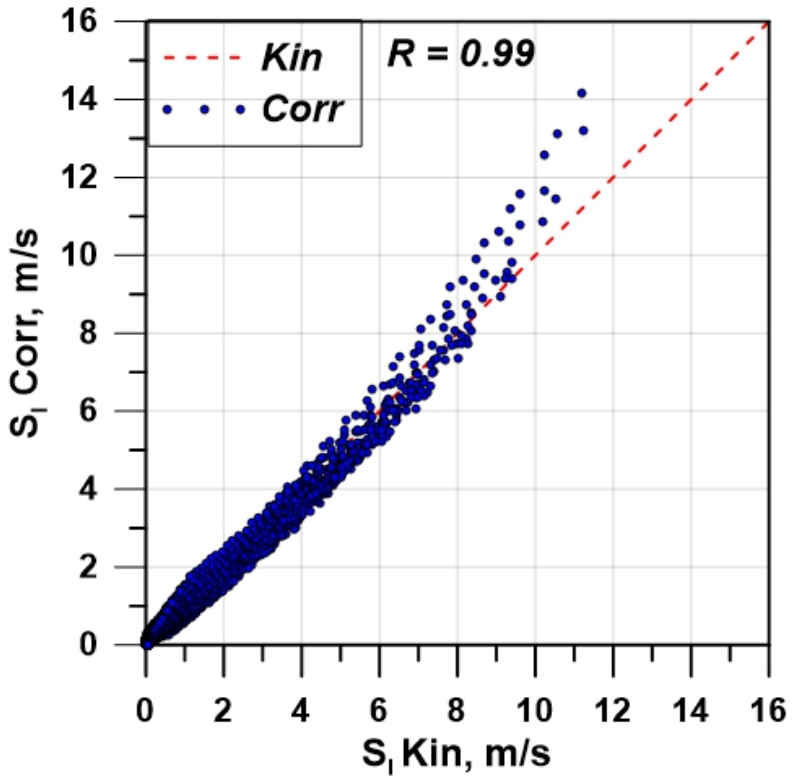

Figure 3.27: Hydrogen laminar flame speed regression plot

Thermo-Diffusive Instability Measurement

As described in Chapter 3.2, lean hydrogen flames are subjected to intrinsic instabilities. The combustion model has been properly modified to take into accounts their effects. The intensities of both Darrieus-Landau (DL) and thermodiffusive (TD) instabilities are influenced by a range of factors, including the properties of reactants, products, and the underlying chemistry. Consequently, it becomes necessary to characterize the response of flame instability concerning the local mixture state. Such characterization enables the modification of models to incorporate the effects of these instabilities. Initial efforts to characterize DL instability involved employing linear stability analysis, assuming an infinitely thin flame. This analysis utilized Rankine-Hugoniot jump conditions applied to the linearized Euler equations.

A comprehensive derivation of the dispersion relation can be found in reference [74]. It was observed that assuming the flame to be of the form $F(x,t) = Ae^{(\omega t+ikx)}$, propagating at a speed S_L with a characteristic thickness

δ_L (and timescale $\tau_L = \delta_L/S_L$), the normalized growth rate of the instability, denoted as $\tilde{\omega}$, follows a dispersion relation:

$$\tilde{\omega} = \frac{1}{\sigma+1}\left(\sqrt{\sigma^3+\sigma^2-\sigma}-\sigma\right)\tilde{k} \tag{3.29}$$

Here, $\tilde{k} = k\delta_L$ represents the normalized wavenumber, and $\sigma = \frac{\rho_u}{\rho_b}$ denotes the density ratio across the flame. However, this growth rate predicts an unbounded increase with respect to the wavenumber, which does not align with experimental and numerical observations. Moreover, it does not account for the effects of viscosity and diffusion, both of which have been demonstrated to play a significant role in the onset of thermodiffusive instability. To address these shortcomings, a new dispersion relation was derived, incorporating the destabilizing effects of diffusion across the flame [75]. This revised relation includes a second-order term, represented as $\tilde{k}^2$, where ω_{DL} is determined by $\omega_{DL} = \frac{1}{\sigma+1}\left(\sqrt{\sigma^3+\sigma^2-\sigma}-\sigma\right)$.

$$\tilde{\omega} = \omega_{DL}\tilde{k} + \omega_2\tilde{k}^2 \tag{3.30}$$

Research conducted in [76, 77] emphasized that the coefficient ω_2 of the second-order term is crucial in characterizing the thermo-diffusive response of lean hydrogen flames. For a more comprehensive consideration of factors such as equivalence ratio, variable transport coefficients, and reaction order, Matalon et al. [75] presented a general form for ω_2:

$$\omega_2 = -\left(B_1 + \beta\left(Le_{eff}-1\right)B_2 + PrB_3\right) \tag{3.31}$$

where B_i are constants depending on the density ratio (σ) and temperature-dependet thermal conducivity (λ), β is the Zeldovich number of the reaction and Pr is the Prandtl number. Assuming unity reaction orders, the effective Lewis number of the unburned mixture is given by:

$$Le_{eff} = \begin{cases} \frac{Le_0+ALe_f}{1+A}, A = 1+\beta\left(\phi^{-1}-1\right) if \phi < 1 \\ \frac{Le_f+ALe_0}{1+A}, A = 1+\beta\left(\phi-1\right) if \phi > 1 \end{cases} \tag{3.32}$$

The coefficients B_i, as defined by Matalon [78], rely on the thermal conductivity distribution across the flame. The functional expressions are explicitly determined by σ and formulated using an integral that relies on the scaling of thermal conductivity ($\tilde{\lambda} = \lambda/\lambda_u$) with respect to the normalized temperature ($x = T/T_u$). The complete formulas are provided below:

$$B_1 = \frac{\sigma}{2\left(\sigma+(\sigma+1)\omega_{DL}\right)}\left(\frac{\sigma(2\omega_{DL}+\sigma+1)}{\sigma-1}\int_1^\sigma \frac{\tilde{\lambda}(x)}{x}\,dx \int_1^\sigma \tilde{\lambda}(x)\,dx\right) \tag{3.33}$$

$$B_2 = \frac{\sigma(1+\omega_{DL})(\sigma+\omega_{DL})}{2\,(\sigma-1)\,(\sigma+(\sigma+1)\omega_{DL})} \int_1^\sigma \log\frac{\sigma-1}{x-1}\frac{\tilde{\lambda}(x)}{x}\,dx \tag{3.34}$$

$$B_3 = \frac{\sigma}{\sigma+(\sigma+1)\omega_{DL}} \left((\sigma-1)\tilde{\lambda}(\sigma) - \int_1^\sigma \tilde{\lambda}(x)\,dx\right) \tag{3.35}$$

It is important to compute the scaling function $\tilde{\lambda}$ for each flame and evaluate the integrals to determine the constants B_i. Among these constants, B_1 and B_3 account for the stabilizing influences of heat and viscous diffusion, respectively, while B_2 represents the stabilizing or destabilizing impact of molecular diffusion. Another term to calculate is the Zeldovich number, which serves as the normalized activation energy for a chemical reaction. For a single-step reaction, the Zeldovich number can be defined as follows:

$$\beta = \frac{E_a\,(T_b - T_u)}{R{T_b}^2} \tag{3.36}$$

where R is the ideal gas constant. The apparent activation energy (E_a) is defined through the formulation:

$$\frac{E_a}{2R} = \frac{\partial \ln(\rho_u S_L)}{\partial\left(\frac{1}{T_b}\right)} \tag{3.37}$$

The expression for E_a is derived using a correlation based on 1D flame computations by CANTERA, where E_a is a function of p and ϕ. Given a specific combination of pressure and equivalence ratio, the temperature of the unburned mixture is perturbed (assuming E_a is independent of T_u), and the derivative on the right-hand side of equation 3.37 is approximated. Subsequently, the obtained values of E_a are fitted using a polynomial with two variables as follows:

$$\begin{aligned} E_a = {} & H_{00} + H_{10}\cdot p_{std} + H_{01}\cdot \phi_{std} \\ & + H_{20}\cdot p_{std}^2 + H_{11}\cdot p_{std}\cdot\phi_{std} + H_{02}\cdot\phi_{std}^2 \\ & + H_{30}\cdot p_{std}^3 + H_{21}\cdot p_{std}^2\cdot\phi_{std} + H_{12}\cdot p_{std}\cdot\phi_{std}^2 \\ & + H_{40}\cdot p_{std}^4 + H_{31}\cdot p_{std}^3\cdot\phi_{std} + H_{22}\cdot p_{std}^2\cdot\phi_{std}^2 \end{aligned} \tag{3.38}$$

$$p_{std} = \frac{p - 41.04}{31.22} \tag{3.39}$$

$$phi_{std} = \frac{phi - 1.345}{1.039} \tag{3.40}$$

Table 3.9: Coefficients for E_a correlation

E_a fitting coefficient	
H_{00}	53.13
H_{10}	10.81
H_{01}	-23.02
H_{20}	-6.323
H_{11}	19.7
H_{02}	13.01
H_{30}	11.35
H_{21}	2.821
H_{12}	-11.56
H_{40}	-5.211
H_{31}	-5.719
H_{22}	0.3952

The values of the fitting coefficient are reported in the table 3.9.

Another consequence of the TD instability, in addition to the increased folding of the flame, is the local thinning and acceleration caused by the enhanced local combustion. Therefore, it is crucial to differentiate between the standard laminar adiabatic unstretched one-dimensional quantities (such as flame speed and thickness), which do not consider the TD effects, and the laminar adiabatic freely propagating values (denoted as s_F and δ_F) obtained through well-resolved multidimensional simulations that incorporate the TD effects.

Howarth et al. [77] argue that the latter should be considered as the reference flame speed when used as an input in various sub-models, such as turbulent flame speed, to partially account for the TD effects. Additionally, Howarth et al. [76] have demonstrated that the ω_2 parameter not only serves as a suitable characteristic for describing the TD instability but also enables the development of correlations for the freely propagating flame speed. These correlations have been derived by fitting data from two- and three-dimensional Direct Numerical Simulations conducted over a wide range of operating conditions in a stationary chemical reactor, encompassing a diverse set of ω_2 values.

$$S_F = \begin{cases} exp(0.08 \cdot \omega_2) \cdot S_L & if \quad p < \Pi_{\text{crit}} \\ (1. + 0.47 \cdot \omega_2) \cdot S_L & if \quad p > \Pi_{\text{crit}} \end{cases} \tag{3.41}$$

$$\Pi_{\text{crit}} = \left(\frac{20 \cdot \phi}{7 - 2 \cdot \theta} \right)^{\frac{150}{21+10 \cdot \theta}} \tag{3.42}$$

$$\theta = \frac{T}{300} \tag{3.43}$$

As can be observed from the above equations, two different fittings have been proposed depending on the parameter Π_{crit}. This parameter represents a "ridge" (actually a two-dimensional surface in the three-dimensional parameter space) where, for a specific temperature and equivalence ratio, there exists a pressure that exhibits the maximum level of instability. Consequently, two distinct regions can be identified in this three-dimensional space. However, the thermodynamic conditions during an engine cycle are highly unsteady, and the application of Equation 3.41 would lead to physically meaningless discontinuities. Therefore, within the scope of this work, the following functional form, (represented in Figure 3.28), is proposed to describe the transition between the two fittings, eliminating the discontinuities.

$$S_F = exp(0.08 \cdot \omega_2) \cdot S_L \cdot (1 - \Sigma) + (1. + 0.47 \cdot \omega_2) \cdot S_L \cdot \Sigma \tag{3.44}$$

$$\Sigma = 1 - exp\left(-7 \cdot \frac{p}{\Pi_{\text{crit}}}\right) \tag{3.45}$$

3D simulations and turbulence model tuning

In order to tune the turbulence model described in Chapter 3.2, for this study, the turbulence intensity and integral length scale were calculated under motoring conditions using a 3D-CFD model developed with the CONVERGE software. A hexahedral grid strategy based on an orthogonal basis was employed to construct the model, as illustrated in Figure 3.29. The computational domain was meshed with a base cell size of 4 mm, which was refined to 2 mm in the intake and exhaust regions, and further refined to 1 mm in the cylinder region. To capture the details near the cylinder walls, including the moving piston and valves, the cell resolution was increased to 0.5 mm. Additionally, an Adaptive Mesh Refinement (AMR) algorithm was utilized to enhance the grid resolution in areas with significant velocity and temperature gradients. The AMR algorithm employed a sub-grid criteria of 1 m/s and 2.5 K, reducing the cell size to a minimum of 0.125 mm. Detailed information regarding the grid definition can be found in Table 4.

The turbulence modeling was performed within the unsteady Reynolds-averaged Navier–Stokes (URANS) framework. Specifically, the Re-Normalization Group variant of the k-epsilon model (RNG k-ϵ model [79]), based on an eddy-viscosity-based two-equation turbulence model, was employed. The gas-to-wall

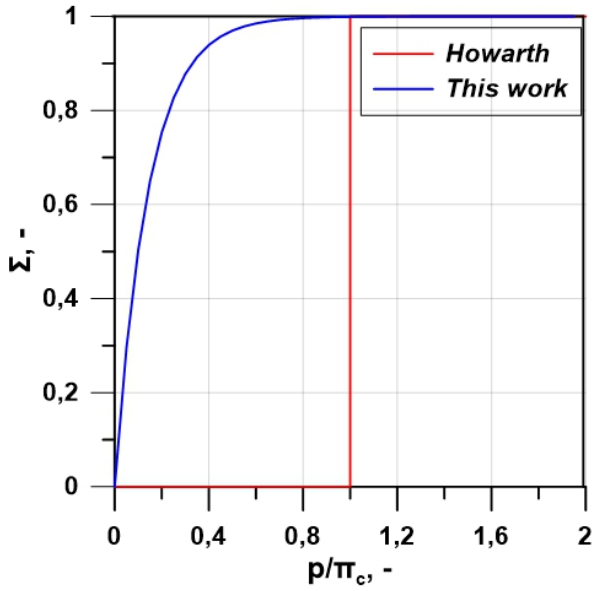

Figure 3.28: Σ as a function of $\frac{p}{\Pi_{crit}}$ according to Howarth [77] and Equation 3.45

Table 3.10: Details of the mesh configuration

Configuration	**Size (mm)**
Base size	4
Intake/exhaust ports	2
Chamber refinement	1
Walls refinement	0.5
AMR min. size	0.125
Number of cells	0.5-4 million

heat transfer was modeled using the approach proposed by Angelberger [80], which has been widely applied in internal ICE applications [81]. The simulations utilized a second-order central difference scheme for spatial discretization and a first-order scheme for temporal discretization. The pressure and velocity fields were coupled using a modified Pressure Implicit with Splitting of Operators (PISO) algorithm developed by [82]. The compressible flow properties were computed using the ideal gas equation of state. The CFD model was validated against experimental data, and a comparison between the experiments and CFD results at 3000 RPM and 11 bar can be found in [83]. The validation

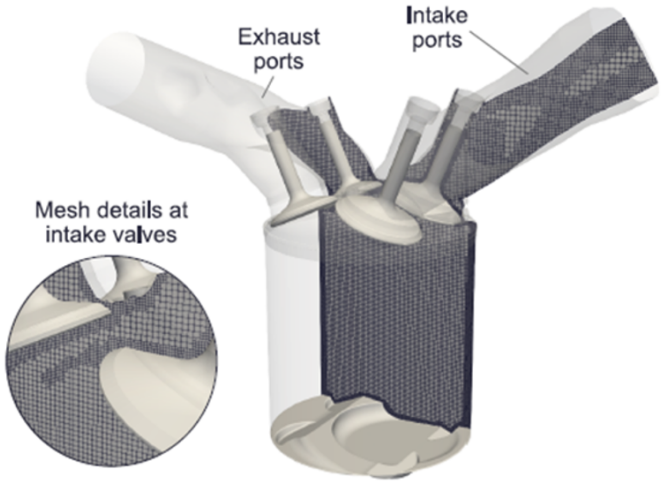

Figure 3.29: General view of the mesh domain.

demonstrated a satisfactory prediction of the in-cylinder pressure and heat release rate.

In figures 3.30-3.31 the comparison between the 3D and 1D model for L_i and u' are depicted. The 1D model is tuned by modifying the tuning constant $C_{Kin0}, C_{PKK}, C_{Tin0}, c_{fd0}, c_{fdm}$ as previously described in Chapter 3.2. Focusing on L_i, the compression phase and the zone near the TDC are the most critical ones and the model tends to reproduce well the CFD data. Some inaccuracies are evident after the TDC, but it doesn't affect too much the combustion process.

Additionally, figure 3.31 compares the turbulence intensity from 1D and 3D simulations. Its decrease during the first 120 to 60 CAD of the compression stroke, which is accompanied by an increase in ordered structures in the flow, is observed. In this regard, the 1D model precisely replicates the 3D data. The collapse of the tumble vortex close to the TDC causes turbulence to accelerate in the second half. The model does a good job of capturing this effect, both in terms of amplitude and phase. Approaching the TDC the turbulence intensity tends to decrease.

Engine model validation

In the first part of this section, the numerical-experimental agreement is presented in terms of pressure cycles and burn rates for some of the test points from Table 3.7, considering low, medium and high loads for different values

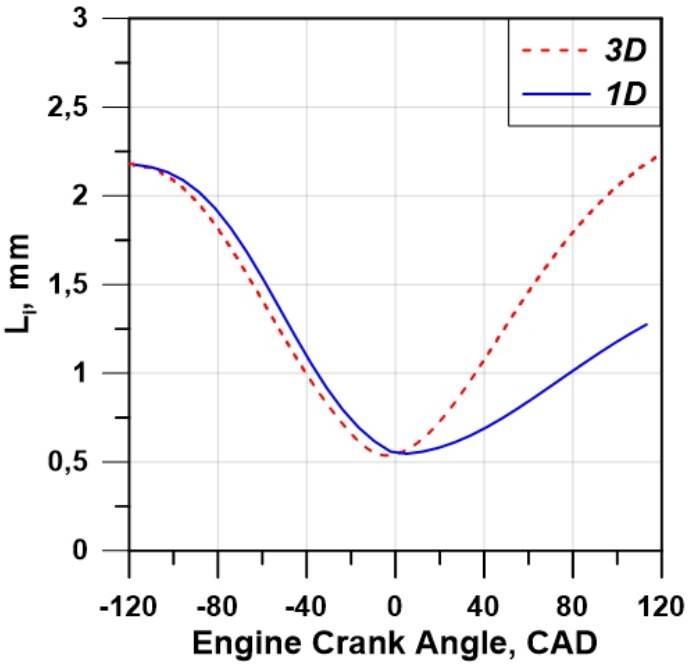

Figure 3.30: CFD and 1D Integral lenght scale evolution.

of λ (Figures 3.32-3.34). Specifically, the results of two different conditions are compared to demonstrate the significance of thermodiffusive instability effects. The first condition corresponds to a model where the laminar flame speed is not affected by thermodiffusive instabilities and follows Equation 3.28 (w/o TD). The second condition considers the flame corrugation effects using Equation 3.44 (w/ TD). For each of the two models, a trial-and-error procedure was used to determine a specific set of tuning constants (c_{trans}, c_{wrk} and x_{wc}) that can replicate the pressure trace as accurately as possible for all the 21 test cases of Table 3.7. It is important to emphasize that, due to flame corrugation caused by TD instabilities, the w/ TD model has different tuning constants compared to the w/o TD model. However, these tuning constants are kept constant for all test points.

In particular, Figure 3.32 presents the numerical comparison of in-cylinder pressure traces and burn rate profiles for test case #1-6-12 (Table 3.7). It can be observed that, due to the consideration of TD effects, the w/ TD model is capable of better reproducing the burn rates across different lambda values compared to the w/o TD model. In the case #12, the decay in laminar flame speed leads to a noticeable underestimation of the burn rate for the w/o TD

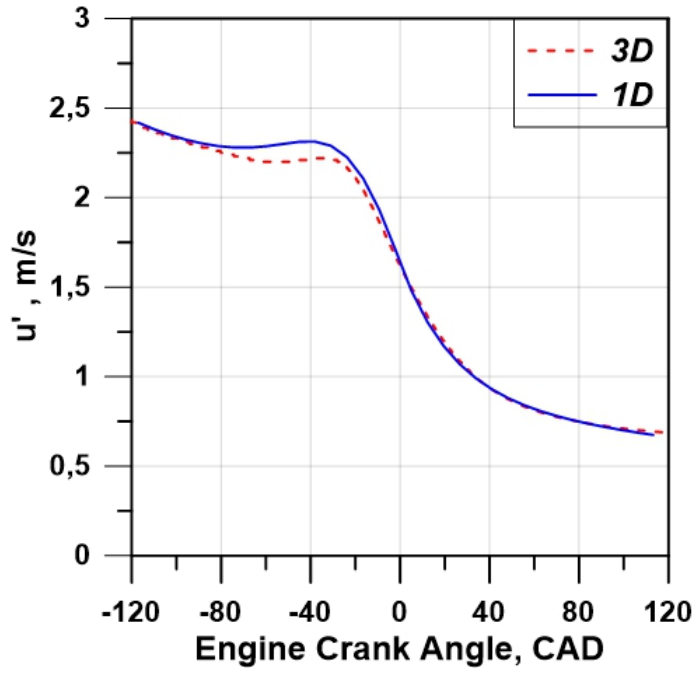

Figure 3.31: CFD and 1D Turbulent intensity evolution.

model. A slight underestimation of the burn rate in the w/ TD model results in a 7% underestimation of the peak pressure for test case # 1.

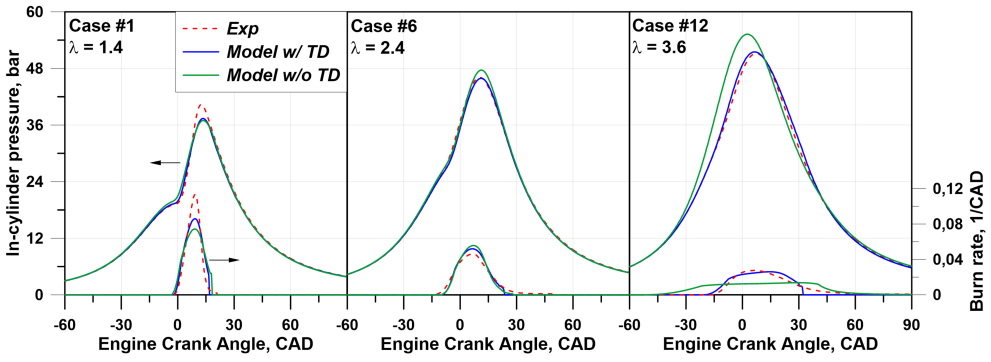

Figure 3.32: Experimental/Numerical comparison of in-cylinder pressure traces and burn rate profiles for the test case #1-6-12 (Table 3.7)

Similar considerations can be made for the numerical/experimental compar-

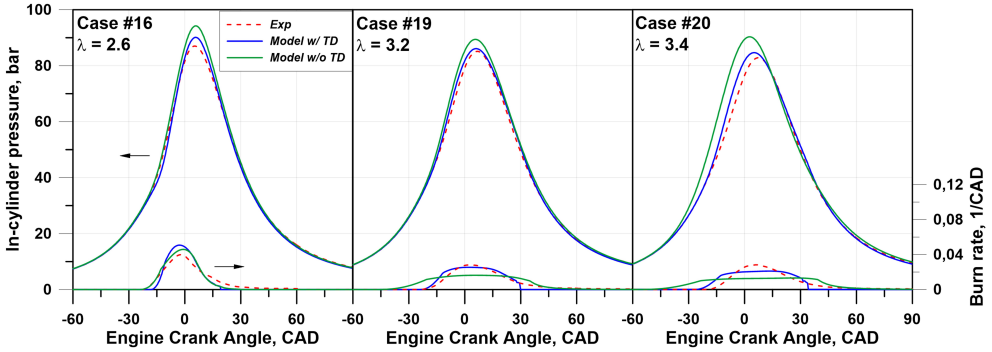

Figure 3.33: Experimental/Numerical comparison of in-cylinder pressure traces and burn rate profiles for the test case #16-19-20 (Table 3.7)

ison of the medium-load test points represented in Figure 3.33. Once again, the w/ TD model proves to be more effective in reproducing the lambda variations, although for test case #16, the burn rate is slightly overestimated. However, for the point at λ=3.4, the predicted combustion velocity is lower than the experimental value. A low laminar flame speed for the high lambda points suggests a transition towards a different combustion regime. Figure 3.34 shows the numerical/experimental comparison for the point at the highest load (test case #21) and the time evolution of ω_2 and the ratio S_f/S_l. It can be observed that, since ω_2 always assumes positive values, the TD instabilities increase the S_f throughout the combustion process, reaching a S_f/S_l peak of approximately 5 during the early combustion stages.

The idea that higher lambda cases may pass to a different combustion regime is confirmed by the analysis of the Borghi diagram in Figure 3.35. The plot illustrates the ratios of characteristic velocities (turbulence intensity over laminar flame speed) and lengths (turbulence integral length scale over flame thickness) during the combustion process for three different cases. It can be observed that most points of the λ=2.4 case lie within the corrugated flamelet regime, where the assumptions of the fractal models are valid. As a result, the respective burn rate of this case is better reproduced compared to the cases #1 and #14 (Figure 3.36). In detail, during the combustion process for test case #14, the combustion regime falls within the thickened flame region, where the assumptions of the fractal model do not hold. This analysis demonstrates the necessity of developing the model further for a more accurate modeling of the combustion process in this specific combustion regime.

Once the improved reliability of the w/ TD model has been demonstrated,

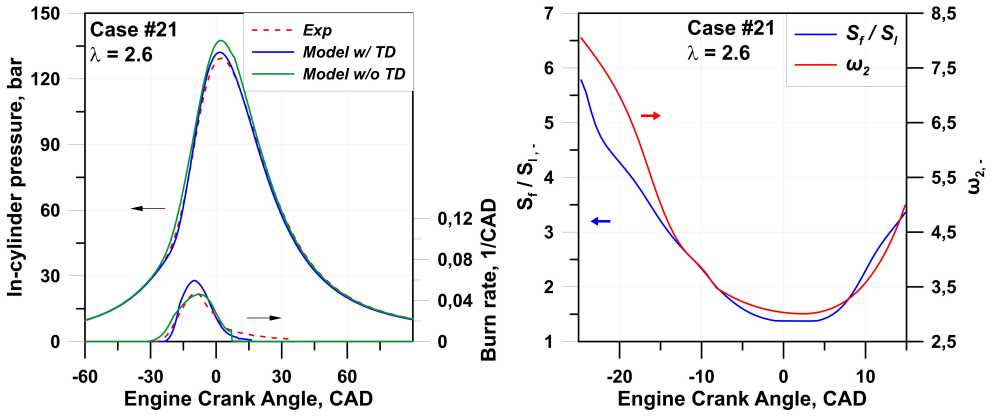

Figure 3.34: Experimental/Numerical comparison of in-cylinder pressure traces and burn rate profiles for the test case #20 (Table 3.7)(left) and S_f/S_L ratio and ω_2 time evolution (right)

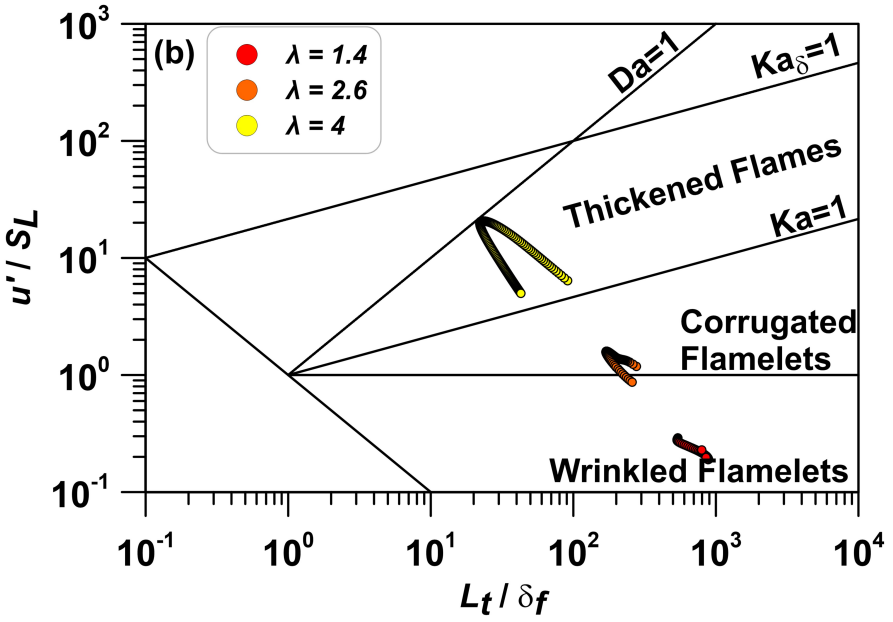

Figure 3.35: Borghi diagram fot the test cases #1-7-14 (Table 3.7) during combustion

Figures 3.37-3.39 report the numerical/experimental assessment and related average error for the overall performance parameters. For the sake of simplicity,

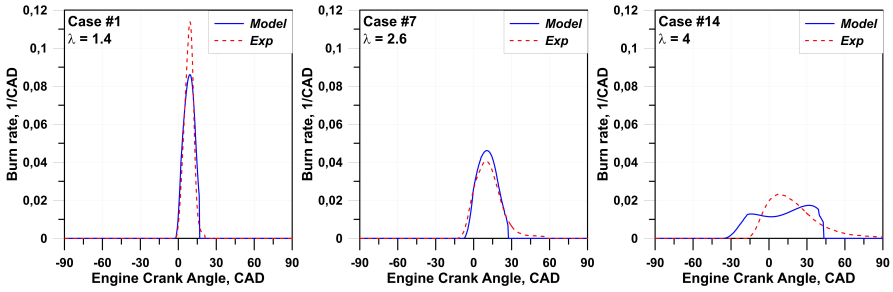

Figure 3.36: Experimental/Numerical comparison of burn rate profiles for the test case #1-7-14 (Table 3.7)

in the following figures the label "model" refers to the w/ TD model. In particular, Figure 3.37 shows the numerical/experimental comparison in terms of gross IMEP, denoting a satisfactory prediction (average percent error of 2.5%). The largest discrepancy occurs for the points at low load and high lambda, as expected from the previous explanation.

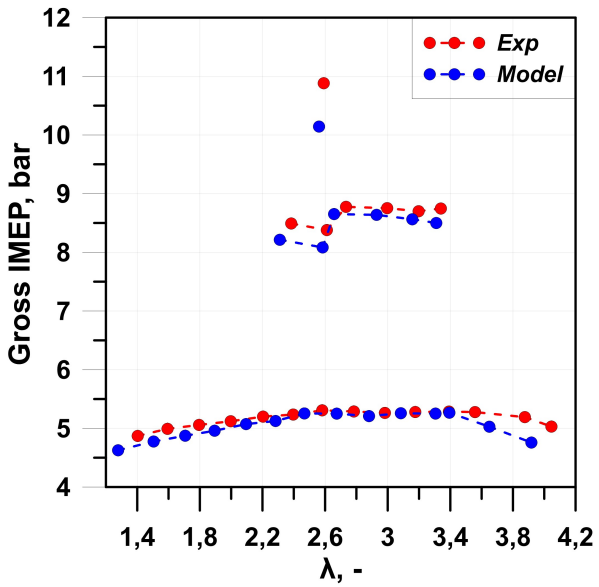

Figure 3.37: Experimental/numerical gross IMEP comparison at different load points and λ

The same behavior is observed for the Gross Indicated Efficiency (GIE) in Figure 3.38. The GIE and the gross IMEP are underestimated by approxi-

mately 10% for test case #21 (highest load condition). This is due to a slight misalignment of the pressure cycle during the expansion phase, caused by an early completion of the combustion process (Figure 3.34).

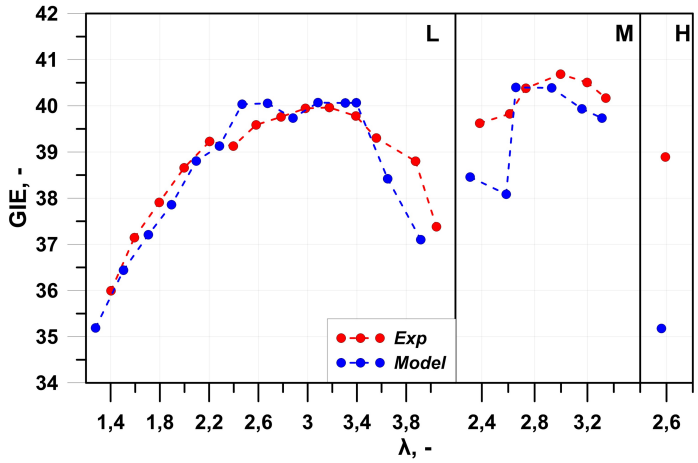

Figure 3.38: Experimental/numerical GIE comparison at different load points and λ

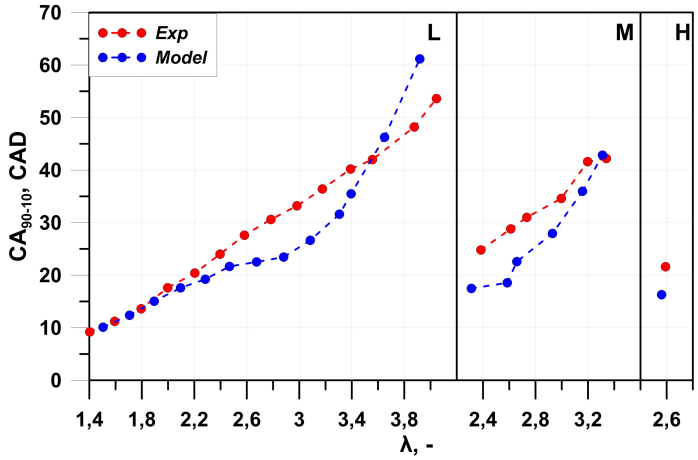

Figure 3.39: Experimental/numerical $CA_{90\text{-}10}$ comparison at different load points and λ

Figure 3.39 demonstrates a good overall alignment for all analyzed points regarding the combustion duration. A rapid increase in the combustion duration is observed for points with high lambda and low load. The good numerical-

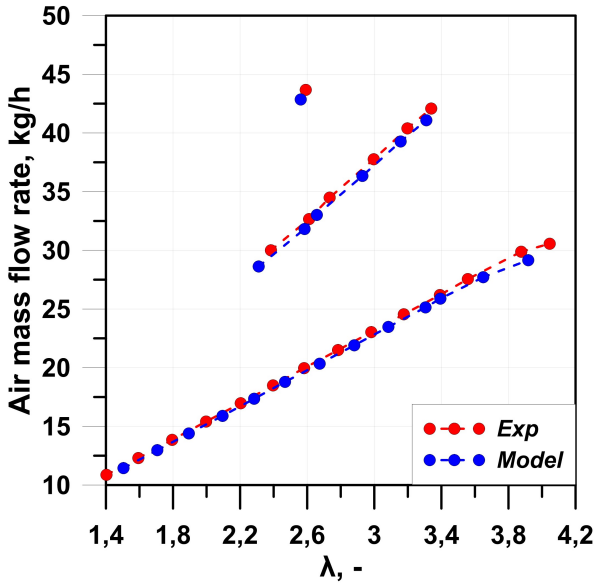

Figure 3.40: Experimental/numerical airflow comparison at different load points and λ

experimental agreement for the air mass flow rate indicates that the model is capable of accurately predicting the cylinder filling (Figure 3.40). In conclusion, this study has led to the development of a model capable of accurately predicting the combustion process and performance of a hydrogen-fueled engine. Starting from the establishment of a new correlation for the laminar flame speed, the results analyzed above have demonstrated the need to consider the effects caused by TD instabilities, typical of lean hydrogen combustions. However, it has been observed that the higher lambda points fall within the regime of thickened flames, where the assumptions underlying the fractal model break down. Therefore, the development of appropriate corrections is necessary for modeling such combustion.

3.4 Summary and conclusions

In this chapter, the fundamental principles of internal combustion engines were explained, providing readers with a comprehensive understanding of their functioning. Additionally, the latest technologies adopted to optimize engine performance and enhance overall efficiency, including VVA, EGR, water injection, and the adoption of lean combustion, were explored. Following a

brief bibliographic analysis on the main 0D combustion models, the simulation platform utilized during this doctoral work was described. Through this simulation platform, two diverse applications were examined. The first application involved investigating the effects of water injection in a PFI small displacement engine developing two different calibration strategies, while the second focused on the model's validation for the analysis of a hydrogen fuelled research engine.

In the first study on water injection, various knock-limited speed/load points were investigated during the experimental campaign, where the water/fuel mass ratio was varied up to 0.3. The experimental results, including main performance and in-cylinder pressure traces, were used to validate the advanced 1D engine model. This model incorporated user-defined in-cylinder sub-models of turbulent combustion and knock, allowing for a detailed analysis of the water injection effect on flame evolution and knock occurrence. The developed 1D engine model demonstrated its ability to accurately reproduce global performance, in-cylinder pressure traces, and burn rates under different speed/load conditions and water content. After validation, the model was utilized to conduct a virtual engine re-calibration, combined with partial re-design, to fully exploit the WI technique for performance improvements at full load. Two calibration strategies were analyzed during this process. The first strategy, named Calibration A, focused on minimizing BSFC while maintaining BMEP levels equivalent to the manufacturer-defined full load curve and considering a maximum W/F ratio of 0.5 at each speed. Calibration A demonstrated BSFC benefits for knock mitigation, achieving a maximum gain of approximately 14% at low speed and up to 32% at 4400 rpm in the medium/high-speed region due to combustion optimization and the suppression of air-fuel mixture enrichment. The second calibration strategy, named Calibration B, introduced a novel approach that combined Torque and BSFC advantages while refining water amount control to minimize consumption. Calibration B improved low-end torque by up to 13.8% with minimal BSFC penalizations at medium speeds.

During the second study presented in this chapter, the engine model was enhanced to accurately simulate hydrogen combustion. The experimental data used for the numerical model spans a wide range of operating conditions, including a variety of IMEP values ranging from 5 to 11 bar, λ values ranging from 1.4 to 4, and spark timings ranging from -36 to 0 CAD aTDC. By incorporating such a diverse range of conditions, the combustion model had the possibility to demonstrate versatility and adaptability, effectively capturing the tendencies and effects of the analyzed external parameters throughout the study. To achieve such an objective, as a first step, a new hydrogen laminar flame speed correlation was developed based on chemical calculations. Subsequently, a thermodiffusive instabilities measurement model was employed

to estimate the freely propagating flame speed, considering the effects of TD instabilities typical of hydrogen lean combustion, on the flame front. The turbulence model was calibrated using results from a CFD simulation, enabling the tuning of the combustion model and facilitating a numerical/experimental comparison of pressure cycles, burn rate traces, and engine performance. The results demonstrated the enhanced model's capability to capture key physical phenomena and accurately reproduce pressure cycles across a wide range of lambda values. However, some cases with significantly higher λ values ($>$3.6) exhibited larger errors, as they fall within the regime of thickened flames where the assumptions of the fractal model break down. Therefore, future development plans include creating a combustion model that more faithfully replicates the phenomena characteristic of this combustion regime.

Valuable insights were gained from these case studies, shedding light on the potential benefits and challenges associated with these advanced combustion technologies. In conclusion, this chapter has been a long and fascinating journey through the world of internal combustion engines, starting from the fundamental phenomena on which they rely and extending to some of the most modern technologies aimed at improving their performance and environmental sustainability. It has shown that their journey is far from over, and there are still many exciting advancements and innovations ahead in the realm of internal combustion engines.

References

[1] Senecal, Kelly and Leach, Felix. *Racing Toward Zero: The Untold Story of Driving Green*. SAE International, 2021.

[2] Stevens, Mark. *How an Internal Combustion Engine Works (4-Stroke Gasoline)*. CarTreatments.com. 2016. URL: `https://cartreatments.com/how-internal-combustion-engine-works/` (visited on 06/09/2023).

[3] Chen, L., Liang, Z., Zhang, X., and Shuai, S. "Characterizing particulate matter emissions from GDI and PFI vehicles under transient and cold start conditions". In: *Fuel* 189 (2017), pp. 131–140. DOI: `10.1016/j.fuel.2016.10.055`.

[4] Heywood, John B. *Internal Combustion Engine Fundamentals*. 2nd. New York: McGraw-Hill Education, 2018.

[5] Bozza, F., Gimelli, A., Merola, S. S., and Vaglieco, B. M. "Validation of a Fractal Combustion Model through Flame Imaging". In: *SAE Transactions* 114 (2005). Publisher: SAE International, pp. 973–987.

[6] Rhodes, D B and Keck, J C. "Laminar burning speed measurements of indolene-air-diluent mixtures at high pressures and temperatures". In: *SAE Technical Paper*. Vol. 850047. 1985. DOI: 10.4271/850047.

[7] Hara, T and Tanoue, K. "Laminar flame speed of ethanol, n-heptane, iso-octane air mixtures". In: *JSAE Paper Number* 20068518 (2006).

[8] Metghalchi, M and Keck, J C. "Burning velocities of mixtures of air with methanol, isooctane, and indolene at high pressure and temperature". In: *Combustion and flame* 48 (1982), pp. 191–210. DOI: 10.1016/0010-2180(82)90127-4.

[9] Tanaka, S, Ayala, F, and Keck, J C. "A reduced chemical kinetic model for HCCI combustion of primary reference fuels in a rapid compression machine". In: *Combustion and Flame* 133.4 (2003), pp. 467–481. DOI: 10.1016/S0010-2180(03)00057-9.

[10] De Bellis, V, Malfi, E, Teodosio, L, Giannattasio, P, and Di Lenarda, F. "Novel Laminar Flame Speed Correlation for the Refinement of the Flame Front Description in a Phenomenological Combustion Model for Spark-Ignition Engines". In: *SAE International Journal of Engines* 12.3 (2019), pp. 251–270. DOI: 10.4271/03-12-03-0018.

[11] Griffiths, J. F. *Flame and Combustion*. 3rd ed. London: Routledge, 2019. 328 pp. DOI: 10.1201/9780203755976.

[12] Millo, F. and Ferraro, C. "Knock in S.I. Engines: A Comparison between Different Techniques for Detection and Control". In: *SAE Technical Paper*. Issue: 982477. 1998. DOI: 10.4271/982477.

[13] Kleeberg, Hagen, Tomazic, Daniel, Dohmen, Joerg, Wittek, Karl, and Balazs, Andreas. "Increasing Efficiency in Gasoline Powertrains with a Two-Stage Variable Compression Ratio (VCR) System". In: *SAE Technical Paper*. Issue: 2013-01-0288. SAE International, 2013. DOI: 10.4271/2013-01-0288.

[14] Tabata, Masayoshi, Yamamoto, Tetsuya, and Fukube, Tatsuya. "Improving NOx and fuel economy for mixture injected SI engine with EGR". In: *SAE transactions* (1995), pp. 1221–1230.

[15] Alger, Terry and Mangold, Brandon. "Dedicated EGR: A New Concept in High Efficiency Engines". In: *SAE Int. J. Engines* 2.1 (2009), pp. 620–631. DOI: 10.4271/2009-01-0694.

[16] Eisazadeh-Far, Kamyar and Younkins, Matt. "Fuel Economy Gains through Dynamic-Skip-Fire in Spark Ignition Engines". In: *SAE Technical Paper*. Issue: 2016-01-0672. 2016. DOI: 10.4271/2016-01-0672.

[17] Obert, EF. "Detonation and internal coolants". In: *SAE Technical Paper*. Issue: 480173. 1948.

[18] Nicholls, J, EI-Messiri, I, and Newhali, H. "Inlet manifold water injection for control of nitrogen oxides-theory and experiment". In: *SAE Technical Paper*. Issue: 690018. 1969.

[19] Rohit, A et al. "Literature survey of water injection benefits on boosted spark ignited engines". In: *SAE Technical Paper*. Issue: 2017-01-0658. 2017.

[20] Rapp, Valentin, Killingsworth, Nick, and Therkelsen, Peter. *Lean Combustion, 2nd Edition*. Publication Title: Lean-Burn Internal Combustion Engines. Elsevier, 2016. 111-146. DOI: 10.1016/C2013-0-13446-0.

[21] Drake, Marcus, Fansler, Todd, and Lippert, Andreas. "Stratified-charge combustion: modeling and imaging of a spray-guided direct-injection spark-ignition engine". In: *Proceedings of the Combustion Institute* 30.2 (2005), pp. 2683–2691. DOI: 10.1016/j.proci.2004.07.028.

[22] Fajardo, Carlos and Sick, Volker. "Flow field assessment in a fired spray-guided spark-ignition direct-injection engine based on UV particle image velocimetry with sub crank angle resolution". In: *Proceedings of the combustion institute* 31.2 (2007), pp. 3023–3031.

[23] Stanglmaier, Rudolf and Roberts, Charles. "Homogeneous charge compression ignition (HCCI): benefits, compromises, and future engine applications". In: *SAE transactions* (1999), pp. 2138–2145. DOI: www.jstor.org/stable/44741335.

[24] Okita, Ryoji. "Mazda SKYACTIV-G Engine with New Boosting Technology". In: *Advanced Clean Cars Symposium: The Road Ahead*. Sacramento, USA, 2016.

[25] Hoang, Anh Tuan. "Critical review on the characteristics of performance, combustion and emissions of PCCI engine controlled by early injection strategy based on narrow-angle direct injection (NADI)". In: *Energy Sources, Part A: Recovery, Utilization, and Environmental Effects* (2020). Publisher: Taylor & Francis, pp. 1–15. DOI: 10.1080/15567036.2020.1805048.

[26] Dwarshala, Siva Krishna Reddy et al. "A Review on Recent Developments of RCCI Engines Operated with Alternative Fuels". In: *Energies* 16.7 (2023). Number: 7 Publisher: Multidisciplinary Digital Publishing Institute, p. 3192. DOI: 10.3390/en16073192.

[27] Tornatore, Cinzia and Sjöberg, Magnus. "Optical Investigation of a Partial Fuel Stratification Strategy to Stabilize Overall Lean Operation of a DISI Engine Fueled with Gasoline and E30". In: *Energies* 14.2 (2021). Number: 2 Publisher: Multidisciplinary Digital Publishing Institute, p. 396. DOI: 10.3390/en14020396.

[28] Sens, Matthias, Binder, Erik, Benz, Andreas, Kramer, Lukas, et al. "Pre-chamber ignition as a Key Technology for Highly Efficient SI Engines-New Approaches and Operating Strategies". In: *39th International Vienna Motor Symposium*. 2018.

[29] Mueller, Christian, Morcinkowski, Britta, Habermann, Klaus, Uhlmann, Thomas, and Schernus, Claus. "Development of a pre-chamber for spark ignition engines in vehicle applications". In: *4th International Conference on Ignition Systems for Gasoline Engines*. 2018.

[30] Iafrate, Nicolas, Matrat, Marc, and Zaccardi, Jean-Marc. "Numerical investigations on hydrogen-enhanced combustion in ultra-lean gasoline spark-ignition engines". In: *International Journal of Engine Research* (2020), p. 1468087419870688. DOI: 10.1177/1468087419870688.

[31] Xin, G. et al. "Monitoring of hydrogen-fueled engine backfires using dual manifold absolute pressure sensors". In: *International Journal of Hydrogen Energy* 47.26 (2022), pp. 13134–13142.

[32] Goto, J. et al. "Spark knock suppression in spark ignition engines with hydrogen addition under low and high engine speeds". In: *International Journal of Hydrogen Energy* 47.41 (2022), pp. 18169–18181. DOI: 10.1016/j.ijhydene.2022.03.286.

[33] Dang, J. and Wang, L. "Optimization control of hydrogen engine ignition system based on ACO-BP". In: *International Journal of Hydrogen Energy* 46.78 (2021), pp. 38903–38912.

[34] Pandey, Jayashish Kumar and Kumar, G. N. "Effect of variable compression ratio and equivalence ratio on performance, combustion and emission of hydrogen port injection SI engine". In: *Energy* 239 (2022), p. 122468. DOI: 10.1016/j.energy.2021.122468.

[35] Park, Cheolwoong, Kim, Yongrae, Oh, Sechul, Oh, Junho, and Choi, Young. "Effect of the operation strategy and spark plug conditions on the torque output of a hydrogen port fuel injection engine". In: *International Journal of Hydrogen Energy* 46.74 (2021), pp. 37063–37070. DOI: 10.1016/j.ijhydene.2021.08.229.

[36] Gao, Jianbing, Wang, Xiaochen, Song, Panpan, Tian, Guohong, and Ma, Chaochen. "Review of the backfire occurrences and control strategies for port hydrogen injection internal combustion engines". In: *Fuel* 307 (2022), p. 121553. DOI: 10.1016/j.fuel.2021.121553.

[37] Babayev, Rafig, Andersson, Arne, Dalmau, Albert Serra, Im, Hong G., and Johansson, Bengt. "Computational characterization of hydrogen direct injection and nonpremixed combustion in a compression-ignition engine". In: *International Journal of Hydrogen Energy* 46.35 (2021), pp. 18678–18696. DOI: https://doi.org/10.1016/j.ijhydene.2021.02.223.

[38] Ilbas, Mustafa, Kumuk, Osman, and Karyeyen, Serhat. "Modelling of the gas-turbine colorless distributed combustion: An application to hydrogen enriched – kerosene fuel". In: *International Journal of Hydrogen Energy*. International Conference on Energy, Environment and Storage of Energy, 15. International Combustion Symposium 47.24 (2022), pp. 12354–12364. DOI: 10.1016/j.ijhydene.2021.06.228.

[39] Ahmadi, Rouhollah and Hosseini, S. Mohammad. "Numerical investigation on adding/substituting hydrogen in the CDC and RCCI combustion in a heavy duty engine". In: *Applied Energy* 213 (2018), pp. 450–468. DOI: 10.1016/j.apenergy.2018.01.048.

[40] Bradley, D., Cresswell, T.M., and Puttock, J.S. "Flame acceleration due to flame-induced instabilities in large-scale explosions". In: *Combust. Flame* 124.4 (2001), pp. 551–559. DOI: 10.1016/S0010-2180(00)00208-X.

[41] Groff, E.G. "The cellular nature of confined spherical propane-air flames". In: *Combust. Flame* 48 (1982), pp. 51–62. DOI: 10.1016/0010-2180(82)90115-8.

[42] "Hydrogen engine operation strategies: Recent progress, industrialization challenges, and perspectives". In: *International Journal of Hydrogen Energy* 48.1 (2023). Publisher: Pergamon, pp. 366–392. DOI: 10.1016/j.ijhydene.2022.09.256.

[43] Hattrell, T., Sheppard, C. G. W., Burluka, A. A., Neumeister, J., and Cairns, A. "Burn Rate Implications of Alternative Knock Reduction Strategies for Turbocharged SI Engines". In: *SAE Tech. Pap.* 2006 (2006). DOI: 2006-01-1110.

[44] Zimont, V. L. "Theory of turbulent combustion of a homogeneous fuel mixture at high Reynolds numbers". In: *Combust. Explos. Shock Waves* 15.3 (1979), pp. 305–311. DOI: 10.1007/BF00785062.

[45] Richard, Sylvain, Bougrine, Said, Font, Gilles, Lafossas, Florian A., and Berr, Fabien le. "On the Reduction of a 3D CFD Combustion Model to Build a Physical 0D Model for Simulating Heat Release, Knock and Pollutants in SI Engines". In: *Oil Gas Science and Technology - Revue d'IFP Energies nouvelles* 64.3 (2009), pp. 223–242. DOI: 10.2516/ogst/2008055.

[46] Weller, H. G., Tabor, G., Gosman, A. D., and Fureby, C. "Application of a flame-wrinkling LES combustion model to a turbulent mixing layer". In: *Symposium (International) on Combustion* 27.1 (1998), pp. 899–907. DOI: 10.1016/S0082-0784(98)80487-6.

[47] Richard, Sylvain and Veynante, Denis. "A 0-D flame wrinkling equation to describe the turbulent flame surface evolution in SI engines". In: *Comptes Rendus Mécanique* 343.3 (2015), pp. 219–231. DOI: 10.1016/j.crme.2014.09.003.

[48] Bougrine, Said. "0-Dimensional Modeling of the Combustion of Alternative Fuels in Spark Ignition Engines". PhD thesis. Ecole Centrale Paris, 2012.

[49] Meneveau, Charles and Poinsot, Thierry. "Stretching and quenching of flamelets in premixed turbulent combustion". In: *Combustion and Flame* 86.4 (1991), pp. 311–332. DOI: 10.1016/0010-2180(91)90126-V.

[50] Charlette, François, Meneveau, Charles, and Veynante, Denis. "A power-law flame wrinkling model for LES of premixed turbulent combustion Part I: non-dynamic formulation and initial tests". In: *Combustion and Flame* 131.1 (2002), pp. 159–180. DOI: 10.1016/S0010-2180(02)00400-5.

[51] Charlette, François, Meneveau, Charles, and Veynante, Denis. "A power-law flame wrinkling model for LES of premixed turbulent combustion Part II: Dynamic formulation". In: *Combustion and Flame* 131.1 (2002), pp. 181–197. DOI: 10.1016/S0010-2180(02)00401-7.

[52] Poinsot, Thierry and Veynante, Denis. *Theoretical and Numerical Combustion*. 3rd. 2012.

[53] Duclos, Julien, Veynante, Denis, and Poinsot, Thierry. "A comparison of flamelet models for premixed turbulent combustion". In: *Combustion and Flame* 95.1 (1993), pp. 101–117. DOI: 10.1016/0010-2180(93)90055-8.

[54] Bozza, Fabio, Teodosio, Luigi, De Bellis, Vincenzo, Fontanesi, Stefano, and Iorio, Agostino. "A Refined OD Turbulence Model to Predict Tumble and Turbulence in SI Engines". In: *SAE International Journal of Engines* 12.1 (2019). Publisher: SAE International, pp. 15–30.

[55] Gouldin, F. "An application of Fractals to Modeling Premixed Turbulent Flames". In: *Combustion and Flame* 68.3 (1987), pp. 249–266. DOI: 10.1016/0010-2180(87)90003-4.

[56] Franke, C., Wirth, A., and Peters, N. "New Aspects of the Fractal Behaviour of Turbulent Flames". In: *23rd Symposium (International) on Combustion*. Orleans, 1990.

[57] Gatowsky, J. A. and Heywood, J. B. "Flame Photographs in a Spark-Ignition Engine". In: *Combustion and Flame* 56 (1984), pp. 71–81.

[58] North, G. L. and Santavicca, D. A. "The fractal nature of premixed turbulent flames". In: *Combustion Science and Technology* 72.4 (1990), pp. 215–232. DOI: 10.1080/00102209008951648.

[59] Bates, C. S. *Flame Imaging Studies of Combustion Completion in a SI Four-Stroke Engine*.

[60] Matthews, R. D. and Chin, Y. W. "A Fractal-Based SI Engine Model: Comparisons of Predictions with Experimental Data". In: *SAE Technical Paper*. Issue: 910075. 1991. DOI: 10.4271/910079.

[61] Lu, Tianfeng and Law, Chung K. "Toward accommodating realistic fuel chemistry in large scale computations". In: *Progress in Energy and Combustion Science* 35.2 (2009), pp. 195–215. DOI: 10.1016/j.pecs.2008.10.002.

[62] Livengood, JC and Wu, P. C. "Correlation of Autoignition Phenomena in Internal Combustion Engines and Rapid Compression Machines". In: *Symposium (International) on Combustion* 5.1 (1955), pp. 347–356. DOI: 10.1016/S0082-0784(55)80047-1.

[63] Bozza, Fabio, De Bellis, Vincenzo, and Teodosio, Luigi. "A Tabulated-Chemistry Approach Applied to a Quasi-Dimensional Combustion Model for a Fast and Accurate Knock Prediction in Spark-Ignition Engines". In: *SAE Technical Paper*. Issue: 2019-01-0471. 2019. DOI: 10.4271/2019-01-0471.

[64] Liu, Yao-Dong, Jia, Ming, Xie, Mao-Zhao, and Pang, Bin. "Development of a New Skeletal Chemical Kinetic Model of Toluene Reference Fuel with Application to Gasoline Surrogate Fuels for Computational Fluid Dynamics Engine Simulation". In: *Energy & Fuels* 27.8 (2013). Publisher: American Chemical Society, pp. 4899–4909. DOI: 10.1021/ef4009955.

[65] Konnov, Alexander A. "Yet another kinetic mechanism for hydrogen combustion". In: *Combustion and Flame* 203 (2019), pp. 14–22. DOI: 10.1016/j.combustflame.2019.01.032.

[66] Woschni, G. *A Universally Applicable Equation for the Instantaneous Heat Transfer Coefficient in the Internal Combustion Engine*. SAE Technical Paper 670931. ISSN: 0148-7191, 2688-3627. Warrendale, PA: SAE International, 1967. DOI: 10.4271/670931.

[67] Teodosio, Luigi, Marchitto, Luca, Tornatore, Cinzia, Bozza, Fabio, and Valentino, Gerardo. "Effect of Cylinder-by-Cylinder Variation on Performance and Gaseous Emissions of a PFI Spark Ignition Engine: Experimental and 1D Numerical Study". In: *Applied Sciences* 11.13 (2021). Number: 13 Publisher: Multidisciplinary Digital Publishing Institute, p. 6035. DOI: 10.3390/app11136035.

[68] Piras, Marco, Teodosio, Luigi, Tornatore, Cinzia, Marchitto, Luca, and Bozza, Fabio. "Exploring the potentials of water injection to improve fuel consumption and torque in a small displacement PFI spark-ignition engine". In: *Fuel* 327 (2022), p. 125224. DOI: 10.1016/j.fuel.2022.125224.

[69] Bozza, Fabio, De Bellis, Vincenzo, Giannattasio, Pietro, Teodosio, Luigi, and Marchitto, Luca. "Extension and Validation of a 1D Model Applied to the Analysis of a Water Injected Turbocharged Spark Ignited Engine at High Loads and over a WLTP Driving Cycle". In: *SAE International Journal of Engines* 10.4 (2017), pp. 2141–2153. DOI: 10.4271/2017-24-0014.

[70] Millo, Federico, Gullino, Fabrizio, and Rolando, Luciano. "Methodological Approach for 1D Simulation of Port Water Injection for Knock Mitigation in a Turbocharged DISI Engine". In: *Energies* 13.17 (2020). Number: 17 Publisher: Multidisciplinary Digital Publishing Institute, p. 4297. DOI: 10.3390/en13174297.

[71] Worm, Julian, Naber, Jeffrey, Duncan, Jason, Barros, Sergio, and Atkinson, William. "Water Injection as an Enabler for Increased Efficiency at High-Load in a Direct Injected, Boosted, SI Engine". In: *SAE International Journal of Engines* 10 (2017), pp. 951–958. DOI: 10.4271/2017-01-0663.

[72] Wang, Chenchen et al. "Experimental study on knock suppression of spark-ignition engine fuelled with kerosene via water injection". In: *Applied Energy* 242 (2019), pp. 248–259. DOI: 10.1016/J.APENERGY.2019.03.123.

[73] Molina, S., Ruiz, S., Gomez-Soriano, J., and Olcina-Girona, M. "Impact of hydrogen substitution for stable lean operation on spark ignition

engines fueled by compressed natural gas". In: *Results in Engineering* 17 (2023), p. 100799. DOI: 10.1016/j.rineng.2022.100799.

[74] Landau, L. "On the Theory of Slow Combustion". In: *Dynamics of Curved Fronts*. Ed. by Pierre Pelcé. San Diego: Academic Press, 1988, pp. 403–411. DOI: 10.1016/B978-0-08-092523-3.50044-7.

[75] MATALON, M., CUI, C., and BECHTOLD, J. K. "Hydrodynamic theory of premixed flames: effects of stoichiometry, variable transport coefficients and arbitrary reaction orders". In: *Journal of Fluid Mechanics* 487 (2003). Publisher: Cambridge University Press, pp. 179–210. DOI: 10.1017/S0022112003004683.

[76] Howarth, T. L., Hunt, E. F., and Aspden, A. J. "Thermodiffusively-unstable lean premixed hydrogen flames: Phenomenology, empirical modelling, and thermal leading points". In: *Combustion and Flame* 253 (2023), p. 112811. DOI: 10.1016/j.combustflame.2023.112811.

[77] Howarth, T. L. and Aspden, A. J. "An empirical characteristic scaling model for freely-propagating lean premixed hydrogen flames". In: *Combustion and Flame* 237 (2022), p. 111805. DOI: 10.1016/j.combustflame.2021.111805.

[78] Matalon, Moshe. "The Darrieus–Landau instability of premixed flames". In: *Fluid Dynamics Research* 50.5 (2018). Publisher: IOP Publishing, p. 051412. DOI: 10.1088/1873-7005/aab510.

[79] Broatch, A., Novella, R., García-Tíscar, J., Gomez-Soriano, J., and Pal, P. "Investigation of the effects of turbulence modeling on the prediction of compression-ignition combustion unsteadiness". In: *International Journal of Engine Research* (2021), p. 1468087421990478.

[80] Angelberger, C., Poinsot, T., and Delhay, B. *Improving near-wall combustion and wall heat transfer modeling in SI engine computations*. SAE Technical Paper, 1997.

[81] Torregrosa, A. J., Broatch, A., Margot, X., and Gomez-Soriano, J. "Understanding the unsteady pressure field inside combustion chambers of compression-ignited engines using a computational fluid dynamics approach". In: *International Journal of Engine Research* 21.8 (2020), pp. 1273–1285.

[82] Issa, R. I. "Solution of the implicitly discretised fluid flow equations by operator-splitting". In: *Journal of computational physics* 62.1 (1986), pp. 40–65.

[83] Serrano, J.R., Martín, J., Gomez-Soriano, J., and Raggi, R. "Theoretical and experimental evaluation of the spark-ignition premixed oxy-fuel combustion concept for future co2 captive powerplants". In: *Energy Conversion and Management* 244 (2021), p. 114498.

Chapter 4

From Fuel to Electricity: Demystifying Fuel Cells

Fuel cell vehicles are emerging as a viable alternative to traditional ICE vehicles, and their market share is steadily growing. To comprehensively address this topic, it is crucial to first grasp the operational principles of fuel cells, as well as their limitations and various types. Accordingly, this chapter adopts a symmetrical approach to that employed for ICE (chapter 3), commencing with an elucidation of the fundamentals of fuel cells before progressing to an exploration of different fuel cell types and their integration into a comprehensive fuel cell system. Subsequently, the fuel cell model employed for the development of advanced control strategies, which will be discussed in chapter 6, is briefly outlined.

4.1 Fundamentals of Fuel Cells

A fuel cell is an electrochemical device that converts the chemical energy of a fuel directly into electrical energy. The fuel and oxidizing agents are supplied separately to the two electrodes of the cell, where they undergo a reaction. An electrolyte facilitates the movement of ions between the electrodes. At the anode or positive electrode, fuel is supplied and electrons are released from the fuel. These electrons flow through the external circuit to the cathode or negative electrode. At the cathode, in combination with positive ions and oxygen, reaction products or exhaust are generated (Figure 4.1).

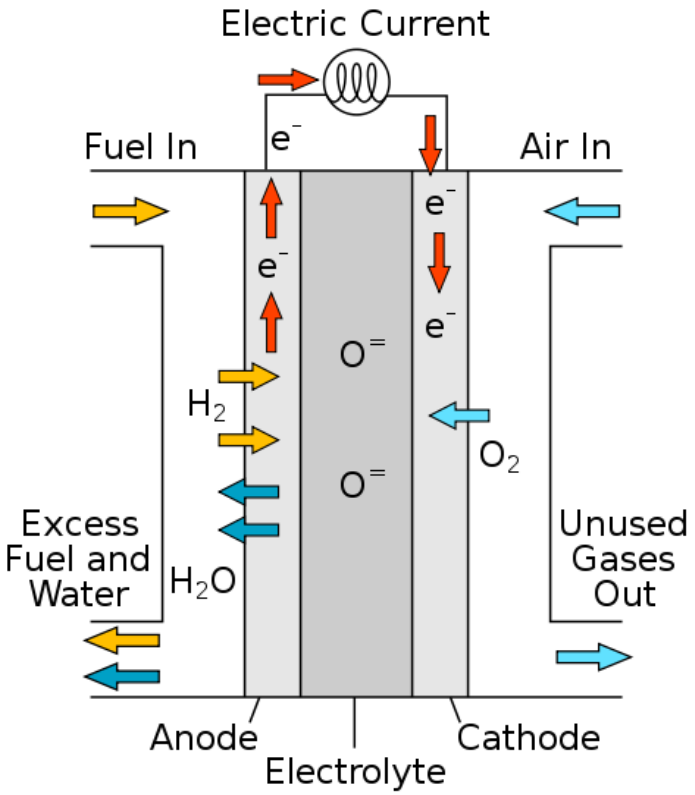

Figure 4.1: Basic operation of a fuel cell. Source [1].

The chemical reaction in a fuel cell can be expressed in terms of Gibbs free energy (ΔG) as:

$$\Delta G = \sum (G_i - G_j) \tag{4.1}$$

where G_i and G_j represent the free energies of the products and reactants, respectively.

The thermodynamic voltage (V_r) of a fuel cell is related to the number of electrons transferred (n) in the reaction and the Faraday constant (F) by the equation:

$$\Delta G = -nFV_r \tag{4.2}$$

At standard conditions (25°C temperature and 1 atm pressure), the open circuit (reversible) voltage (V_{0r}) of a fuel cell can be expressed as:

$$V_{0r} = \frac{\Delta G_0}{nF} \tag{4.3}$$

where ΔG_0 is the change in Gibbs free energy at standard conditions.

The change in Gibbs free energy (ΔG) can be further expressed as the change in enthalpy (ΔH) and entropy (ΔS) of the reaction at the absolute temperature (T) using the equation:

$$\Delta G = \Delta H - T\Delta S \tag{4.4}$$

The voltage of a fuel cell (V_r) depends on the activities of the reactants and, for gaseous reactants and products, can be described as:

$$V_r = V_{0r} - \frac{RT}{nF} \sum V_i ln(\frac{p_i}{p_{i0}}) \tag{4.5}$$

where V_i represents the activities of the reactant species at nonstandard pressure p_i, V_{0r} is the corresponding cell voltage with all gases at the standard pressure p_{i0}.

The efficiency of a reversible galvanic cell (η_{id}) is related to the enthalpy (ΔH) by the equation:

$$\eta_{id} = 1 - \frac{T\Delta S}{\Delta H} \tag{4.6}$$

where T is the absolute temperature.

These equations describe the fundamental principles and thermodynamic aspects of a fuel cell system. The operation of a fuel cell can be summarized as follows:

1. Reactant Transport. Continuous supply of fuel and oxidant is essential for a fuel cell to produce electricity. Efficient delivery of reactants is achieved through flow field plates and porous electrode structures, which distribute the gas flow over the cell's surface. The design of flow channels and electrode geometries plays a significant role in fuel cell performance. Material properties also play a crucial role in meeting specific requirements for electrical, thermal, mechanical, and corrosion resistance.

2. Electrochemical Reaction. Once the reactants reach the electrodes, electrochemical reactions take place. The speed of these reactions directly influences the current output of the fuel cell. Catalysts are commonly used to enhance the efficiency and rate of electrochemical reactions. The selection of appropriate catalysts and careful design of reaction zones are critical for optimizing fuel cell performance.

3. Ionic (and Electronic) Conduction. Electrochemical reactions generate ions and electrons, which must be transported between electrodes. While electrons can easily flow through conductive paths, ions require an electrolyte to facilitate their movement. Ionic transport is less efficient compared to electronic transport, and thin electrolyte layers are employed to minimize resistance loss. The mechanism of ionic conduction involves hopping processes in many electrolytes.

4. Product Removal. Fuel cell reactions produce byproduct species that need to be removed from the cell to prevent accumulation and hinder further reactant reactions. The same principles of mass transport, diffusion, and fluid mechanics used for reactant delivery can be applied to facilitate product removal. Ensuring effective product removal is crucial for maintaining optimal fuel cell performance and preventing issues such as flooding.

These steps encompass the key aspects of fuel cell operation, including reactant transport, electrochemical reactions, ionic and electronic conduction, and product removal. Each step involves intricate considerations and optimization techniques to maximize fuel cell efficiency.

Fuel cell performance

The performance of a fuel cell device can be represented by its current-voltage characteristics, commonly known as the i-V curve. This graph illustrates the voltage output of the fuel cell for a given current output. To make the results comparable, the current values are normalized by the fuel cell area, resulting in current density measured in amperes per square centimeter.

In an ideal scenario, a fuel cell would maintain a constant voltage determined by thermodynamics while supplying any amount of current as long as sufficient fuel is provided. However, in practice, the actual voltage output of a real fuel cell is lower than the ideal thermodynamic prediction. Furthermore, as more current is drawn from the fuel cell, its voltage output decreases, limiting the total power that can be delivered.

The power (P) delivered by a fuel cell is the product of current and voltage, given by the equation $P = iV$. From the information in the i-V curve, a fuel cell power density curve can be constructed. This curve shows the power density delivered by the fuel cell as a function of the current density, obtained by multiplying the voltage at each point on the i-V curve by the corresponding current density. An example is reported in the following Figure 4.2.

Fuel cell voltage is an indicator of fuel cell efficiency since it directly affects the electric power produced per unit of fuel. Maintaining a high fuel cell

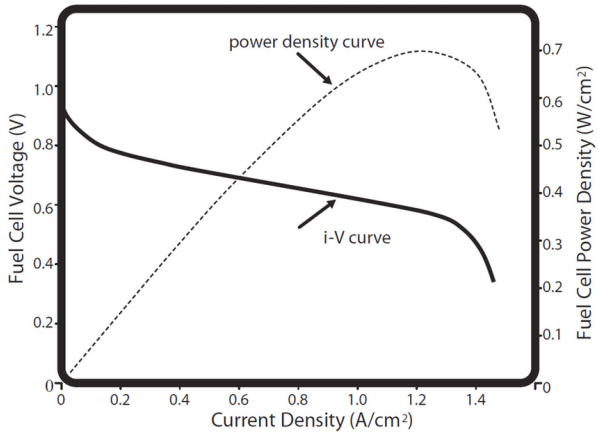

Figure 4.2: Polarization curve of a fuel cell. Source [2].

voltage, even under high current loads, is crucial for successful implementation. However, it is challenging to maintain a high fuel cell voltage under heavy current loads due to irreversible losses. The i-V curve of a fuel cell is shaped by three major types of losses, corresponding to the basic fuel cell steps discussed earlier:

- Activation losses: These losses result from electrochemical reaction kinetics and primarily influence the initial part of the curve.
- Ohmic losses: These losses occur due to ionic and electronic conduction and are most apparent in the middle section of the curve.
- Concentration losses: These losses are associated with mass transport and are significant in the tail of the i-V curve.

The real voltage output of a fuel cell, (represented in Figure 4.3), can be expressed by subtracting the voltage drops due to these losses from the thermodynamically predicted voltage output:

$$V = V_{OC} - V_{act} - V_{ohm} - Vc \tag{4.7}$$

Where V is the real output voltage of the fuel cell, V_{OC} is the open circuit voltage and V_{act}, V_{ohm}, V_c represent the voltage drops due to activation, ohmic and concentration losses. Understanding and quantifying these losses is essential for characterizing and modeling the performance of fuel cell devices. The chapter 4.4 will explain several modeling approaches.

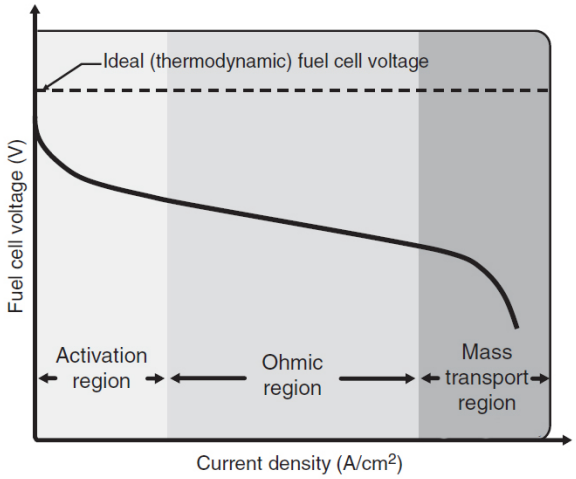

Figure 4.3: Voltage losses. Source [3].

4.2 Fuel cell technologies

Fuel cells can be categorized into six major types based on the type of electrolyte they use. These types are:

- Proton Exchange Membrane (PEM) or Polymer Exchange Membrane Fuel Cells (PEMFCs)
- Direct Methanol Fuel Cells (DMFCs)
- Alkaline Fuel Cells (AFCs)
- Phosphoric Acid Fuel Cells (PAFCs)
- Molten Carbonate Fuel Cells (MCFCs)
- Solid Oxide Fuel Cells (SOFCs)

Each type of fuel cell operates using a different electrolyte, and they have their specific advantages, limitations, and applications. Table 4.1 reports their normal operation temperature and the state of electrolyte.

Table 4.1: Operating Data of Various Fuel Cell Systems [4, 5]

Cell System	Temperature (°C)	Electrolyte State
Proton Exchange Fuel Cells	60–90	Solid
Direct Methanol Fuel Cells	100	Solid
Alkaline Fuel Cells	60-250	Liquid
Phosphoric Acid Fuel Cells	60–200	Liquid
Molten Carbonate Fuel Cells	500–800	Liquid
Solid Oxide Fuel Cells	1000–1200	Solid

4.2.1 Proton Exchange Membrane Fuel Cell and Direct Methanol Fuel Cell

The PEMFC consists of a polymer electrolyte membrane that conducts protons, typically made of a perfluorinated sulfonic acid polymer. The anode and cathode reactions in the PEMFC can be described as follows:

$$\text{Anode: } H_2 \rightarrow 2H^+ + 2e^-$$
$$\text{Cathode: } \tfrac{1}{2}O_2 + 2H^+ + 2e^- \rightarrow H_2O$$

The polymer membrane employed in PEMFCs is thin (20–200 μm), flexible, and transparent. It is coated on both sides with a thin layer of platinum-based catalyst and a porous carbon electrode support material. This configuration is known as a membrane electrode assembly (MEA) and has a thickness of less than 1 mm. To ensure sufficient conductivity, the polymer membrane requires hydration with liquid water, imposing an operating temperature limit of 90°C or lower on the PEMFC. Due to this low operating temperature, platinum-based materials are currently the only viable catalysts. While hydrogen is the preferred fuel, liquid fuels such as methanol and formic acid are also being explored for low-power ($<$ 1 kW) portable applications. The Direct Methanol Fuel Cell (DMFC) is a variant of the PEMFC that directly oxidizes methanol (CH_3OH) to generate electricity. Extensive research is being conducted on DMFCs, and they may be classified as alternative-fuel PEMFCs.

Presently, the PEMFC exhibits the highest power density among all fuel cell types, ranging from 500 to 2500 mW/cm^2. It also demonstrates excellent performance in fast-start and on-off cycling scenarios. As a result, PEMFCs are well-suited for portable power and transportation applications. Major automotive companies primarily focus on the development of PEMFC technologies.

Advantages of PEMFC:

- Highest power density compared to other fuel cell classes

- Excellent start-stop capabilities
- Suitable for low-temperature operations, making them ideal for portable applications

Disadvantages of PEMFC:

- Reliance on expensive platinum catalysts
- Polymer membrane and associated components are costly
- Active water management is often required
- Limited tolerance to carbon monoxide and sulfur compounds

4.2.2 Alkaline Fuel Cells

The AFC utilizes an aqueous potassium hydroxide (KOH) electrolyte. Unlike acidic fuel cells where H+ ions are transferred from the anode to the cathode, in an AFC, OH- ions are conducted from the cathode to the anode. The anode and cathode reactions in an AFC are as follows:

$$\text{Anode: } H_2 + 2OH^- \rightarrow 2H_2O + 2e^-$$
$$\text{Cathode: } \tfrac{1}{2}O_2 + 2e^- + H_2O \rightarrow 2OH^-$$

Consequently, water is consumed at the cathode and produced (at twice the rate) at the anode. If excess water is not removed, it can dilute the KOH electrolyte, leading to performance degradation. Interestingly, the cathode activation overvoltage in an AFC is significantly lower than in an acidic fuel cell at similar temperatures. Additionally, numerous metal-based catalysts remain stable in an alkaline environment. This allows the use of nickel catalysts instead of platinum as the cathode catalyst under certain conditions. Due to the faster kinetics of the oxygen reduction reaction (ORR) in an alkaline medium compared to an acidic medium, AFCs can achieve operating voltages as high as 0.875 V. It's worth noting that higher operating voltages contribute to higher efficiency, which is crucial when fuel availability is limited.

The operating temperature of an AFC can range from 60 to 250°C, depending on the KOH concentration in the electrolyte. Alkaline fuel cells require pure hydrogen and pure oxygen as fuel and oxidant since they cannot tolerate even trace amounts of carbon dioxide. The presence of CO_2 in an AFC leads to degradation of the KOH electrolyte, as shown in the following reaction:

$$2OH^- + CO_2 \rightarrow CO_3^{2-} + H_2O$$

Over time, the OH- concentration in the electrolyte decreases, and K_2CO_3 can precipitate out due to its limited solubility, causing significant issues. CO_2 scrubbers and continuous replenishment of fresh KOH electrolyte can partially alleviate these problems but at a significant cost. Due to these limitations, AFCs are not economically feasible for most terrestrial power applications. However, they demonstrate impressive efficiencies and power densities, making them well-suited for aerospace applications. Alkaline fuel cells were used in the Apollo missions and Space Shuttle orbiters.

Advantages of AFCs:

- Enhanced cathode performance
- Potential for nonprecious metal catalysts
- Low material costs and extremely inexpensive electrolyte

Disadvantages of AFCs:

- Requires pure hydrogen and oxygen (H_2-O_2)
- Occasional replenishment of KOH electrolyte may be necessary
- Water removal from the anode is required

4.2.3 Phosphoric Acid Fuel Cells

A liquid electrolyte of H_3PO_4, either pure or highly concentrated, is housed in a thin SiC matrix that is positioned between two porous graphite electrodes that are coated with a platinum catalyst in a phosphoric acid fuel cell. The fuel used is hydrogen, and the oxidant can be either air or oxygen. The following electrochemical processes take place at a PAFC's anode and cathode:

$$\text{Anode: } H_2 \rightarrow 2H^+ + 2e^-$$
$$\text{Cathode: } \frac{1}{2}O_2 + 2H^+ + 2e^- \rightarrow H_2O$$

Temperatures below 42°C cause pure phosphoric acid to solidify; as a result, PAFCs must function above this limit. Commissioned PAFCs are normally kept at their prescribed operating temperature to avoid stress problems brought on by freeze-thaw cycles. Temperatures between 180 and 210 °C are ideal for performance. H_3PO_4 undergoes an unfavorable phase transition at temperatures above 210°C, making it unsuitable for use as an electrolyte. The

SiC matrix supports the electrolyte mechanically, separates the two electrodes, and reduces reactant gas crossing. H_3PO_4 must be constantly refilled during operation because it gradually evaporates into the environment, especially at higher temperatures. The electrical efficiency of PAFC units is roughly 40%, while that of combined heat and power systems is over 70%. In PAFCs, carbon monoxide and sulfur poisoning at the anode are possible since platinum catalysts are used in these devices. When using pure hydrogen, this vulnerability is minimal, but it increases significantly when using reformed or impure fuel sources. PAFCs operate at greater temperatures than PEMFCs, having a little bit more tolerance to the temperature. Depending on the circumstances, the anode can withstand CO concentrations of between 0.5% and 1.5%. The tolerance for sulfur at the anode, which is normally present as H_2S, is around 50 ppm.

Advantages of PAFCs:

- Established technology with a mature track record
- Excellent reliability and long-term performance
- Relatively low-cost electrolyte

Disadvantages of PAFCs:

- Utilization of expensive platinum catalysts
- Susceptibility to CO and S poisoning
- The corrosive nature of the electrolyte, necessitating periodic replenishment during operation.

4.2.4 Molten Carbonate Fuel Cells

The MCFC utilizes a molten mixture of alkali carbonates, specifically Li_2CO_3 and K_2CO_3, immobilized in a LiO-AlO_2 matrix as its electrolyte. In this system, the mobile charge carrier is the carbonate ion (CO_3^{2-}). The anode and cathode reactions in the MCFC can be described as follows:

$$\text{Anode: } H_2 + CO_3^{2-} \rightarrow CO_2 + H_2O + 2e^-$$
$$\text{Cathode: } \frac{1}{2}O_2 + CO_2 + 2e^- \rightarrow CO_3^{2-}$$

In the MCFC, CO_2 is produced at the anode and consumed at the cathode. To maintain operation, the MCFC systems need to extract CO_2 from the anode and recirculate it to the cathode. Unlike the AFC, which requires excluding CO_2 from the cathode, the CO_2 recycling process in the MCFC is relatively straightforward. Typically, the anode waste stream is fed into a burner, where excess fuel is combusted. The resulting mixture of steam and CO_2 is then combined with fresh air and supplied to the cathode. The heat generated during combustion preheats the reactant air, enhancing efficiency and sustaining the operating temperature of the MCFC.

The electrodes used in the MCFC are typically nickel-based. The anode consists of a nickel/chromium alloy, while the cathode comprises lithiated nickel oxide. Nickel provides both catalytic activity and conductivity at both electrodes. In the anode, chromium additions maintain the electrode's high porosity and surface area, while lithiated nickel oxide at the cathode minimizes nickel dissolution, thereby preserving fuel cell performance.

The MCFC's relatively high operating temperature of 650°C allows for fuel flexibility. It can run on hydrogen, simple hydrocarbons like methane, and simple alcohols. Interestingly, carbon monoxide does not act as a poison for MCFCs; instead, it functions as a fuel.

Due to the stresses caused by the electrolyte's freeze-thaw cycle during startup and shutdown, MCFCs are best suited for stationary, continuous power applications. Typical electrical efficiency of an MCFC unit is around 50%, but in combined heat and power applications, efficiencies can approach 90%.

Advantages of MCFC:

- Fuel flexibility
- Use of nonprecious metal catalysts
- availability of high-quality waste heat for cogeneration applications

Disadvantages of MCFC:

- Implementation CO_2 recycling
- Dealing with the corrosive molten electrolyte
- Degradation and lifetime issues
- Relatively expensive materials

4.2.5 Solid Oxide Fuel Cells

The SOFC utilizes a solid ceramic electrolyte. The commonly used electrolyte material in SOFCs is yttria-stabilized zirconia (YSZ), which acts as an oxygen ion conductor by incorporating oxygen vacancies.

In the SOFC, the mobile conductor is O^{2-}, and as a result, the anode and cathode reactions can be expressed as follows:

$$\text{Anode: } H_2 + O^{2-} \rightarrow H_2O + 2e^-$$
$$\text{Cathode: } \tfrac{1}{2}O_2 + 2e^- \rightarrow O^{2-}$$

Unlike in PEMFC, water is produced at the anode in an SOFC. The anode and cathode materials in an SOFC are distinct. The fuel electrode needs to withstand the highly reducing and high-temperature conditions of the anode, while the air electrode must withstand the highly oxidizing and high-temperature environment of the cathode. The most common material for the anode electrode is a nickel-YSZ cermet, where nickel provides conductivity and catalytic activity, and YSZ adds ion conductivity, thermal expansion compatibility, mechanical stability, and maintains the high porosity and surface area of the anode structure. The cathode electrode usually consists of a mixed ion-conducting and electronically conducting (MIEC) ceramic material. Typical cathode materials include lanthanum-strontium ferrite (LSF), strontium-doped lanthanum manganite (LSM), lanthanum-strontium cobaltite ferrite (LSCF), and lanthanum-strontium cobaltite (LSC). These materials exhibit good oxidation resistance and high catalytic activity in the cathode environment.

The SOFC's working temperature right now falls between 600 and 1000 °C. The advantages and disadvantages of this high working temperature are both present. Issues with stack hardware, sealing, and cell connectivity are among the difficulties. The high temperature makes thermal expansion matching, mechanical requirements, reliability challenges, and mechanical considerations more pressing. On the other hand, benefits include the ability to use cogeneration strategies that make use of the high-quality waste heat produced, fuel flexibility, high efficiency, and these factors. An SOFC has an electrical efficiency of 50–60%, and in applications combining heat and electricity, this efficiency could approach 90%. While keeping the fundamental advantages of SOFCs, an intermediate-temperature (400-700°C) SOFC design could reduce the majority of the difficulties related to high-temperature operation. Such SOFCs could substitute metal stack components for ceramics and more cheap sealing technologies. Even so, they were still capable of achieving a respectably high efficiency and fuel flexibility. However, before lower-temperature SOFCs

can be used on a regular basis, a number of basic issues still need to be solved.

Advantages of SOFC:

- Fuel flexibility
- Use of nonprecious metal catalysts
- Availability of high-quality waste heat for cogeneration applications
- Solid electrolyte
- Relatively high power density

Disadvantages of SOFC:

- Significant high-temperature materials issues
- Sealing challenges
- Relatively expensive components
- Fabrication processes

4.3 Fuel cell propulsion system for automobiles

In contrast to conventional and hybrid vehicles, which rely on ICEs and electric generators, FCVs produce electricity through electrochemical reactions. This electricity is used to power the vehicle's motor directly or stored temporarily in batteries or supercapacitors. PEM fuel cells are widely used in automotive applications for several reasons. Firstly, they offer fast startup and response times, making them suitable for vehicles that require quick power delivery. Additionally, PEM fuel cells operate at relatively low temperatures, enabling efficient operation and reducing the need for complex cooling systems. They also have a compact and lightweight design, which is advantageous for automotive integration. Moreover, PEM fuel cells can be easily scaled up or down to meet various power requirements, making them versatile for different vehicle types.

Figure 4.4 illustrates the typical components of a fuel cell system, including a hydrogen and air supply system, a cooling system, a fuel cell pack, a hydrogen storage tank, and a humidity management system.

The core of the fuel cell system is the fuel cell stack, responsible for the electrochemical reaction that converts chemical energy into electricity. The stack consists of two catalyst layers separated by a PEM, enclosed between two flow plates. Under the right conditions of hydrogen-oxygen ratio and pressure,

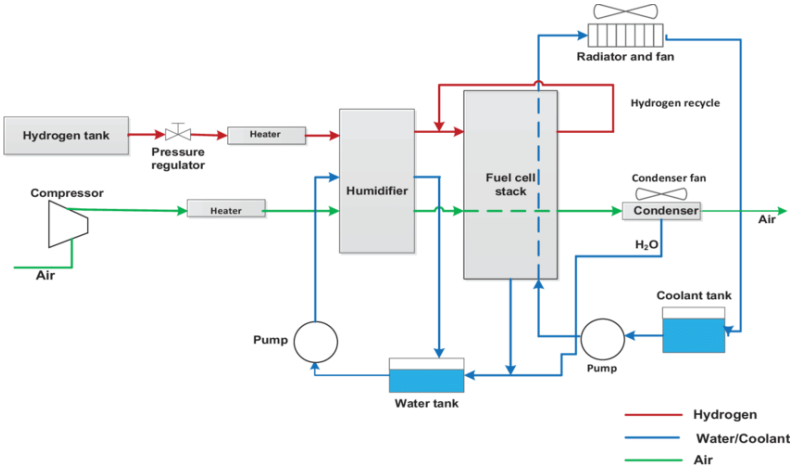

Figure 4.4: Schematic diagram of a PEM fuel cell system. Source [6].

hydrogen within the fuel cell stack undergoes catalysis, splitting into hydrogen ions and electrons with the aid of a platinum catalyst. The PEM allows the hydrogen ions to pass through to the cathode, where they combine with oxygen and create water through oxidation.

In the meantime, the electrons are directed through an external DC/DC circuit to the cathode. To ensure an efficient and continuous electrochemical reaction in the fuel cell stack, various factors must be coordinated and controlled, including the fuel cell's temperature and current density, the humidity of the PEM, and the hydrogen-oxygen ratio along with their respective pressures. Failure to maintain proper control compromises the fuel cell's durability and efficiency.

Hydrogen is stored at high pressures (up to 35 or 70 MPa) but remains in a gaseous state. The gaseous hydrogen at the desired pressure is introduced into the fuel cell via a pressure reduction valve, which is carefully regulated between the hydrogen tank and the fuel cell stack. Moreover, any remaining hydrogen that passes through the anode of the fuel cell stack is recirculated back to the hydrogen pipeline entrance by a recirculation pump. This mechanism ensures nearly complete oxidation of hydrogen (reported utilizations of up to 96% and 99.6% in [7, 8]) for electricity generation. On the other hand, the air supply system generates a large flow of high-pressure air using a compressor driven by a high-speed motor. In automotive applications, the power generated can exceed 10 kW. After passing through the manifold, the pressurized air enters the cathode and is subsequently released into the environment through a controlled valve. The humidity of the PEM is typically adjusted by humidifiers

positioned before the hydrogen and air pipelines, although advanced automotive manufacturers are exploring methods to maintain PEM humidity without the need for humidifiers [9].

In most cases, particularly during high-power operation of the fuel cell, waste heat is generated as a byproduct of the electrochemical reaction, resulting in increased temperature within the fuel cell stack. To maintain optimal performance, the temperature should be regulated at approximately 60°C to 80°C. Therefore, a cooling system is essential for dissipating heat from the fuel cell stack. This cooling system includes a pump and a cooler, a cooling water tank, and corresponding pipelines. The pump circulates the cooling water between the flow plate of the fuel cell stack and the cooler. The speed of the pump and the cooler fan can be adjusted to control the temperature of the fuel cell stack.

Unlike other applications such as portable batteries and power stations, automotive applications require compact fuel cells that can be installed in limited-size engine compartments, similar to those designed for traditional ICEs. Below, the fuel cell stack, the thermal management subsystem, and the power electronics subsystem are described in more detail.

4.3.1 Fuel cell stack

In fuel cell systems, the voltage of a single fuel cell is limited to around 1 V, with typical output voltages under load ranging from 0.6 to 0.7 V. This voltage range corresponds to the optimal operating conditions for fuel cells in terms of electrical efficiency (around 45%) and power density. However, many real-world applications require higher voltages. To meet these requirements, multiple fuel cells can be interconnected in series, a technique known as fuel cell stacking.

Fuel cell stacks are designed with several goals in mind, including simplicity and low cost of fabrication, low-loss electrical interconnects between cells, efficient reactant gas distribution, efficient cooling schemes (especially for high-power stacks), and reliable sealing arrangements between cells. The most common form of fuel cell interconnection is vertical or bipolar plate stacking, where a single conductive flow structure or plate connects the fuel electrode of one cell with the oxidant electrode of the next cell in series. Bipolar stacks provide straightforward electrical connection and exhibit low ohmic loss due to the large contact area between cells [10].

However, sealing bipolar configurations can be challenging. Edge seals are required to prevent gas leakage from the porous electrodes. Planar interconnection designs have also been explored for SOFCs, where cells are connected laterally. While planar designs have increased electrical resistance losses, they offer form factor advantages for portable applications. Ceramic

fuel cells often use planar designs to mitigate manufacturing issues [11]. A tubular geometry can be employed for high-temperature fuel cells to minimize sealing requirements, as it reduces the surface area needed for sealing.

In addition to the fuel cell stack, external equipment is often required to ensure proper operation. This equipment, such as external humidifiers, is considered part of the fuel cell subsystem. Humidifiers are used to supply humidified inlet gases to PEMFCs to control membrane conductivity. Automotive PEMFC stack subsystems typically employ tubular or plate-frame humidifiers upstream of the cathode to regulate humidity levels.

Despite PEM fuel cells being suitable for automotive applications, their widespread adoption is limited by their high cost and lower durability compared to internal combustion engines. The United States Department of Energy has established ambitious lifetime goals for fuel cell systems in transportation and stationary applications. Specifically, the DOE aims for a minimum lifetime of 5,000 hours for transportation applications and 40,000 hours for stationary applications, with a performance degradation of less than 10% [12]. The performance and durability of fuel cells are influenced by various factors, including the state of the MEA and the polar plate, as well as the operating conditions. The MEA, consisting of the membrane, catalyst layer, and gas diffusion layer, is particularly important as it can degrade under certain operating conditions, affecting the overall durability. Contamination from released metal ions in the bipolar plate and an increase in contact resistance due to corrosion and passivation contribute to performance decay. Extensive research has focused on studying the irreversible degradation of specific components such as the perfluorinated sulfonic acid (PFSA) membrane, ionomer in the catalyst layer, Pt catalyst, and carbon support [13, 14]. This degradation involves material aging, loss, changes in morphology, and microstructure. Thermal, mechanical, and chemical effects can age the membrane, causing decomposition, cracks, and pinholes. Chemical degradation can occur due to attack by free radicals. Membrane degradation leads to increased hydrogen permeability and decreased ionic conductivity. Corrosion of the carbon support is accelerated under high potential, while the Pt catalyst undergoes complex degradation processes such as dissolution, re-deposition, Ostwald ripening, agglomeration, sintering, and detachment, resulting in a decrease in the electrochemical surface area. Analyzing the components, reaction products, microstructure, and morphology can provide insights into the origins and mechanisms of aging.

4.3.2 Thermal management subsystem

The heat and temperature management subsystem of a fuel cell system comprises the cooling system for the fuel cell stack and the reactant temperature

control system. When the traction motor draws current, heat is generated within the fuel cell. Due to the size of the stack required for passenger vehicles, passive dissipation of heat through air convection and radiation from the external surface is insufficient. Therefore, active cooling is necessary through the control of reactant flow rate and a dedicated cooling system.

Managing the thermal conditions of the fuel cell stack presents greater challenges compared to internal combustion engines. Firstly, de-ionized water serves as the coolant instead of a more effective coolant fluid. Secondly, the PEM fuel cell operates at around 80°C, resulting in exhaust air temperature of approximately 80°C, which has lower heat-carrying capacity compared to the over 500°C exhaust gas of internal combustion engines. Consequently, the cooling system bears the responsibility of heat rejection for the fuel cell stack. Additionally, the small temperature difference between the stack and the water coolant limits the efficiency of heat transfer from the stack to the coolant. Apart from the coolant flow rate and its temperature, the temperature of the incoming reactant air also affects the stack temperature. The heat management system controls the speed of the cooling fan and recirculation pump while coordinating with the adjustment of a bypass valve. The main objectives of thermal management are rapid warm-up without overshooting the stack temperature and minimizing the power consumption of auxiliary fans and pumps.

4.3.3 Power electronic subsystem

The power electronics subsystem of a fuel cell system encompasses four main tasks: power regulation, power inversion, monitoring and control, and power supply management. Power regulation involves delivering power at a precise voltage and maintaining that voltage constant, even as the current load fluctuates. This task is crucial for fuel cell applications as it ensures a stable power supply. Power inversion, on the other hand, involves converting the DC power generated by the fuel cell into AC power, which is the standard power requirement for most electronic devices. Inversion is typically necessary for stationary and automotive fuel cell systems. Stationary systems supply electricity to the AC electric grid or building power grids, while automotive systems often require AC power for electric motors due to their efficiency, cost-effectiveness, and availability. However, certain portable fuel cell applications, such as fuel cell laptops, may utilize DC power directly and thus do not require inversion. It is important to note that power conditioning, which includes both power regulation and power inversion, comes with certain drawbacks in terms of cost and efficiency. Implementing power conditioning in a fuel cell system typically increases the capital cost by around 10-15%. Moreover, it slightly reduces the

electrical efficiency of the system by approximately 5-20%. Therefore, careful consideration and selection of the most suitable power conditioning solution for a specific application are essential to optimize performance.

4.4 Simulation of fuel cell system

4.4.1 Literature review

In macro-scale numerical models of PEM fuel cells, the focus is on solving transient conservation equations to analyze various transport phenomena. These equations include mass, momentum, energy, species (such as hydrogen, oxygen, and water vapor), as well as electron and proton transport. Solving these equations provides information about flow fields, temperature distribution, gas-phase species concentrations, and electronic and ionic phase potentials. In certain cases, the fast electrochemical double layer processes allow for neglecting the transient terms in the charge transport equations, resulting in steady-state equations [15]. To accurately represent the water content distribution within the cell membrane, a separate transport equation dedicated to water content is typically solved [16]. This equation is coupled with transport equations for water vapor and liquid water, accounting for interfacial boundary conditions [17, 18] or source/sink terms to consider water absorption/desorption into/from the membrane phase. In two-phase PEM fuel cell models, a liquid water transport equation becomes essential to analyze liquid water distribution and its impact on cell performance. This equation is closely linked to the gas-phase water transport equation through water condensation/evaporation. Additionally, an equation describing ice formation is necessary to study cold-start processes of PEM fuel cells operating at subfreezing temperatures. A summary of the conservation equations can be found in Table 4.4.1. It is important to note that slight variations may exist in these equations across different numerical models due to modeling simplifications and assumptions; however, the core terms remain consistent.

Over the past decades, numerous numerical models of PEM fuel cells have been successfully developed, gradually reducing assumptions and simplifications. Initially, one-dimensional models focused on fundamental electrochemical and transport phenomena in the gas diffusion layer, catalyst layer, and membrane [20–23]. Despite their simplifications, these models provided insights into the essential mechanisms of PEM fuel cells. The advancements in one-dimensional models served as crucial foundations for next-generation models.

Later, numerical models evolved to consider gas concentration variations in the flow direction within gas channels, leading to pseudo two-dimensional

Table 4.2: Conservation equations [19]

Description	**Expression**
Mass	$\frac{\partial(\epsilon(1-s_l-s_{ice})\rho)}{\partial t} + \nabla \cdot (\rho \mathbf{u}) = S_m$
Momentum	$\frac{1}{\epsilon(1-s_l-s_{ice})}\frac{\partial(\rho \mathbf{u})}{\partial t} + \frac{1}{\epsilon^2(1-s_l-s_{ice})^2}\nabla \cdot (\rho \mathbf{uu}) = -\nabla p + \nabla \cdot \tau + S_u$
Species	$\frac{\partial(\epsilon_{eff}(1-s_l-s_{ice})c_i)}{\partial t} + \nabla \cdot (uc_i) = \nabla \cdot (D^i_{eff}\nabla c_i) + S_i$
Water content in membrane	$\frac{\partial}{\partial t}(\frac{\rho_m \lambda}{EW}) = \nabla \cdot (D_\lambda \nabla \lambda) + S_\lambda$
Energy	$\frac{\partial}{\partial t}[(\rho c_p)_{eff}T] + \nabla \cdot (\rho c_p \mathbf{u}T) + \nabla \cdot (\rho_l c_{pl} u_l T) = \nabla \cdot (k_{eff}\nabla T) + S_T$
Liquid water	$\frac{\partial(\epsilon \rho_l s_l)}{\partial t} + \nabla \cdot \left(\frac{\rho_l K_{rl} K}{\mu^l} \cdot \frac{\partial_C}{\partial_l}\nabla s_l\right) - \nabla \cdot (\frac{\rho_l K_{rl} K}{\mu^l}\nabla p) = S_{vl} W_w$
Ice	$\frac{\partial(\epsilon \rho_{ice} s_{ice})}{\partial t} = S_{vi} W_w$
Proton	$\nabla \cdot (\kappa_{eff}\nabla \phi_e) + S_e = 0$
Electron	$\nabla \cdot (\sigma_{eff}\nabla \phi_s) + S_s = 0$

models [24–26]. These models examined distributions of chemical species and local current density, addressing practical water and thermal management issues. Further developments involved applying CFD methodology to establish complete flow fields in gas channels, gas diffusion layers, and catalyst layers [27, 28]. Transport equations of chemical species were solved numerically, considering source/sink terms from electrochemical kinetics. The water content's influence on water diffusivity and proton conductivity in the membrane phase was accounted for using empirical correlations.

Three-dimensional numerical models of PEM fuel cells were subsequently developed [29, 30]. These models solved conservation equations of mass, momentum, and species in the gas channels and diffusion media, incorporating electrochemical kinetics through source/sink terms. They also considered electron transfer and its effects on fuel cell performance, enabling the inclusion of electronic contact resistance and the implementation of constant-current boundary conditions. Heat transfer processes and thermal management were numerically studied [31]. Water management plays a vital role in PEM fuel cell design and optimization. Water is introduced through gas channel inlets and produced in the cathode catalyst layer. Inside the fuel cell, water exists in vapor, liquid, and solid forms, depending on temperature and humidity. Water and thermal management are closely intertwined, and rigorous physical models for two-phase flows and liquid water transport have been developed [32, 33]. Methods such as the volume-of-fluid (VOF) approach were employed to track gas-liquid interfaces in porous diffusion layers and gas channels [32]. However, further investigations are needed regarding interfacial phenomena across different porous layers and liquid water transport in gas channels. Transient responses during startup and load changes have been extensively studied. Early work used single-phase or pseudo single-phase models, unable

to consider the effect of liquid water transport and accumulation on dynamic responses. Transient two-phase non-isothermal models were developed to investigate heat transfer and liquid water transport's combined influence on transient response behaviors [34, 35]. Numerical results showed that liquid water presence in porous materials increased current density overshoot and undershoot during voltage changes. The heat transfer process also influenced the dynamic response through its interaction with liquid water variations. Interfacial phenomena, such as liquid water accumulation and droplet coverage at interfaces, played significant roles in transient responses, necessitating further investigation. Successful startup from subfreezing temperatures is crucial for automotive applications. PEM fuel cell models were developed to study the cold-start phenomenon, revealing the impact of inlet water humidity and initial water content on the startup process [36, 37]. Due to the complexity of transport phenomena and limited experimental measurements, direct numerical simulations using various techniques have gained attention. Conventional CFD, lattice Boltzmann modeling, and pore network approaches enable simulations of transport processes in micro- and meso-scales in porous media [38, 39]. These simulations contribute to a deeper understanding of two-phase phenomena, interfacial effects, and the influence of different channel geometries on liquid water movement and interaction with the gas stream.

4.4.2 Fuel cell model development

A previous doctoral thesis addressed the development of a 0D fuel cell model, which was subsequently integrated into an FCHEV. This section highlights its fundamental aspects, as the model has been incorporated into the vehicle model, (described in chapter 5), for which advanced EMSs have been developed. These advanced strategies will be detailed in Chapter 6.

Fuel cell stack model

The fuel cell model encompasses both the fuel cell stack and the Balance of Plant. Regarding the fuel cell, the relationship between its current density and voltage is described by the polarization curve, which is defined by the following set of equations:

$$V_{FC} = V_{OC} - V_{act} - V_{ohm} - V_{mt} \tag{4.8}$$

$$V_{OC} = \frac{-\Delta \overline{g}_f}{2F} \tag{4.9}$$

$$V_{act} = \begin{cases} \frac{R_{gas}T}{2F}\left(\frac{i}{i_0}\right) \\ \frac{R_{gas}T}{2\alpha F} ln\left(\frac{i}{i_0}\right) \end{cases} \tag{4.10}$$

$$V_{ohm} = R\, I \tag{4.11}$$

$$V_{mt} = -C\, ln\left(1 - \frac{i}{i_l}\right) \tag{4.12}$$

Here, V_{OC} represents the open voltage circuit, and V_{act}, V_{ohm}, and V_{mt} correspond to the activation, ohmic, and mass transport losses, respectively.

The ohmic resistance R_{ohm} is modeled according to [22], considering variations in the ionic conductivity of the membrane based on factors such as membrane water content, temperature, and membrane properties. The exchange current density depends on the fuel cell temperature, oxygen partial pressure, electrochemical activation energy, electrode roughness, and reference exchange current density $i_{0,ref}$ [40].

The GT-Suite genetic algorithms toolbox is employed for calibrating the values of the reference exchange current density, reference ohmic resistance, charge transfer coefficient (α), mass transport loss coefficient (C), limiting current density (i_l), and open circuit voltage losses. This calibration process aims to validate the model across different pressure and temperature conditions using experimental data from [41, 42]. The NSGA-III evolutionary global search genetic algorithm is specifically chosen as the optimization algorithm [40]. The objective of the optimization is to minimize the overall error between the experimental and simulated voltage values on the polarization curve under varying temperature and pressure conditions. Convergence of the optimization algorithm is ensured by using 15 generations of solutions, as the error between experimental and simulated results reaches an asymptote after 10-12 generations.

The fuel cell model is validated by simultaneously fitting three different numerical polarization curves (totaling 34 experimental points) to the corresponding experimental data under different temperature and pressure conditions: $T_{cath} = 305, \mathrm{K}$ and $p_{cath} = 1.3, \mathrm{bar}$, $T_{cath} = 346, \mathrm{K}$ and $p_{cath} = 1.3, \mathrm{bar}$, $T_{cath} = 346, \mathrm{K}$ and $p_{cath} = 2.5, \mathrm{bar}$. This validation process is crucial for driving cycle conditions in which the fuel cell stack experiences various operating conditions depending on the external environment and BoP component operation. The synthetic validation results are depicted in Figure 4.5, demonstrating an

overall root mean square (RMS) deviation below 2% between the experimental data and the model predictions.

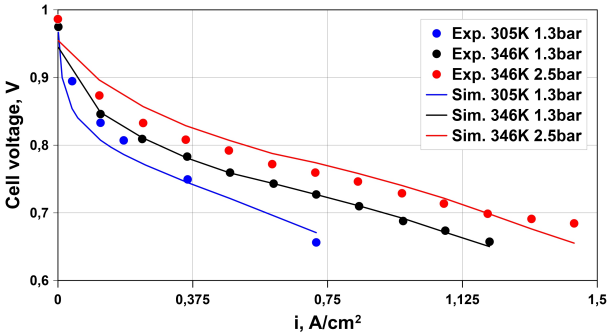

Figure 4.5: Comparison of cell voltage against current density for different cathode pressures and temperatures between the model and experimental data. Source: [43]

Fuel cell system model

The fuel cell stack, described in Table 4.4.2, is integrated into a complete BoP model, optimized in a previous study [44]. The BoP model includes the anode and cathode circuits, conditioning systems, and a cooling system, as shown in Figure 4.6.

Fuel Cell Stack	
Cells number, -	480
Max Power, kW	120
Max efficiency, -	0.62
DC-DC efficiency, -	0.95
Fuel Cell Membrane	
Active surface area, cm^2	250
Membrane dry density, kg/m^3	3280
Membrane thickness, μ	189
Membrane dry equivalent weight, g/mol	1100

The cathode side features an e-charger compressor for high-pressure air supply, an intercooler heat exchanger, and a humidifier system to increase the cathode inlet relative humidity using exhaust water from the fuel cell stack. The centrifugal compressor map is parameterized to meet pressure and air

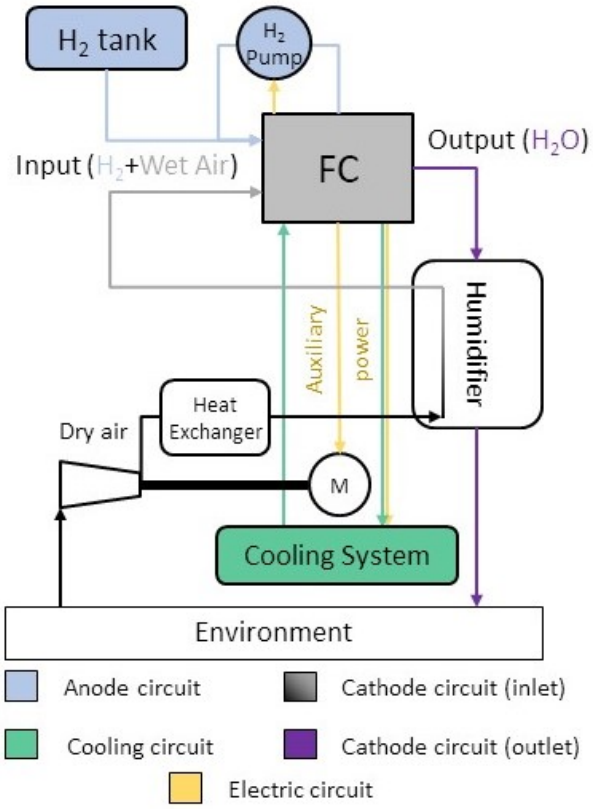

Figure 4.6: Fuel cell system scheme. Source: [43]

mass flow rate requirements. Cathode stoichiometry and pressure are regulated with two PID controllers for e-charger power and exhaust valve area. The heat exchanger is modeled with constant cooling efficiency of 70%, using 70 °C coolant as the cold reservoir. The humidifier system is represented by thermal capacity-connected pipes to incorporate heat transfer. Water transport is simulated using ejectors and injectors. The anode side comprises a 700 bar H_2 tank and an active H_2 recirculating loop with a pump. Anode pressure is regulated by controlling the valve between the recirculating loop and H_2 tank, while anode stoichiometry is controlled by the fuel cell-powered pump.

The BoP optimization assumes:

- Cathode and anode pressure losses are modeled using data from the Ballard FCVelocity-9SSL fuel cell [45], as data from Corbo et al. [41, 42] was unavailable. Membrane properties are listed in Table 4.4.2.

- Cathode stoichiometry is fixed at 1.8 for current densities of 0.4 A/cm^2 or higher to avoid starvation during load changes.
- Target cathode inlet relative humidity is set to 80% for all operating conditions, regulated by a PID controller considering temperature and pressure variations.
- Anode stoichiometry is set to 3 to prevent starvation and improve hydrogen diffusivity through the gas diffusion layer.
- The minimum cathode pressure is 1.2 bar to account for fuel cell pressure losses.

To reduce computational effort, a mean value model is employed for the fuel cell system, as in [44]. Cathode pressure, known as a key variable influencing fuel cell performance, is considered a control variable along with the current, introducing dynamics to the model while maintaining accuracy.

Fuel cell degradation model

Fuel cell degradation is influenced by various factors, including its operating conditions and environmental parameters such as temperature, pressure, and relative humidity. Degradation can occur due to different electrochemical mechanisms that are active at different load conditions, including low-load, medium load, high-load, and load-change conditions. These mechanisms are influenced by the voltage at which each cell operates and the flow of protons through the membrane. The rate of degradation is directly related to the current density.

To capture these degradation phenomena, a comprehensive degradation model is utilized. The model incorporates scaling functions that account for the physical trends observed in degradation mechanisms under different operating conditions. These functions are applied to degradation rate coefficients derived from reference conditions of current density, temperature, and relative humidity. The reference degradation rates, obtained from experimental data by Pei et al. [46], are adjusted to calibrate the degradation model (Table 4.3). While this model has been previously developed and validated, a brief explanation is provided here for completeness. For more in-depth details, readers are referred to Desantes et al. [47].

The degradation model presented in this thesis quantifies degradation using a voltage degraded ratio, denoted as δ, which is defined as the difference between the non-degraded voltage V_{FC} and the degraded voltage V_{deg} divided by the non-degraded voltage: $\delta = 1 - \frac{V_{deg}}{V_{FC}}$. The model incorporates modifications to

Condition	δ [fraction V loss]
Low power [/h] $\left(\frac{d\delta}{dt}\vert_{lp,ref}\right)$	$1.26{\cdot}10^{-5}$
Load change [/cycle] $\left(\frac{d\delta}{dn_{lc}}\vert_{ref}\right)$	$4.94{\cdot}10^{-7}$
High power [/h] $\left(\frac{d\delta}{dt}\vert_{hp,ref}\right)$	$1.03{\cdot}10^{-5}$
Start-stop [/cycle] $\left(\frac{d\delta}{dn_{ss}}\vert_{ref}\right)$	$1.96{\cdot}10^{-5}$

Table 4.3: Reference degradation rates (1^{st} layer) to be scaled.

the reference degradation rates, as listed in Table 4.3, to predict the temporal evolution of the degradation ratio δ. This prediction is influenced by the specific operating conditions and the underlying electrochemical phenomena involved according to:

$$\delta = \int_0^t \left[\left.\frac{d\delta}{dt}\right|_{lp} + \left.\frac{d\delta}{dt}\right|_{lc} + \left.\frac{d\delta}{dt}\right|_{hp} + \left.\frac{d\delta}{dt}\right|_{nt} \right] dt + \frac{d\delta_{ss}}{dn_{ss}} n_{ss} \tag{4.13}$$

$$\left.\frac{d\delta}{dt}\right|_{lp} = \left.\frac{d\delta}{dt}\right|_{lp,ref} \cdot \xi_{lp}(i) \cdot \tau(T) \cdot \eta(\overline{RH}) \tag{4.14}$$

$$\left.\frac{d\delta}{dt}\right|_{lc} = \left.\frac{d\delta}{dn_{lc}}\right|_{ref} \cdot \xi_{lc}\left(\frac{di}{dt}\right) \cdot \tau(T) \cdot \eta(\overline{RH}) \tag{4.15}$$

$$\left.\frac{d\delta}{dt}\right|_{hp} = \left.\frac{d\delta}{dt}\right|_{hp,ref} \cdot \xi_{hp}(i) \cdot \tau(T) \cdot \eta(\overline{RH}) \tag{4.16}$$

$$\begin{aligned} \left.\frac{d\delta}{dt}\right|_{nt} = {} & \frac{\left.\frac{d\delta}{dt}\right|_{hp,ref} \xi_{hp}(i_{hp}) - \left.\frac{d\delta}{dt}\right|_{lp,ref} \xi_{lp}(i_{lp})}{i_{hp} - i_{lp}} (i - i_{lp}) \\ & + \left.\frac{d\delta}{dt}\right|_{lp,ref} \xi_{lp}(i_{lp}) \end{aligned} \tag{4.17}$$

$$\frac{d\delta_{ss}}{dn_{ss}} = \left.\frac{d\delta}{dn_{ss}}\right|_{ref} \tag{4.18}$$

In the degradation model, various scaling functions, namely ξ, τ, and η, are employed to account for the influence of current density, temperature, and relative humidity on the degradation rates. The current density is denoted as i, while i_{hp} and i_{lp} represent the high-power and low-power current densities, respectively. Additionally, the parameter n_{ss} signifies the number of start-stop cycles. These scaling functions and parameters play a crucial role in the degradation model, allowing for the computation of changes in the voltage degraded ratio (δ) under diverse operating conditions.

Specifically, ξ accounts for the electrochemical mechanism activated by the current density, while τ represents the effect of temperature on the degradation rates. Moreover, η captures the impact of relative humidity on the degradation processes. By incorporating these scaling functions into the model, the degradation rates can be appropriately adjusted based on the prevailing operating conditions, enabling a more accurate prediction of the evolution of δ over time.

The degradation model encompasses various aspects, ranging from low-power conditions ($\frac{d\delta}{dt}|_{lp}$) associated with degradation mechanisms affecting the catalyst layer at high cell potential, to load-change operations ($\frac{d\delta}{dt}|_{lc}$) where water and flow management may lead to certain deterioration of the MEA. Additionally, the model considers high-power conditions ($\frac{d\delta}{dt}|_{hp}$) characterized by increased degradation mechanisms at high temperatures. Moreover, it accounts for natural decay ($\frac{d\delta}{dt}|_{nt}$) and start-stop conditions ($\frac{d\delta}{n_{ss}}$).

The scaling functions are expressed as:

$$\xi_{lp}(i) = \begin{cases} \xi_{lp}(i) = -0.176 \cdot \ln i + 0.169 & i \leq i_{lp} \\ 1 & i > i_{lp} \end{cases} \tag{4.19}$$

$$\xi_{lc}\left(\frac{di}{dt}\right) = \frac{|\Delta i|_{dt}}{2\,|\Delta i|_{ref}} \tag{4.20}$$

$$\xi_{hp}(i) = \begin{cases} \frac{i}{i_{hp}} & i > i_{hp} \\ 1 & i \leq i_{hp} \end{cases} \tag{4.21}$$

$$\tau(T) = \tau(T) = -5.390 \cdot 10^{-4} T^2 + 0.399 \cdot T - 71.576 \tag{4.22}$$

$$\eta(\overline{RH}) = 0.10646 e^{0.028 \cdot RH\ [\%]} \tag{4.23}$$

The scaling function τ is applicable within the temperature range of $T \in [310, 373.15]$ K. This range is determined based on the variations in fluoride release rate and electrical surface area, as documented in the studies by Knights et al. [48] and Bi et al. [49], respectively. Furthermore, the scaling function η is derived from experimental findings presented in Dutta et al. [50]. These experiments investigated fuel cell degradation during voltage cycling under different levels of relative humidity (RH). To validate this model, it was employed with data obtained from a real daily bus route, as reported in Pei et al. [46]. Previous studies, specifically Desantes et al. [47], have successfully utilized this model and demonstrated its efficacy in predicting changes in degradation rates and determining the significance of each fuel cell degradation source. Additionally, the applicability and accuracy of this model have been confirmed in other studies conducted by Desantes et al. [51].

4.5 Summary and conclusions

A fuel cell is an electrochemical device that generates electrical power from a fuel source. It is described by a polarization curve, which illustrates the relationship between the cell's voltage and the current it produces. The basic operation of a fuel cell involves several key mechanisms. Firstly, there is the fuel and oxidant supply. The fuel, which can be hydrogen, methanol, or other hydrocarbon-based compounds, is supplied to the anode side of the cell. Meanwhile, the oxidant, usually oxygen or air, is delivered to the cathode side. At the anode, a catalyst facilitates the oxidation of the fuel, breaking it down into electrons and ions. The electrons flow through an external circuit, generating electrical power, while the ions migrate through an electrolyte material to the cathode. On the cathode side, the oxidant combines with the electrons and the ions from the anode, resulting in the production of water, heat, and additional electrical energy. This electrochemical reaction occurring at the cathode completes the circuit within the fuel cell.

There are various types of fuel cells, each designed for specific applications. One of the most widely used fuel cell technologies in the automotive sector is the PEM fuel cell. Indeed, PEM fuel cells offer several advantages for automotive applications. They have quick startup times,allowing for rapid response to power demands. Additionally, their compact size and lightweight nature make them suitable for integration into vehicles. Moreover, PEM fuel cells have high power density, providing sufficient power output for electric vehicles and low operating temperature. They also offer good efficiency and low emissions, contributing to cleaner and more sustainable transportation.

Fuel cells are integrated into a complete system called the balance of plant. The BoP includes key components such as the fuel supply system, air supply system, thermal management system, water management system, power conditioning and electronics, and the control and monitoring system. These devices work together to support the fuel cell's operation, ensuring a reliable fuel supply, managing temperature and humidity levels, converting electrical output, and monitoring performance. The balance of plant plays a vital role in optimizing the efficiency and functionality of fuel cell systems in various applications.

Despite their advantages, PEM fuel cells face challenges related to degradation and durability. Membrane degradation, caused by factors like chemical reactions and contaminants, reduces proton conductivity. Catalyst degradation, from agglomeration or poisoning, lowers activity. These issues require ongoing research for more stable materials, improved catalyst durability, and better system design to enhance PEM fuel cell performance and lifespan.

Also in the field of fuel cells, simulations can play a crucial role in the design and development phase, aiding in improving performance and mitigating degradation issues. Through simulations, researchers and engineers can model and analyze various aspects of fuel cell behavior, such as fluid flow, electrochemical reactions, and heat transfer. These simulations provide insights into optimizing cell designs, materials, and operating conditions to enhance performance, increase efficiency, and minimize degradation. By leveraging simulations, the fuel cell industry can accelerate advancements, leading to more reliable and durable fuel cell systems.

In the final section of the chapter, the fuel cell model utilized for the development of advanced control strategies (chapter 6) is described. It includes a fully validated fuel cell model, inserted in an optimized BoP. It also evaluates the MEA degradation, a key aspect to be considered during vehicle operation.

References

[1] *Fuel cell - Energy Education*. URL: https://energyeducation.ca/encyclopedia/Fuel_cell (visited on 06/15/2023).

[2] O'Hayre, Ryan. "Fuel cells for electrochemical energy conversion". In: *EPJ Web of Conferences* 148 (2017), p. 00013. DOI: 10.1051/epjconf/201714800013.

[3] *Fuel Cell Fundamentals*. 1st ed. _eprint: https://onlinelibrary.wiley.com/doi/pdf/10.1002/9781119 John Wiley & Sons, Ltd, 2016. DOI: 10.1002/9781119191766.

[4] Tran, D., Cummins, M., Stamos, E., Buelow, J., and Mohrdieck, C. "Development of the Jeep Commander 2 fuel cell hybrid electric vehicle". In: *Society of Automotive Engineers (SAE) Journal* 2001 (2002). Place: Warrendale, PA.

[5] Berlowitz, P.J. and Darnell, C.P. "Fuel choices for fuel cell powered vehicles". In: *Society of Automotive Engineers (SAE) Journal* 2000 (2002). Place: Warrendale, PA.

[6] Akroot, Abdulrazzak, Ekici, Özgür, and Koksal, Murat. "Process modeling of an automotive pem fuel cell system". In: *International Journal of Green Energy* 16 (2019), pp. 1–11. DOI: 10.1080/15435075.2019.1641105.

[7] Nishikawa, H., Sasou, H., Kurihara, R., and, et al et. "High fuel utilization operation of pure hydrogen fuel cells". In: *International Journal of Hydrogen Energy* 33 (2008), pp. 6262–6269.

[8] Han, I. S., Jeong, J., and Shin, H. K. "PEM fuel-cell stack design for improved fuel utilization". In: *International Journal of Hydrogen Energy* 38 (2013), pp. 11996–12006.

[9] Mirfarsi, Seyed Hesam, Parnian, Mohammad Javad, and Rowshanzamir, Soosan. "Self-Humidifying Proton Exchange Membranes for Fuel Cell Applications: Advances and Challenges". In: *Processes* 8.9 (2020). Number: 9 Publisher: Multidisciplinary Digital Publishing Institute, p. 1069. DOI: 10.3390/pr8091069.

[10] Tawfik, H., Hung, Y., and Mahajan, D. "Metal bipolar plates for PEM fuel cell—A review". In: *Journal of Power Sources*. Selected Papers presented at the FUEL PROCESSING FOR HYDROGEN PRODUCTION SYMPOSIUM at the 230th American Chemical SocietyNational Meeting Washington, DC, USA, 28 August – 1 September 2005 163.2 (2007), pp. 755–767. DOI: 10.1016/j.jpowsour.2006.09.088.

[11] Donazzi, Alessandro, De Pascali, Stefano, Garavaglia, Francesco, and Bracconi, Mauro. "A quasi 2D model for the interpretation of impedance and polarization of a planar solid oxide fuel cell with interconnects". In: *Electrochimica Acta* 365 (2021), p. 137346. DOI: 10.1016/j.electacta.2020.137346.

[12] Department of Energy of the United States. *Fuel Cell Technologies Office Multi-Year Research, Development, and Demonstration Plan*. 2017.

[13] Yuan, Xiao-Zi, Li, Hui, Zhang, Shengsheng, Martin, Jonathan, and Wang, Haijiang. "A review of polymer electrolyte membrane fuel cell durability test protocols". In: *Journal of Power Sources* 196.22 (2011), pp. 9107–9116. DOI: 10.1016/j.jpowsour.2011.07.082.

[14] Zhang, Shuan-Hong, Zhao, Yue, Yang, Zhen-Yu, He, Zhe-Feng, and Wu, Hai. "The 1.35Ga diabase sills from the northern North China Craton: Implications for breakup of the Columbia (Nuna) supercontinent". In: *Earth and Planetary Science Letters* 288.3 (2009), pp. 588–600. DOI: 10.1016/j.epsl.2009.10.023.

[15] Wang, Yun and Wang, Chao-Yang. "Transient analysis of polymer electrolyte fuel cells". In: *Electrochimica Acta* 50.6 (2005), pp. 1307–1315. DOI: 10.1016/j.electacta.2004.08.022.

[16] Ijaodola, O. S. et al. "Energy efficiency improvements by investigating the water flooding management on proton exchange membrane fuel cell (PEMFC)". In: *Energy* 179 (2019), pp. 246–267. DOI: 10.1016/j.energy.2019.04.074.

[17] Meng, H. "A Three-Dimensional PEM Fuel Cell Model with Consistent Treatment of Water Transport in MEA". In: *Journal of Power Sources* 162 (2006), pp. 426–435.

[18] Meng, H. "A Three-Dimensional Mixed-Domain PEM Fuel Cell Model with Fully-Coupled Transport Phenomena". In: *Journal of Power Sources* 164 (2007), pp. 688–696.

[19] Song, Guang-Hua and Meng, Hua. "Numerical modeling and simulation of PEM fuel cells: Progress and perspective". In: *Acta Mechanica Sinica* 29.3 (2013), pp. 318–334. DOI: 10.1007/s10409-013-0037-y.

[20] Bernardi, D. M. and Verbrugge, M. W. "Mathematical Model of a Gas Diffusion Electrode Bonded to a Polymer Electrolyte". In: *AIChE Journal* 37 (1991), pp. 1151–1163.

[21] Bernardi, D. M. and Verbrugge, M. W. "A Mathematical Model of the Solid-Polymer-Electrolyte Fuel Cell". In: *Journal of The Electrochemical Society* 139 (1992), pp. 2477–2491.

[22] Springer, T.E., Zawodzinski, T.A., and Gottesfeld, S. "Polymer electrolyte fuel cell model". In: *Journal of The Electrochemical Society* 138 (1991). Publisher: The Electrochemical Society, pp. 2334–2342.

[23] Fuller, T. F. and Newman, J. "Water and Thermal Management in Solid-Polymer-Electrolyte Fuel Cells". In: *Journal of The Electrochemical Society* 140 (1993), pp. 1218–1225.

[24] Nguyen, T. V. and White, R. E. "A Water and Heat Management Model for Proton-Exchange-Membrane Fuel Cells". In: *Journal of The Electrochemical Society* 140.8 (1993), pp. 2178–2186.

[25] Yi, J. S. and Nguyen, T. V. "An Along-the-Channel Model for Proton Exchange Membrane Fuel Cells". In: *Journal of The Electrochemical Society* 145.4 (1998), pp. 1149–1159.

[26] Chu, H.-S., Yeh, C., and Chen, F. "Effects of Porosity Change of Gas Diffuser on Performance of Proton Exchange Membrane Fuel Cell". In: *Journal of Power Sources* 123.1 (2003), pp. 1–9.

[27] Hum, B. and Li, X. "Two-dimensional analysis of PEM fuel cells". In: *Journal of Applied Electrochemistry* 34.2 (2004), pp. 205–215.

[28] Gurau, V., Liu, H., and Kakac, S. "Two-dimensional model for proton exchange membrane fuel cells". In: *AIChE Journal* 44.11 (1998), pp. 2410–2422.

[29] Ye, Q. and Nguyen, T. V. "Three-Dimensional Simulation of Liquid Water Distribution in a PEMFC with Experimentally Measured Capillary Functions". In: *Journal of the Electrochemical Society* 154.12 (2007), B1242–B1251.

[30] Mazumder, S. and Cole, J. V. "Rigorous 3-D Mathematical Modeling of PEM Fuel Cells". In: *Journal of the Electrochemical Society* 150.11 (2003), A1503.

[31] Shimpalee, S. and Dutta, S. "Numerical prediction of temperature distribution in PEM fuel cells". In: *Numerical Heat Transfer, Part A: Applications* 38.1 (2000), pp. 111–128.

[32] Shen, Jun, Xu, Liang, Chang, Huawei, Tu, Zhengkai, and Chan, Siew Hwa. "Partial flooding and its effect on the performance of a proton exchange membrane fuel cell". In: *Energy Conversion and Management* 207 (2020), p. 112537. DOI: 10.1016/j.enconman.2020.112537.

[33] Atyabi, Seyed Ali and Afshari, Ebrahim. "Three-dimensional multiphase model of proton exchange membrane fuel cell with honeycomb flow field at the cathode side". In: *Journal of Cleaner Production* 214 (2019), pp. 738–748. DOI: 10.1016/j.jclepro.2018.12.293.

[34] Sun, H., Zhang, G. S., Guo, L. J., et al. "A study of dynamic characteristics of PEM fuel cells by measuring local currents". In: *International Journal of Hydrogen Energy* 34.13 (2009), pp. 5529–5536.

[35] Wang, Y. and Wang, C. Y. "Two-phase transients of polymer electrolyte fuel cells". In: *Journal of The Electrochemical Society* 154.10 (2007), B636–B643.

[36] Liao, Zihao, Wei, Lin, Dafalla, Ahmed Mohmed, Suo, Zhenbang, and Jiang, Fangming. "Numerical study of subfreezing temperature cold start of proton exchange membrane fuel cells with zigzag-channeled flow field". In: *International Journal of Heat and Mass Transfer* 165 (2021), p. 120733. DOI: 10.1016/j.ijheatmasstransfer.2020.120733.

[37] Amamou, A., Kandidayeni, M., Macias, A., Boulon, L., and Kelouwani, S. "Efficient model selection for real-time adaptive cold start strategy of a fuel cell system on vehicular applications". In: *International Journal of Hydrogen Energy* 45.38 (2020), pp. 19664–19675. DOI: 10.1016/j.ijhydene.2020.04.253.

[38] Xing, Lei et al. "Membrane electrode assemblies for PEM fuel cells: A review of functional graded design and optimization". In: *Energy* 177 (2019), pp. 445–464. DOI: 10.1016/j.energy.2019.04.084.

[39] Mukherjee, Partha P., Kang, Qin, and Wang, Chao-Yang. "Pore-scale modeling of two-phase transport in polymer electrolyte fuel cells – Progress and perspective". In: *Energy & Environmental Science* 4.2 (2011), pp. 346–369.

[40] Murschenhofer, M., Hacker, V., Bludszuweit, C., et al. "Impact of operating conditions on the performance of polymer electrolyte membrane fuel cells". In: *Journal of Power Sources* 375 (2018). Publisher: Elsevier, pp. 345–352.

[41] Corbo, P., Migliardini, F., and Veneri, O. "Hydrogen production and utilization for sustainable development". In: *World Journal of Science, Technology and Sustainable Development* 4 (2007). Publisher: Emerald, pp. 149–162.

[42] Corbo, P., Migliardini, F., and Veneri, O. "Sustainable energy: new developments". In: *World Journal of Science, Technology and Sustainable Development* 5 (2008). Publisher: Emerald, pp. 170–183.

[43] Piras, M., De Bellis, V., Malfi, E., Novella, R., and Lopez-Juarez, M. "Adaptive ECMS based on speed forecasting for the control of a heavy-duty fuel cell vehicle for real-world driving". In: *Energy Conversion and Management* 289 (2023), p. 117178. DOI: 10.1016/j.enconman.2023.117178.

[44] Molina, S., Novella, R., Pla, B., and Lopez-Juarez, M. "Optimization and sizing of a fuel cell range extender vehicle for passenger car applications in driving cycle conditions". In: *Applied Energy* 285 (2021). Publisher: Elsevier Ltd. DOI: 10.1016/j.apenergy.2021.116469.

[45] Abid, Raja. "Dynamic Performance of a PEM Fuel Cell System". In: *DTU Mechanical Engineering* (2013). ISBN: 9788774753599 Publisher: APA.

[46] Pei, P., Zeng, K., and Zhang, J. "Durability study of a high temperature PEM fuel cell". In: *Journal of Power Sources* 180.2 (2008), pp. 835–842.

[47] Desantes, J. M., Novella, R., Pla, B., and Lopez-Juarez, M. "A modeling framework for predicting the effect of the operating conditions and component sizing on fuel cell degradation and performance for automotive applications". In: *Applied Energy* 317 (November 2021 2022). Publisher: Elsevier Ltd, p. 119137. DOI: 10.1016/j.apenergy.2022.119137.

[48] Knights, S. *Polymer Electrolyte Membrane and Direct Methanol Fuel Cell Technology: 6 - Operation and durability of low temperature fuel cells*. Publication Title: Volume 1. Woodhead Publishing Limited, 2012. 137–177. DOI: 10.1533/9780857095473.2.137.

[49] Bi, Wu and Fuller, Thomas. F. "Temperature Effects on PEM Fuel Cells PtC Catalyst Degradation". In: *Journal of The Electrochemical Society* 155.2 (2008), B215. DOI: 10.1149/1.2819680.

[50] Dutta, M, Jia, N, Lu, S, Colbow, V, and Wessel, S. "Effects of Upper Potential Dwell Time, Transients and Relative Humidity on PEM Fuel Cell Cathode Catalyst Degradation". In: *The Electrochemical Society 217th Meeting (c)* (2010).

[51] Desantes, J.M., Novella, R., Pla, B., and Lopez-Juarez, M. "Effect of dynamic and operational restrictions in the energy management strategy on fuel cell range extender electric vehicle performance and durability in driving conditions". In: *Energy Conversion and Management* 266 (X 2022). Publisher: Elsevier Ltd, p. 115821. DOI: 10.1016/j.enconman.2022.115821.

Chapter 5

From Combustion to Electrification: A Deep Dive into Powertrains for HEVs, FCHEVs and BEVs

In the first chapter, the urgent need for decarbonization in the transportation sector was explored. It was determined that a notable transition towards sustainable alternatives is necessary for the effective mitigation of climate change. The current chapter aims to investigate the evolution of vehicles, with a particular emphasis on the role played by hybrid, fuel cell, and battery electric vehicles in propelling this transformative process.

To prevent any confusion between "*electric*" and "*electrified*" vehicles, a concise clarification is provided before proceeding with the discussion. In general, an electric powertrain refers to a battery electric vehicle, which exclusively relies on an electric motor for propulsion. It should be noted that electric powertrains also encompass fuel-cell electric vehicles. On the other hand, an electrified powertrain encompasses not only BEVs but also vehicles that combine an ICE with varying degrees of electrification. These include mild hybrid electric vehicles, full hybrid electric vehicles, and plug-in hybrid electric vehicles. Further elaboration on the distinctions between these hybrid vehicle types will be provided later in this chapter. For a concise overview, refer to Table 5.1.

Table 5.1: Overview of the various vehicle types discussed in this chapter.

Type	**Acronym**	**ICE included**	**Features**
Internal combustion engine vehicle	ICEV	Yes	Full internal combustion engine driving
Micro hybrid electric vehicle	HEV	Yes	Stop/start technology
Mild hybrid electric vehicle	MHEV	Yes	HEV + regenerative braking for energy recovery and electric torque assistance (assist acceleration from stop)
Full hybrid electric vehicle	FHEV	Yes	MHEV + electric driving with battery charged from the ICE
Plug-in hybrid electric vehicle	PHEV	Yes	FHEV + electric driving with battery charged from the grid
Extended range electric vehicle	EREV	Yes	PHEV, but the ICE is only used as a generator to recharge the battery
Battery electric vehicle	BEV	No	Full electric driving with battery charged from the grid
Fuel-cell electric vehicle	FCEV	No	Full electric driving with hydrogen fuel cell producing electricity

5.1 Optimizing Performance and Sustainability: the Potential of HEVs

As demonstrated in Chapter 1, a significant portion of the global vehicle fleet will still be powered by internal combustion engines until 2050. Hybrid vehicles, therefore, serve as a bridge between conventional vehicles and electric vehicles, aiming to extract the maximum efficiency from these two technologies until a sustainable electric transition can be fully realized. By integrating an internal combustion engine with electric motors and batteries, hybrids can optimize fuel consumption and reduce emissions. This hybridization approach allows for a more gradual and sustainable shift towards electrification, considering the current limitations in charging infrastructure, battery technology, and the overall readiness of the electrical grid. They achieve improved fuel efficiency and reduced emissions by utilizing electric power during low-load conditions and regenerative braking, effectively harnessing energy that would otherwise be wasted. Furthermore, hybrid vehicles provide drivers with the flexibility of an extended driving range and the convenience of refueling at existing gasoline stations. This addresses concerns regarding range anxiety and the limited availability of electric charging infrastructure. Hybrids also offer a smoother transition for consumers who may not be fully prepared or financially ready to switch to fully electric vehicles.

Their development and evolution have been a fascinating journey. One significant milestone in this journey can be traced back to the early 20th century when Ferdinand Porsche, the renowned automotive engineer, created the world's first hybrid vehicle. In 1900, he introduced the "Semper Vivus," which translates to "Always Alive" in Latin, as the world's first functional hybrid vehicle. This groundbreaking creation integrated an internal combustion engine with electric motors, marking a significant departure from the traditional gasoline-powered vehicles of the time. The Semper Vivus featured two generators driven by a combustion engine, which charged a bank of lead-acid batteries. These batteries, in turn, powered the vehicle's electric motors, providing additional propulsion alongside the internal combustion engine. This innovative concept aimed to enhance efficiency and reduce the reliance on fossil fuels, even in the early days of the automotive industry. Following Porsche's pioneering efforts, early hybrid vehicle developments faced several challenges, primarily due to limitations in battery technology and the relative simplicity of combustion engines. Despite the potential benefits of hybridization, these early prototypes were often overshadowed by the growing popularity and advancements in purely gasoline-powered vehicles. It was not until the late 20th century, driven by mounting environmental concerns and the need

for energy efficiency, that hybrid vehicles experienced a resurgence in interest. Environmental issues, such as air pollution and greenhouse gas emissions, coupled with the desire for reduced dependence on fossil fuels, became key catalysts for renewed efforts in hybrid technology. Advancements in battery technology, particularly the development of more efficient and durable rechargeable batteries, played a pivotal role in enabling the modern hybrid vehicles we see today. The emergence of advanced power electronics, regenerative braking systems, and sophisticated control algorithms further contributed to the viability and performance of hybrid vehicles. The 21st century witnessed a significant shift in the automotive industry towards hybrid technology. Major automakers recognized the potential of hybrid vehicles as a sustainable and efficient mobility solution. This led to the development and mass production of hybrid models, which gradually became more accessible to the general public.

Building upon these considerations, this section provides a comprehensive description of the classification of major architectures of hybrid vehicles, taking into account their varying configurations and operational characteristics. Additionally, the section delves into the challenges faced by ICE-based hybrid electric vehicles and explores future considerations to address their challenges and enhance their performance and sustainability. By examining the current landscape of hybrid technologies and exploring potential advancements, this section aims to provide valuable insights and guidance for the continued development and deployment of hybrid electric vehicles powered by internal combustion engines.

5.1.1 Architectures of ICE-Based Hybrid Electric Vehicles

The classification of hybrid vehicle architectures constitutes a fundamental aspect in understanding the diverse range of designs and configurations adopted in this field. This classification framework enables the categorization of hybrid vehicles based on two critical factors: the positioning of the electric machine within the vehicle and the power capacity of the electric machine. By exploring these distinct architectures, valuable insights can be gained into the engineering decisions made by manufacturers to attain optimal performance and efficiency. Consequently, a comprehensive examination of these architectures provides a solid foundation for comprehending the integration of ICEs and electric powertrains in hybrid vehicles.

Classification according to the electric machine power

The following categories represent the main classifications according to the electric machine power:

- Mild Hybrid
- Full Hybrid
- Plug-in Hybrid
- Extended range electric vehicle

The mild hybrid architecture features a relatively low-power electric machine, typically providing supplemental assistance to the ICE. The electric machine in this configuration assists in specific driving conditions, such as during acceleration or low-load operations, to reduce fuel consumption and enhance overall efficiency. Although the electric machine in a mild hybrid does not solely propel the vehicle, it contributes to improved fuel economy and reduced emissions.

The full hybrid architecture incorporates a more powerful electric machine capable of independently propelling the vehicle, operating in tandem with the ICE, or a combination of both. This allows for a wider range of electric driving modes, including all-electric operation, regenerative braking, and seamless power transitions between the electric and ICE power sources. Full hybrids offer significant fuel efficiency benefits and the potential for reduced emissions, particularly in urban driving conditions where electric operation is more prevalent.

The plug-in hybrid architecture represents an advanced form of hybridization that enables external charging of the vehicle's battery pack. PHEVs feature a higher-capacity electric machine and a larger battery pack, allowing for extended all-electric driving ranges. This configuration offers the flexibility of operating in both hybrid mode and pure electric mode, depending on the driving conditions and the battery's state of charge. By utilizing grid electricity, PHEVs can achieve substantial reductions in fuel consumption and tailpipe emissions, particularly during shorter commutes and urban driving.

Extended Range Electric Vehicles are a type of electrified vehicle that combines the benefits of both electric and conventional powertrains. Unlike other electric vehicles, EREVs are equipped with an onboard gasoline engine or a hydrogen fuel cell that serves as a generator to charge the vehicle's battery pack. This extended range feature allows EREVs to overcome the limitations of pure electric vehicles by providing an extended driving range without relying solely on charging infrastructure. When the battery charge depletes, the

gasoline engine or fuel cell kicks in, providing continuous power generation to sustain the electric motor. This unique design offers the advantage of reduced range anxiety and increased flexibility for long-distance travel, making EREVs a viable option for those seeking a greener alternative with extended driving capabilities.

Classification according to the electric machine position

In addition to electric machine power, the position of the electric machine within the hybrid vehicle architecture also plays a crucial role in determining its performance and functionality. The classification based on the electric machine position provides insights into the integration and power flow between the electric machine and the ICE. The following categories represent the main classifications according to the electric machine position:

- Series hybrid
- Parallel hybrid
- Series/parallel hybrid

In a series hybrid architecture, the electric machine solely propels the vehicle, while the ICE acts as a generator to recharge the battery or provide supplemental power. This configuration allows for efficient power generation and flexibility in optimizing the ICE's operating conditions for improved fuel efficiency. Series hybrids excel in applications that prioritize all-electric operation and reduced emissions, such as urban driving or stop-and-go traffic.

The parallel hybrid architecture combines the power from the electric machine and the ICE, with both power sources capable of propelling the vehicle simultaneously. This configuration allows for seamless blending of electric and ICE power, providing enhanced acceleration, increased power output, and improved overall performance. Parallel hybrids offer versatility in power distribution, allowing the vehicle to operate in different modes depending on the driving conditions and power demands.

The series/parallel hybrid architecture combines elements of both series and parallel configurations, offering a balance between all-electric driving capabilities and ICE power. This configuration allows for efficient power distribution and optimization based on driving conditions, ensuring optimal performance and fuel efficiency. Series/parallel hybrids provide the versatility of utilizing both the electric machine and the ICE to meet power demands while maintaining the benefits of electric operation and reduced emissions.

5.1.2 Challenges and Future Considerations of ICE-Based Hybrid Electric Vehicles

While ICE-based hybrid electric vehicles offer significant benefits in terms of efficiency and reduced emissions, their long-term sustainability poses certain challenges. As the automotive industry continues to transition towards electric mobility, the future viability of ICE-based hybrid architectures must be carefully examined. This section explores the key challenges associated with the long-term sustainability of ICE-based hybrid architectures and discusses potential solutions and advancements needed to address them.

Long-Term Sustainability of ICE-Based Hybrid Architectures

Optimizing the performance of the ICE is a fundamental challenge in ICE-based hybrid architectures. Since hybrid vehicles rely on the ICE for power generation and supplementary propulsion, improving its efficiency and reducing its environmental impact is paramount. Ongoing research is focused on advanced engine technologies such as downsizing, turbocharging, and advanced combustion strategies, all aimed at enhancing the efficiency and reducing emissions of ICE-based hybrid vehicles. Furthermore, exploring alternative fuels and powertrain configurations can contribute to the long-term sustainability of ICE-based hybrid architectures.

The development of advanced battery technologies is a crucial factor in ensuring the long-term sustainability of ICE-based hybrid architectures. The performance, energy storage capacity, and durability of batteries have a significant impact on the overall efficiency and viability of hybrid electric vehicles. Research efforts are directed towards improving battery energy density, reducing charging times, enhancing cycle life, and ensuring the recyclability of battery materials. Advancements in battery technology, including the development of solid-state batteries and the exploration of alternative materials, hold promise for further enhancing the performance and sustainability of ICE-based hybrid architectures.

In order to enhance the sustainability of ICE-based hybrid architectures, the integration of renewable energy sources plays a vital role. By incorporating solar panels or other renewable energy generation systems, hybrid vehicles can harness clean energy to charge their batteries or directly power their electric components. This integration reduces reliance on fossil fuels, minimizes greenhouse gas emissions, and contributes to the overarching goal of creating a greener transportation system. By embracing renewable energy, ICE-based hybrid architectures can foster greater environmental responsibility and pave the way for a more sustainable future.

Role of Hybrid Vehicles in the Transition to Electric Mobility

As previously discussed, hybrid vehicles play a pivotal role as a transitional solution between conventional internal combustion engine vehicles and fully electric vehicles. In the journey towards a more sustainable future, hybrids offer a compelling combination of electric propulsion and the existing infrastructure of conventional vehicles. By reducing fuel consumption and emissions, they serve as a catalyst for a seamless transition to full electrification, introducing consumers to electric drivetrain technology and expanding charging infrastructure and they actively contribute to the reduction of greenhouse gas emissions. Through the intelligent utilization of electric power in specific driving conditions and the optimization of internal combustion engine performance, hybrids significantly curtail tailpipe emissions compared to their conventional counterparts. This reduction plays a crucial role in mitigating the environmental impact of transportation and aligns with global endeavors to combat climate change. Moreover, hybrid vehicles offer a remarkable degree of flexibility and adaptability to accommodate diverse driving conditions and consumer preferences. The ability to seamlessly switch between electric mode, hybrid mode, or solely rely on the internal combustion engine empowers drivers to optimize efficiency, range, and power output based on their specific needs. This versatility makes hybrid vehicles highly appealing to consumers who seek a harmonious blend of environmental sustainability and practicality.

5.2 Exploring FCHEVs: A Promising Path to Clean and Green Mobility

Hydrogen fuel cell vehicles represent a highly promising and transformative technology in the realm of sustainable transportation. These vehicles utilize advanced fuel cell systems as their primary power source, employing electrochemical conversions to generate electricity from the reaction between hydrogen and oxygen. The resulting chemical reaction within the fuel cell produces pure water as the sole byproduct, thereby providing no tailpipe emissions.

The history of fuel cell vehicles can be traced back to the early 19th century when the first fuel cell concept was proposed by Sir William Grove, a British scientist. However, it wasn't until the mid-20th century that significant advancements in fuel cell technology paved the way for practical applications in transportation. In the 1960s, General Electric developed the first practical fuel cell system for NASA's space program. These fuel cells powered the Gemini and Apollo spacecraft, demonstrating the reliability and efficiency of this emerging technology. The success of fuel cells in space exploration sparked

interest in utilizing them for terrestrial applications, including transportation. Throughout the 1970s and 1980s, researchers and engineers continued to refine fuel cell technology for automotive use. Companies such as Ballard Power Systems and Toyota made significant contributions to the development of fuel cell vehicles during this period. However, challenges related to cost, durability, and the lack of hydrogen infrastructure limited widespread commercialization. In the late 1990s and early 2000s, fuel cell vehicles gained attention as a potential solution to address environmental concerns and reduce dependence on fossil fuels. Major automakers, including Toyota, Honda, and Hyundai, invested in research and development efforts to advance fuel cell technology and bring fuel cell vehicles to the market. The year 2015 marked an important milestone in the history of fuel cell vehicles when Toyota launched the Mirai, the world's first mass-produced fuel cell electric vehicle. This landmark achievement signaled a significant step forward in making fuel cell vehicles accessible to a broader consumer base. Since then, fuel cell vehicle technology has continued to evolve, with ongoing improvements in performance, efficiency, and durability. Advancements in hydrogen production, storage, and infrastructure development have also contributed to the growing viability and adoption of fuel cell vehicles.

One of the key advantages of fuel cell vehicles over their conventional counterparts is their capability to produce zero tailpipe emissions, making them pivotal in combatting climate change and addressing air pollution concerns, particularly in densely populated urban areas. The absence of greenhouse gas emissions and other harmful pollutants during operation significantly contributes to reducing atmospheric pollution, improving local air quality, and safeguarding public health. This unique characteristic establishes FCVs as an attractive alternative for both individual consumers and policymakers seeking to transition to a more sustainable and eco-friendly transportation system.

In addition to their substantial environmental benefits, fuel cell vehicles also offer enhanced energy efficiency when compared to conventional vehicles. By employing electrochemical conversion, FCVs are able to achieve higher energy conversion efficiencies, resulting in improved fuel economy. This improved efficiency translates to extended driving ranges and reduced dependence on frequent refueling, offering a more convenient and practical experience for vehicle users. Furthermore, the inherent characteristics of fuel cell technology contribute to the smooth and quiet operation of FCVs, providing a serene and enjoyable driving experience for occupants.

The primary objectives driving the development and deployment of fuel cell vehicles revolve around optimizing efficiency and minimizing costs. In terms of efficiency, FCVs aim to maximize the conversion of the chemical energy stored in hydrogen into electrical energy, while minimizing energy losses

during the electrochemical process. This pursuit of efficiency encompasses advancements in fuel cell materials, designs, and system configurations, all aimed at optimizing the performance, range, and overall operational capabilities of FCVs. By continually pushing the boundaries of efficiency, fuel cell vehicles offer the potential for extended driving ranges, reduced energy consumption, and increased overall sustainability.

5.2.1 Fuel Cell Vehicle Architecture

Fuel cell vehicles exhibit various topologies and hybridization options, each offering unique configurations and advantages. These categories include:

1. **Full FC Vehicles**: Full FC vehicles solely rely on a fuel cell stack as their primary energy source. With a simple structure consisting of a fuel tank, FC stack, DC-DC power converter, inverter, and electric motor, these vehicles provide numerous benefits. They boast a high driving range, fast charging time, high efficiency, cold start capability, silent operation, continuity in energy supply, and low emissions. Full FCEVs find applications in various low-speed vehicles, such as forklifts, buses, airline vehicles, trams, and marine vehicles.

2. **FC + Battery Hybridization**: FC + battery hybridization combines fuel cells with battery units. In this topology, a unidirectional DC-DC converter connects the FC to the DC bus, while a bidirectional DC-DC converter links the battery to the system. During startup, the battery assists by providing a high current to start the electric motor and prevent the FC from operating in low-efficiency zones. Once the vehicle is in motion, the FC takes over to maintain the operation of the electric motor, with the battery charging as required.

3. **FC + UC Hybridization**: FC + UC hybridization replaces the battery with an ultracapacitor (UC). The UC serves the purpose of meeting transient power demands in sudden situations. However, due to its lower energy density, the UC is not used as a permanent energy source.

4. **FC + Battery + UC Hybridization**: FC + Battery + UC hybridization incorporates both a battery and an ultracapacitor as supplementary energy storage units. The FC connects to the DC bus through a unidirectional DC-DC converter, while bidirectional DC-DC converters link the battery and UC. This topology combines the advantages of FC + battery and FC + UC systems, providing continuous energy and enhancing the FC's dynamic response during transient events.

5. **FC + Battery + PV Hybridization**: In recent years, FC-based electric vehicles have been integrated with photovoltaic (PV) panels for hybridization. This topology, known as FC + Battery + PV hybridization, involves PV panels generating DC voltages that are connected to the DC bus using a unidirectional converter. The FC serves as the primary energy source, while the PV panel acts as an additional energy generator. The battery, connected through a bidirectional converter, stores excess energy generated by the PV panels or supplies power directly to the electric motor as needed.

6. **FC + Flywheel Hybridization**: Another hybridization option is FC + flywheel hybridization, which incorporates a flywheel as an alternative energy storage device to batteries. The flywheel stores mechanical energy at high rotational speeds and converts it into electricity through a generator to support high-energy demands. Flywheels offer advantages such as high-speed charging capability, high efficiency, high power rating, environmental friendliness, wide temperature operation range, high energy storage capacity, and long lifespan.

7. **FC + SMES Hybridization**: FC + SMES hybridization involves the utilization of superconducting magnetic energy storage (SMES) alongside the FC stack. SMES stores energy through a magnetic field created by a direct current flowing through a superconducting coil. While still under investigation for hybrid FCEV applications, SMES demonstrates shorter charging and discharging times compared to other storage technologies, high charge/discharge cycles, and a high power conversion ratio. However, the current high cost of SMES restricts its widespread application in FCEVs.

The size of the fuel cell and battery in a FCHEV significantly impact the overall vehicle performance, including fuel economy, driveability, and observed rates of fuel cell degradation. An undersized fuel cell may undergo accelerated aging of the fuel cell membrane and catalyst due to excessive heat and transient loading. The literature proposes various methods for designing the architecture and sizing of FCHEVs, as seen in studies by Xu et al. [1], Fletcher et al. [2], and Gaikwad et al. [3].

In the context of heavy-duty applications, the inherent modularity of fuel cell powertrains emerges as a notable advantage. Peng et al.'s comprehensive investigation [4] explores multi-fuel cell systems tailored for heavy-duty use, featuring 110 kW fuel cells. This prompts a keen interest in determining the optimal power configuration for seamlessly integrating fuel cell systems into

heavy-duty vehicles. Notably, the prevailing trend in fuel cell trucks leans towards an equal-power fuel cell system architecture, as evidenced by recent developments [5].

Modern sizing analyses predominantly prioritize consumption as a pivotal metric for evaluating performance efficiency and cost-effectiveness [6]. Consequently, there is a significant opportunity to quantify consumption concerning the power rating of each individual fuel cell system. This effort holds promise for manufacturers in the transportation sector, facilitating the identification of optimal power distribution tailored to diverse heavy-duty applications. Moreover, a nuanced understanding of production cost is essential for a comprehensive evaluation of the total cost associated with any powertrain. Examining the intricate interplay between component size and lifespan can yield invaluable insights for achieving an optimal configuration. Cox et al.'s work [7] contributes a comparative study scrutinizing both cost (TCO) and emissions (LCA), providing nuanced perspectives that enrich the ongoing scientific discourse in this domain.

5.2.2 Challenges and future aspects of FCVs

Fuel cell technologies for automotive applications still face significant technical challenges, despite the notable progress achieved in recent years. Overcoming these obstacles requires extensive collaboration between automotive manufacturers and researchers in key areas such as hydrogen production, hydrogen storage solutions, FC durability, reliability, and safety measures. Additionally, reducing the high costs associated with FCEVs is essential for their wider adoption. However, considering the numerous advantages of hydrogen-powered FCEVs discussed earlier, it is expected that the demand for these vehicles will increase once these challenges are addressed.

To ensure the future success of FCEVs, it is crucial to enhance the security of hydrogen use and establish an accessible network of hydrogen refueling stations. These factors play a significant role in driving consumer preference for FCEVs. As a result, passenger car manufacturers are likely to increase their production to meet the growing demand in the global transportation industry. This increase in production will lead to higher investments in FCEV technology and accelerate further advancements. With continuous technological developments, increased investments, and supportive incentives, FCEVs are expected to gain a more significant market share in the coming years.

Advancements in hydrogen production techniques, as well as improvements in FC and battery components, are expected to reduce the production costs of hydrogen FCEVs. Consequently, production will rise to meet the increasing demand. The market size of hydrogen FC-based vehicles, valued at $651.9

million in 2018, is projected to reach $42,038.9 million by 2026 [8, 9]. Several factors contribute to this growth, including rising environmental concerns, government initiatives to improve hydrogen FC infrastructure, initial investments, and technological progress. Each of these factors will have a significant impact on the number of vehicles produced and contribute to the overall market expansion.

Projected data on the number of FCEVs from 2013 to 2030, divided by regions such as North America, Europe, and Asia-Pacific, shows a consistent annual increase in FC-based electric vehicle production. While the number of FCEVs was only 20 in 2013, it reached 11,900 in 2018, and it is anticipated to reach approximately 31,000 by the end of 2020, marking a 160% increase compared to 2018. By 2030, the projected total number of FCEVs is estimated to be 582,400, indicating a remarkable 1,784% increase over the next decade [10]. This surge in electric vehicle adoption will undoubtedly drive the demand for hydrogen in the coming years.

Researchers are actively exploring various methods for hydrogen production, including steam treatment, waste gas purification, and electrolysis. Simultaneously, efforts are being made to develop effective hydrogen storage solutions. FCs, which convert hydrogen and oxygen into electricity, offer an efficient energy generation method, particularly for passenger cars. Consequently, ensuring easy access to hydrogen for storage and usage is a vital aspect of the marketing strategy for FCEVs. The availability of a well-established network of hydrogen refueling stations will significantly impact the adoption rates of FCEVs. Therefore, it is expected that the number of hydrogen refueling stations will increase alongside the anticipated growth in the global vehicle population.

5.3 Electrifying the Road: the Potential of BEVs in Sustainable Transportation

BEVs have emerged as a promising solution to address the environmental impact of transportation. This section provides an overview of BEVs, their advantages and disadvantages. In fact, while BEVs offer numerous advantages, it is important to recognize their current limitations in terms of battery production and disposal, as well as their dependence on non-renewable energy sources. The concept of electric vehicles dates back to the early 19th century, but significant advancements in battery technology were made in the late 20th century. The development of rechargeable lithium-ion batteries revolutionized the automotive industry, allowing for longer driving ranges and increased efficiency. This breakthrough marked a turning point for BEVs, enabling them to compete with

conventional internal combustion engine vehicles. Despite initial challenges such as limited range and a lack of charging infrastructure, continuous research and development efforts, coupled with government initiatives and increased public awareness of environmental concerns, have led to substantial improvements. Modern BEVs now offer extended ranges, faster charging times, and enhanced performance, making them a viable alternative to traditional vehicles. However, BEVs also face environmental challenges. The production and disposal of lithium-ion batteries contribute to pollution and resource depletion. The extraction of minerals used in battery production, such as lithium and cobalt, often involves environmentally damaging mining practices. Additionally, the recycling and safe disposal of used batteries remain complex processes that require further attention. Another critical aspect to consider is the source of electricity used to power BEVs. While electric vehicles themselves produce zero tailpipe emissions, the electricity generation process may rely heavily on non-renewable energy sources such as coal or natural gas. This reliance on fossil fuels for electricity generation hinders the overall decarbonization impact of BEVs. To address these challenges, a holistic approach to decarbonization is essential. Ongoing research aims to develop more sustainable and efficient batteries, improving the environmental impact of battery production. Efforts are also being made to enhance recycling processes and ensure the safe disposal of used batteries. Furthermore, transitioning to renewable energy sources for electricity generation is vital. Investing in renewable energy infrastructure, such as solar and wind power, can ensure a greener energy mix for charging electric vehicles.

5.3.1 Electric vehicles Architecture

In the past, electric vehicles EVs were primarily created by converting existing internal combustion engine vehicles by replacing the engine and fuel tank with an electric motor and battery pack. However, this approach had several drawbacks, including increased weight, limited flexibility, and performance degradation, leading to a decline in its popularity. In contrast, modern EVs are designed from the ground up with original body and frame designs, tailored to meet the specific requirements of electric propulsion.

A contemporary electric drivetrain can be conceptualized as consisting of three main subsystems: electric motor propulsion, energy source, and auxiliary components. The electric propulsion subsystem includes a vehicle controller, power electronic converter, electric motor, mechanical transmission, and driving wheels. The energy source subsystem encompasses the energy source itself, an energy management unit, and an energy refueling unit. The auxiliary

subsystem comprises the power steering unit, HVAC, and auxiliary power supply.

The vehicle controller receives inputs from the accelerator and brake pedals and sends appropriate control signals to the electronic power converter. The power converter regulates the power flow between the electric motor and energy source, allowing for the transfer of energy during regenerative braking. The energy management unit works in conjunction with the vehicle controller to control regenerative braking and energy recovery, while also managing the refueling unit and monitoring the usability of the energy source. The auxiliary power supply ensures that all EV auxiliary components, especially the HVAC and power steering units, receive the necessary power at various voltage levels.

There are various EV configurations depending on the characteristics of the electric propulsion and energy sources. These configurations include:

- Replacing the internal combustion engine with an electric motor in a conventional vehicle drivetrain. This configuration typically includes an electric motor, clutch, gearbox, and differential. The clutch allows for the connection or disconnection of power from the electric motor to the driven wheels, while the gearbox provides gear ratios to match the load requirements.

- Using an electric motor with constant power in a wide speed range eliminates the need for a multispeed gearbox and clutch. A fixed gearing system can be employed instead, simplifying the drivetrain and reducing its size and weight.

- Further simplification and compactness can be achieved by integrating the electric motor, fixed gearing, and differential into a single assembly, with both axles connecting to the driving wheels.

- Instead of a mechanical differential, two traction motors can be used, with each motor driving one side wheel and operating at different speeds during cornering.

- The traction motor can be placed inside a wheel, creating an in-wheel drive configuration. A thin planetary gear set may be employed to reduce motor speed and enhance torque, providing high-speed reduction and inline shaft arrangement.

- In an advanced configuration, the mechanical gearing between the electric motor and driving wheel is completely eliminated. The out-rotor of a low-speed electric motor in the in-wheel drive is directly connected to the

driving wheel, with the electric motor's speed control directly controlling the vehicle's speed. However, this arrangement requires the electric motor to have higher torque for vehicle starting and acceleration.

These various configurations offer different advantages in terms of simplicity, compactness, torque distribution, and control. The choice of EV configuration depends on factors such as the intended application, performance requirements, and design priorities. Overall, the shift from retrofitting ICEVs to purpose-built EVs has allowed for greater flexibility in design and improved performance. With ongoing advancements in electric propulsion technology and energy sources, the future of EVs holds the promise of even more innovative and efficient configurations.

5.3.2 Advantages and Challenges

This paragraph provides a non-exhaustive list of the advantages and disadvantages of BEVs.

The electric advantage

- **Zero Exhaust Emissions**: Electric vehicles do not have tailpipes, resulting in no direct emissions during operation. This can lead to cleaner air quality and potentially reduce the overall carbon footprint, depending on factors such as battery production and electricity sources.
- **Reduced Noise**: Unlike conventional vehicles, electric cars are notably quiet at lower speeds due to the absence of a combustion engine. This can contribute to a quieter environment, particularly in urban areas. However, it's important to consider the safety implications, as pedestrians, especially those with impaired vision, may have difficulty detecting silent EVs. To address this, artificial noise generation has been mandated in certain regions.
- **Renewable Energy Potential**: The electricity used to charge EVs can be sourced from renewable energy generation, such as solar, wind, or hydropower. Utilizing renewable energy further reduces the carbon footprint associated with EVs and supports sustainability efforts.
- **Higher Efficiency**: Electric vehicles are significantly more energy-efficient compared to internal combustion engine vehicles. They convert a higher percentage of electrical energy from the grid into power at the wheels, resulting in improved efficiency. In contrast, conventional vehicles waste a significant portion of energy through heat dissipation.

- **Cost Savings**: Charging an electric vehicle with electricity is generally cheaper than refueling a conventional vehicle with gasoline. This can result in long-term cost savings for EV owners, especially considering the potential volatility of fuel prices.
- **Lower Maintenance**: EVs typically require less routine maintenance compared to ICEVs. With fewer moving parts and no need for oil changes, maintenance tasks are simplified. Additionally, regenerative braking in EVs reduces wear on traditional brakes.
- **Acceleration Performance**: Electric cars offer instant torque, providing quick acceleration and responsive performance. This advantage is particularly noticeable during 0–100 km/h sprints, where EVs can often outperform their conventional counterparts.
- **Convenient Charging at Home**: For individuals with a suitable home charging setup and a manageable daily commute, EVs offer the convenience of charging at home. This eliminates the need for frequent stops at gas stations, enhancing the overall user experience.

The electric disadvantage

- **Cost**: Currently, electric cars are considerably more expensive than conventional vehicles or hybrids. Many electric car models fall into the luxury segment and do not have a comparable internal combustion engine model, such as the Tesla Model S, Porsche Taycan, Mercedes-Benz EQ, and Lucid Air EV. However, it is expected that the price gap between different types of cars will narrow as technology continues to evolve. Battery prices have already experienced significant declines over the past decade and this downward trend is projected to continue.
- **Range anxiety**: Although the range of BEVs has substantially improved over the past decade, the median range of all-electric vehicles is still considerably lower than that of conventional internal combustion engine vehicles. The combination of limited range, longer charging times, and inadequate infrastructure can make it challenging to rely solely on a BEV for all driving needs. One potential solution to address range anxiety is the concept of "battery swapping." This approach allows for the immediate exchange of a discharged battery for a fully charged one.
- **Charging Infrastructure**: The availability and accessibility of charging infrastructure are essential factors influencing the adoption of electric vehicles. While there has been significant progress in expanding charging

networks, especially in urban areas, challenges still exist. Many potential electric vehicle owners are concerned about the availability of charging stations and the time required to charge their vehicles. The availability of charging stations varies depending on the region. Urban areas generally have a more extensive charging infrastructure compared to rural or remote locations. However, efforts are underway to expand charging networks and improve accessibility. Governments, utility companies, and private companies are investing in the installation of public charging stations along highways, in parking lots, and at other convenient locations.

- **Charging time**: Currently, there are three main types of charging options for electric vehicles: Level 1, Level 2, and DC Fast Charging (also known as Level 3). Level 1 charging uses a standard household outlet and provides the slowest charging speed, typically adding 2-5 miles of range per hour of charging. Level 2 charging requires a dedicated charging station and provides faster charging speeds, adding around 10-30 miles of range per hour of charging. DC Fast Charging is the fastest option and can provide a significant range boost in a short period, typically adding 60-80 miles of range in just 20 minutes of charging.

- **Mining**: Amnesty International raised concerns about unethical cobalt mining in the Congo, exposing human rights abuses and child labor [11]. Although some improvements have been made, these issues persist. Arthur D. Little's assessment highlights the global environmental impacts of mining for BEV raw materials, particularly affecting rural and disadvantaged communities near mines [12]. The World Economic Forum's Global Battery Alliance proposes steps for a socially responsible and environmentally sustainable battery industry, including supply chain standards and transparent mining practices [13].

- **Weather**: Extreme weather significantly impacts the range and charging of battery-powered vehicles. Tests conducted by the Norwegian Automobile Federation in winter conditions revealed an average loss of nearly 20% in range for BEVs, along with longer charging times [14]. A study by Car and Driver on a 3°C day showed that HVAC settings can further reduce the range, with a 15% decrease at 22°C and a 26% decrease with HVAC on full blast and heated seats activated [15]. Analysis by Geotab demonstrated that temperature variations have a direct effect on range, with a 2019 Chevrolet Bolt achieving the most range at 22°C and reduced ranges at higher and lower temperatures [16]. Another study measured the impact of cold weather on charge time for DC fast chargers, showing a significant deterioration in charging efficiency in colder temperatures,

with state of charge ranging from 49% to 74% after a 30-minute charge in different regions of the USA [17].

5.4 Simulation of vehicles

In the preceding sections, it has been observed that the current and future landscape of the global vehicle fleet is vast and complex, as it encompasses various technologies and design choices. In this context as well, simulations can assist in overcoming the barriers of costs and development timelines. Indeed, vehicle simulations play a pivotal role in both industry and scientific research, serving as a cornerstone of investigation and analysis. Their significance lies in their ability to provide a comprehensive understanding of vehicle behavior and performance, offering a multitude of advantages for advancing automotive engineering and exploring new frontiers in transportation. In the realm of industry, vehicle simulations assume a paramount position in the design and optimization process. By leveraging sophisticated computational models and algorithms, engineers can evaluate and refine vehicle designs before physical prototypes are constructed. This enables them to identify potential design flaws, optimize performance parameters, and enhance overall efficiency. The ability to conduct virtual testing and analysis not only expedites the development timeline but also allows for cost-effective exploration of numerous design configurations, materials, and systems. Furthermore, simulations facilitate the progression of cutting-edge vehicle technologies. They serve as a testing ground for novel concepts, including electric powertrains, autonomous driving systems, and advanced driver-assistance systems. Through the simulation of various driving scenarios and conditions, researchers can assess the behavior and performance of these technologies, unravel their limitations, and formulate strategies to overcome challenges. Simulations also play a crucial role in predicting the real-world impact of emerging technologies on critical aspects such as vehicle performance, energy consumption, emissions, and safety. In the realm of scientific research, vehicle simulations act as a catalyst for in-depth investigations and explorations. They enable researchers to delve into complex phenomena within vehicles, such as aerodynamics, vehicle dynamics, and thermal management. By simulating and analyzing these intricate interactions, a deeper understanding of fundamental principles can be achieved, enabling the development of more accurate mathematical models and theoretical frameworks. Moreover, simulations serve as a powerful tool for studying energy efficiency and environmental impacts in the automotive domain. By simulating different vehicle configurations and driving scenarios, researchers can assess the effectiveness of energy-saving strategies, evaluate the impact of alternative

fuels and powertrain technologies, and optimize overall energy consumption and emissions. These simulations not only provide valuable insights into the potential benefits of sustainable transportation solutions but also contribute to the advancement of environmental stewardship.

Starting from these considerations and within the context described in Chapter 1, during this PhD work, a vehicle model for a light-duty HEV has been developed. Additionally, the existing model for a heavy-duty FCHEV, previously developed in the context of an other PhD thesis, has been further enhanced as part of this study to facilitate the development of advanced energy management strategies (which will be discussed in Chapter 6). In the remainder of this chapter, the main equations necessary for describing the longitudinal dynamics of the vehicle are first recalled. Subsequently, the model of the parallel P3 HEV vehicle and the improved heavy-duty FCHEV model are described.

5.4.1 Vehicle longitudinal dynamics and components modeling

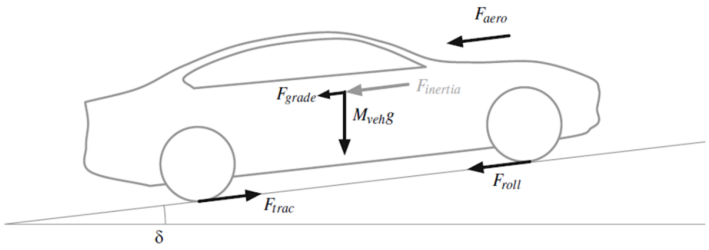

Figure 5.1: Longitudinal forces acting on the vehicle. Source: [18]

The vehicle's longitudinal dynamics can be described by simplifying it as a point mass, considering the forces acting on the vehicle along the longitudinal axis. Figure 5.1 illustrates these forces.

The vehicle dynamic equation can be expressed through the equilibrium of forces, as follows:

$$m_{\text{veh}} \frac{dv_{\text{veh}}}{dt} = F_{\text{inertia}} = F_{\text{trac}} - F_{\text{roll}} - F_{\text{aero}} - F_{\text{grade}} \tag{5.1}$$

In Equation 5.1, m_{veh} represents the effective mass, and v_{veh} represents the longitudinal velocity. F_{inertia} represents the inertial force, which is positive when the vehicle is accelerating and negative when decelerating. On the right-hand side of Equation 5.1, the first term, F_{trac}, represents the tractive force

generated by the powertrain (F_{pwt}) or during braking phases (F_{brake}) at the wheels. F_{roll} accounts for rolling resistance, considering tire deformation and losses. It can be expressed as shown in Equation 5.2, depending on the rolling resistance coefficient (c_{roll}), gravitational acceleration (g), vehicle mass (m_{veh}), and road slope (δ):

$$F_{\text{roll}} = c_{\text{roll}} m_{\text{veh}} g \cos \delta \tag{5.2}$$

In Equation 5.2, the term ($m_{\text{veh}} g \cos \delta$) represents the vertical component of the weight. The rolling resistance coefficient (c_{roll}) can be assumed constant or dependent on factors such as vehicle speed, tire pressure and temperature. The typical range for c_{roll} is approximately 0.01-0.03. This force always opposes the vehicle's motion as it is dissipative.

F_{aero} represents the aerodynamic resistance, which depends on air density (ρ, typically 1.25 kg/m^3 in standard ambient conditions), vehicle frontal area (A_{f}), and the aerodynamic drag coefficient (C_{d}). It is always dissipative, along with F_{roll}.

$$F_{\text{aero}} = \frac{1}{2} \rho C_{\text{d}} A_{\text{f}} v_{\text{veh}}^2 \tag{5.3}$$

Finally, F_{grade} accounts for the force due to road slope. It is positive when the vehicle is driven uphill and negative when going downhill:

$$F_{\text{grade}} = m_{\text{veh}} g \sin \delta \tag{5.4}$$

These equations serve as the foundation for vehicle modeling and can provide sufficient accuracy if the parameters used are appropriately specified. Table 5.2 presents typical values for vehicle-dependent parameters utilized in longitudinal vehicle dynamics models.

Table 5.2: Typical values of vehicle-dependent parameters for longitudinal vehicle dynamics models.

Parameter	Compact Car	Full-size	SUV heightm_{veh} (kg)
1200-1500	1700-2000	1900-2200 C_d	0.3-0.35
0.28-0.33	0.32-0.38 A_f (m^2)	1.3-1.7	1.8-2.2
2-2.5 C_{roll}	0.01-0.03	0.01-0.03	0.01-0.03 height

To explicitly express the tractive force required by the powertrain, Equation 5.1 can be rewritten as:

$$F_{\text{trac}} = F_{\text{pwt}} - F_{\text{brake}} = F_{\text{inertia}} + F_{\text{grade}} + F_{\text{roll}} + F_{\text{aero}} \tag{5.5}$$

The equilibrium of forces in Equations 5.1 and 5.5 corresponds to forward and backward modeling approaches, respectively.

In the forward approach, the vehicle acceleration ($\frac{dv_{\text{veh}}}{dt}$) is determined by balancing the tractive force generated by the powertrain with the passive resistances. The vehicle speed is obtained by integrating the acceleration.

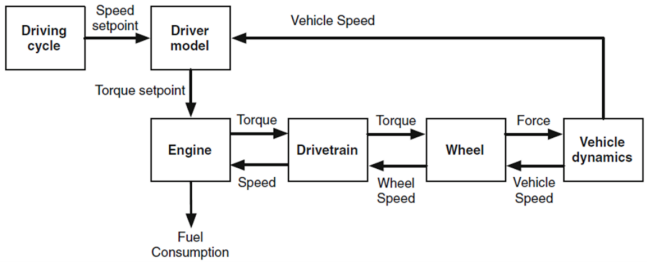

Figure 5.2: Information flow of a forward approach. Source: [18]

The forward approach represents the physical causality of the system and is commonly used in simulations. The information flow in this approach, as shown in Figure 5.2, involves the required speed profile, actual vehicle speed, driver model (often represented by a PID controller), and the supervisory block responsible for issuing actuator setpoints to the powertrain components. The resulting tractive or braking force is applied to the vehicle dynamics model, utilizing Equation 5.1.

In contrast, the backward approach imposes the velocity and calculates the tractive force based on inertia and dissipative forces. It assumes that the vehicle precisely follows the prescribed velocity and acceleration profiles. In this case, F_{trac} represents the force supplied by the powertrain. A driver model is unnecessary since the required speed is directly inputted, and the outputs are the engine torque and fuel consumption. The information flow for the backward approach is depicted in Figure 5.3.

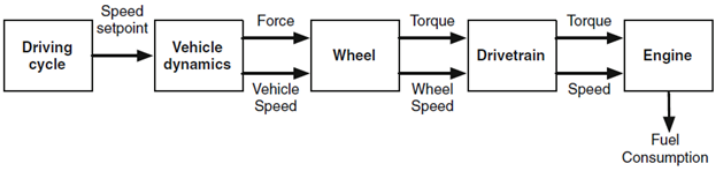

Figure 5.3: Information flow of a backward approach. Source: [18]

In addition to force balance equilibrium, a vehicle simulation can include

power and energy balances. By multiplying all terms of Equation (5.5) by the vehicle speed (v_{veh}), the power balance can be expressed as:

$$P_{\text{trac}} = P_{\text{inertia}} + P_{\text{grade}} + P_{\text{roll}} + P_{\text{aero}} \tag{5.6}$$

If P_{trac} is positive, the powertrain produces power to drive the vehicle. For conventional vehicles, negative P_{trac} represents power lost in the brakes and engine pumping losses, while for hybrid vehicles, some of this power can be recovered by the electric unit to recharge the battery.

By integrating Equation 5.6 over the duration of a prescribed route, the energy balance can be obtained as:

$$E_{\text{trac}} = \int_{t_o}^{t_f} P_{\text{trac}}(t), dt = E_{\text{kin}} + E_{\text{pot}} + E_{\text{roll}} + E_{\text{aero}} \tag{5.7}$$

Here, the integral of the inertial power represents the variation of kinetic energy (E_{kin}), and the integral of the grade powers represents the variation of potential energy (E_{pot}).

Solving Equations 5.1, 5.6, and 5.7 enables an energetic and dynamic analysis of a driving mission. For conventional vehicles, E^{+}_{trac} is entirely supplied by the thermal engine, while E^{-}_{trac} is dissipated as friction losses in the brakes or engine pumping losses. In the case of hybrid architectures, E^{+}_{trac} can be provided by the thermal unit and/or electric units, depending on the chosen architecture and energy strategy. E^{-}_{trac} is recovered by the electric units. Describing the energy flow from the thermal engine, fuel cell or battery to the wheels requires proper modeling of all powertrain components, including the ICE, the fuel cell system, electric units, and the battery, which will be briefly discussed in the following.

Two primary approaches are commonly employed in vehicle simulation for modeling the thermal engine: the static map approach or a combination of static map and lumped-parameter dynamic mode. In the static map approach, the engine is treated as a perfect actuator that immediately responds to demands. All variables, including fuel consumption, are computed from a map or table based on known engine speed and torque. This approach can be modified into the second approach by incorporating dynamic limitations in torque output, resulting in a lumped-parameter dynamic model. In this approach, a delay between the demanded torque and actual torque generated is considered. To account for this, a transfer function is coupled with the map to represent air/fuel dynamics during transients, and if possible, crankshaft inertia.

Concerning the FCS, simplified approaches based on simple and constant polarization curves [3, 19], simple polynomials [20, 21], or a simplified fuel cell efficiency curve depending only on the fuel cell power [22, 23] are generally preferred for vehicle simulations.

Regarding the electric machine, its efficiency can be assumed constant or modeled using a map-based approach. The map can be expressed based on speed and torque or speed and electric power. The relationship between mechanical torque and electric power is given by:

$$P_{\text{mec}} = \omega_{\text{EM}} \cdot T_{\text{EM}} = \begin{cases} \eta_{\text{EM}}(\omega_{\text{EM}}, P_{\text{el}}) \cdot P_{\text{el}} & \text{if } P_{\text{el}} \geq 0 \text{ (motoring mode)} \\ \frac{1}{\eta_{\text{EM}}(\omega_{\text{EM}}, P_{\text{el}})} \cdot P_{\text{el}} & \text{if } P_{\text{el}} < 0 \text{ (generating mode)} \end{cases} \tag{5.8}$$

Here, η_{EM} represents the efficiency of the electric unit, ω_{EM} is its rotational speed, and T_{EM} is the mechanical torque.

Various models have been proposed for the battery system in the existing literature, offering different levels of accuracy. Accurately predicting battery dynamics in a hybrid electric vehicle presents a challenge due to the interdependence among key variables characterizing battery behavior, such as State of Charge (SoC), voltage, and temperature. SoC is defined as the amount of electrical charge stored in the battery ($Q(t)$) normalized by its total capacity (Q_{nom}).

$$\text{SoC}(t) = \frac{Q(t)}{Q_{\text{nom}}} = \begin{cases} -\frac{1}{\eta_{\text{coul}}(I(t))/Q_{\text{nom}}} & \text{if } I(t) > 0 \\ -\eta_{\text{coul}}(I(t))/Q_{\text{nom}} & \text{if } I(t) < 0 \end{cases} \tag{5.9}$$

Here, $I(t)$ represents the battery current, positive/negative during discharge/charge, and η_{coul} is the Coulombic efficiency, which depends on current intensity and temperature. Although battery capacity and Coulombic efficiency are parameter-dependent, the SoC evaluation in Equation 5.9 typically assumes them as constants. To describe battery behavior, a simplified circuit linear model is chosen. According to this approach, battery current and voltage are related to the power exchanged with the powertrain by:

$$I \cdot V_{\text{oc}} - I^2 R_{\text{int}} - \eta_{\text{coul}} P_{\text{batt}} = 0 \tag{5.10}$$

The current can be explicitly determined by solving Equation 5.10, where V_{oc} is the open circuit voltage and R_{int} is the internal resistance of the battery. These values can be obtained from appropriate maps that account for temperature and SoC.

$$I = \frac{-V_{\text{oc}} + \sqrt{V_{\text{oc}}^2 - 4R_{\text{int}}P_{\text{batt}}\eta_{\text{coul}}}}{2R_{\text{int}}} \tag{5.11}$$

During battery charging, Equation 5.11 always yields real roots since P_{batt} is negative. However, during battery discharge, imaginary roots can be obtained from the quadratic equation above. This occurs when the power requested by the motor exceeds the available power from the battery. To account for this, an additional equation is included in the model to determine the maximum current that the battery can supply:

$$I_{\max} = \frac{V_{\text{oc}}}{2R_{\text{int}}}; \quad V = V_{\text{oc}} - I_{\max}R_{\text{int}}; \quad P_{\text{batt}} = I_{\max}V \tag{5.12}$$

It is important to note that while integrating the current to calculate SoC is a widely adopted approach, it has some limitations. In practical applications, this approach lacks stability and accuracy. Therefore, different algorithms are used to estimate SoC based on available measurements of terminal voltage and current. Additionally, this method does not consider battery aging, which leads to capacity loss, increased internal resistance, and reduced vehicle performance. However, in the short term, battery performance is not significantly affected by aging, which is why this aspect has not been addressed in this study. In conjunction with the components responsible for supplying power to the powertrain, it is essential to model the devices involved in its transmission or conversion, such as the gearbox and wheels. The gearbox is responsible for altering the speed and torque between two shafts while ideally maintaining a continuous power flow. However, due to friction losses, the output power is always reduced compared to the input power. Therefore, a lossy gear model is introduced to account for these power losses. This model incorporates a fixed speed ratio (γ_{GB}) for a selected gear and expresses the output power as a function of the transmission efficiency (η_{GB}).

$$T_{out} = \begin{cases} \frac{\eta_{GB}}{\gamma_{GB}} T_{in} & \text{if } P_{in} = T_{in}\omega_{in} \geq 0 \\ \frac{1}{\eta_{GB}\gamma_{GB}} T_{in} & \text{if } P_{in} = T_{in}\omega_{in} < 0 \end{cases} \tag{5.13}$$

In equation 5.13, the efficiency η_{GB} can be assumed constant or variable, depending on the gear ratio, speed, and input torque, either through a map or an analytical expression. More intricate models are employed for drivability studies. When it comes to the wheels and brakes, a simplified quasi-static approach is typically utilized for longitudinal vehicle simulation. The tractive force can be expressed as follows:

$$F_{trac} = \frac{1}{R_{wh}}(T_{pwt} - T_{brake}) \quad \omega_{wh} = \frac{v_{veh}}{R_{wh}} \tag{5.14}$$

Here, T_{pwt} represents the torque generated by the powertrain at the wheel shaft, T_{brake} is the braking torque, and R_{wh} denotes the wheel radius. The wheel angular speed, ω_{wh}, as mentioned in equation 5.14, can be calculated based on the longitudinal vehicle speed.

As for the passive power of the engine associated with the auxiliary systems, it is often represented by a simplified model due to the limited availability of detailed data during a driving cycle. Typically, this energy is considered as an additional load on the battery, dependent on the current operating point.

5.4.2 A Parallel P3 plug-in HEV model

The simulation model of the parallel P3 PHEV is here described. The powertrain configuration consists of several components including a 3-cylinder spark ignition engine, a manual clutch (CLT), a manual transmission (MT), an electric reversible machine (EM), a DC-DC converter, a battery pack (BA), and an electric motor starter (STRT). The powertrain architecture is depicted in Figure 1, where the solid black lines represent mechanical connections and the blue dotted lines represent electrical connections. The main characteristics of the vehicle are provided in Table 5.3.

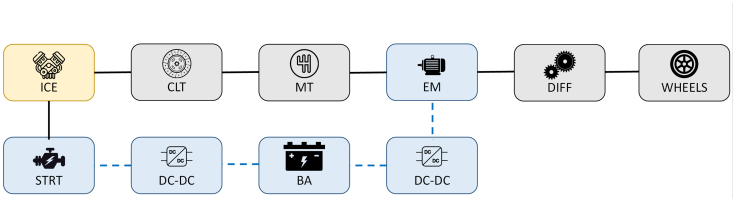

Figure 5.4: Powertrain schematic of tested PHEV. Source: [24]

The vehicle can operate in three modes: pure electric mode, pure thermal mode, and parallel mode, depending on the driver's power demand. In pure thermal and pure electric modes, the entire power required is respectively provided by the thermal engine or the electric machine. In parallel mode, both the engine and the motor contribute in supplying the demanded power.

The simulation model, developed in the MATLAB/Simulink environment, adopts a forward dynamic approach. The driver model employs a typical PID controller. The fuel consumption of the thermal engine and the efficiency of the motor/generator are estimated using speed-load lookup tables, illustrated in Figure 5.5 and Figure 5.6, respectively. The battery module calculates the state of charge based on the internal resistance and open-circuit voltage, which are dependent on the SoC. The electric starter is a series excited DC motor that

Table 5.3: Main characteristics of the tested PHEV.

Plug-in Hybrid Electric Vehicle Features	
Vehicle	
Mass, kg	1100
Car aero drag, m^2	2.46
Wheel diameter, m	0.366
Axle ratio, -	3.32
Internal Combustion Engine	
Displacement, cm^3	999
Max Power, kW	46
Max Torque, Nm	90
Electric Machine	
Max Power, kW	60
Max Torque, Nm	207
Battery	
Rated Capacity, Ah	6.8
Gearbox	
Gear 1 Ratio, -	4.212
Gear 2 Ratio, -	2.637
Gear 3 Ratio, -	1.8
Gear 4 Ratio, -	1.386
Gear 5 Ratio, -	1
Gear 6 Ratio, -	0.772

draws energy from the battery to provide power during the engine's starting phases. The torque of the starter motor is described by:

$$T_{STRT} = i_{af}^2 \cdot L_{af} \tag{5.15}$$

where i_{af}^2 and L_{af} denote the field and armature current, and the field and armature mutual inductance, respectively. The powertrain also includes a disk clutch to disengage the engine from the driveline. The clutch model incorporates friction and dynamic characteristics that depend on the clutch lockup condition. A detailed control logic is therefore necessary for both the clutch and the motor starter. The engine operation is represented by a finite

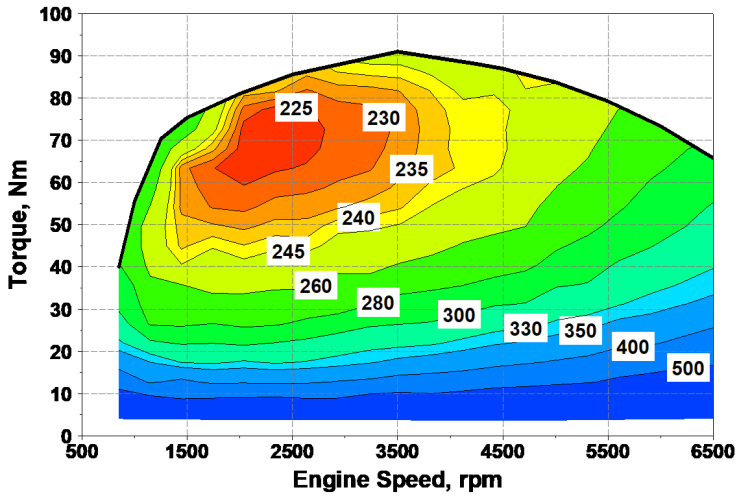

Figure 5.5: Engine BSFC map, g/kWh. Source: [24]

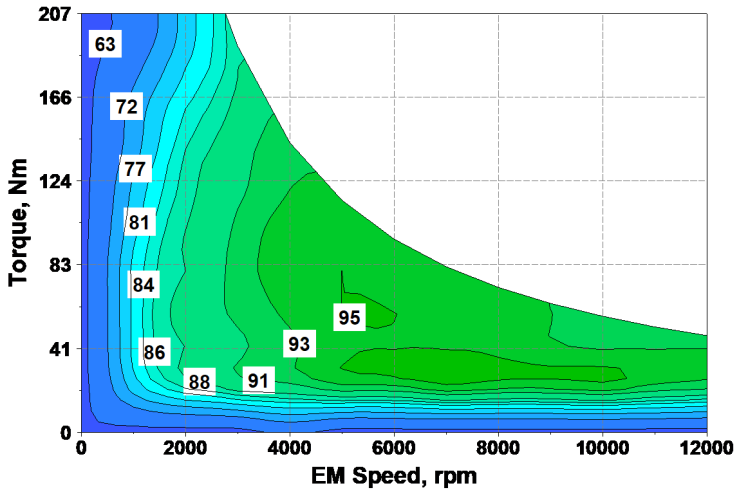

Figure 5.6: Electric machine efficiency map, %. Source: [24]

state machine, as depicted in Figure 5.7. Upon receiving the engine activation command from the EMS, the motor starter supplies the necessary power to accelerate the engine to its idle speed. In the next stage, a PI controller adjusts the engine torque to synchronize its speed with that of the driveline. At this point, the clutch pedal pressure is commanded to prevent mechanical losses during clutch engagement. When power to the thermal engine is not required

by the EMS, the engine control module commands clutch disengagement. To simplify the control logic and reduce computational effort, the desired gear is selected by the transmission control module (TCM) using a lookup table based on vehicle speed and accelerator pedal position. The TCM also handles clutch disengagement during gear shifting to facilitate smooth transitions.

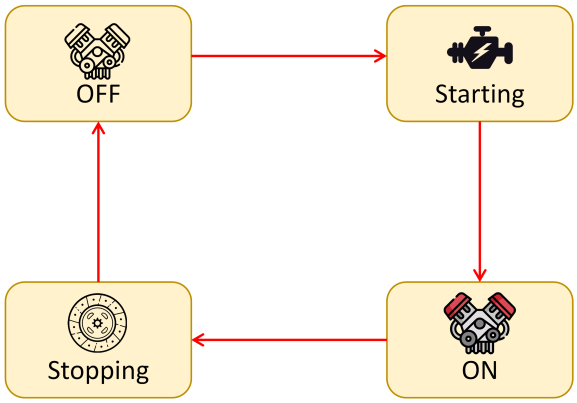

Figure 5.7: Engine finite state machine scheme. Source: [24]

5.4.3 A heavy-duty fuel cell HEV model

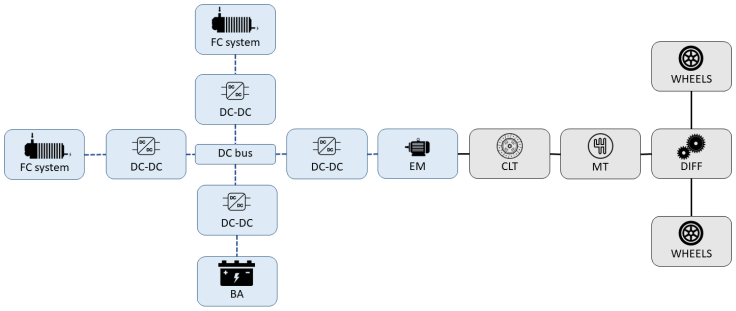

Figure 5.8: Heavy-duty fuel cell hybrid electric vehicle powertrain scheme

A heavy-duty vehicle with a multi-FC system, based on the Hyundai XCIENT FCV [25], is used as the simulation model for the developing of EMSs for FCHEV (that will be described in Chapter 6). Figure 5.8 depicts how its powertrain is set up. It is made up of a battery pack, two fuel cell systems, DC-DC converters, an electric motor, a gearbox, and a differential. Table 5.4

lists the primary characteristics of the vehicle and its components. The indirect electronic configuration was chosen, similar to modern FCVs, to shield the FC systems from electric oscillations originating from the DC bus while also enabling the FC systems to be scaled down. The vehicle model is implemented in the GT-Suite 2020 software. As discussed in the previous section, an estimate of the electric machine's efficiency was made using a speed-torque map. According to SoC-dependent calculations, the battery module determines the battery pack's SoC. The FCS model has been previously described in Chapter 4.4.2. The decision to simplify it into a mean values model was driven by the need to reduce computation times for simulations of the vehicle model just described. Given the steady nature of the model, some deviation between the complete model and the simplified mean values model are expected, particularly due to thermal dynamics of fuel cells that influence their transient behavior. Despite this deviation, the chosen approach was based on a validated model that accounted for various factors such as pressure, temperature, and stoichiometry variations in an FC stack integrated into a Balance of Plant system with optimized air management strategy. Consequently, the simplified model was able to replicate the actual operation of the FC system, albeit with simplified dynamics, yielding results of higher fidelity compared to other approaches that oversimplified the entire FC system to a single polarization curve without incorporating the power demand of the BoP and the inefficiencies associated with driving cycle conditions [26]. The mean values model results in lower hydrogen consumption since the FC system consistently operates under pseudo-steady conditions, disregarding inefficiencies linked to transient operation such as slow thermal dynamics.

Fuel Cell Hybrid Electric Vehicle Features	
Vehicle	
Mass (vehicle+cargo), kg	18000
Car aero drag, m^2	9.38
Wheel diameter, m	0.468
Axle ratio, -	4.875
Fuel Cell Stacks	
Cells number, -	480
Max Power, kW	120
Max efficiency, -	0.62
DC-DC efficiency, -	0.95
Electric Machine	
Max Power, kW	350
Max Torque, Nm	3400
DC-DC efficiency, -	0.95
Battery	
Rated Capacity, Ah	110.55
DC-DC efficiency, -	0.95
Gearbox	
Gear 1 Ratio, -	4.484
Gear 2 Ratio, -	2.872
Gear 3 Ratio, -	1.842
Gear 4 Ratio, -	1.414
Gear 5 Ratio, -	1.000
Gear 6 Ratio, -	0.742

Table 5.4: Main characteristics of the tested FCHEV, based on the Hyundai XCIENT FCV [25]

5.5 Summary and conclusions

The automotive sector is currently facing significant challenges, particularly regarding global pollution. However, many automotive companies are investing in electrification and low-emission vehicles to reduce their carbon footprint. The industry is transitioning towards more sustainable technologies to meet emission reduction targets. The purpose of this chapter was therefore to describe the main current and future vehicular alternatives for achieving this green transition, namely HEVs, FCHEVs, and BEVs, providing details on their different construction possibilities and the main advantages and disadvantages

associated with their production and use.

HEVs serve as a bridge between conventional and electric vehicles, maximizing efficiency until a sustainable electric transition is fully realized. By integrating internal combustion engines with electric motors and batteries, hybrids optimize fuel consumption and reduce emissions. They offer improved fuel efficiency by utilizing electric power during low-load conditions and regenerative braking. Hybrids also provide drivers with an extended driving range and the convenience of refueling at existing gasoline stations. They offer a smoother transition for consumers not yet ready for fully electric vehicles and address concerns about range anxiety and limited charging infrastructure.

Hydrogen FCHEVs are a promising and transformative technology for sustainable transportation. They produce zero tailpipe emissions and improve air quality. They also are highly energy-efficient, offering extended driving ranges and reducing refueling needs. They provide a serene driving experience and contribute to a more eco-friendly transportation system. However they face challenges including limited hydrogen infrastructure and higher production costs. Nonetheless, ongoing advancements aim to optimize efficiency, range, and overall sustainability.

BEVs have emerged as an other promising solution to combat the environmental impact of transportation. Advancements in battery technology have allowed for longer ranges and increased efficiency. Despite challenges like limited range and charging infrastructure, continuous research and government initiatives have led to substantial improvements. However, BEVs face environmental challenges in battery production and disposal, as well as their dependence on non-renewable energy sources. The extraction of minerals for battery production and the recycling of used batteries require attention. Additionally, the reliance on fossil fuels for electricity generation hinders decarbonization efforts. To address these challenges, a holistic approach is needed. Ongoing research focuses on sustainable battery development and improving recycling processes. Transitioning to renewable energy sources for electricity generation is crucial for greener charging infrastructure.

In the latter part of the chapter, the primary approaches for vehicle simulation were presented, recognizing the pivotal role that vehicle simulations play in industry and scientific research. In fact, vehicle simulations serve as a cornerstone for investigation and analysis, offering a comprehensive understanding of vehicle behavior and performance. Lastly, the two vehicle models used throughout the thesis work, namely the parallel P3 HEV and the FCHEV heavy-duty model, were thoroughly described. These vehicle models were chosen to investigate and analyze specific aspects related to hybrid and fuel cell technologies in the context of different vehicle applications. Detailed explana-

tions and specifications were provided to ensure a comprehensive understanding of the characteristics and capabilities of each model.

References

[1] Xu, Liangfei et al. "Optimal sizing of plug-in fuel cell electric vehicles using models of vehicle performance and system cost". In: *Applied Energy* 103 (2013), pp. 477–487. DOI: 10.1016/j.apenergy.2012.10.010.

[2] Fletcher, Tom and Ebrahimi, Kambiz. "The Effect of Fuel Cell and Battery Size on Efficiency and Cell Lifetime for an L7e Fuel Cell Hybrid Vehicle". In: *Energies* 13.22 (2020). Number: 22 Publisher: Multidisciplinary Digital Publishing Institute, p. 5889. DOI: 10.3390/en13225889.

[3] Gaikwad, Shrihari D. and Ghosh, Prakash C. "Sizing of a fuel cell electric vehicle: A pinch analysis-based approach". In: *International Journal of Hydrogen Energy* 45.15 (2020), pp. 8985–8993. DOI: 10.1016/j.ijhydene.2020.01.116.

[4] Peng, F., Xie, X., Wu, K., Zhao, Y., and Ren, L. "Online hierarchical energy management strategy for fuel cell-based heavy-duty hybrid power systems aiming at collaborative performance enhancement". In: *Energy Conversion and Management* 276 (2023), p. 116501. DOI: 10.1016/j.enconman.2022.116501.

[5] Pardhi, S. et al. "A review of fuel cell powertrains for long-haul heavy-duty vehicles: Technology, hydrogen, energy and thermal management solutions". In: *Energies* 15.24 (2022). DOI: 10.3390/en15249557.

[6] Sim, K., Vijayagopal, R., Kim, N., and Rousseau, A. "Optimization of component sizing for a fuel cell-powered truck to minimize ownership cost". In: *Energies* 12.6 (2019). DOI: 10.3390/en12061125.

[7] Cox, B., Bauer, C., Mendoza Beltran, A., Vuuren, D. P. van, and Mutel, C. L. "Life cycle environmental and cost comparison of current and future passenger cars under different energy scenarios". In: *Applied Energy* 269 (2020), p. 115021. DOI: 10.1016/j.apenergy.2020.115021.

[8] Arvind, Noel, Xavier, Leo, and Kumar, AH. "Fuel cell electric vehicles: genesis of a new era or a myth-busting in new energy vehicle technology?" In: (2018).

[9] Jadhav, AJA. *Hydrogen fuel cell vehicle market by vehicle type (passenger vehicle and commercial vehicle) and technology (proton exchange membrane fuel cell, phosphoric acid fuel cells, and others)*. Pages: 2019–2026. 2020.

[10] İnci, Mustafa, Büyük, Mehmet, Demir, Mehmet Hakan, and İlbey, Göktürk. "A review and research on fuel cell electric vehicles: Topologies, power electronic converters, energy management methods, technical challenges, marketing and future aspects". In: *Renewable and Sustainable Energy Reviews* 137 (2021), p. 110648. DOI: https://doi.org/10.1016/j.rser.2020.110648.

[11] International, Amnesty. *'This Is What We Die For': Human Rights Abuses in the Democratic Republic of the Congo Power the Global Trade in Cobalt*. 2016.

[12] Brennan, J.W. and Barder, T.E. *Battery Electric Vehicles vs. Internal Combustion Engine Vehicles*. Arthur D. Little, 2016.

[13] Lightfoot, M. *Three Steps to Clean up Electric Vehicle Supply Chains*. Publisher: World Economic Forum. 2019. URL: https://www.weforum.org/agenda/2019/09/clean-vehicles-have-a-dirty-secret-and-it-s-time-we-took-action/.

[14] Federation (NAF), Norwegian Automobile. *20 Popular EVs Tested in Norwegian Winter Conditions*. 2020.

[15] Mortimer, M.B. *How Much Does Climate Control Affect EV Range?* 2020.

[16] Geotab. *Temperature Tool for EV Range*. 2020.

[17] Motoaki, Y., Yi, W., and Salisbury, S. "Empirical Analysis of Electric Vehicle Fast Charging under Cold Temperatures". In: *Energy Policy* 122 (2018), pp. 162–168. DOI: 10.1016/j.enpol.2018.07.036.

[18] Miller, John M. *Propulsion Systems for Hybrid Vehicles*. Google-Books-ID: uTiSu1mbBa8C. IET, 2004. 476 pp.

[19] Feng, Y. and Dong, Z. "Integrated design and control optimization of fuel cell hybrid mining truck with minimized lifecycle cost". In: *Applied Energy* 270 (2020), p. 115164. DOI: 10.1016/J.APENERGY.2020.115164.

[20] Wu, X. et al. "Convex programming energy management and components sizing of a plug-in fuel cell urban logistics vehicle". In: *Journal of Power Sources* 423 (2019), pp. 358–366. DOI: 10.1016/J.JPOWSOUR.2019.03.044.

[21] Wu, X., Hu, X., Yin, X., Peng, Y., and Pickert, V. "Convex programming improved online power management in a range extended fuel cell electric truck". In: *Journal of Power Sources* 476 (2020), p. 228642. DOI: 10.1016/J.JPOWSOUR.2020.228642.

[22] Ferrara, A., Jakubek, S., and Hametner, C. "Energy management of heavy-duty fuel cell vehicles in real-world driving scenarios: Robust design of strategies to maximize the hydrogen economy and system lifetime". In: *Energy Conversion and Management* 232 (2021), p. 113795. DOI: 10.1016/j.enconman.2020.113795.

[23] Fu, Z., Zhu, L., Tao, F., Si, P., and Sun, L. "Optimization based energy management strategy for fuel cell/battery/ultracapacitor hybrid vehicle considering fuel economy and fuel cell lifespan". In: *International Journal of Hydrogen Energy* 45.15 (2020), pp. 8875–8886. DOI: https://doi.org/10.1016/j.ijhydene.2020.01.017.

[24] Bellis, Vincenzo De, Piras, Marco, and Malfi, Enrica. "Assessment of an Adaptive Efficient Thermal/Electric Skipping Control Strategy for the Management of a Parallel Plug-in Hybrid Electric Vehicle". In: *Energies* 15.19 (2022). Number: 19 Publisher: Multidisciplinary Digital Publishing Institute, p. 7122. DOI: 10.3390/en15197122.

[25] FuelCellsWorks. *World's first fuel cell heavy-duty truck, Hyundai XCIENT Fuel Cell, heads to Europe for commercial use*. 2020.

[26] Molina, S., Novella, R., Pla, B., and Lopez-Juarez, M. "Optimization and sizing of a fuel cell range extender vehicle for passenger car applications in driving cycle conditions". In: *Applied Energy* 285 (2021). Publisher: Elsevier Ltd. DOI: 10.1016/j.apenergy.2021.116469.

Chapter 6

Optimizing Efficiency: Energy Management Strategies for Hybrid Vehicles

Hybrid powertrains require efficient control from both a numerical and real-world perspective, which is achieved through a proper energy management strategy. The primary objective of the EMS is to determine the power allocation from the available energy sources in the powertrain while adhering to various constraints. Most EMSs focus on minimizing a cost function, primarily considering fuel consumption and maintaining the battery's SoC. Broadly, two categories of energy management problems can be identified: rule-based and model-based optimization.

Rule-based strategies are executed in real-time and do not involve explicit minimization or optimization. These approaches use a set of predefined rules to determine the appropriate control variable for each instance. On the other hand, model-based optimization involves a power split optimization to minimize a cost function over a given driving cycle, resulting in a globally optimal solution. While these optimizations are not practical for real-time implementation due to the lack of future information and computational complexity, they are valuable during the design phase. They can guide the development of rule-based strategies or serve as benchmark solutions for comparing different control strategies.

Model-based optimization problems can be solved numerically or analytically. Numerical methods consider the entire driving cycle to find the

global optimum, with Dynamic Programming (DP) being the most widely used method in vehicle applications. Analytical solutions, on the other hand, aim to solve the optimization problem in closed or analytical form, providing faster numerical solutions compared to purely numerical methods. One such commonly used analytical method is Pontryagin's minimum principle. An other possibility is to classify these strategies based on how the SoC varies over time. One common strategy is the Charge-Sustaining (CS) approach, typically employed in HEVs. The primary objective of CS strategies is to maintain the battery SoC stable around a predefined target. This is because HEVs lack the ability to recharge the battery from an external grid source. In contrast, PHEVs can achieve longer driving distances compared to traditional fuel vehicles and produce fewer tailpipe emissions when operating in pure electric mode. To take advantage of these characteristics, different battery management strategies are required for PHEVs. One widely implemented strategy for PHEVs is the Charge-Depleting/Charge-Sustaining (CDCS) approach, which is often used in heuristic hybrid control modules [1, 2]. The CDCS strategy involves a logic that first discharges the battery until it reaches a predefined SoC value and then maintains the SoC around that level. An alternative strategy is the Charge-Blended (CB) approach, which resembles the CS method but with a gradual decrease in the desired SoC trajectory as the driving distance increases [3]. CB strategies are particularly suitable for PHEVs that commence their driving missions with a high SoC and aim to complete them with a lower SoC. Moreover, in the CB mode, the ICE operates more in its most efficient region, resulting in improved fuel economy [4].

In this context, the current chapter presents an in-depth analysis of advanced EMSs, exploring the final decarbonization level studied in this PhD thesis. Initially, the most extensively studied EMSs and the development of a Charge-Blended strategy for controlling the PHEV, as discussed in Chapter 5.4.2, are presented. Following that, fundamental concepts of artificial neural networks are introduced, providing a comprehensive understanding of AI-enhanced EMSs. Lastly, the operation and simulation results of the FCHEV, as described in Chapter 5.4.3, and the multi-level EMS developed for it, are thoroughly examined and evaluated.

6.1 Literature review

6.1.1 The optimal problem in HEV

The main objective of any vehicle powertrain control strategy is to minimize specific quantities, such as fuel consumption or pollutant emissions, throughout

a driving mission while adhering to various constraints. A common approach involves minimizing a combination of these parameters, leading to the following mathematical expression:

$$\min J[x(t), u(t)] \quad \text{subject to:} \quad u(t) \in U, \quad x(t) \in X \tag{6.1}$$

In this expression, J represents the performance index to minimize, where x is a generic state variable, and u is a generic control variable. X and U represent their respective ranges of variation. The performance index is based on the integral of a cost function L over the time interval from t_0 to t, plus a penalization factor β multiplied by the difference between the current and initial state variable.

$$J[x(t), t] = \int_{t_0}^{t} [L[x(t), u(t), t]dt + \beta(x(t_0) - x(t))] \tag{6.2}$$

When the aim is to minimize fuel consumption during the driving cycle, the state variable is simplified to the battery State of Charge (SoC), and the power-split between the thermal engine (or fuel cell) and electric units ($u = P_{el}/P_{trac}$) represents the control variable. Under these assumptions, the cost function is reformulated as:

$$J(x(t), t) = \int_{t_0}^{t} (\dot{m}_f(u(t), t)dt + \beta(SoC(t_0) - SoC(t)) \tag{6.3}$$

The second term on the right side of equation 6.3 represents a global constraint on the state variable, ensuring the energy-storage balance. Typically, optimization problems involve several constraints. Some constraints are integral, like the one mentioned above, while others are local in nature, such as instantaneous power limits or state of charge boundaries. The local constraints related to SoC are essential for battery efficiency and cycle-life preservation. Constraints on the control variable ensure physical operation limits and can be expressed as follows:

$$\begin{aligned} &SoC_{\min} \leq SoC(t) \leq SoC_{\max} \\ &P_{\text{batt,min}} \leq P_{\text{batt}}(t) \leq P_{\text{batt,max}} \\ &T_{x,\min} \leq T_x(t) \leq T_{x,\max} \\ &\omega_{x,\min} \leq \omega_x(t) \leq \omega_{x,\max} \end{aligned} \tag{6.4}$$

for $x =$ eng, mot, gen

Here, $SoC_{\min}$ and $SoC_{\max}$ are the minimum and maximum values of the State of Charge at each instant, and similar definitions apply to power, torque,

and speed. Additionally, certain constraints may be inherent in the model, such as limiting the frequency of switching between operating modes or gear numbers to ensure acceptable vehicle drivability.

6.1.2 Dynamic programming

Dynamic programming is a numerical method employed for solving multistage decision-making problems [5, 6]. It can provide the optimal solution to problems of any complexity level (within computational capabilities). However, it is important to note that dynamic programming is non-causal and only implementable in a simulation environment since it requires a priori information about the entire optimization horizon. The study of dynamic programming dates back to Richard Bellman, who authored the first book on the subject in 1957 [5]. In his work, Bellman introduced what is now known as Bellman's principle of optimality: an optimal policy has the property that, regardless of the initial state and decision, the remaining decisions must constitute an optimal policy with regard to the state resulting from the first decision.

The discrete-time system considered is represented as $x_{k+1} = f_k(x_k, u_k)$, where k takes integer values, for example, $k = 0, 1, ...$ The control variable u_k, whose value is chosen at time k, is bounded and discretized. Specifically, $u_k \in U_k$ and $xk \in \Omega_k$, where U_k and Ω_k denote the respective domains.

A control policy $u = \{u_0, u_1, ..., u_{N-1}\}$ is considered over the first N time steps. The cost of this policy, starting from initial conditions x_0, is determined by the cost function

$$J(x_0, u) = L_N(x_N) + \sum_{k=1}^{N-1} L_k(x_k, u_k) \tag{6.5}$$

The optimal solution leads to the cost function $J^*(x_0) = min(u)J(x_0, u)$ and the corresponding optimal policy is $u^* = \{u_1^*, u_2^*, \ldots, u_{N-1}^*\}$.

Now, the focus is on the "tail subproblem," which aims to minimize the cost-to-go Y from time i (and state x_i) to time N. This is represented as

$$Y(x_i, i) = L_N(x_N) + + \sum_{k=1}^{N-1} L_k(x_k, u_k) \tag{6.6}$$

Bellman's principle of optimality asserts that the "tail policy"

$$u^* = \{u_1^*, u_2^*, \ldots, u_{N-1}^*\}$$

represents the optimal policy for the tail subproblem.

The dynamic programming algorithm operates based on Bellman's principle of optimality. Starting from the final step N, the algorithm proceeds backward by utilizing the sequence of controls that yield the optimal cost-to-go, represented as follows:

$$u_k = \mu^*(x_k, k) = \arg\min_{u \in U_k} \left(L_k(x_k, u) + Y_{k+1} f_k(x_k, u) \right),$$
$$\text{for } k = N-1, N-2, ..., 1.$$

At the last iteration, the value of $Y(x_1, 1)$ equals the optimal (minimum) cost $J^*(x_0)$. Also, the terminal cost $Y(x_N, N) = L_N(x_N)$ depends on the final state x_N. It's important to note that $Y(x_k, k)$ represents the optimal cost-to-go from state x_k at time k to the end of the optimization horizon. On the other hand, $Y_k(x_k, u_k)$ is a function that relies on the control value u_k and reflects the alternative values that the cost-to-go from the same state can assume, depending on u_k. Essentially, $Y(x_k, k)$ denotes the minimum value that $Y_k(x_k, u_k)$ can take as u_k varies.

To determine the optimal control sequence, the algorithm proceeds backward from the final state, choosing at each step the control that minimizes the cost-to-go $Y_k(x_k, u_k)$, and stores this optimal choice in a matrix μ^* at each time instant k and state value x_k.

Since the algorithm discretizes state values while most physical systems have continuous states, applying a given control action from the discrete control set may lead to the system reaching a state that lies between two discretized values Ω_k. In such cases, the computation of the cost at grid values relies on interpolation.

In summary:

- The optimal control sequence μ^* is solely a function of x_k and k.
- The optimal control law is expressed in closed-loop form and remains optimal, independent of the past control policy.
- The Bellman equation is solved through backward induction, with decisions made based on future policies first.

6.1.3 Pontryagin Minimum principle

The Pontryagin Minimum Principle is a widely used analytical optimization method for solving the problem of Hybrid Electric Vehicle energy management. This principle involves the instantaneous minimization of the Hamiltonian function, which, once the optimal trajectory of the costate is determined, is mathematically defined as follows:

$$H(u(t), SoC(t), t, \lambda(t)) = \dot{m_f}(u(t), t) + \lambda(t)\dot{SoC}(u(t), SoC(t), t) \tag{6.7}$$

In the Hamiltonian function 6.7, the first term represents the instantaneous cost, while $\lambda(t)$ is a vector of optimization variables, also known as costate of the system. Its dynamic equation is given by:

$$\dot{\lambda}(t) = -\frac{H[u(t), SoC(t), t, \lambda(t)]}{\partial SoC} = -\lambda(t)\frac{\partial(\dot{SoC}[u(t), SoC(t), t])}{\partial SoC} \tag{6.8}$$

Based on the main assumption that the time derivative of SoC is independent of its current level [7], the costate remains constant over time. The optimal costate λ^* only needs to satisfy the energy balance for the battery between the beginning and the end of the driving cycle:

$$SoC(t_0) = SoC(t_f)$$

The evaluation of λ^* requires defining the vehicle driving mission "a priori" based on future information knowledge. When the Hamiltonian cannot be explicitly expressed as a function of the control variable, the problem can be solved by discretizing the control variable domain at each simulation step. However, the choice of grid sizing can significantly affect the solution, leading to variations in the minimum cost function and control variable trajectory. While finer grids provide better outcomes, computational time becomes a potential concern.

When state constraints are included in the problem definition, the application of PMP may encounter challenges. To address this, a possible solution is to combine PMP with a penalty function approach [8]. This involves increasing the Hamiltonian value whenever the optimal trajectory violates the constraints. An effective penalty approach through implicit Hamiltonian minimization is employed in [9], considering several states and inputs under mixed input-state constraint.

Optimizing the process in real-time may lead to prolonged optimization time and increased computational complexity [10]. Therefore, various solutions have been proposed to improve efficiency, such as the application of an approximate PMP algorithm [11]. This strategy introduces a simple convex approximation to the local Hamiltonian, requiring the calculation and comparison of only five candidate Hamiltonians before determining the optimal powertrain control. Another significant aspect of these approaches is the discretization of the operating domain of powertrain components, which involves balancing computational effort and fine control requirements.

6.1.4 Equivalent consumption minimization strategy

To address the challenge of limited information about future events, on-line versions of off-line strategies can be employed. One common methodology is the Equivalent Consumption Minimization Strategy (ECMS) [12], which extends the Pontryagin Minimum Principle. This approach aims to minimize an equivalent fuel consumption on-the-fly, taking into account the battery power consumption through an equivalence factor s_0. The suitability for real-time applications is achieved by adaptively adjusting s_0 using either a fuzzy PI controller [13] or a correction term related to the battery State of Charge (SoC) [14]. Another option for the correction is the use of a 2-dimensional look-up table derived from an equivalence factor optimization, which can be applied for real-time adjustments [15]. Once tuned, these approaches exhibit sub-optimal performance but remain quite similar to off-line approaches [16–18]. However, if a dense discretization is required to explore the performance maps of powertrain sub-components, computational time becomes a significant concern.

As mentioned earlier, the ECMS involves minimizing an equivalent fuel rate at each time, which consists of the actual fuel rate and a contribution from the battery electrical power through an equivalence factor, given by:

$$\dot{m}_{\text{eq}}(u(t),t) = \dot{m}_f(u(t),t) + s_0 \cdot \frac{P_{\text{batt}}(u(t),t)}{LHV} \tag{6.9}$$

Here, LHV is the lower heating value of the fuel, P_{batt} represents the power released or absorbed by the battery, and s_0 is the equivalence factor. A piecewise linear description of s_0, different for battery charge and discharge phases, can closely approximate optimal powertrain management, but it requires adjustment based on vehicle characteristics and driving mission [17]. Various methodologies have been developed for an adaptive adjustment of the equivalence factor [14, 15, 17, 18]. Some of them rely on outputs derived from off-line optimization strategies [14, 15]. The impact of using a constant value for s_0 is evaluated in [17], revealing results very close to optimality.

Among the available alternatives, a robust approach involves an equivalence factor correction dependent on the difference between the current SoC level and a target value [13]. The correction is computed by a PID controller expressed as follows:

$$s_{\text{corr}}(t) - s_0 = K_p \cdot \Delta\text{SoC} + K_i \int_0^t \Delta\text{SoC} \cdot d\tau + K_d \frac{d}{dt}\Delta\text{SoC} \tag{6.10}$$

where $\Delta\text{SoC} = \text{SoC}(t) - \text{SoC}_{\text{target}}$

Here, $\text{SoC}_{\text{target}}$ is a reference SoC level, and ΔSoC is the error between the current SoC and the reference. The first term on the right-hand side of eq.

6.10 represents the proportional correction, while the second and third terms represent integral and derivative corrections, respectively. As will be further elaborated in the course of this chapter, another method for adapting the equivalence factor is based on the utilization of artificial intelligence techniques.

6.1.5 Efficient thermal/electric skipping strategy

The ETESS (Efficient thermal/electric skipping strategy) strategy has been previously investigated in [19]. In this PhD work, the application of ETESS is extended to improve energy management in HEVs/PHEVs equipped with small size engines. The core principle involves an alternative utilization of the thermal engine and electric machine to satisfy the power demanded for traction. Three operating modes are defined: pure thermal mode, pure electric mode, and parallel mode. Additionally, a fourth traction-charging mode is also considered in this investigation.

The choice between the pure thermal mode, pure electric mode, and the traction-charging mode depends, at each time, on the comparison between the total equivalent fuel consumption of each mode. The total equivalent fuel consumption is defined as the sum of the actual fuel rate $\dot{m}_f$ and an equivalent fuel rate $\dot{m}_{f,el}$ related to the electric energy drawn from the battery, as described by:

$$\dot{m}_{f,tot} = \dot{m}_f, th + \dot{m}_{f,el}$$

In the comparison, the parallel mode is considered only if the thermal engine cannot satisfy the entire power demand. The concept of the equivalent electric fuel rate is based on the idea that the power provided by the electric motor is produced by the thermal engine in an undefined time, while operating at its minimum brake-specific fuel consumption ($BSFC_{min}$). To consider the power losses along the driveline, the power demand is adjusted through the efficiencies of all the driveline components.

The ETESS logic is represented in the flowchart presented in Figure 6.1. Furthermore, referring to the PHEV architecture previously described in Chapter 5.4.2, the detailed description of each mode and the analytical expressions for the evaluation of the total equivalent fuel consumption are provided below.

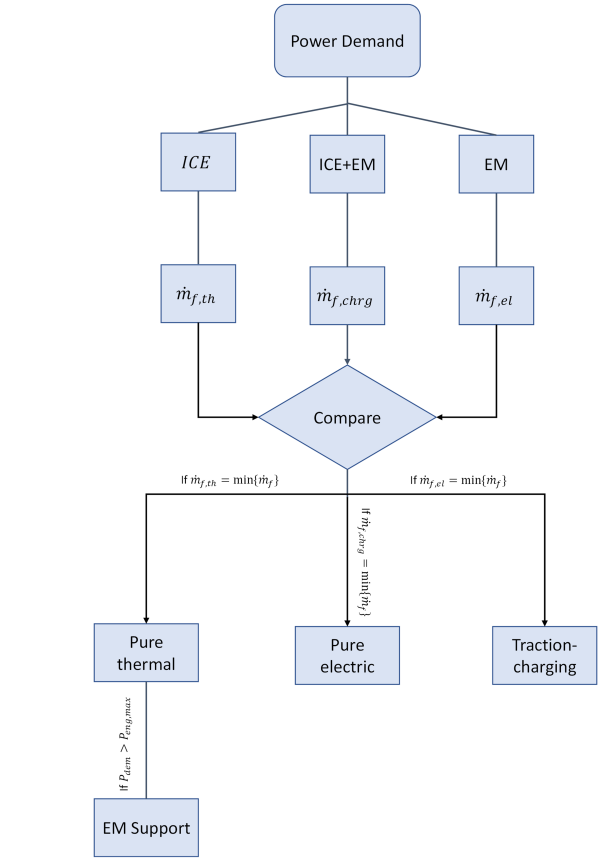

Figure 6.1: Flowchart that schematizes the ETESS logics. Source: [20]

As seen in Figure 6.2, in pure thermal mode, the engine supplies all of the necessary power. Figure 6.2-6.5 depicts the energy flows between each drivetrain component as red arrows. The actual fuel consumption rate of the thermal engine is determined by its operating conditions, characterized by torque output and rotational speed:

$$\dot{m}_{f,th} = \frac{P_{dem} \cdot BSFC}{\eta_{GB}\eta_{diff}} \tag{6.11}$$

Where P_{dem} represents the demanded wheel power, and η_{GB} and η_{diff} are the efficiencies of the differential and gearbox, respectively. As the entire power is supplied by the engine, the equivalent fuel consumption rate of the electric powertrain section is zero .

$$\dot{m}_{f,el} = 0 \tag{6.12}$$

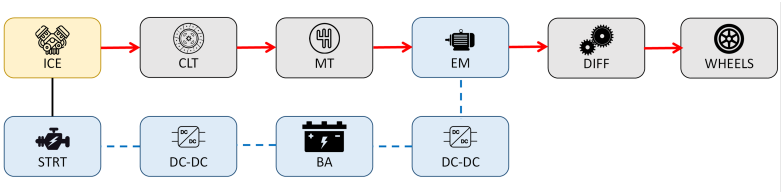

Figure 6.2: Energy fluxes in pure thermal mode. Source: [20]

While operating in parallel, the thermal engine is loaded to its full capacity, and the electric motor supplies the extra power needed to meet the demand (Figure 6.3). The actual fuel rate and the equivalent one are defined as following:

$$\dot{m}_{f,th} = \frac{P_{eng,max} \cdot BSFC}{\eta_{GB}\eta_{diff}} \tag{6.13}$$

$$\dot{m}_{f,el} = c_0 \cdot \frac{(P_{dem} - P_{eng,max} \cdot \eta_{GB} \cdot \eta_{diff})\, BSFC_{min}}{\eta_{EM}\eta_{diff}\eta_{EM}\eta_{EM}} \tag{6.14}$$

where η_{EM}, η_{EM}, η_{EM}, are respectively the efficiencies of the electric motor, battery, and inverter. c_0 is a tuning constant and represents the fuel-equivalent consumption of electric driving. $P_{eng,max}$ is the maximum engine power.

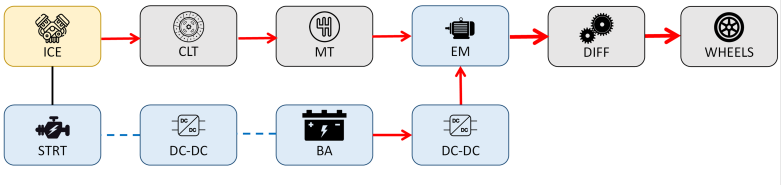

Figure 6.3: Energy fluxes in parallel mode. Source: [20]

In contrast to pure thermal mode, pure electric mode completely relies on the motor to supply the required power (Figure 6.4). In this mode, the real fuel rate is zero, while Eq. 6.16 provides the corresponding fuel rate:

$$\dot{m}_{f,th} = 0 \tag{6.15}$$

$$\dot{m}_{f,el} = c_0 \cdot \frac{P_{dem} BSFC_{min}}{\eta_{EM}\eta_{diff}\eta_{EM}\eta_{EM}} \tag{6.16}$$

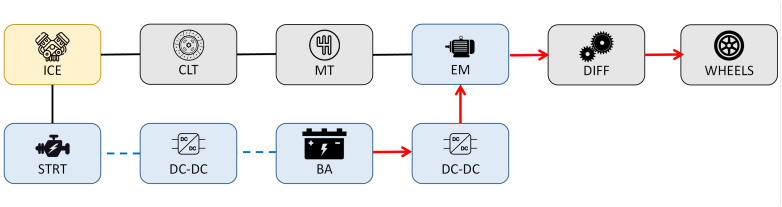

Figure 6.4: Energy fluxes in pure electric mode. Source: [20]

The purpose of the traction-charging mode is to improve battery charge that would otherwise be possible solely through regenerative braking. This could result in a lower SoC, particularly in high-power, demanding driving missions. Because of the engine's limited maximum power (Table 5.3), the car would frequently operate in parallel mode, running the danger of entirely draining the battery. The electric machine functions as a generator in traction-charging mode, using the thermal engine's extra power to replenish the battery while the engine is running at its maximum load (Figure 6.5). Only when the power necessary for traction is less than the engine's maximum power is the traction-charging mode permissible (properly scaled by the drivetrain component efficiencies).

$$\dot{m}_{f,th} = \frac{P_{eng,max} \cdot BSFC}{\eta_{GB}\eta_{diff}} \tag{6.17}$$

$$\dot{m}_{f,el} = c_0 \cdot (P_{dem} - P_{eng,max} \cdot \eta_{GB} \cdot \eta_{diff})\, BSFC_{min} \cdot (\eta_{EM}\eta_{diff}\eta_{EM}\eta_{EM}) \tag{6.18}$$

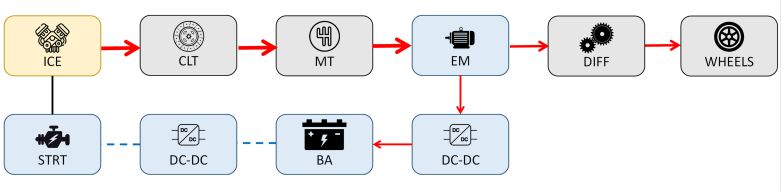

Figure 6.5: Energy fluxes in traction-charging mode. Source: [20]

Based on the aforementioned considerations, whether the engine should be started by the motor starter in pure thermal mode, parallel mode, or traction-charging mode, the actual fuel rate is increased by an analogous activation fuel rate $\dot{m}_{f,th,ON}$ determined as follows:

$$\dot{m}_{f,th,ON} = c_0 \cdot \frac{P_{strt} BSFC_{min}}{\eta_{strt}\eta_{batt}\eta_{inv2}} \tag{6.19}$$

$$\dot{m}_{f,th} = \frac{P_{eng} \cdot BSFC}{\eta_{GB}\eta_{diff}} + \dot{m}_{f,th,ON} \tag{6.20}$$

where η_{inv2} is the efficiency of the starting DC-DC converter, P_{eng} is the engine power, and P_{strt} is the motor starter power. It is important to note that the clutch efficiency is described using a simplified technique in the control logic. Although such operations are more thoroughly detailed in the physical model of the drivetrain, it is believed that clutch engagement and disengagement maneuvers are instantaneous and characterized by a unitary efficiency. The benefit of ETESS is reduced computational cost.

6.2 Adaptive efficient thermal/electric skipping strategy for the management of a parallel plug-in HEV

As previously mentioned, EMSs are strictly related to battery SoC management strategies. In this work, significant enhancements were made to the ETESS logics to improve battery SoC management in a parallel P3 PHEV equipped with a small size gasoline engine. The vehicle model used as a case study was introduced in Chapter 5.4.2. An adaptive function was integrated into the ETESS to tailor the strategy to a charge blended control, assuming a linear battery discharge with respect to the distance traveled and realizing an Adaptive-ETESS (A-ETESS). This hypothesis is commonly found in the literature [3]. In order to establish an appropriate comparison baseline, the ECMS is also equipped with the identical adaptive function, resulting in the implementation of an Adaptive-ECMS (A-ECMS).

6.2.1 Adaptive strategies

As previously mentioned, a Charge Blended strategy is proposed by introducing an adaptive variant of the ECMS and ETESS. The CB strategy involves the linear decrease of the SoC target with respect to the driven distance, represented by the equation:

$$SoC^*(t) = \frac{SoC_{ini} - SoC_{fin}}{L_m} \cdot (L_m - x(t)) + SoC_{fin} \tag{6.21}$$

where SoC_{ini} and SoC_{fin} represent the battery SoC at the beginning and end of the driving mission, $x(t)$ denotes the vehicle's position at time t, and L_m is

the total distance to be covered. The necessary information to evaluate the SoC target can be obtained from a map service provider or other sources. The ETESS, previously presented in Section 6.1.5, is extended to incorporate the adaptive CB strategy by adjusting the tuning constant c_0. This adaptation takes into account the variation of battery properties with respect to SoC. For each operating mode defined in Section 6.1.5, the equivalent fuel consumption (Eq. 6.12-6.14-6.16-6.18) and the total equivalent fuel consumption are reformulated as follows:

$$\bar{\dot{m}}_{f,el} = k_{pen} \cdot \dot{m}_{f,el} \tag{6.22}$$

$$\dot{m}_{tot,eq} = \dot{m}_{f,th} + \bar{\dot{m}}_{f,el} \tag{6.23}$$

where a penalization factor, k_{pen}, is introduced. During the driving mission, two scenarios may occur:

1. When the actual SoC is higher than the reference SoC^*, the CB strategy promotes pure electric driving by reducing the cost associated with it.

2. Conversely, when the actual SoC is lower than the reference SoC^*, the CB strategy penalizes pure electric driving by increasing the cost related to it.

To handle these scenarios, two different functions are developed based on the difference between the actual SoC and the reference value, as well as the normalized distance to travel ($\Delta x = (L_m - x)/L_m$). To maintain control stability, logarithmic functions are chosen, assuming that the adaptive cost correction increases with the traveled distance and the SoC error. To optimize model performance, these functions are implemented as a lookup table, and their respective values are illustrated in Figure 6.6-6.7.

Aiming at achieving consistent comparisons, an adaptive term is introduced in the ECMS, leading to the following expression:

$$J = \dot{m}_f + s_0 \cdot k_{pen} \cdot \frac{P_{\text{batt}}}{LHV} \tag{6.24}$$

The optimal values of parameters c_0 and s_0 were determined through a series of preliminary tests conducted on four driving cycles: WLTC, US_{06}, Artemis Highway, and a Real Driving Cycle. For this purpose, an automated and iterative procedure was devised to minimize the time-integral difference between the actual SoC and its target SoC^*. During each iteration, the values of c_0 and s_0 remained constant and were automatically updated at the

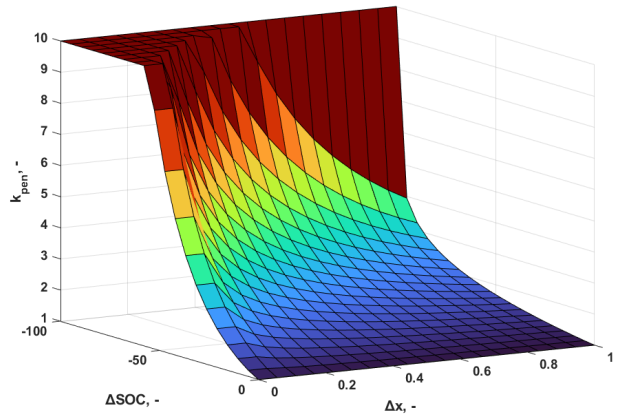

Figure 6.6: Adaptive function k_{pen} for $SoC(x) < SoC^*(x)$. Source: [20]

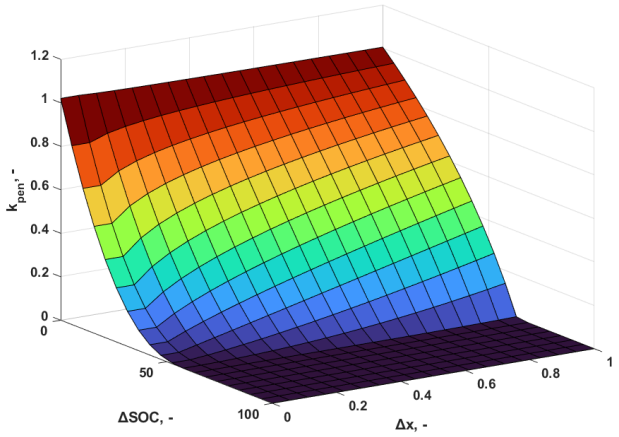

Figure 6.7: Adaptive function k_{pen} for $SoC(x) > SoC^*(x)$. Source: [20]

beginning of each driving cycle using a gradient method. This iterative process continued until the integrated SoC error reached its minimum level. In these analyses, typical values of SoC_{ini} and SoC_{fin} (80% and 30%, respectively) were employed. The SoC^* function was evaluated using Equation 6.21. Exemplary results of this tuning procedure are illustrated in Figure 6.8, depicting the SoC tendencies during the WLTC for the selected value of c_0 (1.18 in black), and the discarded values (1.24 in red and 1.12 in blue). The figure clearly

demonstrates that the optimal value of c_0 leads to a better agreement between the actual SoC and the target SoC^* in comparison to the other considered values of c_0.

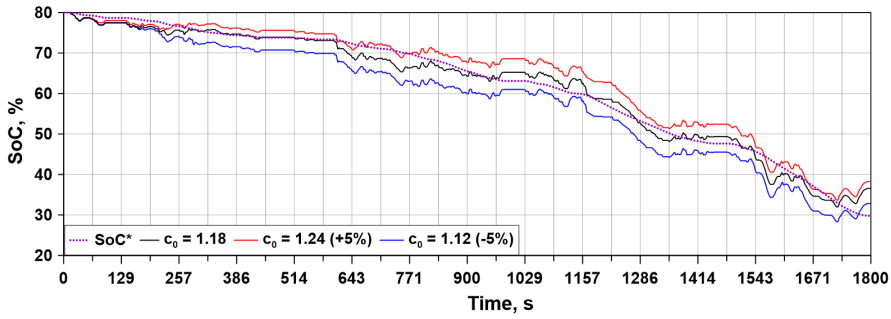

Figure 6.8: Parametric analysis of c_0 on SoC evolution along WLTC; comparison with SoC^*. Source: [20]

The assessed values of c_0 and s_0 from the preliminary tests exhibit a noticeable correlation with the distance traveled, as illustrated in Figure 6.9. In light of this observation, suitable fitting functions (depicted as dashed lines in Figure 6.9) have been determined for both c_0 and s_0. These functions enable the assignment of initial values to the two tuning constants, regardless of the specific driving cycle, solely based on the total distance to be covered. Subsequently, these functions are utilized in the subsequent results presented in this study.

6.2.2 Test cases

A set of 8 driving cycles, as detailed in Table 6.1, has been carefully chosen to facilitate a comprehensive comparison between A-ETESS and A-ECMS. The main objective is to examine the performance of these strategies across diverse scenarios, encompassing a wide range of maximum and mean speeds, accelerations, and distances to be covered. To ensure the relevance of the evaluation, the initial and final battery SoC values have been standardized to 80% and 30%, respectively, consistent with typical plug-in hybrid operations. Additionally, the comparison is reinforced by incorporating two Real Driving Emission-compliant cycles, obtained from GPS data, specifically cycle #7 and #8 from Table 6.1. These RDE-compliant cycles contribute to the robustness and practicality of the assessments.

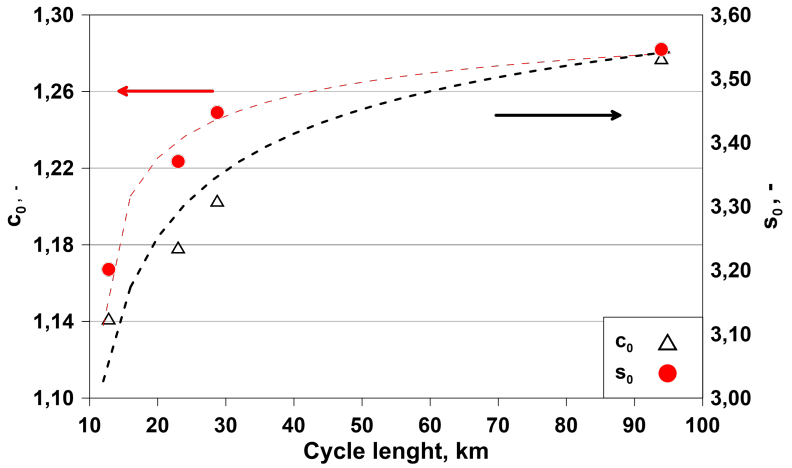

Figure 6.9: Parametric analysis of c_0 on SoC evolution along WLTC; comparison with SoC. Source: [20]*

Table 6.1: Tested Driving Cycles

TC	Cycle	L_m (km)	V_{mean} (km/h)	a_{max} (m/s^2)	V_{max} (km/h)
1	WLTC	23.00	46.5	1.75	131.3
2	FTP75	17.77	25.9	1.48	91.2
3	LA92	15.80	39.6	3.08	108.1
4	US06	12.80	77.9	3.755	129.2
5	ARTEMIS HIGHWAY	28.74	96.9	1.92	131.8
6	ARTEMIS RURAL	17.27	57.5	2.36	111.5
7	RDE1	93.94	50.5	3.33	126.0
8	RDE2	78.85	50.7	5.04	128.8

6.2.3 Fuel consumption correction related to battery discharge

To facilitate a meaningful comparison between the two analyzed EMSs, the total consumed fuel is selected as the assessment parameter to evaluate energy consumption across different test cases. The driving mission involves the consumption of two distinct energy sources: fuel and electrical energy stored in the battery. To assess the total fuel consumption, the overall battery discharge at the end of the driving cycle is converted into an equivalent amount of fuel. This conversion is based on the assumption that the energy drawn from the battery (ΔE_{batt}) has been produced by the engine operating at its average

efficiency point ($\bar{\eta}$) for the given driving mission. The additional equivalent consumed fuel is mathematically represented as:

$$\Delta m_{\text{eq}} = \frac{\Delta E_{\text{batt}}}{LHV \cdot \bar{\eta}} \tag{6.25}$$

Subsequently, the total fuel consumed (m_{tot}) during the driving mission is expressed as:

$$m_{\text{tot}} = m_{ICE} + \Delta m_{\text{eq}} \tag{6.26}$$

Where m_{ICE} represents the actual fuel consumed during the driving cycle.

Equation 6.25 emphasizes that to minimize Δm_{eq} the engine should operate at the highest possible average efficiency ($\bar{\eta}$). This consideration underscores the importance of maximizing the engine's average efficiency to reduce the equivalent consumed fuel during the driving mission.

6.2.4 Results

In the following, the detailed results for three different test cases (representative of a high-speed cycle, low-medium speed cycles, and an RDE-compliant cycle) are discussed for the sake of brevity. Regarding test case 1 (Table 6.1), both A-ECMS and A-ETESS demonstrate adherence to the SoC target profile and nearly achieve the desired SoC at the end of the mission (Figure 6.10(b)). The adaptive factor effectively reflects the difference between the instantaneous SoC and the corresponding target profile (6.10(c)). During the high-speed portion of the cycle (between 1400 and 1800s), both strategies engage the electric motor to assist the ICE. The ICE delivers its maximum torque to meet the power requirements at the wheels, resulting in similar SoC trends for A-ETES and A-ECMS (6.10(b)). Occasionally, A-ETESS commands battery recharges through the ICE, causing the ICE to operate at high load for brief periods. On the other hand, A-ECMS experiences longer battery recharge phases with a lower power delivered by the ICE due to the ability to regulate power-split. Overall, the strategies exhibit very similar behavior, as evident from comparable levels of accumulated fuel consumption (6.10(f)).

Figure 6.11 illustrates the detailed results for the FTP75 cycle, which corresponds to test case #2 from Table 6.1. In Figure 6.11(c), the adaptive term is frequently observed close to the unit, and the SoC trends (Figure 14(b)) closely align with the target. While both A-ETESS and A-ECMS exhibit similar management of the electric motor, discrepancies emerge in the utilization of the ICE, as depicted in Figure 6.11(d) and Figure 6.11(e), respectively. The final consumed fuels are comparable, but A-ETESS involves

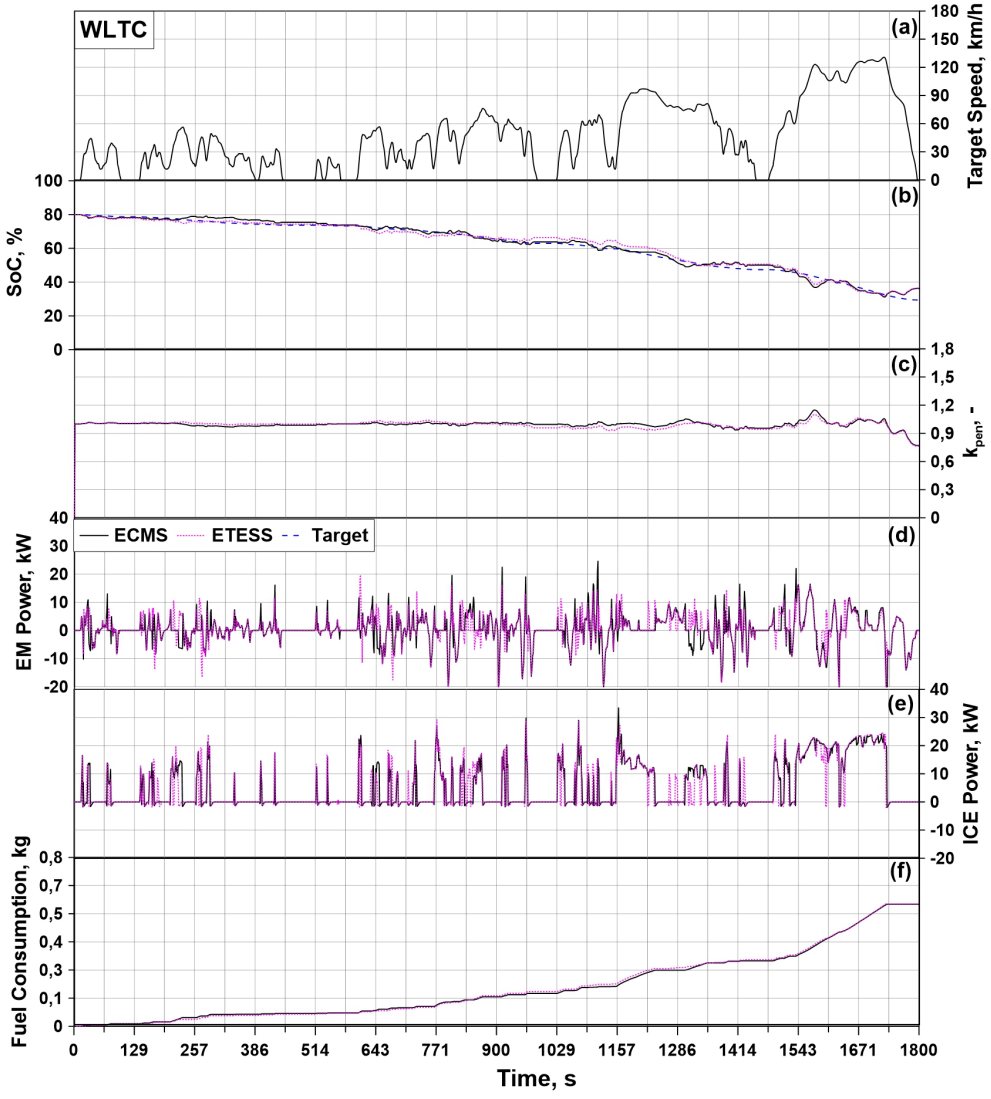

Figure 6.10: WLTC,(a) Target speed. ETESS/ECMS comparisons of battery SoC (b), k_{pen} (c), EM power (d), ICE power (e), and cumulated consumed fuel (f). Source: [20]

a higher battery discharge towards the end of the cycle compared to A-ECMS, resulting in slightly lower fuel economy. These observed differences in battery recharge management between A-ECMS and A-ETESS, as discussed for the WLTC cycle, are confirmed once again in the FTP75 cycle.

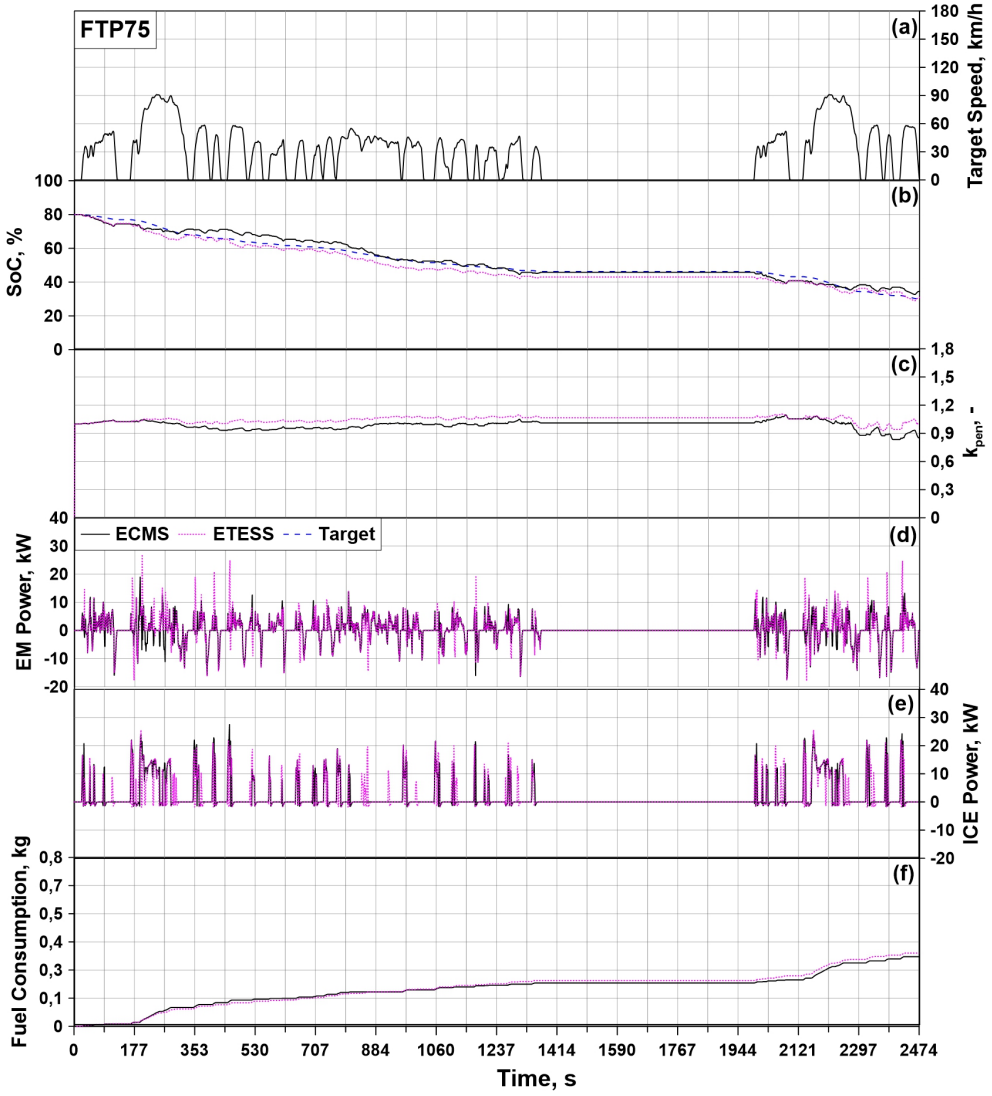

Figure 6.11: FTP75,(a) Target speed. ETESS/ECMS comparisons of battery SoC (b), k_{pen} (c), EM power (d), ICE power (e), and cumulated consumed fuel (f). Source: [20]

Figure 6.12 presents the instantaneous trends of SoC (Figure 6.12(b)) and the adaptive term (Figure 6.12(c)) throughout the RDE2-compliant cycle (test case #8 Table 6.1). Additionally, the evaluations of ICE and electric motor powers, along with the consumed fuel, are represented in Figure 6.12(d), (e),

and (f), respectively. Upon comparing the SoC and electric machine power trends for both strategies, subtle distinctions arise in electrical energy usage due to the capability of A-ECMS to explore intermediate power-split options. Throughout the majority of the cycle, both strategies opt for driving the vehicle in the same mode. In the final portion of the cycle (approximately between 4400 and 5400s), both strategies direct the ICE to operate at its maximum torque working point, concurrently initiating some battery recharge. These similar management strategies result in comparable final values for the cumulative fuel consumed.

In Figure 6.13 bar chart, a comprehensive and comparative overview of the total fuel consumed per kilometer for the two strategies is presented. The percentage difference between the strategies is displayed above each pair of bars and is calculated as follows:

$$\Delta m_{tot} = \frac{m_{tot}^{A-ECMS} - m_{tot}^{A-ECMS}}{m_{tot}^{A-ETESS}} \cdot 100 \tag{6.27}$$

As evident from the results, the average total fuel consumed difference between A-ETESS and A-ECMS remains below 2.4%. However, notable discrepancies arise primarily in test case , attributed to the management of battery recharge. Regarding vehicle drivability, both strategies exhibit comparable performance, as indicated by the maximum and averaged values of vehicle acceleration derivatives presented in Table 6.2.4. Analyzing the number of Engine ON occurrences per minute (also in Table 6.2.4), the differences between A-ETESS and A-ECMS are not significant. Due to its inherent concept, A-ETESS may require more frequent engine switch-on events, but in most cases, these occurrences are only slightly higher than those of A-ECMS. Surprisingly, A-ETESS even outperforms A-ECMS in case #5. In future endeavors, additional efforts could focus on reducing the number of engine switch-on events in real on-vehicle applications. This optimization aims to enhance the thermal management and effectiveness of after-treatment devices for the ICE.

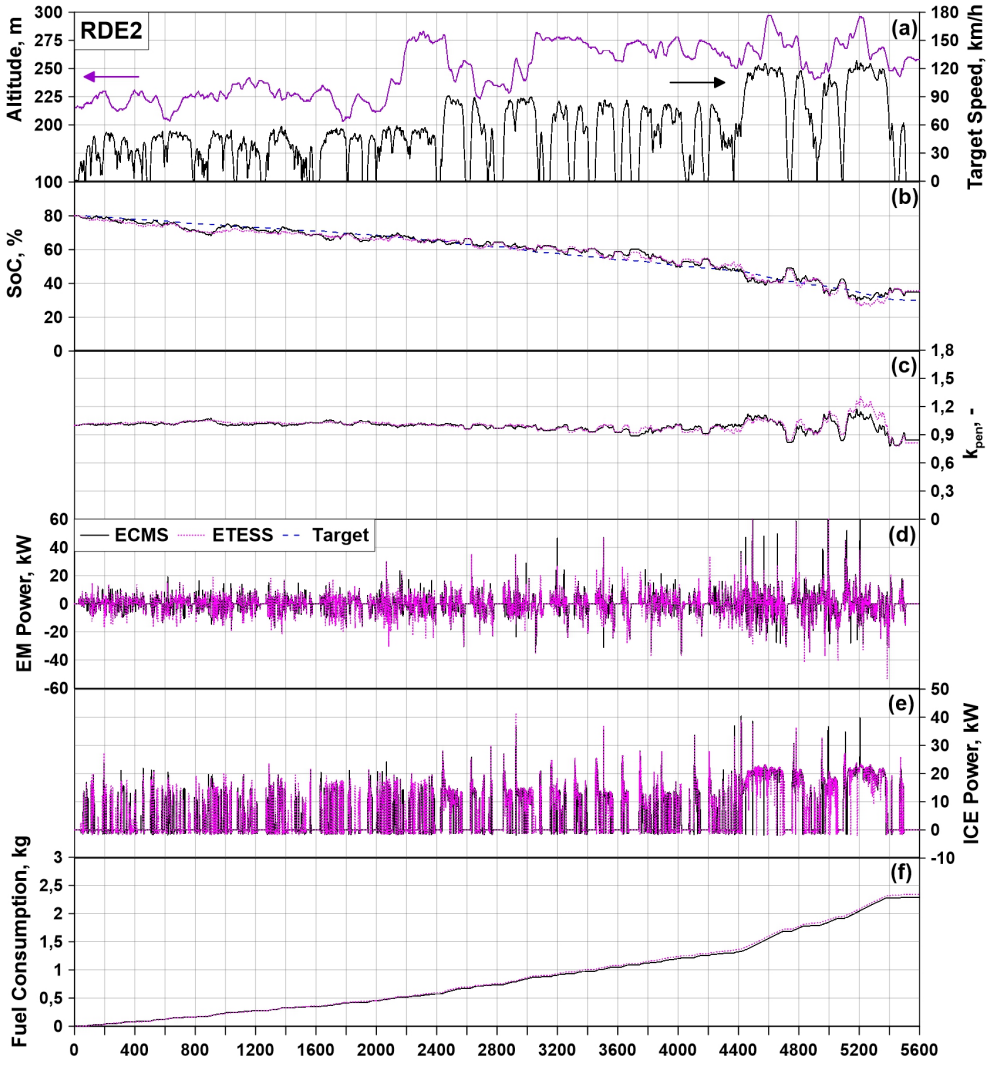

Figure 6.12: RDE2,(a) Target speed. ETESS/ECMS comparisons of battery SoC (b), k_{pen} (c), EM power (d), ICE power (e), and cumulated consumed fuel (f). Source: [20]

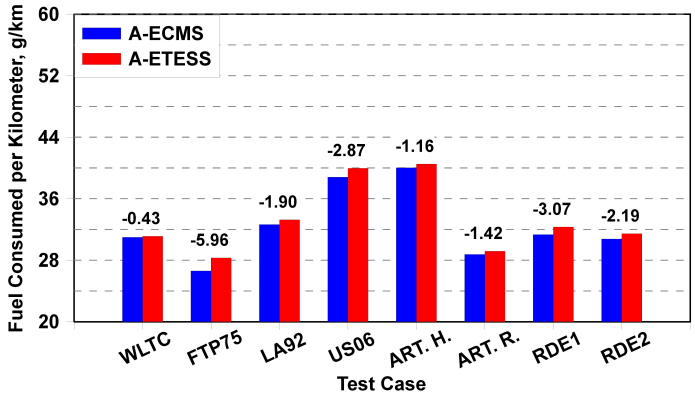

Figure 6.13: Comparison between A-ECMS and A-ETESS of kilometric consumed fuel and percent difference for the test cases of Table 6.1. Source: [20]

Table 6.2: Number of engine ON per minute and maximum and mean of vehicle acceleration derivative for the test cases of Table 6.1.

TC	Strategy	Engine ON/min	max($\frac{da}{dt}$) (m/s^3)	mean($\lvert\frac{da}{dt}\rvert$) (m/s^3)
1	A-ETESS	1.500	1.775	0.135
	A-ECMS	1.333	1.334	0.131
2	A-ETESS	1.189	1.384	0.120
	A-ECMS	0.994	1.384	0.118
3	A-ETESS	1.923	2.863	0.284
	A-ECMS	1.714	2.723	0.279
4	A-ETESS	1.100	2.090	0.319
	A-ECMS	1.100	2.092	0.313
5	A-ETESS	0.899	2.325	0.220
	A-ECMS	0.787	2.326	0.215
6	A-ETESS	2.052	3.009	0.263
	A-ECMS	1.941	3.014	0.264
7	A-ETESS	1.560	2.659	0.223
	A-ECMS	1.470	2.853	0.223
8	A-ETESS	1.597	2.447	0.218
	A-ECMS	1.511	2.563	0.218

6.2.5 PIL Tests

Additional analyses were conducted to assess the computational effort and execution time of A-ETESS and A-ECMS using a Processor in the Loop (PIL) testing approach. For this purpose, a C-Code was generated through a Simulink Coder and loaded onto the high-performance NUCLEO-H743 board. This board is equipped with an ARM Cortex-M7 processor running at up to 480 MHz, with 424 Core-Mark/1027 DMIPS executing from flash memory. The GNU Tools for ARM Embedded Processors were employed for the building process. During the PIL tests, the powertrain control strategy ran on the NUCLEO board, while the vehicle and powertrain physical models were executed on a PC-Host. Asynchronous serial communication was used for the interaction between the two components. After completing the simulations in PIL mode, Simulink generated a code execution profiling report. The outcomes for all the test cases in Table 6.1 were similar. For brevity, Table 6.2.5 presents only the results related to the WLTC test case. In Table 6.2.5, it is evident that A-ETESS outperforms A-ECMS significantly, as it is two orders of magnitude faster. The maximum CPU utilization for A-ETESS is merely 0.022%, while for A-ECMS, it is 18.18%. Both strategies exhibit average execution times lower than the typical cycle time of a CAN message for an updated engine torque request (10 ms). However, A-ETESS demonstrates reduced computational effort, confirming the potential to run multiple control strategies on the same micro-controller and optimize its utilization.

Table 6.3: PIL testing results for WLTC.

Task	A-ETESS	A-ECMS	Difference, %
Maximum CPU Utilization, %	0.022	18.18	-99.87
Average CPU Utilization, %	0.008	17.8	-99.96
Maximum Execution Time, ms	0.045	1.817	-97.52
Average Execution Time, ms	0.016	1.780	-99.10

6.3 Artificial intelligence empowering energy management strategies: harnessing the power of AI

In recent times, due to the swift advancement of artificial intelligence (AI) and computer technologies, learning algorithms have been progressively employed in the EMS domain, emerging as a fresh and popular area of research. In

addition to achieving desirable optimization effects, learning-based EMSs also offer significant possibilities for real-time applications, presenting a trade-off between rule-based EMSs and model-based optimization EMSs. Nonetheless, the development of learning-based EMSs poses certain challenging issues that need to be addressed, including the need for extensive driving-related training datasets, lengthy training times, the instability of the training process, and the complexity of setting objective functions.

In this chapter, following a review of the principles of neural network operation, a bibliographic analysis is conducted on EMSs enhanced through the utilization of artificial intelligence techniques.

6.3.1 Fundamentals of Artificial Intelligence: A Basic Overview

Artificial Intelligence encompasses a broad array of computer science disciplines focused on replicating human intelligence in tasks such as visual perception, speech recognition, decision-making, and language translation. The term "deep learning" has gained prominence in recent years due to the increased emphasis on creating models capable of autonomous learning from data, utilizing a mathematical concept called an "artificial neuron," which was originally theorized by Alan Turing in 1943 and incorporated into more intricate structures known as neural networks. Given the vastness of the challenge of creating intelligent machines and the various interpretations of "intelligence" concerning human actions, AI addresses multiple sub-problems. It facilitates problem-solving and reasoning models that employ algorithms mimicking human logical reasoning processes, as well as knowledge representation for different types of information. Furthermore, AI's significance extends to natural language processing, a sub-field dedicated to enabling machines to comprehend human language. Prominent examples include Amazon's Alexa and various voice recognition devices. Lastly, AI has significantly impacted the realm of learning, leading to the emergence of machine learning (ML).

ML is a subset of artificial intelligence that aims to design models capable of learning relationships and patterns from input data without explicit programming. The term "learning" refers to the ability of models to auto-learn from the data, while "machine" denotes the computational aspect of these models. There are three broad categories of machine learning techniques based on the structure of training data and feedback available to the learning method [Source: [21]]:

- **Supervised Learning**: This approach uses labeled data, where input data and corresponding output data are provided. The model's goal is to find a general rule to associate inputs with their correct outputs.

- **Unsupervised Learning**: Here, the model only receives input data without labeled outputs. The objective is to discover hidden relationships and similarities among the data points, often used in conjunction with supervised learning for classification tasks.

- **Reinforcement Learning**: In this category, models interact with dynamic environments to pursue specific goals. The model receives rewards based on its actions, encouraging it to find optimal solutions to achieve the goal. These models find applications in control systems and energy management for hybrid vehicles.

Another classification can be made based on the output structure of the model:

- **Classification**: Models in this category have discrete outputs representing different classes. These are supervised models used for tasks like classifying inputs into predefined classes.

- **Regression**: In regression problems, the model's output is a continuous variable, making it a supervised model. An example could be predicting the electric motor torque in a hybrid electric vehicle.

- **Clustering**: Unsupervised clustering models divide input data into groups, with the number of groups not known in advance. These models are useful for discovering patterns and relationships among data points.

There are many types of Machine Learning algorithms, each with its own characteristics, advantages, and specific applications. Some of the most common algorithms include Support Vector Machines [21], Decision Trees [22], Random Forest [23], K-Means [24], Principal Component Analysis [25] and Q-Learning [26]. In this study, the focus was on employing supervised learning techniques to address the EMS design problem. Specifically, the utilization of Long Short-Term Memory (LSTM) neural network is discussed in detail due to their ability to retain temporal relationships within time series input data.

Introduction to Artificial Neural Networks

Artificial Neural Networks (ANNs), commonly known as Neural Networks (NNs), aim to replicate the functioning of the human brain, enabling machines to mimic human thinking. Traditional computer programming and simple machine learning models fall short in solving tasks that the human brain handles effortlessly, such as speech and image recognition. To address these

challenges, deep learning emerged as a new branch of artificial intelligence and machine learning, leveraging the concept of artificial neural networks and increasing complexity through larger architectures and deeper networks. However, the true potential of deep learning models could only be realized in the past decade, with the advancement of computational power in computers and the availability of cluster computation and cloud computing.

The human brain relies on structures called neurons, which communicate with each other through electrical impulses. Similarly, artificial neurons, also known as perceptrons, are interconnected within artificial networks and exchange information using numerical data. Although these models do not perfectly replicate biological neural networks, they are inspired by the brain's operating principles and serve as mathematical models for computation. To gain a comprehensive understanding of the link between biological and artificial neurons, it is essential to grasp the functioning of biological neurons. This discussion does not aim to extensively delve into the biological neuron's structure, but rather focuses on the mechanism governing the information flow within it. A biological neuron comprises three main components:

- Dendrites: Acting as the input channel, dendrites receive information from other neurons in the network.
- Soma: Also known as the cell body, the soma plays a central role. It accumulates the inputs received from dendrites around the axon hillock. The summation process takes into account the synaptic strength, which represents the connection between neurons in the network. A stronger connection results in a higher weight applied to the corresponding input. After this weighted sum is computed, it is compared to a threshold. If the sum exceeds this threshold, the neuron generates an action potential, indicating its activation.
- Axon: Serving as the neuron's output, the axon carries the action potential and employs synaptic connections to relay this information to other neurons in the network.

The artificial neural network aims to imitate the behavior of biological neurons and comprises essential components: an input, an output, a cell that performs a mathematical operation, and finally, an output passed to subsequent neurons. The operation within the neuron's cell, or perceptron, can be described as follows:

$$a = \bar{x} \cdot \bar{W} + b = \sum_{i=1}^{N} W_i x_i + b \tag{6.28}$$

Where:

- $\bar{x} \in \mathbb{R}^N$ represents the input vector, which gathers outputs from other N interconnected neurons.
- $\bar{W} \in \mathbb{R}^N$ denotes the weight vector, signifying the synaptic strengths and determining the influence of specific inputs on the output.
- $b \in \mathbb{R}$ is the bias of the pre-activation function, a.

This initial part of the model simulates the processes occurring within the cell of a biological neuron. The subsequent step involves modeling the action potential and neuron activation, achieved through the activation function $f(\cdot)$, operating on the pre-activation function to yield the output of the respective neuron:

$$y = f(a) = f\left(\sum_{i=1}^{N} W_i x_i + b\right) \tag{6.29}$$

The purpose of the activation function is to determine whether a neuron should produce a value higher, lower, or equal to 0, similar to the threshold concept in the biological counterpart. Different activation functions proposed in the literature characterize each neuron, rendering them more suitable for specific applications.[27] Several commonly used functions are:

- Hyperbolic tangent function: $\tanh(a) = \frac{e^a - e^{-a}}{e^a + e^{-a}}$
- Softsign function: $\text{softsign}(a) = \frac{a}{1+|a|}$
- Sigmoid function: $\sigma(a) = \frac{1}{1+e^{-a}}$
- Threshold function: $f(a) = \begin{cases} k, & \text{if } a > 0 \\ 0, & \text{if } a \leq 0 \end{cases}$

Structure of Neural Networks

An artificial neural network comprises multiple neurons interconnected in a predetermined manner, shaping the overall architecture. Each layer contains neurons that connect only with the neurons in the preceding and succeeding layers, illustrated in Figure 6.14. These layers are categorized into three types based on their functions: Input layer, Hidden layer, and Output layer. The input layer prepares the input data for further processing by the network, which is especially useful for complex networks that require data pre-processing such

as normalization and mini-batch assembly. The hidden layer performs essential mathematical computations, and the number of hidden layers determines the depth of the network. Networks with more than one hidden layer are considered deep neural networks. Finally, the output layer collects and processes information from the hidden layers to present the desired output to the user.

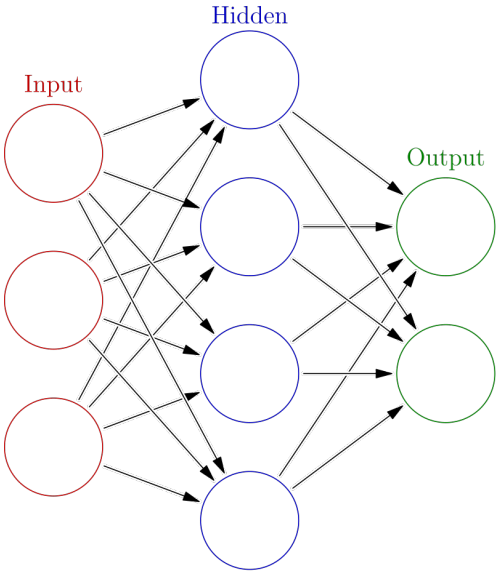

Figure 6.14: Neural Network Architercture

Neural Networks Training

Training a neural network involves iteratively adjusting its parameters, (weights and biases), to minimize the difference between its predictions and the actual target values in the training data. Several algorithms are used for neural network training, each with its strengths and weaknesses. Some commonly used training algorithms are:

- Gradient Descent: Gradient Descent is the most fundamental optimization algorithm for training neural networks. It aims to find the optimal set of weights and biases by minimizing the loss function. The algorithm calculates the gradient of the loss function with respect to each parameter and updates them in the opposite direction of the gradient. Learning rate, which determines the step size during updates, is a critical hyperparameter that affects the algorithm's convergence and stability.

- Stochastic Gradient Descent (SGD): SGD is a variation of Gradient Descent that updates the model's parameters after each individual data point or a small batch of data points. It introduces randomness during updates, which helps escape local minima and can lead to faster convergence. However, the randomness might cause instability and noise in the learning process.

- Adaptive Learning Rate Algorithms: To overcome the sensitivity of learning rate choice in standard gradient-based methods, adaptive learning rate algorithms like AdaGrad, RMSprop, and Adam adjust the learning rate dynamically for each parameter during training. These algorithms enable efficient learning by individually adapting the learning rate based on the historical gradient information.

- Backpropagation: Backpropagation is a key algorithm for computing the gradients needed in neural network training. It efficiently calculates the gradient of the loss function with respect to each parameter by propagating the errors backward through the network. It allows neural networks with multiple layers to learn complex representations and patterns.

- Mini-batch Gradient Descent: Mini-batch Gradient Descent combines the benefits of both Gradient Descent and SGD by updating parameters using a small batch of data points. This approach strikes a balance between computational efficiency and stability, making it one of the most widely used algorithms in practice.

Utilizing the stochastic gradient descent method, the network's weights are updated in each training iteration based on the partial derivative of the error function with respect to the current weight. Common activation functions such as tanh or sigmoid have output ranges within (0, 1), causing their gradients to also remain in this range. In deep neural networks, this limitation can lead to the vanishing gradient problem, where the error function's gradient becomes exceedingly small, impeding parameter updates and stalling the training process. This issue arises due to the chain rule used in backpropagation with SGD, as the neural network model can be seen as a composition of n functions, each representing a neuron, and their product tends to 0 with an increasing number of neurons. Conversely, the exploding gradient problem occurs when the error function's gradient approaches infinite values, influenced by the activation functions used in the network.

Recurrent Neural Networks

In the preceding section, feed-forward neural networks were analyzed, where data flows only from the input layer to the output layer through the hidden layers. This setup ensures the absence of cyclic connections between layers, isolating each observation in the dataset from others. However, in certain scenarios, it becomes necessary to consider correlations between observations. For instance, the vehicle speed at a specific time instant is not an isolated value; it is closely related to both the preceding and succeeding time points. In such cases, the EMS of a hybrid vehicle needs to consider the entire sequence of speed, SoC, and other powertrain parameters rather than a single time instant. For HEV EMS applications, feed-forward neural networks are not optimal since they cannot work with sequences and capture the temporal trends in input features. Instead, a neural network capable of handling sequences and incorporating temporal dynamics is required. Recurrent Neural Networks (RNNs) are a class of artificial neural networks that address this need. RNNs allow connections between nodes in the network architecture to occur in a temporal sequence, enabling dynamic temporal behavior. As depicted in Figure 6.15, each neuron in an RNN is connected in a loop, and the output from the previous time step becomes an additional input.

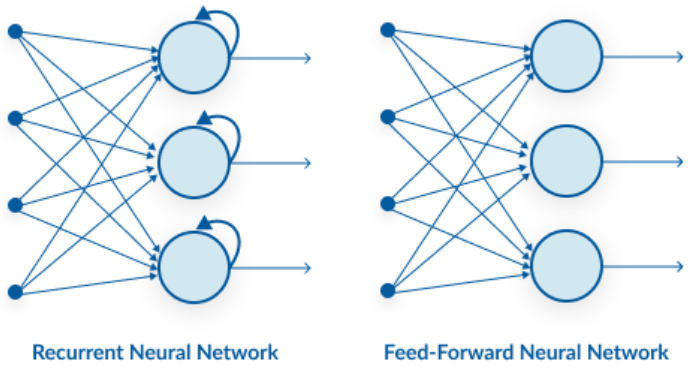

Figure 6.15: Difference between RNN and feed-forward NN

The ability of RNNs to maintain a state memory for each neuron makes them well-suited for dynamic and time-variant applications, such as designing the energy management system for a hybrid vehicle. They can effectively handle time-series data and capture dependencies between different time steps, making them ideal for modeling sequential processes. Moreover, RNNs can also be utilized for predictive tasks, where they can forecast future time steps based

on previously known sections. Several types of different layers can be used to build the network, such as Gated Recurrent Unit (GRU) and Long Short-Term Memory (LSTM) layers. A GRU layer enables the consideration of previous segments in a sequence to compute the current step's output. This capability is facilitated by the hidden state, which holds the output of the GRU layer at a specific time step. The layer incorporates information into or removes information from the state using gates, known as the reset gate and the update gate. Each gate performs typical operations of a standard perceptron with weights and biases, which are appropriately adjusted during the training phase, akin to a traditional neural network. The fully gated version of the GRU layer consists of two gates: the reset gate, which regulates the extent of state reset, and the update gate, which controls the level of state update. These gates play a crucial role in determining how the previous information is utilized to compute the current output of the GRU layer.

The LSTM layer[40] represents an enhanced version of the traditional GRU layer, specifically designed to address the challenges of recurrent neural networks. One prominent issue with RNNs using the GRU layer is their struggle to learn long-time dependencies, mainly due to the vanishing or exploding gradient problem. This problem becomes especially apparent when the network attempts to retain long-time dependencies during the training phase with the backpropagation algorithm. LSTM overcomes this problem by allowing gradients to flow without vanishing, although it does not completely prevent explosion. In Figure 6.16, the information flow within an LSTM layer is illustrated. The working principle of the LSTM cell can be described by its constituent elements: the input gate (i_t), forget gate (f_t), output gate (o_t), cell state (C_t), and hidden state (h_t). These gates and states can be mathematically represented as follows:

$$i_t = \sigma(W_{ig}[h_{t-1}, x_t] + b_{ig}) \tag{6.30}$$

$$f_t = \sigma(W_{fg}[h_{t-1}, x_t] + b_{fg}) \tag{6.31}$$

$$o_t = \sigma(W_{og}[h_{t-1}, x_t] + b_{og}) \tag{6.32}$$

$$\tilde{C_t} = tanh(W_c[h_{t-1}, x_t] + b_c) \tag{6.33}$$

$$C_t = f_t \bigodot C_{t-1} + i_t \bigodot \tilde{C_t} \tag{6.34}$$

$$h_t = o_t \bigodot tanh(C_t) \tag{6.35}$$

where W_{ig}, b_{ig} are weights, bias of input gate, W_{fg}, b_{fg} are weights, bias of forget gate, W_{og}, b_{og} are weights, bias of output gate, W_c,b_c are weights, bias of cell state, $\tilde{C_t}$ is the candidate cell state, σ denotes activation function, $\bigodot$ represents the scalar product of the two vectors. In equation 6.34, the

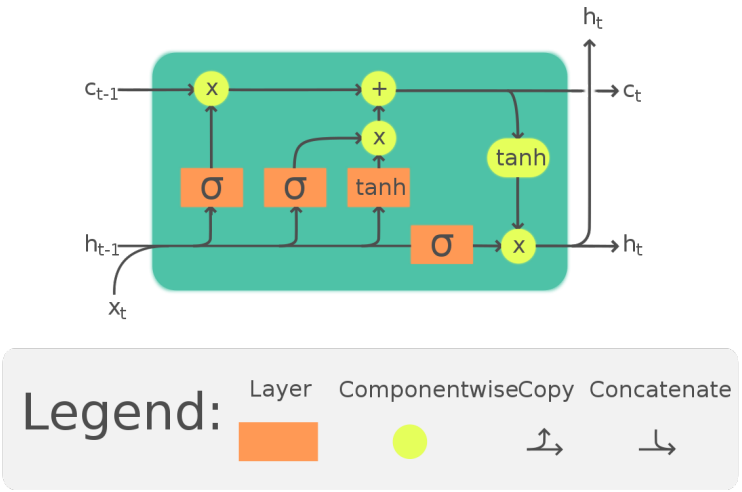

Figure 6.16: LSTM cell. Source: www.wikipedia.com

input gate determines the amount of candidate cell state that is incorporated into the new cell state, while the forget gate determines whether to retain or discard the old cell state. By means of these gates, the LSTM architecture enables the selective addition (removal) of information to (from) the cell state. This mechanism empowers the LSTM to effectively mitigate the challenges posed by vanishing and exploding gradients, as the cell state can serve as an intermediary that preserves information from previous input and hidden states. Ultimately, the output gate provides the final output of the LSTM model.

6.3.2 Literature review

Data-driven energy management control strategies for HEVs are being employed more frequently as a result of the deep learning capabilities of neural networks and the quick advancement of huge data processing technologies. These strategies can achieve approximative optimal control performance. Neural networks and reinforcement learning (RL) constitute the two primary components of a learning-driven energy management system designed for hybrid vehicles. In the NN-based EMS, the selection of input models involves considering various environmental factors, driver behavior, and vehicle specifications. Subsequently, the system generates an optimal power distribution model as its output for training NNs. Most research papers on NN-based EMS for hybrid vehicles predominantly employ NN algorithms for tasks such as classifying working

conditions or predicting vehicle speeds [28–31]. In contrast to NN algorithms primarily applied in fuel cell vehicle contexts, RL methods are more versatile in EMS applications, accommodating both small and large datasets. The prevalent RL algorithms employed in EMS include Q-learning, deep Q-network (DQN), deep deterministic policy gradient (DDPG), and twin delay deep deterministic policy gradient (TD3).

In their research, Zhou et al. [32] propose a multi-objective power allocation strategy aimed at improving the operational efficiency of plug-in hybrid electric vehicles equipped with both fuel cells and batteries. This strategy integrates several key components, including an adaptive online-learning enhanced Markov velocity-forecast, state-of-charge reference planning, and model predictive control. The findings of their study indicate a notable 12% reduction in hydrogen consumption, signifying enhanced efficiency in vehicle operation. The research presented in Song et al.'s work [33] introduces an energy management strategy that relies on nonlinear model predictive control (NMPC) to tackle economic and durability challenges in FCHEVs. This strategy leverages a multi-scale operating conditions prediction model generated through the Markov Monte Carlo method. Furthermore, it employs dynamic programming to achieve optimal control within the projected time horizon. To enhance prediction accuracy for real-time implementation, a "constant speed prediction" method is introduced. The results of simulations demonstrate substantial reductions in both degradation costs (11.1% and 23.9%) and overall operational costs (11.0% and 23.5%) when compared to traditional strategies such as thermostat-based and power-following approaches. The article by Sun et al. [34] introduces an EMS designed for a fuel cell hybrid bus. Its primary objectives are to enhance operational durability, power efficiency, and fuel economy. The EMS employs a PMP algorithm, augmented by driving feature recognition, to address issues related to motor power estimation and real-time implementation. Remarkably, this approach achieves a notable reduction in hydrogen consumption, ranging from 20.3% to 28.9%, in comparison to conventional rule-based methods. This strategy not only reduces hydrogen consumption rates but also excels in real-time performance. A novel reinforcement learning-based energy management technique for the fuel cell/lithium battery hybrid system is put out in the paper [35]. In comparison to other widely-used approaches, the suggested method can successfully lower the life decay rate of fuel cells and increase fuel efficiency by up to 6%. A PMP-based A-EMS has been studied in the reference [36], where the co-state adaptation was carried out using driving cycle prediction. The proposed A-EMS produced a 4% reduction in hydrogen consumption when compared to a rule-based strategy by using an improved Markov-based velocity prediction method that took into account driving behavior under various

driving patterns.

6.4 Development of a P-ECMS for the control of a heavy-duty FCHEV for real world driving

In the context of this PhD thesis, leveraging the use of artificial intelligence, a control strategy has been developed for the control of the fuel cell vehicle described in Chapter 4.4.2. This chapter elaborates on the development of this strategy and presents the results of its applications.

6.4.1 Preliminary study on an a velocity predictor based adaptive-ECMS for the control of a heavy-duty FCHEV for real world driving

As discussed in the previous section 6.1.4, the ECMS is significantly impacted by the equivalence factor, which plays a critical role in ensuring sufficient battery charge-sustaining capacity. Setting the appropriate value for this factor is heavily contingent on the driving conditions, and it is imperative to possess advanced knowledge of the driving mission to establish a constant equivalence factor for achieving optimal control. However, in situations where the specific driving cycle is unpredictable, a fixed equivalence factor may prove inadequate to ensure practical battery charge sustainability. In response to this challenge, the implementation of an adaptive equivalence factor, capable of adjusting in accordance with the dynamic driving conditions, may offer a more effective approach to maintain the battery's SoC. For this reason, during this PhD work, an adaptive-neural network-ECMS (ANN-ECMS) was developed. As the name suggests, the core algorithm of the strategy is the ECMS, complemented by a neural network for vehicle velocity prediction. This kind of strategy is based on the concept that, by leveraging velocity prediction information, the equivalence factor can be continuously updated, making the strategy adaptive to driving conditions that cannot be known in advance. The first step in the strategy development was the creation of a velocity forecasting layer.

Velocity predictor

In the context of this research, an LSTM neural network velocity predictor was employed, starting from the architecture described in [37]. This neural network configuration consists of three LSTM layers, each incorporating 128 neurons, in addition to a dense layer. The implementation of this network was carried out using Matlab software. The neural network training was executed

using the Adaptive Moment Estimation optimizer, utilizing a learning rate set at 0.00611. The performance of this neural network was assessed through sensitivity analyses conducted on its parameters, using actual driving data. The results obtained from these analyses verified that the proposed neural network achieved prediction accuracy that aligned with previous research findings [37–40]. Further details pertaining to these outcomes can be found in the following. The input sequence provided to the neural network comprises a historical series of three features: vehicle velocity, vehicle acceleration, and distance to the next intersection or traffic light, that is the distance to the next point where the vehicle will stop and therefore have zero velocity. In fact, it is assumed that the vehicle consistently comes to a halt at each intersection or traffic light, with the position of these traffic control points being determined by the map service provider. Given these assumptions, the EMS can function effectively without relying on external traffic information. Owing to the information given by the map service provider, the distance can be evaluated as:

$$d_{jt} = \frac{D_j - \int_{t_j}^{t-t_j} v dt}{D_j}, t \in [t_j, t_{j+1}] \tag{6.36}$$

where d_{jt} is the distance feature from the intersection j to the intersection $j+1$, D_j is the distance from the intersection j to the intersection $j+1$, and t_j is the FCV arrival time at the intersection j. The historical sequence length (H_s) is fixed as 10 seconds while three different forecasting horizons (H_f) are considered, respectively 5, 10, and 20 seconds, to analyze their effects on the prediction accuracy and on the EMS. The neural network was subjected to training and testing using real driving data generated via GT-Real Drive, a tool within the GT-Suite (Gamma Technologies) framework. The data was simulated along the Trans European Network (TEN-T) routes, which represent the anticipated operational environment for future heavy-duty FCVs. GT-Real Drive possesses the capability to generate routes on public roads worldwide, utilizing map data from the MAPBOX service. These routes take into account various factors, including real-time or historical traffic conditions, time of day, day of the week, traffic signals, driver preferences, and specific waypoints. All that is required to generate these routes is information about the vehicle's starting position and its intended destination. The additional hypothesis for developing the velocity predictor is to assume that the vehicle is equipped with a standard GPS system for route planning. This scenario is particularly applicable to heavy-duty vehicles that typically navigate predetermined routes connecting specific points of interest such as airports, ports, and industrial zones. For this study, six distinct routes (as shown in Table 6.4) that connect nodes within the TEN-T network have been selected. The choice of these routes

for training and testing the EMS developed in this research was deliberate, aiming to encompass a wide range of speed profiles and validate the algorithm's adaptability to diverse driving conditions.

Route	**Country**	**Distance, km**	**Mean speed, km/h**
Budapest-Tatabánya	Hungary	60	62.3
Fiumicino-Civitavecchia	Italy	71	67.4
Hamburg-Ahrensburg	Germany	34	27.9
Paris-Rouen	France	143	61.5
Siviglia-Algeciras	Spain	184	59.1
Ventspils-Riga	Latvia	184	36.7

Table 6.4: TENT-T routes for the dataset generation

It is worth emphasizing that the integration of GT-Real Drive with the TEN-T network facilitates the inclusion of authentic driving data from significant European road corridors. This integration allows for the development of a dependable EMS tailored for practical heavy-duty vehicle applications. Standardization of the dataset precedes the training process, with 90% of the data allocated for training and the remaining 10% reserved for testing purposes. As an illustrative instance, Figure 6.17 displays the generated speed profile for the Napoli-Nola route.

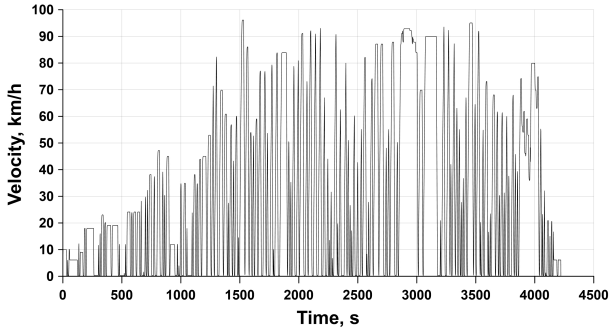

Figure 6.17: Generated driving cycle in the route Napoli-Nola. Source: [41]

To assess the accuracy of the velocity predictor on the testing dataset, speed Root Mean Square Error (RMSE) and R^2 (R-squared) are employed as performance metrics. The corresponding values can be observed in Figure 6.18.

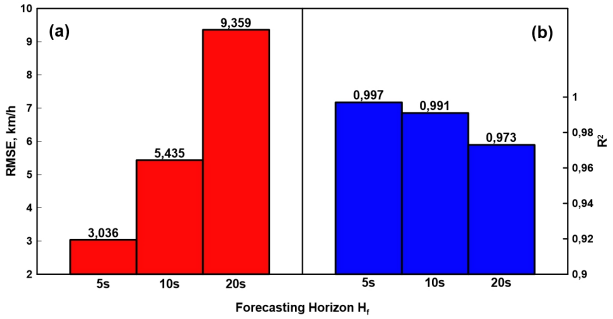

Figure 6.18: NN performance on the Test data: (a) velocity RMSE, (b) prediction R^2. Source: [41]

As expected, it is observed that the prediction accuracy diminishes as the forecasting horizon extends. Nonetheless, the correlation between the predicted and actual data remains highly favorable, as indicated by the R^2 values, which consistently exceed 0.97 even in the most challenging scenarios.

ANN-ECMS framework

After its training and testing, the velocity predictor was integrated into the EMS. Its overall scheme is represented in Figure 6.19.

Considering the ECMS approach, power is distributed minimizing the instantaneous equivalent fuel consumption that can be expressed as:

$$J = \dot{m}_f + s\frac{P_{batt}}{LHV} + \delta \tag{6.37}$$

where $\dot{m}_f$ and P_{batt} represent the actual fuel rate and the net electrical power as seen at the battery terminals, respectively, LHV and s are the lower heating value of the fuel and the equivalence factor, which represents the cost of the electric power drawn from the battery, and δ is a cost term to impose limitations on the fuel cells dynamic behavior, that can be expressed as:

$$\delta = \begin{cases} 0 & |di/dt|(t+dt) \leq |di/dt|_{max} \\ inf & |di/dt|(t+dt) > |di/dt|_{max} \end{cases} \tag{6.38}$$

Exploring the effects of different levels of allowable dynamic for the fuel cell system (that affects membrane electrode assembly's degradation) was

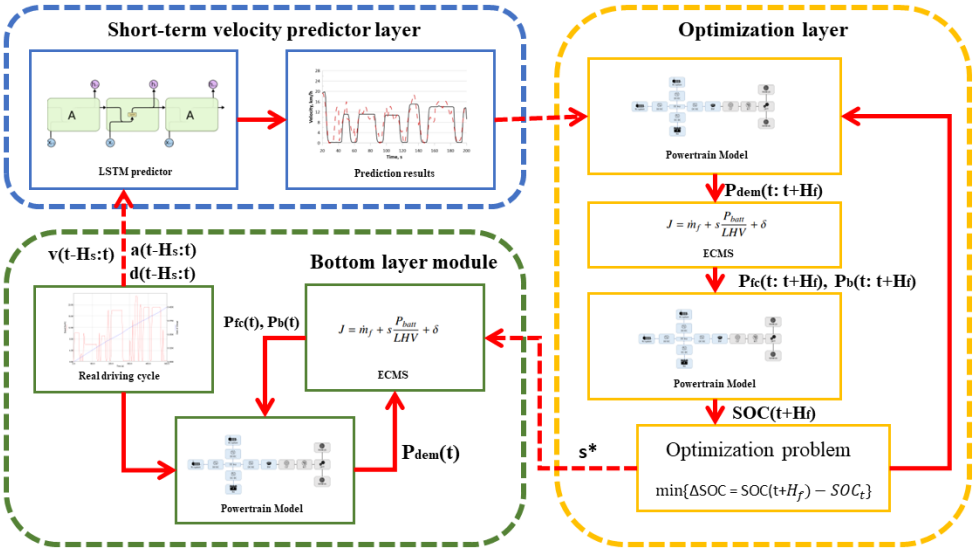

Figure 6.19: Framework of the Adaptive-EMS. Source: [41]

not considered in preliminary studies, for this reason, a high limit on the current derivative with time ($|di/dt| \leq 0.1\, A/cm^2 s$) was selected for all the test cases. This level of dynamics is high enough for the FC system to follow the e-motor power demand level with small support from the battery while avoiding undesired phenomena such as anode or cathode starvation that may lead to severe FC degradation. The control algorithm has been fully developed using Matlab/Simulink, while the vehicle simulation is carried out using the GT-suite software. The integration of these two platforms is achieved through the use of a dedicated S-function Simulink block designed for GT-Suite models. To address the limitations of the ECMS in unknown driving scenarios, the ANN-ECMS based on neural networks has been implemented. This implementation can be divided into two main phases: the offline design phase and the online application phase. The offline phase encompasses the design and training of the neural network and has been discussed in the previous section. On the other hand, the online implementation involves velocity forecasting, followed by equivalence factor optimization, and subsequently, the execution of the control sequence. Specifically, the equivalence factor that minimizes the difference between the target SoC and the predicted SoC at the end of the prediction horizon is calculated by an iterative process. To reduce the computational load of the EMS, the equivalence factor updating horizon length is set to be equal

to H_f. For clarity, the EMS pseudo code is presented in Table 6.5.

Algorithm: ECMS based on speed forecasting
while (not terminate-condition)
%Short term velocity prediction layer
input: speed, acceleration and distance historical sequences;
$v_f(t+1, t+2, ..., t+H_f)$ = NN prediction (input);
%Optimization layer
Optimize s in $[t; t+H_f]$;
%Bottom layer
Powertrain model+ECMS with s_{opt} for H_f seconds;
end

Table 6.5: Pseudo code for the control algorithm

Simulation settings

A series of four distinct driving cycles, outlined in Table 6.6, were chosen to evaluate the proposed ANN-ECMS. Four EMS configurations were examined in this assessment:

- The standard ECMS, employing a constant and optimized equivalence factor, serving as a reference (referred to as S-ECMS).
- The proposed ANN-ECMS with three distinct forecasting horizons: 5, 10, and 20 seconds, denoted as ANN-ECMS-H5, ANN-ECMS-H10, and ANN-ECMS-H20, respectively.

The HDDT cycle was employed as the reference standard driving cycle, while the other test cases were designed to represent realistic driving scenarios encountered in various European regions. These scenarios were selected to encompass a range of average route speeds, travel distances, and to reflect conditions across different European countries. It's worth emphasizing that all four test cases were distinct from the neural network training dataset, consequently, the A-EMS was assessed in the context of unknown driving conditions. Regarding the S-ECMS, the equivalence factor was fine-tuned individually for each test case to ensure battery SoC sustainability. Considering the range extender architecture, the initial SoC was set to 30%, simulating only the charge-sustaining condition. The initial equivalence factor value for the ANN-ECMS was adopted from the optimal value identified for the S-ECMS in the HDDT cycle, for all the test cases. This approach eliminates the need for offline tuning for the ANN-ECMS, setting it apart from the S-ECMS.

Route	Country	Distance, km	Mean speed, km/h
HDDT	-	37.2	64.2
Napoli-Nola	Italy	33.5	29.9
Strasburg-Metz	France	165.2	75.3
Bucarest-Giurgiu	Romania	62.3	39.4

Table 6.6: Test cases definition based on TENT-T routes

Results and discussion

Now results of the simulations are discussed. The analysis is conducted in two stages. Firstly, an extensive examination of the HDDT case is undertaken. Subsequently, the results pertaining to the scenarios involving realistic driving cycles are assessed with regard to speed prediction accuracy, battery SoC sustainability, and hydrogen consumption. To assess speed prediction accuracy, the RMSE is utilized. In the context of battery SoC sustainability, several metrics are considered, including maximum SoC (SoC_{max}), minimum SoC (SoC_{min}), maximum SoC variation ($\Delta = SoC_{max} - SoC_{min}$), and SoC RMSE, as expressed by equation 6.39:

$$RMSE = \sqrt{\frac{\sum_{k=1}^{N}(SoC_k - SoC_{target})^2}{N}} \tag{6.39}$$

The equivalent hydrogen consumption takes into account the difference between the initial and final energy of the battery (ΔE_b), converted into an equivalent mass of hydrogen $H_{2,eq}$ as expressed by:

$$H_{2,eq} = H_2 + \frac{\Delta E_b}{\overline{\eta_b}\overline{\eta_{FCS}} LHV_{H_2}} \tag{6.40}$$

where $\overline{\eta_b}$, $\overline{\eta_{FCS}}$ are the battery and FC systems efficiencies, respectively, while LHV_{H_2} is the hydrogen lower heating value.

Regarding prediction accuracy, detailed speed forecasting results for various H_f values within the HDDT driving cycle are depicted in Figure 6.20 and Figure 6.21-a. An examination of Figures 6.20-a-b-c reveals that all three neural networks exhibit superior performance during periods of speed fluctuation, with relatively larger errors occurring during acceleration and deceleration phases. It's noteworthy that as the forecasting horizon extends, the error tends to increase, as confirmed by the RMSE data in Figure 6.21-a. In the

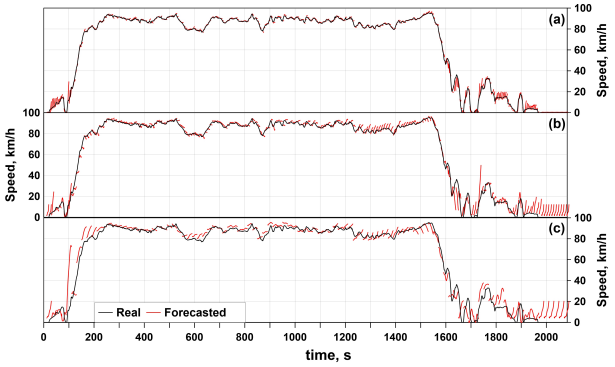

Figure 6.20: Speed forecasting in the driving cycle HDDT for different forecasting horizons: (a) 5s, (b) 10s, (c) 20s. Source: [41]

latter portion of the data, it becomes apparent that the short-term velocity predictor layer struggles to accurately predict vehicle restarts following a stop. However, this reduced accuracy during restart phases does not significantly impact the overall performance of the EMS. The RMSE values consistently demonstrate a favorable agreement between predicted speed and actual speed for each forecasting horizon. Leveraging the forecasted speed data, the ANN-ECMS demonstrates an enhanced ability to maintain battery charge compared to the S-ECMS (see Figure 6.22 and Table 6.7). Under the S-ECMS, the battery experiences a more profound discharge, reaching a minimum SoC of 23.4% and exhibiting a maximum SoC variation of 7.6%. In contrast, the ANN-ECMS-H5 reduces this variation by 76%, resulting in a maximum SoC variation of 1.7%. Across all forecasting horizons, the ANN-ECMS consistently reduces SoC fluctuations, starting from an RMSE of 3.6% in the S-ECMS case and decreasing to less than 1% for all three ANN-ECMS variants.

Strategy	SoC_{min}, %	SoC_{max}, %	Δ, %	**Difference, %**	**SoC RMSE, %**	**Difference, %**
S-ECMS	23.45	31.09	7.64	-	3.64	-
ANN-ECMS-H5	29.17	30.91	1.74	-76.27	0.86	-77.22
ANN-ECMS-H10	29.19	30.91	1.72	-76.42	0.86	-77.51
ANN-ECMS-H20	29.38	30.94	1.56	-75.74	0.88	-79.54

Table 6.7: SoC analysis for the tested strategies in the HDDT cycle

Maintaining a stable SoC offers several advantages in real-world driving conditions, especially when prior knowledge of the driving mission is unavailable [42, 43]. In the charge-sustaining mode, a fuel cell range extender vehicle often operates with a relatively low battery SoC. By keeping the SoC near the target

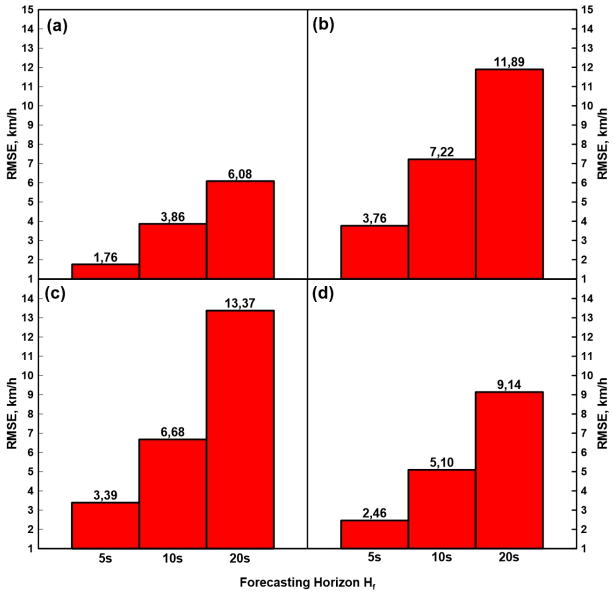

Figure 6.21: RMSE for the forecasted speed comparisons for different forecasting horizons in the driving cycle: HDDT (a), Bucarest-Giurgiu (b), Napoli-Nola (c), Strasburgo-Metz (d). Source: [41]

value, deep battery discharges that lead to battery damage and degradation can be avoided. Conversely, in the ANN-ECMS scenarios aimed at reducing SoC fluctuations, the fuel cell system operates more frequently at less efficient points, delivering lower power during the latter part of the driving cycle compared to the S-ECMS. Specifically, during the last 500 seconds of the driving cycle, when motor power demands are low (as seen in Figure 6.22-b), the S-ECMS selects higher fuel cell power to recover from the deeper battery discharge while maintaining FC system efficiency at around 60%. In contrast, the adaptive strategies do not necessitate battery SoC recovery, allowing the FC system to operate at lower power levels while meeting the traction power requirements. Consequently, the adaptive strategies exhibit an increase in equivalent hydrogen consumption (Figure 6.23-a). Interestingly, hydrogen consumption decreases as the forecasting horizon lengthens, even though forecasting accuracy diminishes. This phenomenon is attributed to a reduction in the frequency of equivalence factor updates. As previously elaborated, the equivalence factor updating horizon is set equal to the forecasting horizon. A higher updating frequency results in more frequent load fluctuations for the fuel cell systems, leading to exceptionally low current densities that correspond to lower efficiencies when the battery SoC exceeds the target value. This, in turn, leads to frequent and

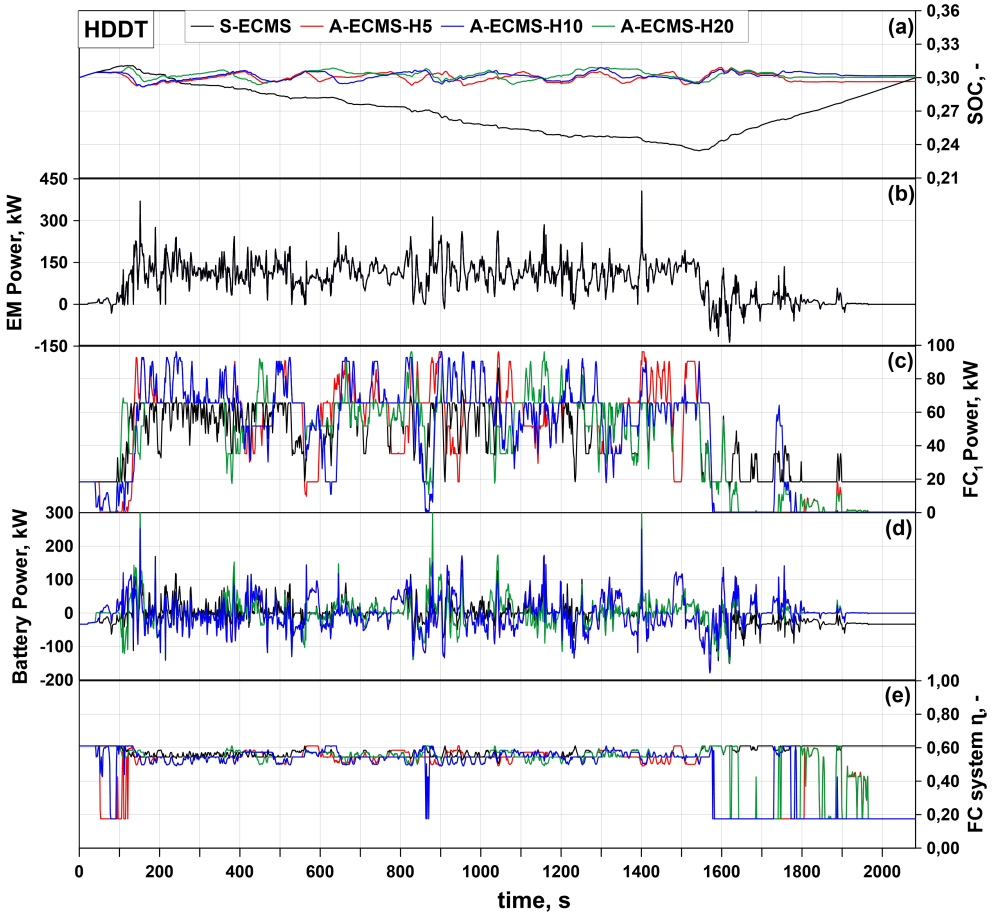

Figure 6.22: HDDT, (a) S-ECMS/ANN-ECMS comparisons for different H_f of battery SoC, (b) Electric machine power, (c) Fuel cell system 1 net power, (d) Battery power and (e) and Fuel cell systems efficiency. Source: [41]

inefficient fuel cell shutdowns.

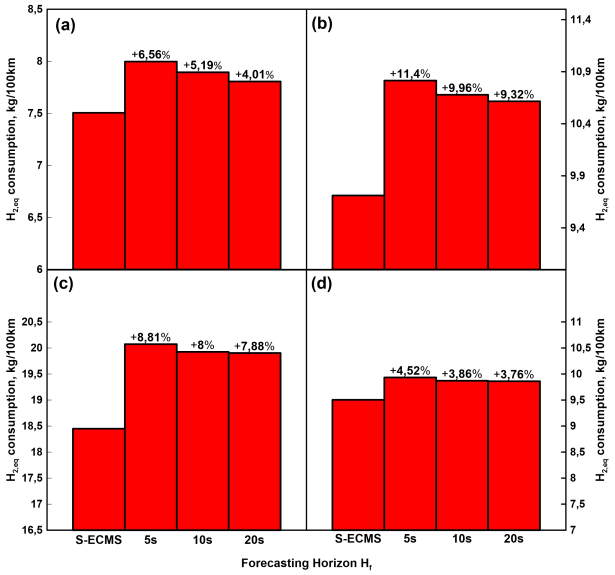

Figure 6.23: H_2 consumption comparisons for different forecasting horizons in the driving cycle: HDDT (a), Bucarest-Giurgiu(b), Napoli-Nola (c), Strasburgo-Metz (d). Source: [41]

The reduction in speed forecasting accuracy with increasing forecasting horizons has been consistently observed across all the tested scenarios, as illustrated in Figure 6.21. The highest accuracy is achieved by ANN-ECMS-H5 in the HDDT cycle, with an RMSE of 1.76 km/h, while the least accurate prediction is made by ANN-ECMS-H20 for the Napoli-Nola route, resulting in an RMSE of 13.37 km/h. In each case, the prediction accuracy aligns with current literature standards [37–40].

For simplicity, only the battery SoC evolution is presented in Figure 6.24 for the realistic driving cycles. The corresponding statistics for battery charge sustaining are summarized in Tables 6.8, 6.9, and 6.10.

The improved charge sustaining observed in the HDDT cycle is consistently confirmed for real-world driving missions. As an example, the results for the Bucarest-Giurgiu route are examined. In this case, the SoC RMSE decreases by 85%, decreasing from 11.01% in the S-ECMS to 1.08% in the ANN-ECMS-H10. The maximum SoC variation also decreases, dropping from 24.99% in the S-ECMS to 3.74% in the ANN-ECMS-H10, a reduction of 90.19%. It's worth noting that the ANN-ECMS results are consistent across all considered forecasting horizons, demonstrating the robustness of the proposed control

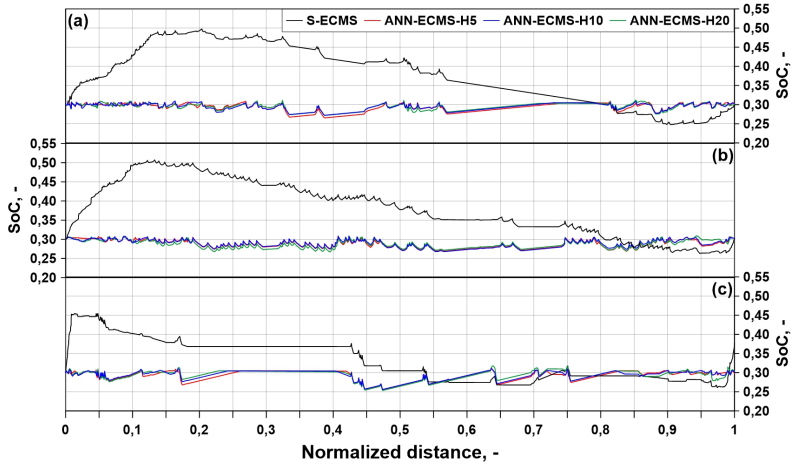

Figure 6.24: S-ECMS/ANN-ECMS comparisons for different H_f of battery SoC for the real driving cycle: Bucarest-Giurgiu (a), Napoli-Nola (b), Strasburgo-Metz (c). Source: [41]

algorithm.

The highest S-ECMS SoC maximum variation is attributed to significant initial battery charging in the simulation. While reaching a SoC_{max} of 49.77% isn't detrimental to battery health, this deviation from the target value is only possible due to prior knowledge of the driving cycle. In contrast, the ANN-ECMS optimally allocates power between the battery and FC systems to maintain SoC nearly constant without knowledge of the future. This offers practical implementation possibilities, where planning an optimal battery SoC trajectory would require challenging long-term forecasts. The EMS operates to maintain SoC at a target value, preventing excessive fluctuations and potential battery damage.

However, due to the improved charge sustaining, suboptimal solutions are found for the control problem by the ANN-ECMS, and the powertrain operates with reduced efficiency. This is evident in the higher equivalent hydrogen consumption for each test case (Figure 6.23). Similar observations apply to the Napoli-Nola and Strasburg-Metz routes.

6.4.2 Development of a predictive ECMS based on short-term velocity forecasting

The preceding discussion has highlighted the advantages of periodically updating the equivalence factor. However, this approach comes with certain

Strategy	SoC_{min}, %	SoC_{max}, %	Δ, %	Difference, %	SoC RMSE, %	Difference, %
S-ECMS	24.79	49.77	24.99	-	11.01	-
ANN-ECMS-H5	26.54	30.92	4.39	-89.30	1.18	-82.44
ANN-ECMS-H10	27.22	30.96	3.74	-90.19	1.08	-85.05
ANN-ECMS-H20	27.18	31.19	4.01	-90.03	1.10	-83.95

Table 6.8: SoC analysis for the tested strategies in the Bucarest-Giurgiu road

Strategy	SoC_{min}, %	SoC_{max}, %	Δ, %	Difference, %	SoC RMSE, %	Difference, %
S-ECMS	26.33	50.75	24.42	-	11.37	-
ANN-ECMS-H5	26.89	30.74	3.84	-84.26	1.38	-87.87
ANN-ECMS-H10	26.77	30.85	4.07	-83.31	1.33	-88.27
ANN-ECMS-H20	26.99	30.93	4.24	-82.63	1.47	-87.05

Table 6.9: SoC analysis for the tested strategies in the Napoli-Nola road

Strategy	SoC_{min}, %	SoC_{max}, %	Δ, %	Difference, %	SoC RMSE, %	Difference, %
S-ECMS	26.09	45.47	19.37	-	6.64	-
ANN-ECMS-H5	25.57	31.19	5.62	-70.99	1.37	-79.45
ANN-ECMS-H10	25.61	31.07	5.47	-71.78	1.27	-80.94
ANN-ECMS-H20	25.34	31.77	6.43	-66.82	1.37	-79.40

Table 6.10: SoC analysis for the tested strategies in the Strasburg-Metz road

trade-offs. One notable drawback is the increased computational time incurred by the iterative process required to determine the optimal equivalence factor. Moreover, the stringent constraints imposed on the battery SoC can potentially lead to a significant increase in hydrogen consumption. In response to these challenges, an alternative algorithm for updating the equivalence factor has been integrated into the EMS, giving rise to a Predictive-ECMS (P-ECMS). For this study, the impact of different control strategies on the fuel cell's lifespan was also assessed, utilizing the degradation model described in Chapter 4.4.2.

Predictive ECMS

As stated in Section 6.1.4, several approaches exist in the literature to adapt the equivalence factor realizing different kinds of Adaptive-ECMS. The first and simplest A-ECMS concept is based on the iterative updating of the equivalence factor using a feedback-oriented law that adjusts the equivalence factor based on the error between the reference SoC value and the real-time feedback SoC value, according to the adaptation law proposed in [44]:

$$s_{n+1} = s_n + k_p(SoC_{ref} - SoC_n) \tag{6.41}$$

where SOC_{ref} is the reference SoC value, SOC_n and s_n are the SoC and the EF at time $t = n$, k_p is a fixed control gain and s_{n+1} is the equivalence factor at the following time step $n + 1$. The equivalence factor is updated at a rate of 1 s per sample. For the following analysis, this law is used as a benchmark.

To enhance the performance of the reference A-ECMS (following Equation 6.41), Chen el al. [45] proposed the subsequent adaptation law:

$$s_{n+1} = s_n + k_p(SoC_{ref} - S\hat{o}C_n(n + H_f)) \tag{6.42}$$

In contrast to Eq. 6.41, Eq. 6.42 incorporates feedback from the short-term predicted future SoC ($S\hat{o}C_n(n + H_f)$). However, the study in [45] did not investigate the impact of realistic velocity predictions and treated future velocity as an external input. Additionally, their EMS was applied to a hybrid electric vehicle with an internal combustion engine, which does not share the same dynamic limitations as an FCS due to membrane degradation. This study addresses this knowledge gap by integrating the adaptation law of Eq. (6.42) into the multi-level control strategy shown in Figure 6.25. The EMS operates as follows:

1. The velocity forecasting layer predicts the vehicle velocity H_f seconds ahead.

2. The predicted velocity is transmitted to the powertrain model, which uses instantaneous Hamiltonian minimization to forecast a SOC trajectory for H_f seconds in the future considering the EF value of the previous iteration.

3. The EF is then updated according to Eq. 6.42, based on the discrepancy between the reference SOC and the predicted SOC

4. The updated EF is sent to the bottom layer, which solves the ECMS in the time window $[t, t + H_f]$, and the process repeats from step 1 using the updated EF as the value for the subsequent iteration.

The EF update time step is equivalent to H_f. The advantages of this approach and the procedure to select the initial EF for the first iteration are discussed in the results section.

Simulation setup

Table 6.4.2 provides an overview of the two chosen driving cycles selected as a testing ground for the comprehensive evaluation of the proposed P-ECMS.

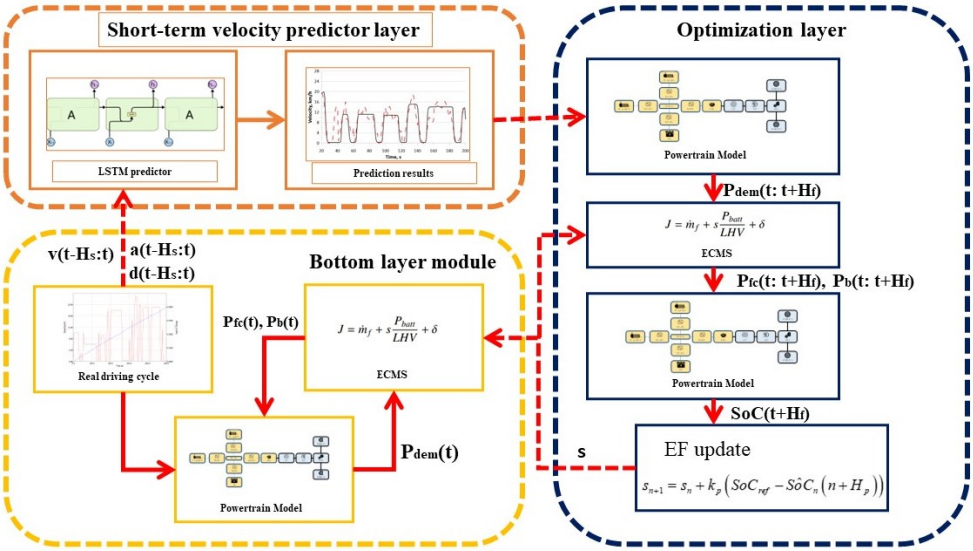

Figure 6.25: Framework of the Predictive-EMS

In this scientific context, the P-ECMS is subjected to a comparative analysis alongside established EMS approaches, including the standard ECMS (S-ECMS) with a fixed and optimally tuned equivalence factor, the adaptive A-ECMS (following the adaptation law defined in Equation 6.41), and a rule-based EMS, denoted as RBS, as described in [46]. It is important to note that the driving scenarios used for these test cases were intentionally excluded from the training dataset of the neural network. This deliberate omission is designed to assess how well the P-ECMS adapts to previously unencountered driving conditions.

Route	**Country**	**Distance, km**	**Mean speed, km/h**
HDDT	-	37.2	64.2
Bucarest Giurgiu	Romania	62	39

Table 6.11: Test cases definition.

To align with the typical configuration of range-extender systems, the simulations commence with an initial SoC set at 30%. Achieving the optimal calibration for both the A-ECMS and P-ECMS necessitates the determination of initial values for s (s_0) and k_p (as per Equation 6.41 and Equation 6.42). In the forthcoming section, a sensitivity analysis is conducted, primarily focusing

on the HDDT cycle. The objective of this analysis is to identify the optimal calibration settings. This entails exploring the effects of varying k_p within the range [2, 20] and s_0 within the interval [2, 2.5] on the terminal SoC and hydrogen fuel consumption. As for s calibration, the update process outlined in Equation 6.41 and 6.42 is applied within the range [1.5, 3]. It is noteworthy that the RBS method does not require any specific initialization parameters. The performance evaluation of each EMS involves subjecting them to three distinct stack current dynamic constraints: 0.1, 0.01, and 0.001 A/cm^2s ($|di/dt|_{max}$ in Equation 6.38). The first constraint, set at 0.1 A/cm^2s, represents a highly dynamic scenario. The second constraint, at 0.01 A/cm^2s, is implemented to mitigate cathode/anode starvation while maintaining dynamic operation and promoting system stability with stoichiometry closely aligned to target values. The final constraint, set at 0.001 A/cm^2s, represents a high level of dynamic control, where minimal fuel cell degradation is expected. It is critical to highlight that preliminary analyses in the lowest dynamic case ($|\mathrm{di/dt}|_{max}$= 0.001 A/cm^{2}s) have revealed that the battery SoC may fall below or exceed the acceptable thresholds due to the strong dynamic restrictions. Consequently, in this case, to enable the fuel cell system to respond with high dynamics in adverse conditions that may damage the battery or hinder the completion of the driving mission, the maximum current derivative is corrected as:

$$|di/dt|_{max}= \begin{cases} 0.001 & 0.25 < SoC < 0.35 \\ 0.1 & otherwise \end{cases} \tag{6.43}$$

Sensitivity analysis

As previously discussed, both the A-ECMS and P-ECMS algorithms necessitate the determination of key parameters, namely k_p and s_0. To address this requirement, the HDDT cycle served as the reference case for the high FC dynamic case ($|\mathrm{di/dt}|_{max}$= 0.1) scenario. Subsequently, the same set of k_p and s_0 values was applied to the Bucharest-Giurgiu cycle for all the dynamic limitations. This approach was adopted to assess the robustness of the EMS under varying driving conditions. By selecting the HDDT cycle as the optimization benchmark, the need to establish distinct s_0 and k_p values for different driving missions was obviated. The P-ECMS consistently exhibits lower adjusted hydrogen consumption compared to the A-ECMS across a range of s_0 and k_p parameter combinations. This outcome can be attributed to the P-ECMS's capacity to access short-term future information, as demonstrated in Figure 6.26. Notably, the primary influence on H_2 consumption for both adaptive strategies is exerted by the value of k_p, with the impact of s_0 being

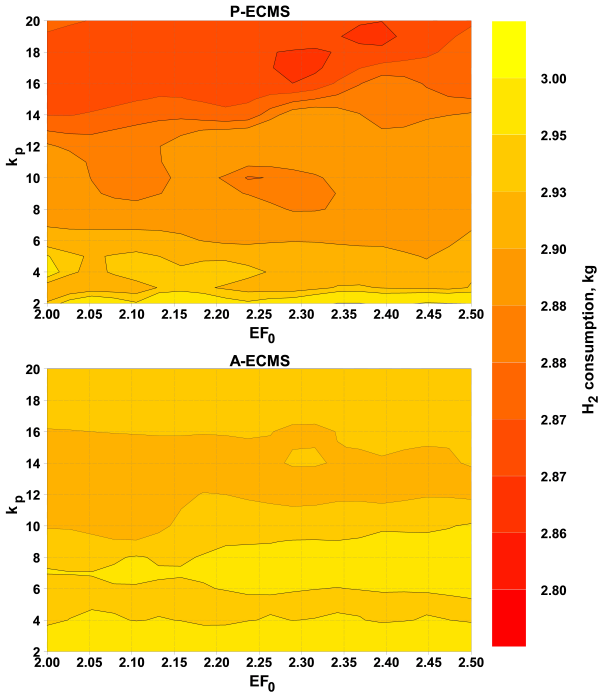

Figure 6.26: Corrected hydrogen consumption distribution for P-ECMS and A-ECMS.

relatively negligible. The final SoC tracking error, as illustrated in Figure 6.27, follows a similar pattern. Specifically, for lower k_p values, the P-ECMS records a significantly higher error than the A-ECMS. This difference arises from the distinct update intervals of the EF: whereas the A-ECMS adapts the EF every second, the P-ECMS updates it every H_f seconds. This update frequency was chosen to simplify the strategy and reduce computational overhead, without significantly amplifying the SoC tracking error for higher k_p values, where H_2 consumption generally remains lower within the relevant map region. Figure 6.28 illustrates the distribution of the percentage increase in adjusted H_2 consumption of the A-ECMS relative to the P-ECMS. It is evident that, for equivalent k_p and s_0 values, the P-ECMS consistently yields superior fuel efficiency, with the most substantial reduction reaching approximately 3%. This improvement stems from the additional information derived from speed forecasts.

Subsequently, k_p and s_0 values that minimized H_2 consumption while ensuring the terminal SoC tracking error remains below 1% during this sensitivity analysis, were selected for all the following test cases, eliminating the necessity

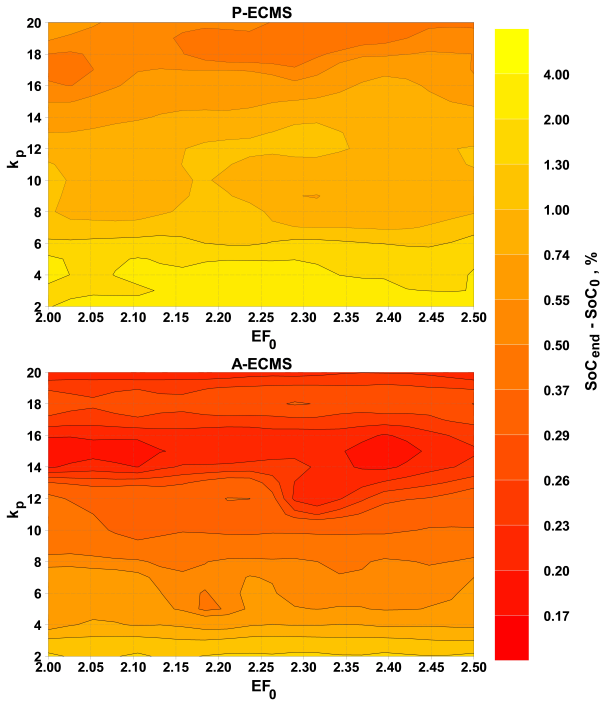

Figure 6.27: Terminal SoC tracking error distribution for P-ECMS and A-ECMS.

to establish distinct s_0 values for different driving missions. Consequently, the following sections present a comprehensive analysis and comparison of simulation results obtained for the four tested strategies, along with the corresponding tuned parameter values.

HDDT results

Figures 6.29 and 6.30 present a comparative analysis of the time-evolution of SoC, FC current density, and EF under various FC dynamic constraints. To enhance clarity, the RBS results are omitted from the figures but are discussed separately in Figures 6.31, 6.32, 6.33.

Figures 6.29(d) and 6.29(f) vividly illustrate that imposing severe FC dynamic constraints, reducing them to 0.01 A/cm^{2}s and 0.001 A/cm^{2}s, leads to noticeable alterations in the current density profile throughout the cycle. These alterations are expected to have substantial repercussions on both hydrogen consumption and the durability of the FC stack.

Under such stringent constraints, the FC stack less frequently attains its

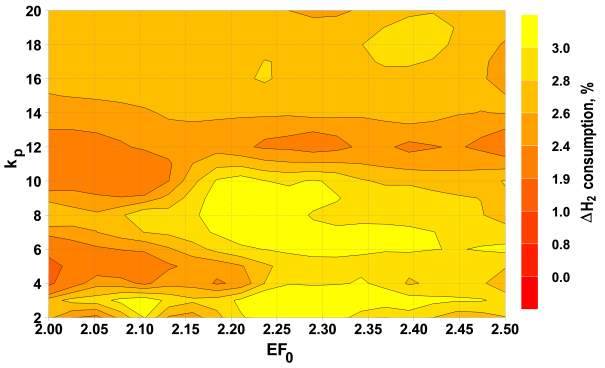

Figure 6.28: Hydrogen consumption percent difference between P-ECMS and A-ECMS. A positive percentage number indicates that A-ECMS leads to greater hydrogen consumption than P-ECMS.

maximum current density. This may potentially result in increased medium-power or natural degradation mechanisms to compensate for the decline in SoC when high power demands are placed on the electric motor. Moreover, the intensity of load-change experiences evident modifications, affecting both the rate of change and amplitude of load-change oscillations. This implies an overall reduction in the total degradation rate, given that the primary source of degradation, load-change, is directly impacted.

The implications on durability should be assessed by considering the physical condition of the FC stack, not solely the evolution of current density, but, a decrease in load-change degradation of this significant magnitude carries positive implications for FC stack durability.

Figures 6.29(e) and 6.29(f) emphasize a dip in current density around the 1700 s mark due to excessively high SoC values and a sudden surge in current density around 300 s in the A-ECMS case, as the SoC reaches its lower limit of 0.25. These fluctuations justify the adaptive adjustments in dynamic limits aimed at enhancing SoC sustenance (as per Eq. 6.43). The distinct time evolution of current density between P-ECMS and A-ECMS can be attributed to the forecasting capabilities of P-ECMS and the differing update frequencies, as depicted in Figure 6.30.

With the exception of S-ECMS, P-ACMS, A-ECMS, and RBS, all maintain the battery SoC in proximity to the target value of 30% (Figure 6.31). However, charge sustenance declines when the system operates with reduced dynamics. The implementation of velocity prediction and improved EF adaptation in P-ECMS results in reduced H_2 consumption in comparison to A-ECMS and RBS (Figure 6.32), with only a marginal 1.7% increase compared to S-ECMS.

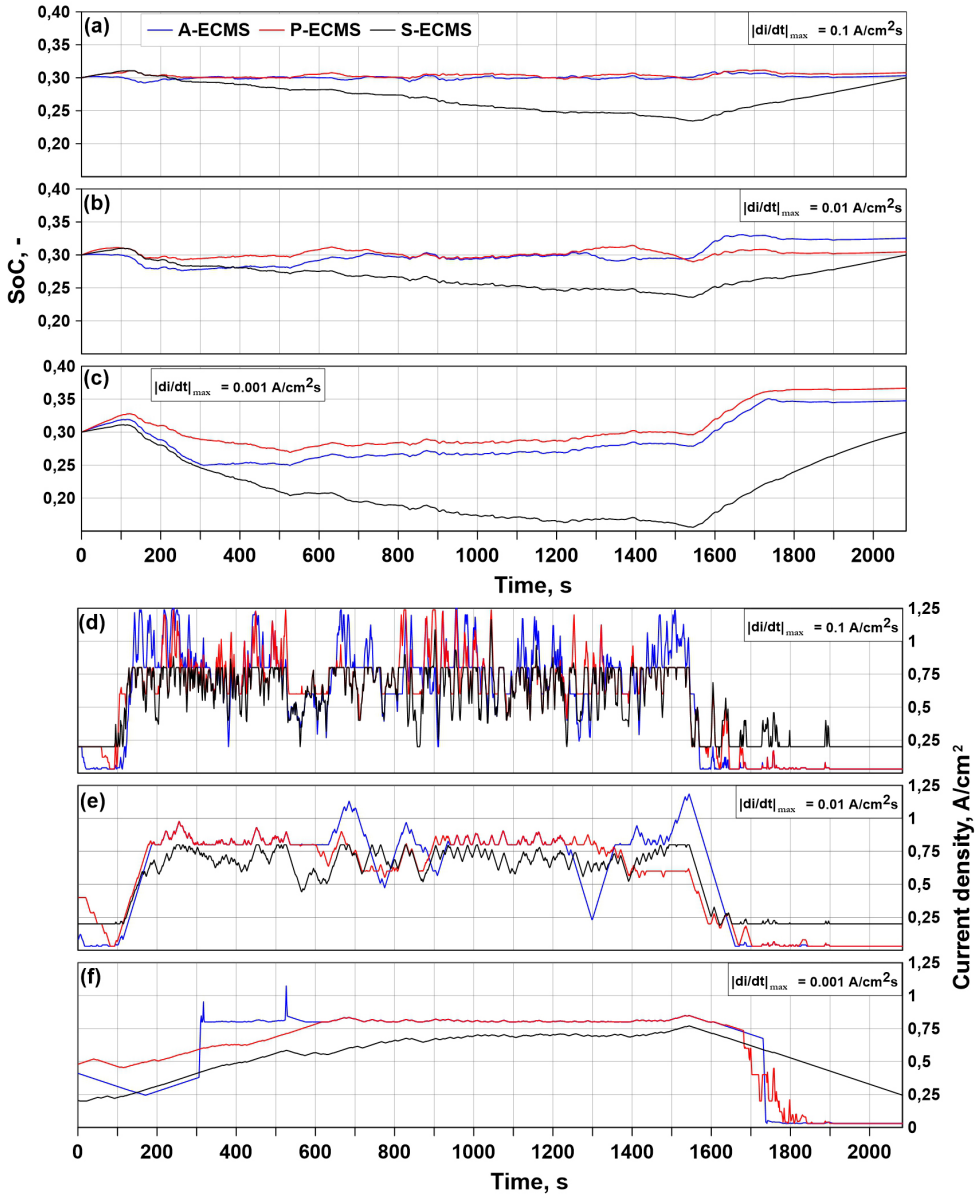

Figure 6.29: Comparison of time evolution SoC (a-b-c) and fuel cell current density (d,e,f) for different fuel cell dynamic limitations in the HDDT cycle.

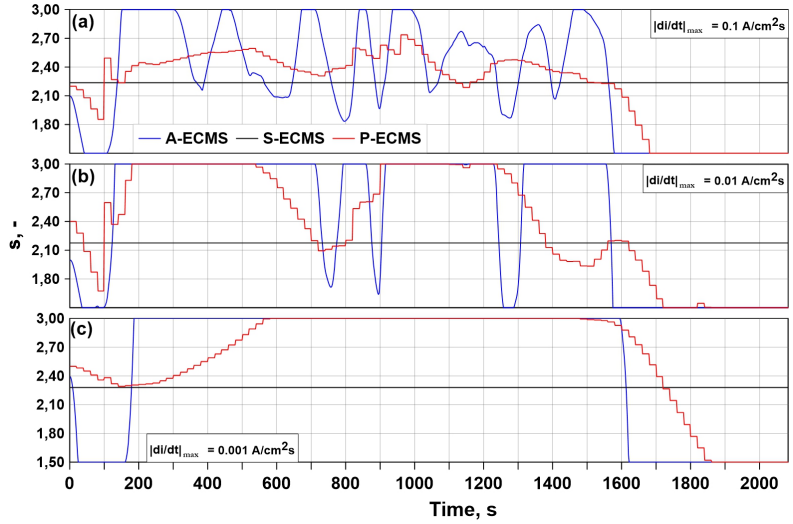

Figure 6.30: Comparison of time evolution equivalence factor for different fuel cell dynamic limitations in the HDDT cycle.

Note that in Figure 6.32, the values displayed above the bars represent the increment in H_2 consumption relative to S-ECMS operating with high current dynamics. Across all EMS configurations, elevating the dynamic constraint to 0.01 and 0.001 A/cm^2 results in a 1-3% augmentation in H_2 consumption compared to employing the same EMS with high FC dynamics.

Conversely, the FC stack's durability experiences an increase of up to 2.24 times concerning the S-ECMS case with high dynamics, demonstrating that P-ECMS can effectively enhance FC durability operating with a low dynamic FC. In a broader context, all EMS alternatives exhibit a durability enhancement when subjected to high dynamic restrictions, and the discrepancies are primarily attributed to the evolution of current density and its consequential impact on the FC physical conditions. For instance, the utilization of S-ECMS leads to lower current density levels during periods of elevated electric motor power demand, thereby enabling the FC stack to operate at lower temperatures and reducing its degradation rate. Lifetime calculations adhere to end-of-life (EOL) criteria defined by the Department of Energy, where an FC stack is deemed to have reached EOL status when the voltage decreases by 10% relative to nominal conditions at a current density of 1 A/cm^2 [47].

The notable improvement in FC durability can be chiefly attributed to the substantial reduction in load-change degradation, which constitutes the predominant contributor to overall degradation. This degradation source

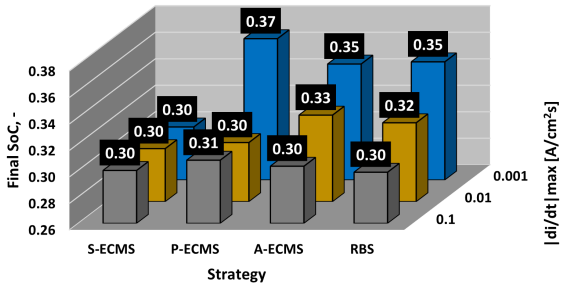

Figure 6.31: Terminal SoC evolution as a function of the EMS and the dynamic limitations in the HDDT cycle.

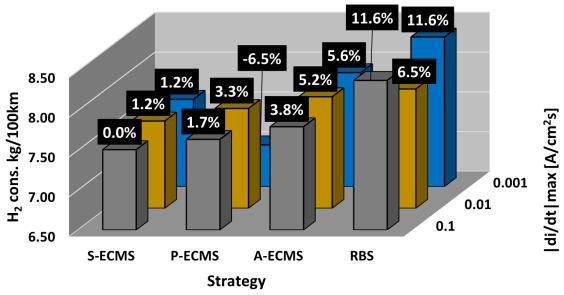

Figure 6.32: H_2 consumption evolution as a function of the EMS and the dynamic limitations in the HDDT cycle.

decreases significantly, declining from 55% to 10% when dynamic constraints are enforced at 0.001 A/cm^{2}s, as illustrated in Figure 6.34. Consequently, this reduction in load-change degradation underscores the growing importance of other degradation mechanisms, notably start-stop degradation, which may potentially emerge as the predominant source of degradation, closely followed by natural degradation, overcoming load-change degradation in significance.

This shift in the prevalence of degradation mechanisms within the FC has implications for FC manufacturers, potentially guiding the design of membrane electrode assemblies based on the expected mechanisms of degradation, depending on the stack's operational dynamics (low or high dynamics). It provides an opportunity to tailor MEA designs to mitigate specific degradation pathways, thereby enhancing FC stack longevity.

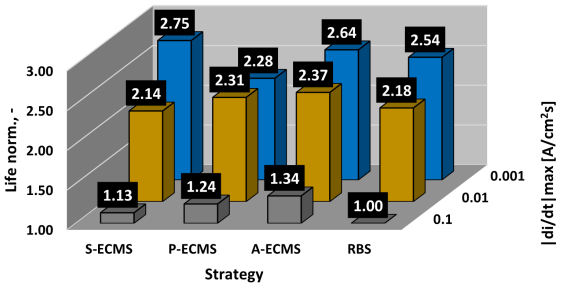

Figure 6.33: Normalized FC stack durability (life) evolution as a function of the EMS and the dynamic limitations in the HDDT cycle.

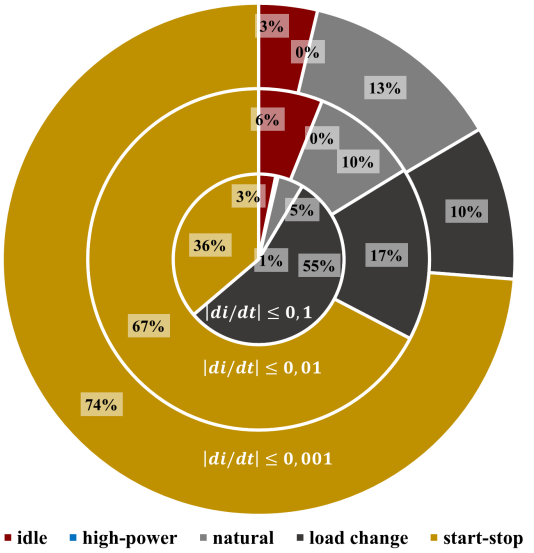

Figure 6.34: Degradation source relative effect on FC stack durability for the P-ECMS with different dynamic limitations. $|di/dt|$ is in A/cm^2s.

Bucarest-Giurgiu results

Figure 6.35 clearly illustrates that the S-ECMS falls short in achieving optimal battery charge sustenance during the Bucarest-Giurgiu test case. In each case with varying dynamic limitations (Figure 6.35-a-c-e), the S-ECMS attains an almost 50% maximum SoC, resulting in reduced load on the FCS during the latter stages of the driving mission (Figure 6.35-b-d-f). This, in turn, leads

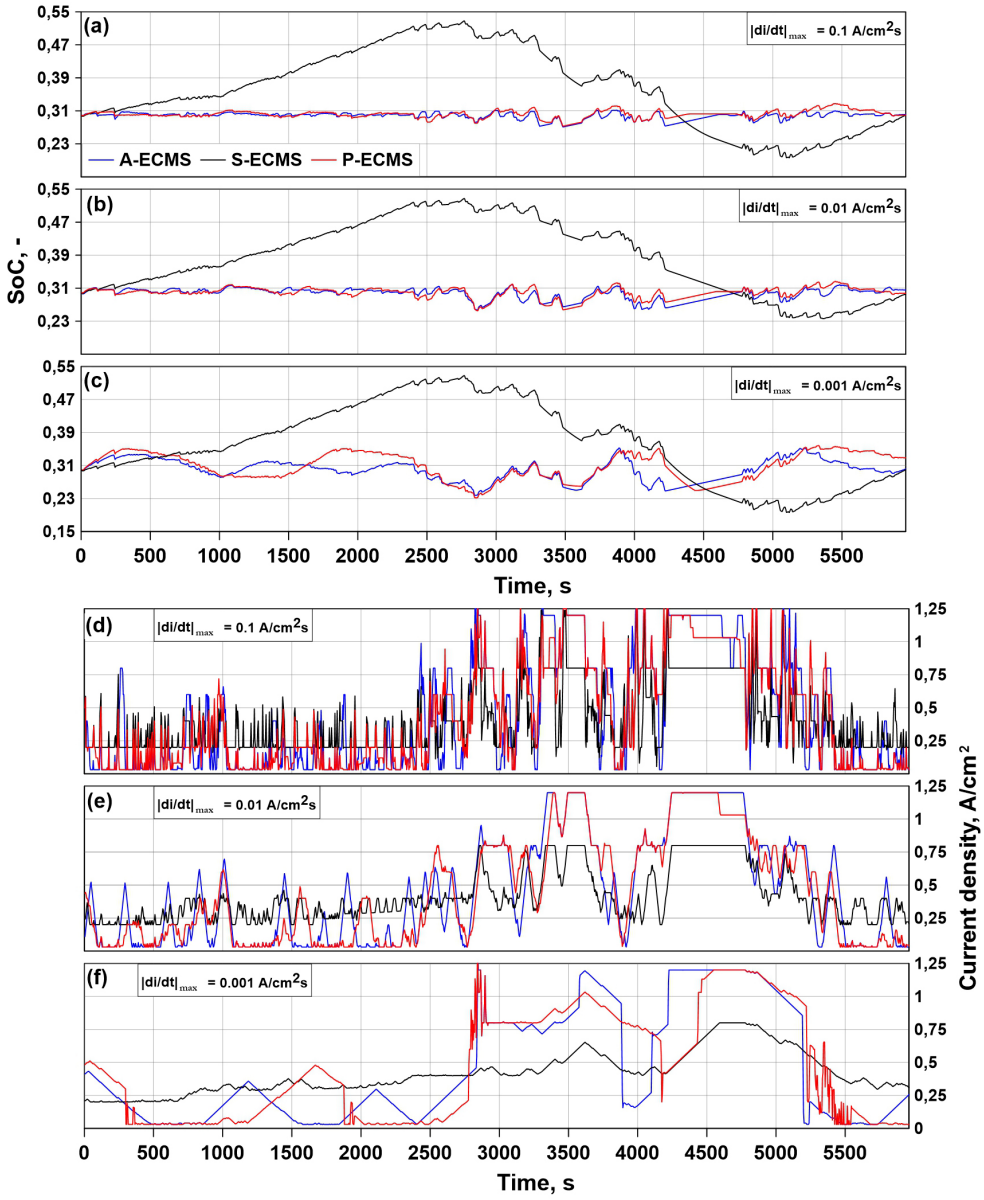

Figure 6.35: Comparison of time evolution SoC (a-b-c) and fuel cell current density (d,e,f) for different fuel cell dynamic limitations in the Bucarest-Giurgiu cycle.

to decreased hydrogen consumption (Figure 6.36), which is approximately 6% lower than that of the P-ECMS in the high dynamic scenario. Notably, this difference becomes more pronounced as the dynamic limitation is lowered (Figure 6.36).

The S-ECMS's behavior can only be replicated with prior knowledge of the driving cycle since it involves proactive battery charging during periods of low electric motor power demand. In such a way, the overall powertrain efficiency during high-demand situations is enhanced, where using the FCS together with the battery effectively mitigates hydrogen consumption. While this approach offers optimal performance, it lacks practicality and feasibility in charge-sustaining modes without a prior knowledge of the driving cycle.

Both the P-ECMS and A-ECMS exhibit similar performance characteristics. However, the P-ECMS outperforms the A-ECMS by being able to predict the future velocity profile, resulting in a reduction in hydrogen consumption by approximately 0.7-3.2%, depending on the $|\mathrm{di/dt}|_{max}$. The impact of hydrogen consumption when comparing the P-ECMS to the A-ECMS is more pronounced at high dynamics (3.2%) due to the less restrictive FC control, enabling the vehicle to fully leverage the speed forecast. As the dynamic limitation on the FCS increases, this benefit diminishes because the current density's evolution cannot match the optimal trajectory predicted by the P-ECMS, resulting in a performance penalty.

In contrast to the HDDT cycle, all EMSs in this test case demonstrate improved final SoC tracking accuracy, with the least favorable scenario being a 2% battery discharge with the P-ECMS for $|\mathrm{di/dt}|_{max}$= 0.001 A/cm^{2}s. To achieve these SoC values at the end of the cycle, both the P-ECMS and the A-ECMS occasionally need to bypass the dynamics constraint multiple times to maintain the SoC within predefined limits. This underscores the critical importance of having the flexibility to occasionally disregard this constraint in both the P-ECMS and A-ECMS, particularly in realistic driving conditions, where charge-sustaining operation would be unfeasible without this capability.

Figures 6.38 and 6.39 provide further affirmation that the imposition of dynamic limitations substantially enhances the FC stack's durability, more than doubling it for each EMS. Agaqin this marked improvement primarily arises from the reduction in load-change degradation. In contrast to the results obtained during the HDDT cycle (Figure 6.34), high-power degradation assumes greater significance, albeit remaining the least impactful. This discrepancy can be attributed to the possibility of encountering high-power demand conditions during real-world driving, causing the FC stack to operate at current densities exceeding 1 A/cm^2 (Figure 6.35).

To streamline presentation, the relative contributions of each degradation

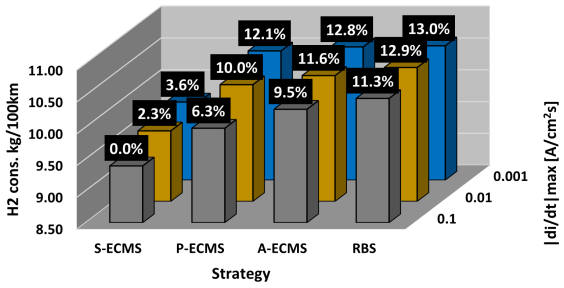

Figure 6.36: H_2 consumption evolution as a function of the EMS and the dynamic limitations in the Bucarest-Giurgiu cycle.

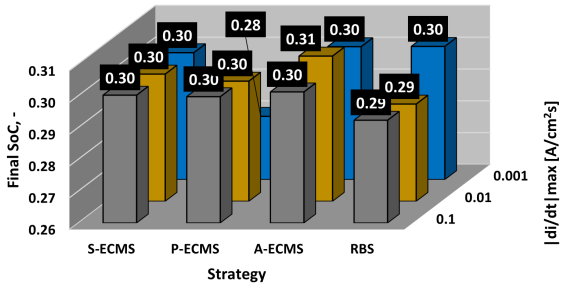

Figure 6.37: Terminal SoC evolution as a function of the EMS and the dynamic limitations in the Bucarest-Giurgiu cycle.

source are illustrated solely for the P-ECMS in Figure 6.39. This representation underscores a substantial reduction in the significance of load-change degradation, decreasing from 63% to 23%.

When comparing the predicted FC durability for cases with $|di/dt|_{max}$= 0.01 A/cm^{2}s and $|di/dt|_{max}$= 0.001 A/cm^{2}s, it becomes evident that durability increases by a modest 6.2-22% (excluding the S-ECMS case, which is not realistic). This effect is particularly marginal in the case of the P-ECMS, where durability only improves by 6.2%, accompanied by a 2.1% penalty in hydrogen consumption. These findings suggest that, for real-world driving scenarios with the P-ECMS or A-ECMS, imposing highly restrictive FC dynamics does not yield significant durability benefits. Therefore, it may be worthwhile, in terms of the trade-off between performance and durability, to consider moderate

dynamics ($|di/dt|_{max}$= 0.01 A/cm^{2}s) for practical driving conditions. However, such a decision should be complemented by a life cycle assessment or total cost of ownership calculation, depending on the optimization objectives.

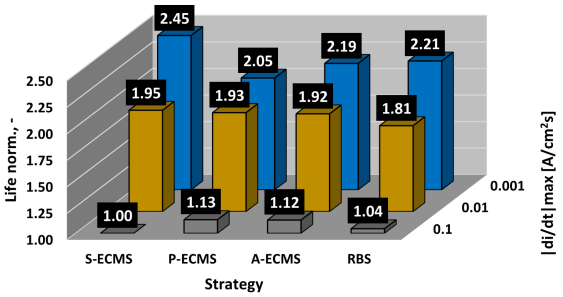

Figure 6.38: Normalized FC stack durability (life) evolution as a function of the EMS and the dynamic limitations in the Bucarest-Giurgiu cycle.

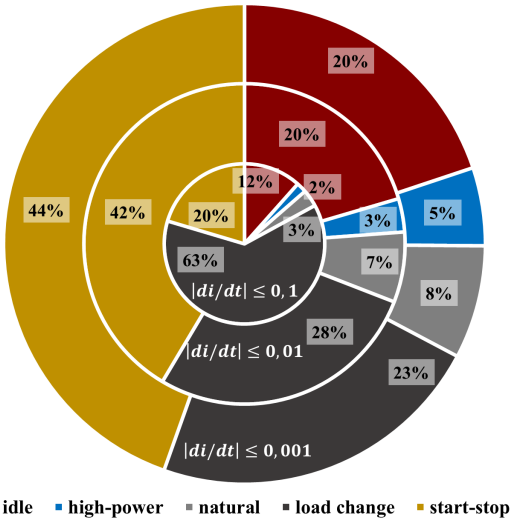

Figure 6.39: Degradation source relative effect on FC stack durability for the P-ECMS with different dynamic limitations in the Bucarest-Giurgiu cycle. $|di/dt|$ is in A/cm^2s.

6.4.3 Integration of an intelligent SoC planner for controlling a heavy-duty FCV controlled by a P-ECMS

In the context of operating in charge-depleting mode, effective planning of the battery SoC trajectory becomes pivotal for optimizing battery utilization. In real-world scenarios, acquiring comprehensive trip information, encompassing precise data on distances, elevation profiles, and speed profiles, can prove challenging or even unfeasible. However, map service providers offer simplified information, such as road networks, speed limits, and estimated distances between various locations. This work introduced a SoC planner layer under this assumption.

Battery state of charge planning

Recognizing the intricate interplay among vehicle speed, distance to be covered, and SoC, a feed-forward neural network approach has been adopted. The dataset employed for training the network comprises simulations conducted using the ECMS as the EMS. These simulations span four distinct driving cycles and encompass varying initial SoC levels (ranging from 30% to 80%, in increments of 10%), as detailed in Table 6.12 and exemplified in Figure 6.40 for the Napoli-Nola cycle. The desired final SoC is standardized at 30% across all simulations, aligning with the vehicle's range extender architecture, as demonstrated in previous works [48–50]. Table 6.12 introduces the concept of "2*HDDT," signifying a sequence comprising two HDDT cycles combined to form a longer driving cycle, consistent with charge-depleting operations. These simulations encompass a diverse array of scenarios, facilitating the neural network's ability to discern underlying patterns and correlations between input variables and resultant SoC variations. The SoC planner operates by partitioning the driving cycle into fixed-length segments, assuming that average speed information can be supplied within each segment. Its primary objective is to determine the desired SoC at the conclusion of each segment. To achieve this, the neural network takes into account four input variables: initial SoC, average speed within each segment, remaining distance as a percentage of the total, and segment length as a percentage of the total. Subsequently, the neural network generates predictions for the SoC at the conclusion of each segment.

The architecture of the neural network is optimized using a Bayesian optimization to minimize the mean square error, which quantifies the discrepancy between the predicted and actual SoC values (Equation 6.44):

$$MSE = \frac{1}{N}\sum_{i=1}^{N}(SoC_{end}(i) - SoC_{tar}(i))^2 \tag{6.44}$$

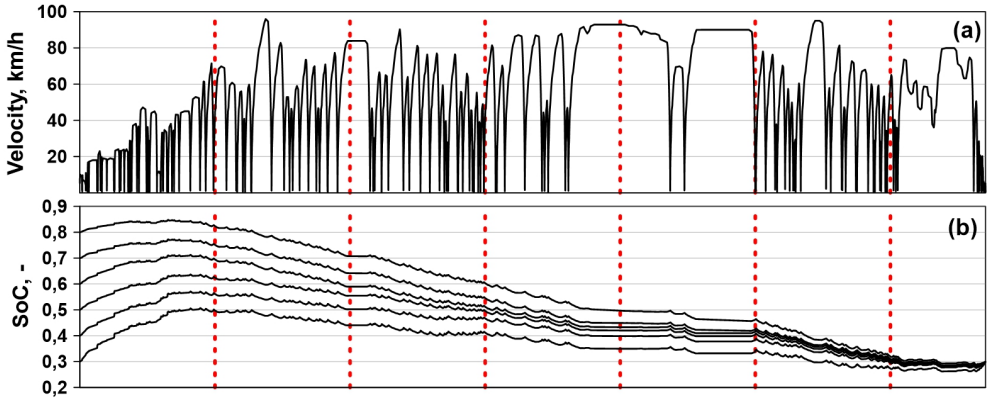

Figure 6.40: Optimal battery SoC curves under Napoli-Nola driving cycle divided in 5km long driving segments

Route	Country	Distance, km
2*HDDT	-	74.4
Napoli-Nola	Italy	33.5
Budapest-Tatabanya	Hungary	60.3
Hamburg-Ahrensburg	Germany	39.7

Table 6.12: Routes for the SoC planning layer dataset generation based on TENT-T routes

where N is the number of data, and $SoC_{end}(i)$, $SoC_{tar}(i)$ are the neural network output and target SoC. To avoid overfitting, a cross-validation scheme is used. Following optimization, the neural network architecture has been configured with three hidden layers, comprising 37, 211, and 4 neurons, respectively, all utilizing the sigmoid activation function. This fine-tuned architecture has achieved a Mean Squared Error of 0.0097. The SoC planning algorithm operates through the following sequence: at the commencement of each trip, the SoC planner is furnished with average speed data and segment length information for each driving segment by the map service provider. Utilizing this information, the SoC planned for the conclusion of the initial segment is determined, subsequently serving as the initial SoC for the following segment. To address the inherent lack of detailed information within these segments, a linear reference SoC assumption is invoked. This assumption posits a linear relationship between successive predicted points and is expressed as:

$$SOC_{ref}(t) = SOC_{start} - \frac{x(t)}{L_s}(SOC_{start} - SOC_{end}) \tag{6.45}$$

Here, SOC_{start} and SOC_{end} represent the initial and final SOC values for each segment, respectively. Meanwhile, $x(t)$ denotes the cumulative traveled distance at time t, and L_s signifies the length of the road segment. Consequently, the neural network produces an initial approximate SoC trajectory, providing predictions for the SoC at the conclusion of each segment. The specific length of each segment hinges upon the data supplied by the map service provider, as well as the overall length of the driving mission itself. Further elaboration on this aspect is presented in the following section.

Charge depleting operation results

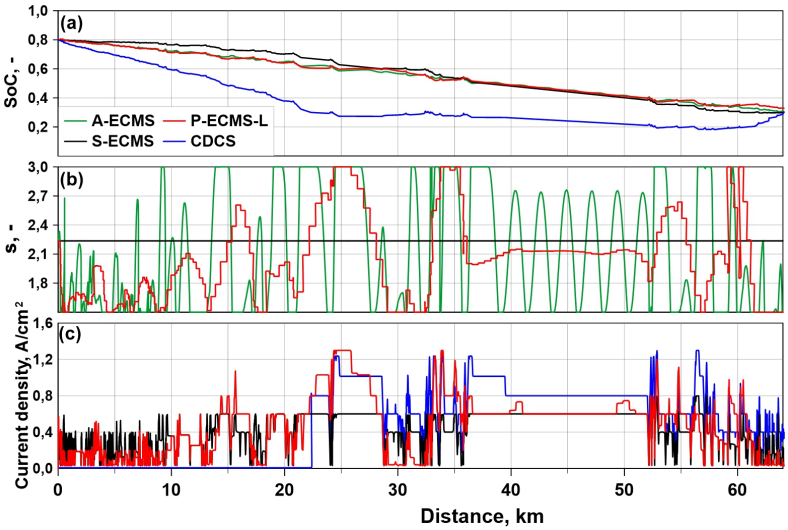

Figure 6.41: Comparisons of (a) Battery SoC, (b) EF, (c) Fuel cell current density for S-ECMS, CDCS, P-ECMS-L and A-ECMS in the Bucarest-Giurgiu cycle.*

The simulation results for the fuel cell vehicle operating in charge-depleting mode on two different driving cycles are examined in this section. According to equations 6.41 and 6.42, when operating in charge depleting operation, both the P-ECMS and the A-ECMS need a reference SoC trajectory to update the equivalence factor. During this work, an initial assumption is made, wherein a linear battery discharge with respect to the traveled distance is considered. Subsequently, the integration of the P-ECMS with the SoC planning layer is

evaluated across various planning segment lengths. In the forthcoming, the P-ECMS based on linear SoC planning will be referred to as P-ECMS-L, while the P-ECMS utilizing SoC planning through the SoC planning layer with a planning segment length of X kilometers will be referred to as P-ECMS-Xkm. This study compares both strategies with the S-ECMS and an optimal charge-depleting/charge-sustaining strategy denoted as CDCS*. The CDCS* strategy operates by exclusively using the battery as the energy source until the battery SoC reaches 30%. Subsequently, power distribution is calculated using the S-ECMS approach, with the equivalence factor suitably tuned to maintain a 30% SoC at the conclusion of the driving cycle. The previously tuned values of EF_0 and k_p (P-ECMS with $EF_0 = 2.2$, $k_p = 14$, and A-ECMS with $EF_0 = 2.1$, $k_p = 10$)(section 6.4.2) are applied in the subsequent simulations involving equations 6.41 and 6.42. The initial SoC is set to 80% for all the simulations. The analysis begins by analyzing the results obtained during the realistic Bucarest-Giurgiu driving cycle, followed by an examination of the results from the 2*HDDT driving cycle.

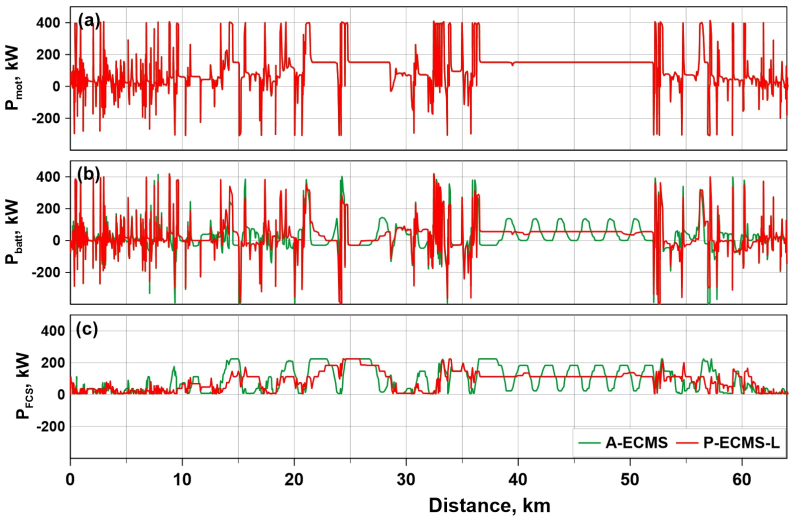

Figure 6.42: Comparisons of (a) Electrical motor power, (b) Battery power, (c) Fuel cell systems power for P-ECMS-L and A-ECMS in the Bucarest-Giurgiu cycle.

Figure 6.41 compares the evolution of battery SoC, equivalence factor, and fuel cell current density across the S-ECMS, CDCS*, P-ECMS-L, and A-ECMS strategies in the Bucarest-Giurgiu cycle. This comparative analysis is conducted to demonstrate the effectiveness of the P-ECMS strategy, even under battery discharge conditions. Notably, P-ECMS-L exhibits a smoother

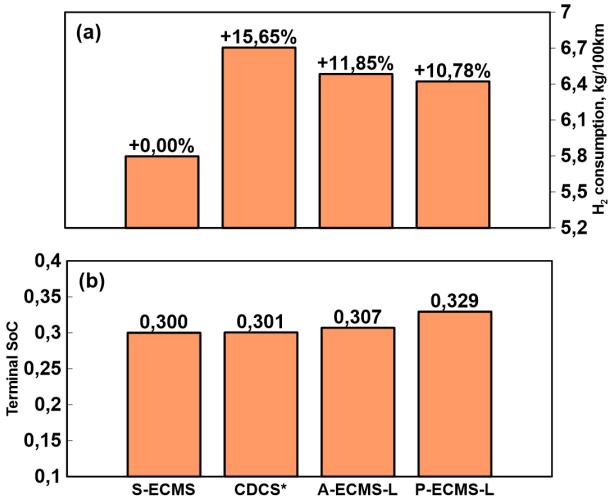

Figure 6.43: Performance comparison in the Bucarest Giurgiu cycle between S-ECMS, CDCS, P-ECMS-L, A-ECMS. (a) Hydrogen consumption. (b) Terminal SoC.*

correction of the equivalence factor in comparison to A-ECMS, resulting in reduced hydrogen consumption (Figure 6.43), despite often having similar fuel cell utilization. This smoother equivalence factor correction also leads to a more stable power output from the fuel cell, as evidenced in the range between 35 and 50 kilometers in Figure 6.42. During this period, both the fuel cell and the battery operate at nearly constant power levels. This not only contributes to reduced hydrogen consumption but is also expected to decrease component degradation. Figure 6.43 offers a detailed comparison of hydrogen consumption and final battery SoC. The percentage value displayed above each histogram indicates the increase in hydrogen consumption relative to the S-ECMS strategy. Due to the difference in equivalence factor update frequency, P-ECMS-L slightly exceeds the SoC target during battery discharge, resulting in a final SoC of 32.9% and a consequent penalty on hydrogen consumption. Nevertheless, both P-ECMS-L and A-ECMS strategies lead to a reduction in hydrogen consumption when compared to the CDCS* strategy, highlighting the well-established significance of optimal battery utilization.

The effectiveness of the SoC planning layer is demonstrated through the results presented in Figure 6.44. Specifically, the P-ECMS-L is compared with the same strategy integrated with the SoC planning layer, considering different lengths for the SoC planning segment. In Figure 6.44, the percentage value displayed above each histogram indicates the variation in hydrogen consumption

compared to P-ECMS-L. Interestingly, for a planning segment length of 2 km, a slight increase in hydrogen consumption is observed, while the minimum consumption occurs for a segment length of 6 km, resulting in a reduction of about 5.7%. Additionally, an improvement in battery discharge is noticeable, with SoC values approaching the designated 30% target.

Figure 6.45 illustrates the comparison of different planning segment lengths, including the optimal length (6 km), the minimum length (2 km), and the maximum length (9 km). The dot symbols in Figure 6.45-a represent the SoC trajectory planning results. The P-ECMS-2 km trajectory exhibits the greatest difference in SoC compared to the optimal trajectory of S-ECMS and also displays the highest fuel consumption 6.44. This difference is attributed to the reduced utilization of the fuel cell in the first part of the mission and increased usage in the second part, as observed in Figure 6.45-b. Consequently, the FCS exhibits lower efficiency overall. The P-ECMS-9 km trajectory maintains a higher SoC throughout the entire simulation at the expense of slightly higher fuel cell current density and reduced efficiency compared to the P-ECMS-6 km trajectory. Furthermore, the larger error in the final SoC contributes to an increased equivalent hydrogen consumption.

A more detailed analysis of the results is presented in Figure 6.46, where the S-ECMS and P-ECMS-L strategies are compared with the P-ECMS-6 km (representing the optimal case provided by the SoC planning layer integration) in terms of battery SoC, equivalence factor, fuel cell current density, and hydrogen consumption. From the analysis of the results, it can be observed that during the first 20 km of the driving mission, the P-ECMS-6 km plans for a higher battery SoC compared to P-ECMS-L, bringing it closer to the performance of S-ECMS. This leads to a generally higher equivalence factor, resulting in a higher fuel cell current density and hydrogen consumption. In the subsequent portion of the driving cycle, although the planned SoC deviates further from the trajectory of S-ECMS, P-ECMS-6 km is able to provide a lower overall hydrogen consumption throughout the driving cycle and a final SoC closer to the 30% target. It should be emphasized that the Bucharest-Giurgiu cycle is not part of the training dataset for the SoC planning layer; therefore, this tool has been tested under unknown driving conditions for both the velocity predictor layer and the SoC planning layer, demonstrating the robustness of the proposed methodology.

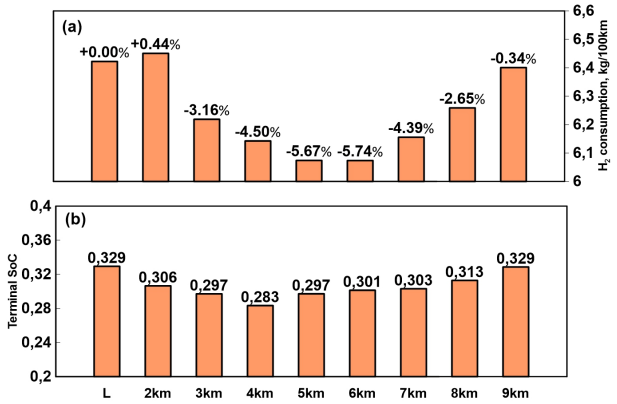

Figure 6.44: Performance comparison in the Bucarest Giurgiu cycle between P-ECMS with linear SoC planning (L) and different planning road segment length: (a) Hydrogen consumption. (b) Terminal SoC.

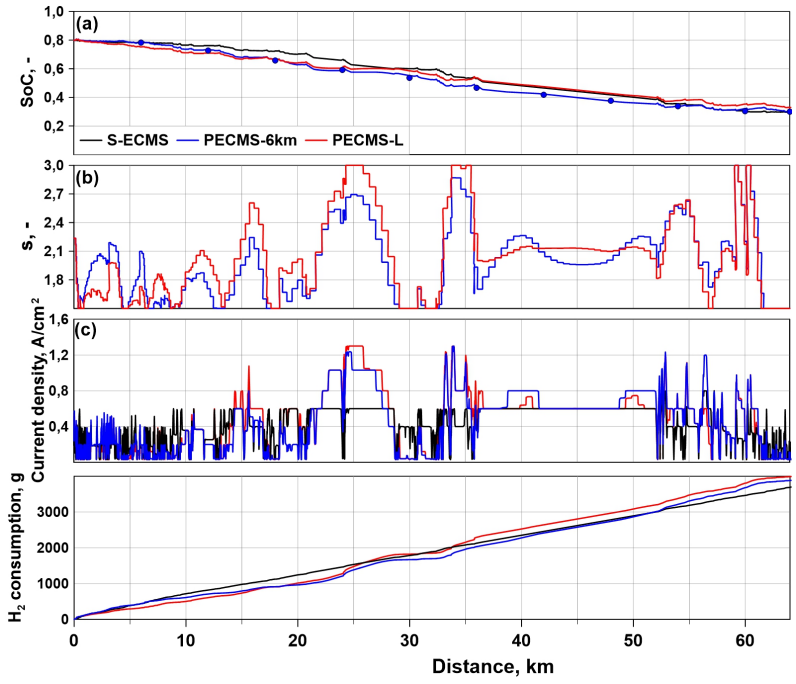

Figure 6.45: Comparisons of (a) Battery SoC, (b) Fuel cell current density, (d) FCS efficiency for P-ECMS-2km, P-ECMS-6km and P-ECMS-9km in the Bucarest-Giurgiu cycle. The dots in (a) represent the SoC trajectory planning.

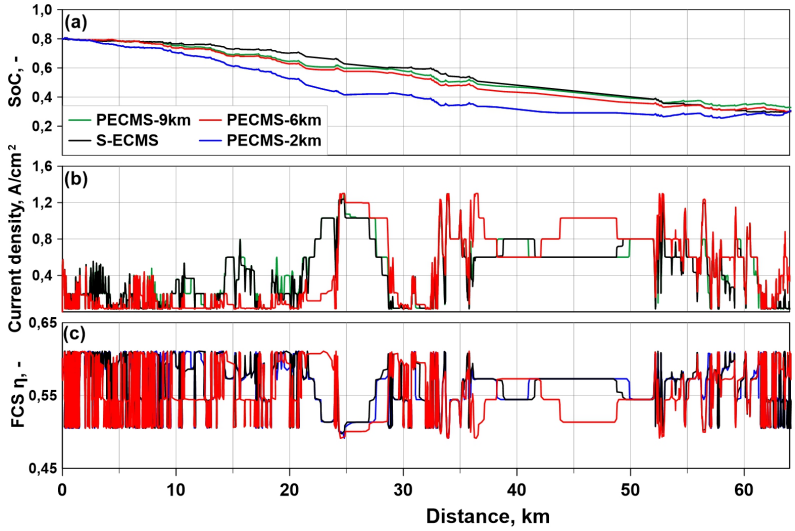

Figure 6.46: Comparisons of (a) Battery SoC, (b) EF, (c) Fuel cell current density (d) Hydrogen consumption for S-ECMS, P-ECMS-L and P-ECMS-6km in the Bucarest-Giurgiu cycle. The dots in (a)represent the SoC trajectory planning.

In the case of the 2*HDDT driving cycle, the P-ECMS-L strategy exhibits performance closest to that of the S-ECMS, resulting in a modest increase in hydrogen consumption of approximately 2.9% (Figure 6.48). The corrections applied by P-ECMS-L to the equivalence factor are consistently smaller compared to A-ECMS (Figure 6.47). As a consequence, there are significant alterations in the utilization of both the fuel cell and the battery, thereby influencing hydrogen consumption.

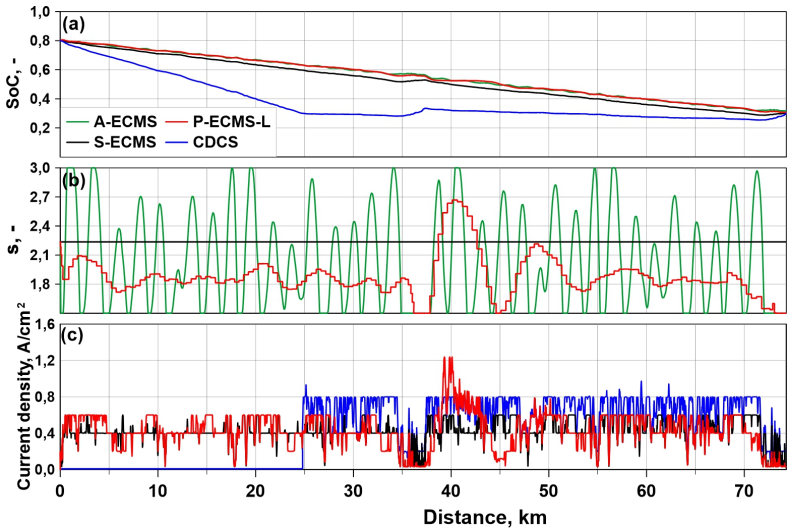

Figure 6.47: Comparisons of (a) Battery SoC, (b) EF, (c) Fuel cell current density (d) Hydrogen consumption for S-ECMS, CDCS, P-ECMS-L and A-ECMS-L in the 2*HDDT cycle.*

In this specific test scenario, the consumption pattern of the A-ECMS strategy differs from that of the CDCS* strategy, exhibiting higher consumption levels. This discrepancy can be ascribed to notable fluctuations in the equivalence factor, stemming from the use of proportional control as delineated in equation 6.41. These fluctuations manifest predominantly under conditions of steady-speed driving, where the system lacks foreknowledge of future conditions. Consequently, variations in the equivalence factor lead to amplified oscillations in fuel cell power output, as illustrated in Figure 6.49. Notably, the driving cycle under examination constitutes a unique case characterized by extended periods of high-speed highway driving with minimal speed variations, maintaining a nearly constant speed of approximately 95 km/h.

For the S-ECMS strategy, which approximates the policy closest to optimality within the framework of this analysis, it operates with a constant

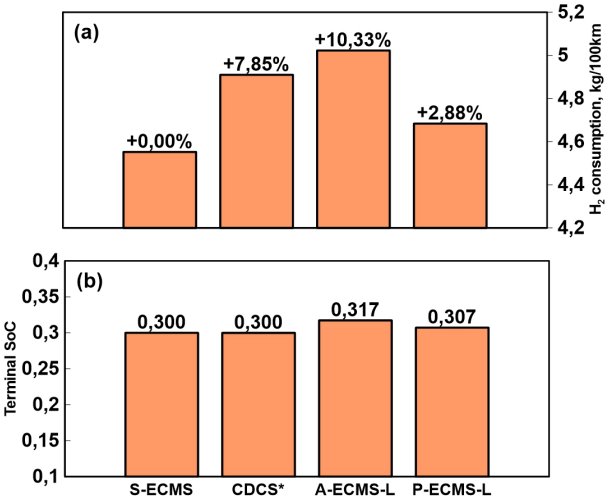

*Figure 6.48: Performance comparison in the 2*HDDT cycle between S-ECMS, CDCS*, P-ECMS-L, A-ECMS . (a) Hydrogen consumption. (b) Terminal SoC.*

equivalence factor. Consequently, a constant power demand at the wheels results in a stable cost function (as defined in equation 6.37), translating into a sustained output of power from both the fuel cell and the battery.

This contextual understanding clarifies why, in this particular scenario, SoC trajectory planning for P-ECMS-Xkm provides marginal advantages when contrasted with P-ECMS-L (as depicted in Figure 6.50). The comparative analysis involving S-ECMS, P-ECMS-L, and P-ECMS-6km is delineated in Figure 6.51. As elucidated, P-ECMS-L and P-ECMS-6km exhibit highly similar behaviors for the majority of the driving cycle. The most notable distinction becomes evident within the segment spanning 40 km to 50 km, where P-ECMS-6km strategizes for a lower SoC that closely aligns with the one achieved by S-ECMS. Consequently, P-ECMS-6km realizes a noteworthy reduction in hydrogen consumption, approximately amounting to 1.8%.

In a broader context, it's evident that the outcomes achieved with P-ECMS-Xkm are contingent on the length of the SoC prediction segment. Assuming that the necessary data can be reliably supplied by a map service provider, it's advisable to select a segment length within the range of 3 km to 8 km. Deviating from this range might lead to a marginal deterioration in consumption compared to the performance of P-ECMS-L. In situations characterized by high-speed highway driving, where the vehicle consistently maintains a constant velocity, it's recommended to plan for a linear battery discharge profile.

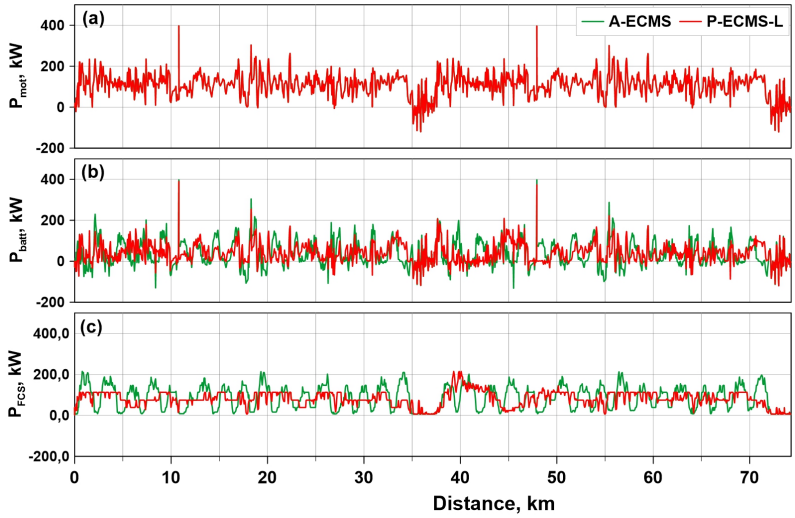

*Figure 6.49: Comparisons of (a) Electrical motor power, (b) Battery power, (c) Fuel cell systems power for P-ECMS-L and A-ECMS in the 2*HDDT cycle.*

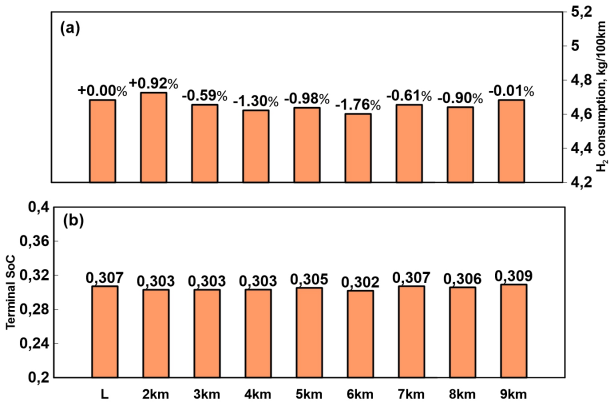

*Figure 6.50: Performance comparison in the 2*HDDT cycle between P-ECMS with linear SoC planning (L) and different planning road segment length: (a) Hydrogen consumption. (b) Terminal SoC.*

The forthcoming research endeavors will encompass the application of this proposed strategy in Hardware-in-the-Loop (HiL) simulations, aimed at evaluating its adaptability under diverse driving conditions. Furthermore, the strategy's performance and its impact on fuel cell degradation under varying dynamic constraints on the fuel cell will be explored. To facilitate this

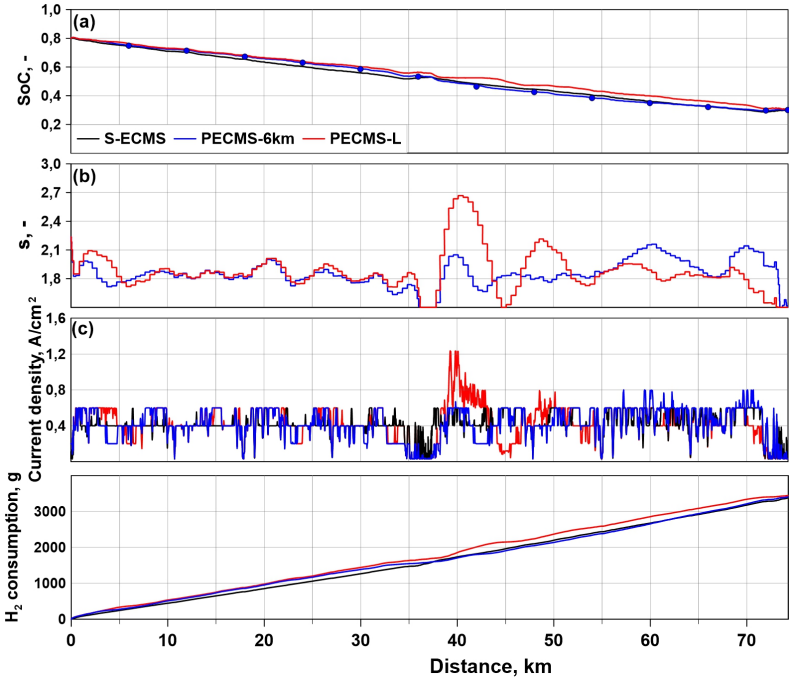

*Figure 6.51: Comparisons of (a) Battery SoC, (b) EF, (c) Fuel cell current density (d) Hydrogen consumption for S-ECMS, P-ECMS-L and P-ECMS-6km in the 2*HDDT cycle. The dots in (a) represent the SoC trajectory planning.*

investigation, enhancements to the SoC planning layer are planned, which will enable the consideration of variable dynamic limits for the fuel cell, given their expected influence on battery behavior.

6.5 Summary and conclusions

This chapter has demonstrated that hybrid powertrains require efficient control from both a numerical and real-world perspective, accomplished through the implementation of a well-designed EMS. In the existing literature, numerous control strategies have been proposed to address the energy distribution challenge, employing both analytical and numerical approaches.

Following a brief literature review, this PhD work presents the extension of the ETESS strategy, applied to enhance energy management in Plug-in Hybrid Electric Vehicles equipped with small-sized engines. The fundamental principle underlying this approach involves an alternative utilization of

both the thermal engine and electric machine to meet the power demands for propulsion. This strategy defines three primary operating modes: pure thermal mode, pure electric mode, and parallel mode. In addition to these, a fourth traction-charging mode has been considered in this comprehensive investigation. The simulation study is conducted using a vehicle model within the MATLAB/Simulink environment. To create an adaptive-EMS, an adaptive logarithmic-based function is implemented, selected for its stability, and represented as a two-dimensional lookup table. The same adaptive function is incorporated into the ECMS to enable a meaningful comparison between the two strategies in terms of fuel consumption and computational efficiency. In the initial phase, both strategies are finely tuned to minimize the average difference between actual SoC and target SoC for various driving cycles, including US06, WLTC, Artemis Highway, and an RDE cycle, through cycle-dependent tuning parameters. These parameters are then correlated with the distance traveled using a fitting function, making the approach applicable to any driving cycle. Simulation results reveal that A-ETESS and A-ECMS exhibit an average total fuel consumption difference of less than 2.5%. PIL tests are conducted to compare the computational time required by A-ETESS and A-ECMS and to assess the feasibility of implementing A-ETESS in a real-time vehicle application. The EMSs are executed on the NUCLEO-H743 board, while the vehicle model runs on a PC host. PIL results demonstrate that A-ETESS can operate significantly faster than A-ECMS, with execution times well below the typical cycle time of a CAN message, making real-time control of engine and motor torque requests viable for on-vehicle applications.

In recent years, the rapid progress of artificial intelligence and computer technologies has led to the increasing utilization of learning algorithms within the EMS field, establishing it as a novel and highly regarded research frontier. For this reason, following an explanation of the principles of artificial intelligence and neural networks, this chapter provides an account of the development of an EMS enhanced by the incorporation of neural networks, with a detailed analysis of the results of its application. An innovative approach to enhance the energy management of heavy-duty Fuel Cell Vehicle under real-world driving conditions has been introduced in the form of a P-ECMS. This strategy is tailored to meet the specific demands and challenges posed by heavy-duty FCVs, ensuring optimal performance while taking into account the unique characteristics of these vehicles. The P-ECMS has been enhanced through the integration of an LSTM prediction layer. This enhancement operates by dynamically adjusting the equivalence factor based on the difference between the predicted SoC and the desired target SoC. To facilitate the training of the velocity predictor, a realistic driving dataset has been generated using GT-

Real Drive, utilizing data from the TEN-T routes. Furthermore, an in-depth sensitivity analysis has been conducted on the P-ECMS, examining its response to variations in the initial equivalence factor and update gain value. The performance of the P-ECMS has been rigorously compared with several other strategies, including a conventional A-ECMS, the reference S-ECMS, and an RBS, across two distinct driving cycles and three dynamic restrictions on the fuel cell current (0.1, 0.01, and 0.001 A/cm^2s). This comparison encompasses a comprehensive evaluation of battery SoC management, equivalence factor dynamics, hydrogen consumption, and fuel cell degradation. The velocity prediction accuracy has been verified, with a velocity RMSE of 6.08km/h and 11.80km/h recorded for the HDDT and a realistic cycle, respectively. Notably, both the P-ECMS and A-ECMS exhibit improvements in battery SoC management compared to the S-ECMS. However, the P-ECMS stands out by achieving a reduction in hydrogen consumption ranging from 1.4% to 2% for the HDDT cycle and up to 3% for the realistic driving cycle, depending on the dynamic limitations, compared to the A-ECMS. When compared to an RBS, the P-ECMS achieves an impressive reduction in fuel consumption of up to 6.1%. Additionally, the results underscore the influence of dynamic limitations on hydrogen consumption and FC durability across all tested strategies. As dynamic limitations increase, H_2 consumption rises, and the importance of various degradation sources shifts. Notably, load-change degradation, which holds significance under low dynamic restrictions, becomes less significant. In contrast, start-stop and low-power degradation take on greater importance. This finding has implications for FC stack manufacturers designing systems for FCREx vehicles, potentially leading to a shift in focus towards addressing degradation in high-voltage conditions and prioritizing materials with low degradation characteristics.

In addition, the P-ECMS has been integrated with a SoC planning layer to enable the vehicle to operate in charge-depleting mode. In fact, the SoC planning layer plays a crucial role in managing battery discharge during driving missions. It effectively plans a target SoC trajectory by utilizing data from a map service provider, enabling pre-mission planning. This layer incorporates a neural network trained on simulation outcomes derived from the S-ECMS strategy, considering four distinct driving cycles and various initial SoC values. The training objective is to achieve a final SoC of 30%, aligning with typical plug-in vehicle operations. The benefits of the P-ECMS are further validated in scenarios involving battery discharge, encompassing both a realistic driving cycle and a composite driving cycle consisting of consecutive HDDT cycles. In both cases, the P-ECMS demonstrates a noteworthy reduction in consumption, with improvements of up to 5% compared to an optimal CDCS strategy

employing linear battery discharge planning. The advantages stemming from the integration of the SoC planning layer are underscored through a comparison between the P-ECMS with linear battery discharge planning and the P-ECMS-Xkm, where the SoC trajectory is planned by the SoC planning layer for varying prediction segment lengths. Furthermore, the study unveils that the performance of the P-ECMS, enhanced by the SOC planning layer, is contingent on the length of the SoC prediction segment. The presented results indicate that a segment length ranging from 3 km to 8 km, supplemented by data from a map service provider, yields superior outcomes. Deviating from this range may result in a marginal increase in consumption when compared to P-ECMS-L.

References

[1] Huang, Y., Wang, H., Khajepour, A., He, H., and Ji, J. "Model Predictive Control Power Management Strategies for HEVs: A Review". In: *Journal of Power Sources* 341 (2017), pp. 91–106. DOI: 10.1016/J.JPOWSOUR.2016.11.106.

[2] Tribioli, L. et al. "A Real Time Energy Management Strategy for Plug-in Hybrid Electric Vehicles Based on Optimal Control Theory". In: *Energy Procedia* 45 (2014), pp. 949–958. DOI: 10.1016/J.EGYPRO.2014.01.100.

[3] Gissing, J., Themann, P., Baltzer, S., Lichius, T., and Eckstein, L. "Optimal Control of Series Plug-In Hybrid Electric Vehicles Considering the Cabin Heat Demand". In: *IEEE Transactions on Control Systems Technology* 24 (2016), pp. 1126–1133. DOI: 10.1109/TCST.2015.2468055.

[4] Shankar, R., Marco, J., and Assadian, F. "Design of an Optimized Charge-Blended Energy Management Strategy for a Plugin Hybrid Vehicle". In: *Proceedings of the 2012 UKACC International Conference on Control, CONTROL 2012*. 2012, pp. 619–624. DOI: 10.1109/CONTROL.2012.6334701.

[5] Bellman, Richard E. *Dynamic Programming*. Princeton: Princeton University Press, 1957.

[6] Brahma, A., Guezennec, Y., and Rizzoni, G. "Optimal energy management in series hybrid electric vehicles". In: *Proceedings of the 2000 American Control Conference*. Vol. 1. Issue: 6. 2000, pp. 60–64.

[7] Sciarretta, Antonio and Guzzella, Lino. "Control of hybrid electric vehicles". In: *IEEE Control Systems Magazine* 27.2 (2007), pp. 60–70. DOI: 10.1109/MCS.2007.338280.

[8] Kareemulla, Thayyil, Delprat, Sebastien, and Czelecz, Loic. "State constrained hybrid vehicle optimal energy management: an interior penalty approach". In: *IFAC-PapersOnLine* 50.1 (2017), pp. 10040–10045. DOI: 10.1016/j.ifacol.2017.08.1774.

[9] Sánchez, Marco, Delprat, Sebastien, and Hofman, Tom. "Energy management of hybrid vehicles with state constraints: A penalty and implicit Hamiltonian minimization approach". In: *Applied Energy* 260 (2020), p. 114149. DOI: 10.1016/j.apenergy.2019.114149.

[10] Yeqin, Wang et al. "Research on energy optimization control strategy of the hybrid electric vehicle based on Pontryagin's minimum principle". In: *Computers & Electrical Engineering* 72 (2018), pp. 203–213. DOI: 10.1016/j.compeleceng.2018.09.018.

[11] Chong, Huang, Minggao, Ouyang, Liangfei, Xiong, and Hewu, Wang. "Approximate Pontryagin's minimum principle applied to the energy management of plug-in hybrid electric vehicles". In: *Applied Energy* 115 (2014), pp. 174–198. DOI: 10.1016/j.apenergy.2013.11.002.

[12] Paganelli, Giovanni, Delprat, Sebastien, Guerra, Thierry M., Rimaux, Jerome, and Santin, Jose J. "Equivalent consumption minimization strategy for parallel hybrid powertrains". In: *Vehicular Technology Conference IEEE 55th Vehicular Technology Conference VTC Spring 2002*. Vol. 4. 2002, pp. 2076–2081. DOI: 10.1109/VTC.2002.1002989.

[13] Zhang, Feilong, Xi, Jianquan, and Langari, Reza. "An adaptive equivalent consumption minimization strategy for parallel hybrid electric vehicle based on Fuzzy PI". In: *Proceeding of 2016 IEEE Intelligent Vehicles Symposium (IV)*. 2016, pp. 460–465. DOI: 10.1109/IVS.2016.7535426.

[14] Pei, Di and Leamy, Michael J. "Dynamic Programming-Informed Equivalent Cost Minimization Control Strategies for Hybrid-Electric Vehicles". In: *J. Dyn. Sys., Meas., Control* 135.5 (2013), p. 051013. DOI: 10.1115/1.4024788.

[15] Chao, Siyu D, Liang, Liang, Sixong, Yang, Yiyong, Yu, and Yue, Z. "Adaptive real-time optimal energy management strategy based on equivalent factors optimization for plug-in hybrid electric vehicle". In: *Appl Energy* 203 (2017), pp. 883–869. DOI: 10.1016/j.apenergy.2017.06.106.

[16] Serrao, Lorenzo, Onori, Simona, and Rizzoni, Giorgio. "A comparative analysis of energy management strategies for hybrid electric vehicles". In: *J. Dyn. Sys., Meas., Control* 133.3 (2011), p. 031012. DOI: 10.1115/1.4003267.

[17] Musardo, Christian, Rizzoni, Giorgio, Guezennec, Yann, and Staccia, Barbara. "A-ECMS: An Adaptive Algorithm for Hybrid Electric Vehicle Energy Management". In: *European Journal of Control* 11.4 (2013), pp. 509–524. DOI: 10.3166/ejc.11.509-524.

[18] Chao, Siyu, Fengchun, Sun, and Hongwen, He. "Investigating adaptive-ECMS with velocity forecast ability for hybrid electric vehicles". In: *Appl Energy* 185 (2017), pp. 1644–1653. DOI: 10.1016/j.apenergy.2016.02.026.

[19] De Bellis, Vincenzo, Malfi, Enrica, and Zaccardi, Jean-Marc. "Development of an Efficient Thermal Electric Skipping Strategy for the Management of a Series/Parallel Hybrid Powertrain". In: *Energies* 14.4 (2021). Number: 4 Publisher: Multidisciplinary Digital Publishing Institute, p. 889. DOI: 10.3390/en14040889.

[20] Bellis, Vincenzo De, Piras, Marco, and Malfi, Enrica. "Assessment of an Adaptive Efficient Thermal/Electric Skipping Control Strategy for the Management of a Parallel Plug-in Hybrid Electric Vehicle". In: *Energies* 15.19 (2022). Number: 19 Publisher: Multidisciplinary Digital Publishing Institute, p. 7122. DOI: 10.3390/en15197122.

[21] Pisner, Derek A. and Schnyer, David M. "Chapter 6 - Support vector machine". In: *Machine Learning*. Ed. by Andrea Mechelli and Sandra Vieira. Academic Press, 2020, pp. 101–121. DOI: 10.1016/B978-0-12-815739-8.00006-7.

[22] Kingsford, Carl and Salzberg, Steven L. "What are decision trees?" In: *Nature Biotechnology* 26.9 (2008). Number: 9 Publisher: Nature Publishing Group, pp. 1011–1013. DOI: 10.1038/nbt0908-1011.

[23] Parmar, Aakash, Katariya, Rakesh, and Patel, Vatsal. "A Review on Random Forest: An Ensemble Classifier". In: *International Conference on Intelligent Data Communication Technologies and Internet of Things (ICICI) 2018*. Ed. by Jude Hemanth, Xavier Fernando, Pavel Lafata, and Zubair Baig. Lecture Notes on Data Engineering and Communications Technologies. Cham: Springer International Publishing, 2019, pp. 758–763. DOI: 10.1007/978-3-030-03146-6_86.

[24] Bock, Hans-Hermann. "Clustering Methods: A History of k-Means Algorithms". In: *Selected Contributions in Data Analysis and Classification*. Ed. by Paula Brito, Guy Cucumel, Patrice Bertrand, and Francisco de Carvalho. Studies in Classification, Data Analysis, and Knowledge Organization. Berlin, Heidelberg: Springer, 2007, pp. 161–172. DOI: 10.1007/978-3-540-73560-1_15.

[25] Greenacre, Michael et al. "Principal component analysis". In: *Nature Reviews Methods Primers* 2.1 (2022). Number: 1 Publisher: Nature Publishing Group, pp. 1–21. DOI: 10.1038/s43586-022-00184-w.

[26] Jang, Beakcheol, Kim, Myeonghwi, Harerimana, Gaspard, and Kim, Jong Wook. "Q-Learning Algorithms: A Comprehensive Classification and Applications". In: *IEEE Access* 7 (2019). Conference Name: IEEE Access, pp. 133653–133667. DOI: 10.1109/ACCESS.2019.2941229.

[27] Nielsen, Michael A. "Neural Networks and Deep Learning". In: (2015). Publisher: Determination Press.

[28] Liu, Y., Li, J., Chen, Z., Qin, D., and Zhang, Y. "Research on a Multi-Objective Hierarchical Prediction Energy Management Strategy for Range Extended Fuel Cell Vehicles". In: *J. Power Sources* 429 (2019), pp. 55–66. DOI: 10.1016/j.jpowsour.2019.04.082.

[29] Wolter, M., Guercke, H., Isermann, T., and Hofmann, L. "Multi-Agent Based Distributed Power Flow Calculation". In: *Proceedings of the IEEE PES General Meeting*. 2010, pp. 1–6.

[30] Li, W. et al. "A Speedy Reinforcement Learning-Based Energy Management Strategy for Fuel Cell Hybrid Vehicles Considering Fuel Cell System Lifetime". In: *Int. J. Precis. Eng. Manuf. Green Technol.* 9 (2022), pp. 859–872. DOI: 10.1007/s40684-022-00263-4.

[31] Zheng, W., Zhu, J., and Luo, Q. "Distributed Dispatch of Integrated Electricity-Heat Systems with Variable Mass Flow". In: *IEEE Trans. Smart Grid* (2022). DOI: 10.1109/TSG.2022.3143030.

[32] Zhou, Yang, Ravey, Alexandre, and Péra, Marie-Cécile. "Multi-objective energy management for fuel cell electric vehicles using online-learning enhanced Markov speed predictor". In: *Energy Conversion and Management* 213 (2020), p. 112821. DOI: 10.1016/j.enconman.2020.112821.

[33] Song, Ke, Huang, Xing, Cai, Zhen, Huang, Pengyu, and Li, Feiqiang. "Research on energy management strategy of fuel-cell vehicles based on nonlinear model predictive control". In: *International Journal of Hydrogen Energy* (2023). DOI: https://doi.org/10.1016/j.ijhydene.2023.07.304.

[34] Sun, Xiaoxiao, Zhou, Yafu, Huang, Lijian, and Lian, Jing. "A real-time PMP energy management strategy for fuel cell hybrid buses based on driving segment feature recognition". In: *International Journal of Hydrogen Energy* 46.80 (2021), pp. 39983–40000. DOI: https://doi.org/10.1016/j.ijhydene.2021.09.204.

[35] Yang, D., Wang, L., Yu, K., and Liang, J. "A reinforcement learning-based energy management strategy for fuel cell hybrid vehicle considering real-time velocity prediction". In: *Energy Conversion and Management* 274 (2022), p. 116453. DOI: 10.1016/J.ENCONMAN.2022.116453.

[36] Li, Huan, Ravey, Alexandre, N'Diaye, Abdoul, and Djerdir, Abdesslem. "Online adaptive equivalent consumption minimization strategy for fuel cell hybrid electric vehicle considering power sources degradation". In: *Energy Conversion and Management* 192 (2019), pp. 133–149. DOI: 10.1016/j.enconman.2019.03.090.

[37] Zhang, Zhendong, He, Hongwen, Guo, Jinquan, and Han, Ruoyan. "Velocity prediction and profile optimization based real-time energy management strategy for Plug-in hybrid electric buses". In: *Applied Energy* 280 (2020). Publisher: Elsevier Ltd. DOI: 10.1016/j.apenergy.2020.116001.

[38] Lin, Xinyou, Wu, Jiayun, and Wei, Yimin. "An ensemble learning velocity prediction-based energy management strategy for a plug-in hybrid electric vehicle considering driving pattern adaptive reference SOC". In: *Energy* 234 (2021). Publisher: Elsevier Ltd. DOI: 10.1016/j.energy.2021.121308.

[39] Zeng, Tao et al. "Optimization-oriented adaptive equivalent consumption minimization strategy based on short-term demand power prediction for fuel cell hybrid vehicle". In: *Energy* 227 (2021). Publisher: Elsevier Ltd. DOI: 10.1016/j.energy.2021.120305.

[40] Han, Shaojian, Zhang, Fengqi, Xi, Junqiang, Ren, Yanfei, and Xu, Shaohang. "Short-term Vehicle Speed Prediction Based on Convolutional Bidirectional LSTM Networks". In: *2019 IEEE Intelligent Transportation Systems Conference (ITSC)* (2019), pp. 4055–4060. DOI: 10.1109/ITSC.2019.8917345.

[41] Piras, M., De Bellis, V., Malfi, E., Novella, R., and Lopez-Juarez, M. "Adaptive ECMS based on speed forecasting for the control of a heavy-duty fuel cell vehicle for real-world driving". In: *Energy Conversion and Management* 289 (2023), p. 117178. DOI: 10.1016/j.enconman.2023.117178.

[42] Li, Xiyun, Wang, Yujie, Yang, Duo, and Chen, Zonghai. "Adaptive energy management strategy for fuel cell/battery hybrid vehicles using Pontryagin's Minimal Principle". In: *Journal of Power Sources* 440 (2019). Publisher: Elsevier B.V. DOI: 10.1016/j.jpowsour.2019.227105.

[43] Li, Huan, Ravey, Alexandre, N'Diaye, Abdoul, and Djerdir, Abdesslem. "A novel equivalent consumption minimization strategy for hybrid electric vehicle powered by fuel cell, battery and supercapacitor". In: *Journal of Power Sources* 395 (2018). Publisher: Elsevier B.V., pp. 262–270. DOI: 10.1016/J.JPOWSOUR.2018.05.078.

[44] Onori, Simona, Serrao, Lorenzo, and Rizzoni, Giorgio. "Adaptive equivalent consumption minimization strategy for hybrid electric vehicles". In: *ASME 2010 Dynamic Systems and Control Conference, DSCC2010* 1 (2010). ISBN: 9780791844175, pp. 499–505. DOI: 10.1115/DSCC2010-4211.

[45] Chen, Di, Kim, Youngki, and Stefanopoulou, Anna G. "Predictive Equivalent Consumption Minimization Strategy with Segmented Traffic Information". In: *IEEE Transactions on Vehicular Technology* 69.12 (2020). Publisher: Institute of Electrical and Electronics Engineers Inc., pp. 14377–14390. DOI: 10.1109/TVT.2020.3034552.

[46] Luciani, Sara and Tonoli, Andrea. "Control Strategy Assessment for Improving PEM Fuel Cell System Efficiency in Fuel Cell Hybrid Vehicles". In: *Energies* 15.6 (2022). Publisher: MDPI. DOI: 10.3390/en15062004.

[47] "DoE - Department of Energy. DOE Technical Targets for Polymer Electrolyte Membrane Fuel Cell Components." In: ().

[48] Zhou, Y., Li, H., Ravey, A., and Péra, M.-C. "An integrated predictive energy management for light-duty range-extended plug-in fuel cell electric vehicle". In: *Journal of Power Sources* 451 (2020), p. 227780. DOI: 10.1016/j.jpowsour.2020.227780.

[49] Fernández, Roberto Álvarez, Cilleruelo, Fernando Beltrán, and Martínez, Iñaki Villar. "A new approach to battery powered electric vehicles: A hydrogen fuel-cell-based range extender system". In: *International Journal of Hydrogen Energy* 41.8 (2016), pp. 4808–4819. DOI: 10.1016/j.ijhydene.2016.01.035.

[50] Álvarez Fernández, Roberto, Corbera Caraballo, Sergio, Beltrán Cilleruelo, Fernando, and Lozano, J. Antonio. "Fuel optimization strategy for hydrogen fuel cell range extender vehicles applying genetic algorithms". In: *Renewable and Sustainable Energy Reviews* 81 (2018), pp. 655–668. DOI: 10.1016/j.rser.2017.08.047.

Chapter 7

Conclusions and Future Works

7.1 Summary

This thesis represents an extensive exploration of potential solutions for decarbonizing the transportation sector on various levels. The first chapter provided an overarching view of the current and future automotive landscape, referencing market data, future projections, and the latest European regulations. Through this, the reader gained an understanding that there is unfortunately no silver bullet, and it is essential for all technologies to continue progressing, from internal combustion engines to fuel cells, electric motors, and batteries.

The first level of intervention focuses on decarbonizing the energy source itself—the fuel burned in internal combustion engines or converted in fuel cells. It is possible to produce biofuels and synthetic fuels that can significantly reduce or even eliminate their environmental impact in terms of net CO_2 emissions. Among synthetic fuels, hydrogen stands out due to its exceptional versatility.

The second level of decarbonization lies in optimizing the machines that transform the chemical energy contained in these fuels into mechanical energy for engines or electrical energy for fuel cells. Therefore, the third chapter aimed to provide a comprehensive understanding of the fundamentals underlying the operation of internal combustion engines. It then described the key present and future technological advancements for maximizing engine efficiency—a technology that has been with us for over a century and still has much potential.

In contributing to the development and optimization of internal combustion engines, this thesis explored the potential benefits of two different solutions:

water injection in SI engines and the development of hydrogen-powered engines.

In symmetry with the third chapter, the fourth chapter delved into the operating principles of fuel cells, their primary types, and their integration within a complex system necessary for their proper and optimal functioning (Balance of Plant). Additionally, it described a zero-dimensional fuel cell model, originally developed for another doctoral thesis but utilized within the context of this work.

The third level of decarbonization pertains to the optimization of vehicles incorporating internal combustion engines, fuel cells, and batteries. In this context, the fifth chapter outlined the main structural solutions, advantages, and disadvantages of HEVs, FCHEVs, and BEVs. Despite their different design approaches, these vehicles share the need for correct and optimized energy management during their operation, particularly in the case of HEVs and FCHEVs, which employ two or more energy sources. This is where the fourth level of decarbonization came into play. Following a brief literature review, the sixth chapter introduced an extension of the ETESS strategy. This extension is designed to improve energy management in PHEVs equipped with small-sized engines. The fundamental principle behind this approach centers on the alternative utilization of both the thermal engine and electric motor to meet the power demands for propulsion. Subsequently, considering the rapid advancements in artificial intelligence and computer technologies that have led to the growing integration of learning algorithms within the domain of EMSs, an EMS enhanced through the incorporation of neural networks has been developed and tested for a Heavy-Duty FCHEV.

The main conclusions drawn from the conducted analyses are summarized in the following sections.

7.2 Conclusions

7.2.1 Water injection to improve fuel consumption and torque in a small displacement PFI spark-ignition engine

Water injection can be employed as a viable aftermarket solution to enhance the efficiency of engines in existing vehicles that are nearing the end of their lifecycle while minimizing their environmental impact, contributing then to the decarbonization of the transport sector. This experimental/numerical study demonstrated that water injection is a promising method to reduce CO_2 emissions of ICEs by lowering the in-cylinder and exhaust temperature, improving combustion phasing and mitigating combustion knock. It also showed the potential of an innovative calibration strategy to increase the full

load torque curve complying with compressor surge, knock and turbine inlet temperature limits, while minimizing the water consumption. The main steps and results of the activity are as follows:

- The validated model was deployed for a virtual engine recalibration, coupled with a partial redesign, with the aim of fully exploiting the potential of the water injection technique, particularly to enhance performance under full load conditions.

- Throughout this optimization process, two distinct calibration strategies were thoroughly examined and compared. The first strategy, known as Calibration A, centered on the reduction of BSFC while maintaining BMEP levels consistent with the manufacturer's specified full load curve. Additionally, it adhered to a maximum W/F ratio of 0.5 at each speed point. Calibration A yielded significant BSFC improvements, particularly in mitigating engine knock, achieving a maximum reduction of approximately 14% at low speeds and up to 32% at 4400 rpm in the medium/high-speed range, primarily attributed to combustion optimization and a reduction in air-fuel mixture enrichment.

- The second calibration strategy, termed Calibration B, introduced an innovative approach that aimed to optimize both torque output and BSFC while fine-tuning water injection control to minimize consumption. Calibration B delivered impressive results, enhancing low-end torque by up to 13.8%, with minimal BSFC penalties primarily observed at medium speeds.

7.2.2 Phenomenological model for a hydrogen fueled single cylinder research engine

Recently, the utilization of hydrogen as the primary fuel in the transportation industry has become a pivotal strategy in achieving the decarbonization objectives of the transport sector. A hydrogen engine operates on the same fundamental principles as a conventional internal combustion engine. However, due to hydrogen's distinct properties compared to gasoline or diesel, modifications are necessary for the engine to effectively complete its typical operational cycle. To facilitate the development of new engines and retrofit existing ones, this study focused on the development of a one-dimensional model of a hydrogen-powered ICE. The main steps and results of the activity are as follows:

- The experimental dataset utilized for the numerical model covered a broad spectrum of operating conditions, including:
  - Various IMEP values, ranging from 5 to 11 bar.
  - A diverse range of λ values, representing air-fuel equivalence ratios, spanning from 1.4 to 4.
  - Varied spark timings, extending from -36 to 0 CAD aTDC .
- This comprehensive dataset was carefully selected to enable the combustion model to showcase its adaptability and versatility. It effectively captured the trends and impacts associated with the examined external parameters.
- To achieve this objective, several key steps were undertaken:
  - Development of a new hydrogen laminar flame speed correlation based on thorough chemical calculations.
  - Utilization of a thermodiffusive instabilities measurement model to estimate the freely propagating flame speed. This model took into account the typical thermodiffusive instabilities encountered in lean hydrogen combustion and their influence on the flame front.
- The turbulence model was calibrated using data derived from a CFD simulation. This calibration process enabled precise fine-tuning of the combustion model. It also facilitated a thorough numerical/experimental comparison of various critical aspects, including:
  - Pressure cycles.
  - Burn rate traces.
  - Engine performance.
- The results unequivocally showed the enhanced model's capability to accurately capture essential physical phenomena and faithfully reproduce pressure cycles over an extensive range of λ values. However, it's important to note that in certain scenarios, particularly those characterized by significantly higher λ values (>3.6), more substantial errors were observed. These errors were primarily due to the transition into the regime of thickened flames, where the assumptions of the fractal model no longer held.

7.2.3 A-ETESS for the management of a parallel plug-in HEV

In the present context, where environmental concern drive the evolution of passenger cars, HEVs serve as a focal point in the automotive sector for achieving net-zero CO_2 emissions. To fully exploit the energy conversion capabilities of advanced powertrains, effective energy management strategies are imperative and represent the last level of decarbonization investigated in this thesis. Thereferore, this work introduced a simulation study aimed at developing a novel control strategy for a P3 parallel PHEV according to the following key-points:

- This strategy for the management of a parallel plug-in HEV includes three primary operational modes: pure thermal mode, pure electric mode, and parallel mode. Additionally, it includes a fourth traction-charging mode considered in this comprehensive investigation.
- To create an adaptive EMS, an adaptive logarithmic-based function was implemented. This function was selected for its stability and represented as a two-dimensional lookup table.
- The same adaptive function was integrated into the ECMS to enable a meaningful comparison between the two strategies concerning fuel consumption and computational efficiency.
- In the initial phase, both strategies were calibrated to minimize the average difference between the actual SoC and the target SoC across various driving cycles. These cycles include US06, WLTC, Artemis Highway, and an RDE cycle. The calibration was achieved through cycle-dependent tuning parameters.
- These tuning parameters were subsequently correlated with the distance traveled using a fitting function, allowing the approach to be applicable to any driving cycle.
- Simulation results demonstrated that A-ETESS and A-ECMS exhibit an average total fuel consumption difference of less than 2.5%.
- PiL tests are conducted to compare the computational time required by A-ETESS and A-ECMS and assess the feasibility of implementing A-ETESS in a real-time vehicle application.
- PiL results demonstrated that A-ETESS can operate significantly faster than A-ECMS, with execution times well below the typical cycle time of a CAN message. This capability makes real-time control of engine and motor torque requests viable for on-vehicle applications.

7.2.4 P-ECMS for the management of a heavy-duty FCHEV

In recognition of the significance of FCHEVs in decarbonizing the transportation sector, this study focused on the development of an EMS for a heavy-duty vehicle. This strategy is enhanced with the implementation of a neural network, which has demonstrated a reduction in fuel consumption compared to conventional "non-intelligent" strategies. Presented below is an overview of the primary phases and accomplishments of this study:

- An innovative approach was introduced to enhance the energy management of heavy-duty FCVs under real-world driving conditions known as P-ECMS.
- The P-ECMS strategy was customized to address the specific requirements and challenges presented by heavy-duty FCVs, ensuring optimal performance while considering the vehicle's unique characteristics.
- The P-ECMS was enhanced through the integration of an LSTM prediction layer. This enhancement dynamically adjusted the equivalence factor based on the predicted SoC compared to the target SoC.
- A realistic driving dataset was generated using GT-Real Drive, incorporating data from the TEN-T routes to facilitate the training of the velocity predictor.
- A comprehensive sensitivity analysis was conducted on the P-ECMS to assess its response to variations in the initial equivalence factor and update gain value.
- The performance of the P-ECMS was compared with several other strategies, including:
  - Conventional A-ECMS.
  - Reference S-ECMS.
  - RBS .
- The evaluation was conducted across two distinct driving cycles and three dynamic restrictions on the fuel cell current (0.1, 0.01, and 0.001 A/cm^2s).
- A comprehensive assessment was made of battery SoC management, equivalence factor dynamics, hydrogen consumption, and fuel cell degradation.

- The velocity prediction accuracy was verified with recorded velocity RMSE values of 6.08 km/h and 11.80 km/h for the HDDT and a realistic cycle, respectively.
- Notable improvements were observed in battery SoC management in both the P-ECMS and A-ECMS compared to the S-ECMS.
- A remarkable reduction in hydrogen consumption ranging from 1.4% to 2% for the HDDT cycle and up to 3% for the realistic driving cycle was achieved by the P-ECMS compared to the A-ECMS.
- An impressive reduction in fuel consumption of up to 6.1% was achieved by the P-ECMS compared to an RBS.
- The results highlighted the influence of dynamic limitations on hydrogen consumption and fuel cell durability across all tested strategies.
- Increased dynamic limitations resulted in higher H_2 consumption and a shift in the importance of various degradation sources.
- Under low dynamic restrictions, load-change degradation was significant, but it became less so as dynamic limitations increased.
- Start-stop and low-power degradation gained importance under higher dynamic limitations.
- Implications for FC stack manufacturers were evident in designing systems for FCREx vehicles, potentially emphasizing degradation in high-voltage conditions and prioritizing materials with low degradation characteristics.

7.2.5 Integration of a SoC planning layer into a P-ECMS for the management of a heavy-duty FCHEV

The P-ECMS, developed in the context of the previous study, was integrated with a SoC planning layer, thereby enabling charge-depleting mode operation for the vehicle and demonstrating significant advantages in comparison to other reference strategies.

- The SoC planning layer played a critical role in effectively managing battery discharge during driving missions. It predicted a target SoC trajectory using data from a map service provider, facilitating pre-mission planning.

- This layer featured the incorporation of a neural network, trained on simulation outcomes derived from the S-ECMS strategy. It considered four distinct driving cycles and various initial SoC values, with the objective of achieving a final SoC of 30%, aligning with standard plug-in vehicle operations.
- The advantages of the P-ECMS were validated through scenarios involving battery discharge, encompassing both a realistic driving cycle and a standard one. In both cases, the P-ECMS exhibited a substantial reduction in consumption, with improvements of up to 5% compared to an optimal CDCS.
- The benefits resulting from the integration of the SoC planning layer were highlighted through a comparison between the P-ECMS with linear battery discharge planning and the P-ECMS-Xkm. In the latter, the SoC trajectory was planned by the SoC planning layer for varying prediction segment lengths.
- Furthermore, the study revealed that the performance of the P-ECMS, enhanced by the SoC planning layer, depended on the length of the SoC prediction segment. The presented results indicated that a segment length ranging from 3 km to 8 km, supplemented by data from a map service provider, yielded superior outcomes. Deviating from this range might lead to a marginal increase in consumption when compared to P-ECMS-L.

7.3 Future works

In the course of this work, some questions that could not be answered at the moment appeared. To answer these questions, some recommendations for future work were formulated.

- The hydrogen-powered engine's digital twin, during validation, revealed that certain cases with considerably higher λ values (>3.6) displayed notable discrepancies. These discrepancies were observed as the combustion entered the domain of thickened flames, where the assumptions of the fractal model no longer held true. Consequently, upcoming development initiatives should focus on establishing a combustion model that accurately reproduces the phenomena specific to this combustion regime.
- Subsequently, the developed model can be employed as a foundation for the development of calibration strategies for a hydrogen-powered engine

across its entire operating range, generating the required map for the development of a hydrogen ICE based hybrid electric vehicle model.

- The developed A-ETESS relies on future knowledge of the driving mission. Its capabilities in harnessing vehicle connectivity-derived information or when coupled with a speed predictor, a methodology employed in the FCHEV's P-ECMS, have yet to be fully investigated and remain unexplored aspects warranting further research.

- Lithium-ion batteries, that serve as the backbone of many HEVs and FCHEVs, can experience degradation, which can impact the overall performance and longevity of the hybrid vehicle. Understanding the factors that contribute to battery degradation and developing strategies to mitigate it are crucial for advancing HEVs technology. The studies conducted on the FCHEV have solely focused on the degradation of the fuel cell. Then, the development of a battery degradation model and a health-conscious EMS, while considering both battery and fuel cell degradation, is a future step that warrants further investigation.

- A life cycle assessment is essential when evaluating different vehicle technologies like ICE-based vehicles, fuel cells vehicles, and battery electric vehicles because it provides a holistic view of their environmental impact. The models developed during this doctoral research can be used to generate some of the data needed to conduct an LCA analysis.

- HiL simulations are an essential tool for engineering system development and validation across industries. The EMS developed during this doctoral research should undergo testing through HiL simulations to validate their real-time applicability.

Global Bibliography

Abe, J. O., Popoola, A. P. I., Ajenifuja, E., and Popoola, O. M. "Hydrogen energy, economy and storage: Review and recommendation". In: *International Journal of Hydrogen Energy* 44.29 (2019), pp. 15072–15086. DOI: 10.1016/j.ijhydene.2019.04.068 (cited on page 18).

Abid, Raja. "Dynamic Performance of a PEM Fuel Cell System". In: *DTU Mechanical Engineering* (2013). ISBN: 9788774753599 Publisher: APA (cited on page 123).

AECC key messages on Fit for 5. AECC. URL: https://www.aecc.eu/aecc-key-messages-on-fit-for-55/ (visited on 06/21/2023) (cited on page 5).

Ahmadi, Rouhollah and Hosseini, S. Mohammad. "Numerical investigation on adding/substituting hydrogen in the CDC and RCCI combustion in a heavy duty engine". In: *Applied Energy* 213 (2018), pp. 450–468. DOI: 10.1016/j.apenergy.2018.01.048 (cited on page 43).

Akroot, Abdulrazzak, Ekici, Özgür, and Koksal, Murat. "Process modeling of an automotive pem fuel cell system". In: *International Journal of Green Energy* 16 (2019), pp. 1–11. DOI: 10.1080/15435075.2019.1641105 (cited on page 114).

Alger, Terry and Mangold, Brandon. "Dedicated EGR: A New Concept in High Efficiency Engines". In: *SAE Int. J. Engines* 2.1 (2009), pp. 620–631. DOI: 10.4271/2009-01-0694 (cited on page 38).

Álvarez Fernández, Roberto, Corbera Caraballo, Sergio, Beltrán Cilleruelo, Fernando, and Lozano, J. Antonio. "Fuel optimization strategy for hydrogen fuel cell range extender vehicles applying genetic algorithms". In: *Renewable and Sustainable Energy Reviews* 81 (2018), pp. 655–668. DOI: 10.1016/j.rser.2017.08.047 (cited on page 231).

Amamou, A., Kandidayeni, M., Macias, A., Boulon, L., and Kelouwani, S. "Efficient model selection for real-time adaptive cold start strategy of a fuel cell system on vehicular applications". In: *International Journal of Hydrogen Energy* 45.38 (2020), pp. 19664–19675. DOI: 10.1016/j.ijhydene.2020.04.253 (cited on page 120).

Angelberger, C., Poinsot, T., and Delhay, B. *Improving near-wall combustion and wall heat transfer modeling in SI engine computations*. SAE Technical Paper, 1997 (cited on page 81).

Artz, Jens et al. "Sustainable Conversion of Carbon Dioxide: An Integrated Review of Catalysis and Life Cycle Assessment". In: *Chemical Reviews* 118.2 (2018). Publisher: American Chemical Society, pp. 434–504. DOI: 10.1021/acs.chemrev.7b00435 (cited on page 14).

Arvind, Noel, Xavier, Leo, and Kumar, AH. "Fuel cell electric vehicles: genesis of a new era or a myth-busting in new energy vehicle technology?" In: (2018) (cited on page 147).

Atyabi, Seyed Ali and Afshari, Ebrahim. "Three-dimensional multiphase model of proton exchange membrane fuel cell with honeycomb flow field at the cathode side". In: *Journal of Cleaner Production* 214 (2019), pp. 738–748. DOI: 10.1016/j.jclepro.2018.12.293 (cited on page 119).

Average age of the EU vehicle fleet, by country. ACEA - European Automobile Manufacturers' Association. 2023. URL: https://www.acea.auto/figure/average-age-of-eu-vehicle-fleet-by-country/ (visited on 06/08/2023) (cited on page 12).

Babayev, Rafig, Andersson, Arne, Dalmau, Albert Serra, Im, Hong G., and Johansson, Bengt. "Computational characterization of hydrogen direct injection and nonpremixed combustion in a compression-ignition engine". In: *International Journal of Hydrogen Energy* 46.35 (2021), pp. 18678–18696. DOI: https://doi.org/10.1016/j.ijhydene.2021.02.223 (cited on page 42).

Basic Hydrogen Properties | Hydrogen Tools. URL: https://h2tools.org/hyarc/hydrogen-data/basic-hydrogen-properties (visited on 06/09/2023) (cited on page 20).

Bates, C. S. *Flame Imaging Studies of Combustion Completion in a SI Four-Stroke Engine* (cited on pages 50, 51).

Bellis, Vincenzo De, Piras, Marco, and Malfi, Enrica. "Assessment of an Adaptive Efficient Thermal/Electric Skipping Control Strategy for the Management of a Parallel Plug-in Hybrid Electric Vehicle". In: *Energies* 15.19 (2022). Number: 19 Publisher: Multidisciplinary Digital Publishing Institute, p. 7122. DOI: 10.3390/en15197122 (cited on pages 160, 162, 163, 179–181, 184–186, 188, 189, 191, 192).

Bellman, Richard E. *Dynamic Programming*. Princeton: Princeton University Press, 1957 (cited on page 174).

Berlin and Brussels should realise that e-fuels for trucks are a bad, expensive bet. www.euractiv.com. Section: Transport. 2019. URL: https://www.euractiv.com/section/transport/opinion/berlin-and-brussels-should-realise-that-e-fuels-for-trucks-are-a-bad-expensive-bet/ (visited on 06/08/2023) (cited on page 16).

Berlowitz, P.J. and Darnell, C.P. "Fuel choices for fuel cell powered vehicles". In: *Society of Automotive Engineers (SAE) Journal* 2000 (2002). Place: Warrendale, PA (cited on page 107).

Bernardi, D. M. and Verbrugge, M. W. "Mathematical Model of a Gas Diffusion Electrode Bonded to a Polymer Electrolyte". In: *AIChE Journal* 37 (1991), pp. 1151–1163 (cited on page 118).

Bernardi, D. M. and Verbrugge, M. W. "A Mathematical Model of the Solid-Polymer-Electrolyte Fuel Cell". In: *Journal of The Electrochemical Society* 139 (1992), pp. 2477–2491 (cited on page 118).

Bi, Wu and Fuller, Thomas. F. "Temperature Effects on PEM Fuel Cells PtC Catalyst Degradation". In: *Journal of The Electrochemical Society* 155.2 (2008), B215. DOI: 10.1149/1.2819680 (cited on page 126).

Bock, Hans-Hermann. "Clustering Methods: A History of k-Means Algorithms". In: *Selected Contributions in Data Analysis and Classification*. Ed. by Paula Brito, Guy Cucumel, Patrice Bertrand, and Francisco de Carvalho. Studies in Classification, Data Analysis, and Knowledge Organization. Berlin, Heidelberg: Springer, 2007, pp. 161–172. DOI: 10.1007/978-3-540-73560-1_15 (cited on page 195).

Bougrine, Said. "0-Dimensional Modeling of the Combustion of Alternative Fuels in Spark Ignition Engines". PhD thesis. Ecole Centrale Paris, 2012 (cited on page 47).

Bozza, F., Gimelli, A., Merola, S. S., and Vaglieco, B. M. "Validation of a Fractal Combustion Model through Flame Imaging". In: *SAE Transactions* 114 (2005). Publisher: SAE International, pp. 973–987 (cited on page 31).

Bozza, Fabio, De Bellis, Vincenzo, Giannattasio, Pietro, Teodosio, Luigi, and Marchitto, Luca. "Extension and Validation of a 1D Model Applied to the Analysis of a Water Injected Turbocharged Spark Ignited Engine at High Loads and over a WLTP Driving Cycle". In: *SAE International Journal of Engines* 10.4 (2017), pp. 2141–2153. DOI: 10.4271/2017-24-0014 (cited on page 57).

Bozza, Fabio, De Bellis, Vincenzo, and Teodosio, Luigi. "A Tabulated-Chemistry Approach Applied to a Quasi-Dimensional Combustion Model for a Fast and Accurate Knock Prediction in Spark-Ignition Engines". In: *SAE Technical Paper*. Issue: 2019-01-0471. 2019. DOI: 10.4271/2019-01-0471 (cited on page 53).

Bozza, Fabio, Teodosio, Luigi, De Bellis, Vincenzo, Fontanesi, Stefano, and Iorio, Agostino. "A Refined OD Turbulence Model to Predict Tumble and Turbulence in SI Engines". In: *SAE International Journal of Engines* 12.1 (2019). Publisher: SAE International, pp. 15–30 (cited on page 48).

Bradley, D., Cresswell, T.M., and Puttock, J.S. "Flame acceleration due to flame-induced instabilities in large-scale explosions". In: *Combust. Flame* 124.4 (2001), pp. 551–559. DOI: 10.1016/S0010-2180(00)00208-X (cited on page 43).

Brahma, A., Guezennec, Y., and Rizzoni, G. "Optimal energy management in series hybrid electric vehicles". In: *Proceedings of the 2000 American Control Conference*. Vol. 1. Issue: 6. 2000, pp. 60–64 (cited on page 174).

Brennan, J.W. and Barder, T.E. *Battery Electric Vehicles vs. Internal Combustion Engine Vehicles*. Arthur D. Little, 2016 (cited on page 152).

Broatch, A., Novella, R., García-Tíscar, J., Gomez-Soriano, J., and Pal, P. "Investigation of the effects of turbulence modeling on the prediction of compression-ignition combustion unsteadiness". In: *International Journal of Engine Research* (2021), p. 1468087421990478 (cited on page 80).

Burger, Andrew. *US Wind Energy Selling At Record Low Price of 2.5 Cents per kWh*. Renewable Energy World. 2015. URL: https://www.renewableenergyworld.com/wind-power/us-wind-energy-selling-at-record-low-price-of-2-5-cents-per-kwh/ (visited on 06/12/2023) (cited on page 17).

Cells, {and} Fuel and Undertaking, Hydrogen 2 Joint. *Hydrogen roadmap Europe : a sustainable pathway for the European energy transition*. Publications Office, 2019. DOI: doi/10.2843/341510 (cited on pages 5, 7, 16).

Chao, Siyu, Fengchun, Sun, and Hongwen, He. "Investigating adaptive-ECMS with velocity forecast ability for hybrid electric vehicles". In: *Appl Energy* 185 (2017), pp. 1644–1653. DOI: 10.1016/j.apenergy.2016.02.026 (cited on page 177).

Chao, Siyu D, Liang, Liang, Sixong, Yang, Yiyong, Yu, and Yue, Z. "Adaptive real-time optimal energy management strategy based on equivalent factors optimization for plug-in hybrid electric vehicle". In: *Appl Energy* 203 (2017), pp. 883–869. DOI: 10.1016/j.apenergy.2017.06.106 (cited on page 177).

Charlette, François, Meneveau, Charles, and Veynante, Denis. "A power-law flame wrinkling model for LES of premixed turbulent combustion Part I: non-dynamic formulation and initial tests". In: *Combustion and Flame* 131.1 (2002), pp. 159–180. DOI: 10.1016/S0010-2180(02)00400-5 (cited on page 47).

Charlette, François, Meneveau, Charles, and Veynante, Denis. "A power-law flame wrinkling model for LES of premixed turbulent combustion Part II: Dynamic formulation". In: *Combustion and Flame* 131.1 (2002), pp. 181–197. DOI: 10.1016/S0010-2180(02)00401-7 (cited on page 47).

Chen, Di, Kim, Youngki, and Stefanopoulou, Anna G. "Predictive Equivalent Consumption Minimization Strategy with Segmented Traffic Information". In: *IEEE Transactions on Vehicular Technology* 69.12 (2020). Publisher: Institute of Electrical and Electronics Engineers Inc., pp. 14377–14390. DOI: 10.1109/TVT.2020.3034552 (cited on page 217).

Chen, L., Liang, Z., Zhang, X., and Shuai, S. "Characterizing particulate matter emissions from GDI and PFI vehicles under transient and cold start conditions". In: *Fuel* 189 (2017), pp. 131–140. DOI: 10.1016/j.fuel.2016.10.055 (cited on page 27).

Chong, Huang, Minggao, Ouyang, Liangfei, Xiong, and Hewu, Wang. "Approximate Pontryagin's minimum principle applied to the energy management of plug-in hybrid electric vehicles". In: *Applied Energy* 115 (2014), pp. 174–198. DOI: 10.1016/j.apenergy.2013.11.002 (cited on page 176).

Chu, H.-S., Yeh, C., and Chen, F. "Effects of Porosity Change of Gas Diffuser on Performance of Proton Exchange Membrane Fuel Cell". In: *Journal of Power Sources* 123.1 (2003), pp. 1–9 (cited on page 119).

Corbo, P., Migliardini, F., and Veneri, O. "Hydrogen production and utilization for sustainable development". In: *World Journal of Science, Technology and Sustainable Development* 4 (2007). Publisher: Emerald, pp. 149–162 (cited on pages 121, 123).

Corbo, P., Migliardini, F., and Veneri, O. “Sustainable energy: new developments”. In: *World Journal of Science, Technology and Sustainable Development* 5 (2008). Publisher: Emerald, pp. 170–183 (cited on pages 121, 123).

Cox, B., Bauer, C., Mendoza Beltran, A., Vuuren, D. P. van, and Mutel, C. L. “Life cycle environmental and cost comparison of current and future passenger cars under different energy scenarios”. In: *Applied Energy* 269 (2020), p. 115021. DOI: 10.1016/j.apenergy.2020.115021 (cited on page 146).

Dang, J. and Wang, L. “Optimization control of hydrogen engine ignition system based on ACO-BP”. In: *International Journal of Hydrogen Energy* 46.78 (2021), pp. 38903–38912 (cited on page 41).

De Bellis, V, Malfi, E, Teodosio, L, Giannattasio, P, and Di Lenarda, F. “Novel Laminar Flame Speed Correlation for the Refinement of the Flame Front Description in a Phenomenological Combustion Model for Spark-Ignition Engines”. In: *SAE International Journal of Engines* 12.3 (2019), pp. 251–270. DOI: 10.4271/03-12-03-0018 (cited on page 32).

De Bellis, Vincenzo, Malfi, Enrica, and Zaccardi, Jean-Marc. “Development of an Efficient Thermal Electric Skipping Strategy for the Management of a Series/Parallel Hybrid Powertrain”. In: *Energies* 14.4 (2021). Number: 4 Publisher: Multidisciplinary Digital Publishing Institute, p. 889. DOI: 10.3390/en14040889 (cited on page 178).

Department of Energy of the United States. *Fuel Cell Technologies Office Multi-Year Research, Development, and Demonstration Plan*. 2017 (cited on page 116).

Desantes, J. M., Novella, R., Pla, B., and Lopez-Juarez, M. “A modeling framework for predicting the effect of the operating conditions and component sizing on fuel cell degradation and performance for automotive applications”. In: *Applied Energy* 317 (November 2021 2022). Publisher: Elsevier Ltd, p. 119137. DOI: 10.1016/j.apenergy.2022.119137 (cited on pages 124, 126).

Desantes, J.M., Novella, R., Pla, B., and Lopez-Juarez, M. “Effect of dynamic and operational restrictions in the energy management strategy on fuel cell range extender electric vehicle performance and durability in driving conditions”. In: *Energy Conversion and Management* 266 (X 2022). Publisher: Elsevier Ltd, p. 115821. DOI: 10.1016/j.enconman.2022.115821 (cited on page 126).

"DoE - Department of Energy. DOE Technical Targets for Polymer Electrolyte Membrane Fuel Cell Components." In: () (cited on page 224).

Donazzi, Alessandro, De Pascali, Stefano, Garavaglia, Francesco, and Bracconi, Mauro. "A quasi 2D model for the interpretation of impedance and polarization of a planar solid oxide fuel cell with interconnects". In: *Electrochimica Acta* 365 (2021), p. 137346. DOI: 10.1016/j.electacta.2020.137346 (cited on page 116).

Drake, Marcus, Fansler, Todd, and Lippert, Andreas. "Stratified-charge combustion: modeling and imaging of a spray-guided direct-injection spark-ignition engine". In: *Proceedings of the Combustion Institute* 30.2 (2005), pp. 2683–2691. DOI: 10.1016/j.proci.2004.07.028 (cited on page 40).

Duclos, Julien, Veynante, Denis, and Poinsot, Thierry. "A comparison of flamelet models for premixed turbulent combustion". In: *Combustion and Flame* 95.1 (1993), pp. 101–117. DOI: 10.1016/0010-2180(93)90055-8 (cited on page 48).

Dutta, M, Jia, N, Lu, S, Colbow, V, and Wessel, S. "Effects of Upper Potential Dwell Time, Transients and Relative Humidity on PEM Fuel Cell Cathode Catalyst Degradation". In: *The Electrochemical Society 217th Meeting (c)* (2010) (cited on page 126).

Dwarshala, Siva Krishna Reddy et al. "A Review on Recent Developments of RCCI Engines Operated with Alternative Fuels". In: *Energies* 16.7 (2023). Number: 7 Publisher: Multidisciplinary Digital Publishing Institute, p. 3192. DOI: 10.3390/en16073192 (cited on page 40).

Edalati, Kaveh et al. "Design and synthesis of a magnesium alloy for room temperature hydrogen storage". In: *Acta Materialia* 149 (2018), pp. 88–96. DOI: 10.1016/j.actamat.2018.02.033 (cited on page 18).

Eisazadeh-Far, Kamyar and Younkins, Matt. "Fuel Economy Gains through Dynamic-Skip-Fire in Spark Ignition Engines". In: *SAE Technical Paper*. Issue: 2016-01-0672. 2016. DOI: 10.4271/2016-01-0672 (cited on page 38).

Europe steps back from 2035 ICE ban. URL: https://www.sae.org/news/2023/03/european-ice-ban (visited on 06/21/2023) (cited on page 5).

European Green Deal. 2022. URL: https://www.consilium.europa.eu/en/policies/green-deal/ (visited on 06/21/2023) (cited on page 4).

Fajardo, Carlos and Sick, Volker. "Flow field assessment in a fired spray-guided spark-ignition direct-injection engine based on UV particle image velocimetry with sub crank angle resolution". In: *Proceedings of the combustion institute* 31.2 (2007), pp. 3023–3031 (cited on page 40).

Federation (NAF), Norwegian Automobile. *20 Popular EVs Tested in Norwegian Winter Conditions*. 2020 (cited on page 152).

Feng, Y. and Dong, Z. "Integrated design and control optimization of fuel cell hybrid mining truck with minimized lifecycle cost". In: *Applied Energy* 270 (2020), p. 115164. DOI: 10.1016/J.APENERGY.2020.115164 (cited on page 158).

Fernández, Roberto Álvarez, Cilleruelo, Fernando Beltrán, and Martínez, Iñaki Villar. "A new approach to battery powered electric vehicles: A hydrogen fuel-cell-based range extender system". In: *International Journal of Hydrogen Energy* 41.8 (2016), pp. 4808–4819. DOI: 10.1016/j.ijhydene.2016.01.035 (cited on page 231).

Ferrara, A., Jakubek, S., and Hametner, C. "Energy management of heavy-duty fuel cell vehicles in real-world driving scenarios: Robust design of strategies to maximize the hydrogen economy and system lifetime". In: *Energy Conversion and Management* 232 (2021), p. 113795. DOI: 10.1016/j.enconman.2020.113795 (cited on page 158).

Fletcher, Tom and Ebrahimi, Kambiz. "The Effect of Fuel Cell and Battery Size on Efficiency and Cell Lifetime for an L7e Fuel Cell Hybrid Vehicle". In: *Energies* 13.22 (2020). Number: 22 Publisher: Multidisciplinary Digital Publishing Institute, p. 5889. DOI: 10.3390/en13225889 (cited on page 145).

Franke, C., Wirth, A., and Peters, N. "New Aspects of the Fractal Behaviour of Turbulent Flames". In: *23rd Symposium (International) on Combustion*. Orleans, 1990 (cited on pages 50, 51).

Fu, Z., Zhu, L., Tao, F., Si, P., and Sun, L. "Optimization based energy management strategy for fuel cell/battery/ultracapacitor hybrid vehicle considering fuel economy and fuel cell lifespan". In: *International Journal of Hydrogen Energy* 45.15 (2020), pp. 8875–8886. DOI: https://doi.org/10.1016/j.ijhydene.2020.01.017 (cited on page 158).

Fuel cell - Energy Education. URL: https://energyeducation.ca/encyclopedia/Fuel_cell (visited on 06/15/2023) (cited on page 102).

Fuel Cell Fundamentals. 1st ed. _eprint: https://onlinelibrary.wiley.com/doi/pdf/10.1002/9781119191766. John Wiley & Sons, Ltd, 2016. DOI: 10.1002/9781119191766 (cited on page 106).

FuelCellsWorks. *World's first fuel cell heavy-duty truck, Hyundai XCIENT Fuel Cell, heads to Europe for commercial use*. 2020 (cited on pages 163, 165).

FuelsEurope. *Clean Fuels for All* (cited on page 11).

Fuller, T. F. and Newman, J. "Water and Thermal Management in Solid-Polymer-Electrolyte Fuel Cells". In: *Journal of The Electrochemical Society* 140 (1993), pp. 1218–1225 (cited on page 118).

Gaikwad, Shrihari D. and Ghosh, Prakash C. "Sizing of a fuel cell electric vehicle: A pinch analysis-based approach". In: *International Journal of Hydrogen Energy* 45.15 (2020), pp. 8985–8993. DOI: 10.1016/j.ijhydene.2020.01.116 (cited on pages 145, 158).

Gao, Jianbing, Wang, Xiaochen, Song, Panpan, Tian, Guohong, and Ma, Chaochen. "Review of the backfire occurrences and control strategies for port hydrogen injection internal combustion engines". In: *Fuel* 307 (2022), p. 121553. DOI: 10.1016/j.fuel.2021.121553 (cited on page 42).

Gatowsky, J. A. and Heywood, J. B. "Flame Photographs in a Spark-Ignition Engine". In: *Combustion and Flame* 56 (1984), pp. 71–81 (cited on page 50).

Geotab. *Temperature Tool for EV Range*. 2020 (cited on page 152).

Gissing, J., Themann, P., Baltzer, S., Lichius, T., and Eckstein, L. "Optimal Control of Series Plug-In Hybrid Electric Vehicles Considering the Cabin Heat Demand". In: *IEEE Transactions on Control Systems Technology* 24 (2016), pp. 1126–1133. DOI: 10.1109/TCST.2015.2468055 (cited on pages 172, 182).

Global Greenhouse Gas Emissions: 1990-2020 and Preliminary 2021 Estimates. Rhodium Group. URL: https://rhg.com/research/global-greenhouse-gas-emissions-2021/ (visited on 06/21/2023) (cited on page 2).

Goto, J. et al. "Spark knock suppression in spark ignition engines with hydrogen addition under low and high engine speeds". In: *International Journal of Hydrogen Energy* 47.41 (2022), pp. 18169–18181. DOI: 10.1016/j.ijhydene.2022.03.286 (cited on page 41).

Gouldin, F. "An application of Fractals to Modeling Premixed Turbulent Flames". In: *Combustion and Flame* 68.3 (1987), pp. 249–266. DOI: 10.1016/0010-2180(87)90003-4 (cited on page 50).

Greenacre, Michael et al. "Principal component analysis". In: *Nature Reviews Methods Primers* 2.1 (2022). Number: 1 Publisher: Nature Publishing Group, pp. 1–21. DOI: 10.1038/s43586-022-00184-w (cited on page 195).

Griffiths, J. F. *Flame and Combustion*. 3rd ed. London: Routledge, 2019. 328 pp. DOI: 10.1201/9780203755976 (cited on page 35).

Groff, E.G. “The cellular nature of confined spherical propane-air flames”. In: *Combust. Flame* 48 (1982), pp. 51–62. DOI: 10.1016/0010-2180(82)90115-8 (cited on page 43).

Gurau, V., Liu, H., and Kakac, S. “Two-dimensional model for proton exchange membrane fuel cells”. In: *AIChE Journal* 44.11 (1998), pp. 2410–2422 (cited on page 119).

Han, I. S., Jeong, J., and Shin, H. K. “PEM fuel-cell stack design for improved fuel utilization”. In: *International Journal of Hydrogen Energy* 38 (2013), pp. 11996–12006 (cited on page 114).

Han, Shaojian, Zhang, Fengqi, Xi, Junqiang, Ren, Yanfei, and Xu, Shaohang. “Short-term Vehicle Speed Prediction Based on Convolutional Bidirectional LSTM Networks”. In: *2019 IEEE Intelligent Transportation Systems Conference (ITSC)* (2019), pp. 4055–4060. DOI: 10.1109/ITSC.2019.8917345 (cited on pages 205, 214).

Hara, T and Tanoue, K. “Laminar flame speed of ethanol, n-heptane, iso-octane air mixtures”. In: *JSAE Paper Number* 20068518 (2006) (cited on page 32).

Hattrell, T., Sheppard, C. G. W., Burluka, A. A., Neumeister, J., and Cairns, A. “Burn Rate Implications of Alternative Knock Reduction Strategies for Turbocharged SI Engines”. In: *SAE Tech. Pap.* 2006 (2006). DOI: 2006-01-1110 (cited on page 46).

Heywood, John B. *Internal Combustion Engine Fundamentals*. 2nd. New York: McGraw-Hill Education, 2018 (cited on pages 29, 32, 40, 46).

Hoang, Anh Tuan. “Critical review on the characteristics of performance, combustion and emissions of PCCI engine controlled by early injection strategy based on narrow-angle direct injection (NADI)”. In: *Energy Sources, Part A: Recovery, Utilization, and Environmental Effects* (2020). Publisher: Taylor & Francis, pp. 1–15. DOI: 10.1080/15567036.2020.1805048 (cited on page 40).

Hombach, Laura E. et al. “Economic and environmental assessment of current (2015) and future (2030) use of E-fuels in light-duty vehicles in Germany”. In: *Journal of Cleaner Production* 207 (2019), pp. 153–162. DOI: 10.1016/j.jclepro.2018.09.261 (cited on page 14).

Howarth, T. L. and Aspden, A. J. “An empirical characteristic scaling model for freely-propagating lean premixed hydrogen flames”. In: *Combustion and Flame* 237 (2022), p. 111805. DOI: 10.1016/j.combustflame.2021.111805 (cited on pages 77, 79, 81).

Howarth, T. L., Hunt, E. F., and Aspden, A. J. "Thermodiffusively-unstable lean premixed hydrogen flames: Phenomenology, empirical modelling, and thermal leading points". In: *Combustion and Flame* 253 (2023), p. 112811. DOI: 10.1016/j.combustflame.2023.112811 (cited on pages 77, 79).

Huang, Y., Wang, H., Khajepour, A., He, H., and Ji, J. "Model Predictive Control Power Management Strategies for HEVs: A Review". In: *Journal of Power Sources* 341 (2017), pp. 91–106. DOI: 10.1016/J.JPOWSOUR.2016.11.106 (cited on page 172).

Hum, B. and Li, X. "Two-dimensional analysis of PEM fuel cells". In: *Journal of Applied Electrochemistry* 34.2 (2004), pp. 205–215 (cited on page 119).

"Hydrogen engine operation strategies: Recent progress, industrialization challenges, and perspectives". In: *International Journal of Hydrogen Energy* 48.1 (2023). Publisher: Pergamon, pp. 366–392. DOI: 10.1016/j.ijhydene.2022.09.256 (cited on page 44).

Iafrate, Nicolas, Matrat, Marc, and Zaccardi, Jean-Marc. "Numerical investigations on hydrogen-enhanced combustion in ultra-lean gasoline spark-ignition engines". In: *International Journal of Engine Research* (2020), p. 1468087419870688. DOI: 10.1177/1468087419870688 (cited on page 41).

Ijaodola, O. S. et al. "Energy efficiency improvements by investigating the water flooding management on proton exchange membrane fuel cell (PEMFC)". In: *Energy* 179 (2019), pp. 246–267. DOI: 10.1016/j.energy.2019.04.074 (cited on page 118).

Ilbas, Mustafa, Kumuk, Osman, and Karyeyen, Serhat. "Modelling of the gas-turbine colorless distributed combustion: An application to hydrogen enriched – kerosene fuel". In: *International Journal of Hydrogen Energy*. International Conference on Energy, Environment and Storage of Energy, 15. International Combustion Symposium 47.24 (2022), pp. 12354–12364. DOI: 10.1016/j.ijhydene.2021.06.228 (cited on page 42).

İnci, Mustafa, Büyük, Mehmet, Demir, Mehmet Hakan, and İlbey, Göktürk. "A review and research on fuel cell electric vehicles: Topologies, power electronic converters, energy management methods, technical challenges, marketing and future aspects". In: *Renewable and Sustainable Energy Reviews* 137 (2021), p. 110648. DOI: https://doi.org/10.1016/j.rser.2020.110648 (cited on page 147).

International, Amnesty. *'This Is What We Die For': Human Rights Abuses in the Democratic Republic of the Congo Power the Global Trade in Cobalt*. 2016 (cited on page 152).

International Energy Agency. *Technology roadmap: hydrogen and fuel cells.* 2015 (cited on page 19).

International Energy Outlook - U.S. Energy Information Administration (EIA). URL: https://www.eia.gov/outlooks/ieo/index.php (visited on 06/21/2023) (cited on pages 1–3).

Intralink. *The hydrogen economy South Korea, market intelligence report.* 2021 (cited on page 19).

Issa, R. I. "Solution of the implicitly discretised fluid flow equations by operator-splitting". In: *Journal of computational physics* 62.1 (1986), pp. 40–65 (cited on page 81).

J2600_201211: Compressed Hydrogen Surface Vehicle Fueling Connection Devices - SAE International. URL: https://www.sae.org/standards/content/j2600_201211/ (visited on 06/10/2023) (cited on page 19).

Jadhav, AJA. *Hydrogen fuel cell vehicle market by vehicle type (passenger vehicle and commercial vehicle) and technology (proton exchange membrane fuel cell, phosphoric acid fuel cells, and others).* Pages: 2019–2026. 2020 (cited on page 147).

Jang, Beakcheol, Kim, Myeonghwi, Harerimana, Gaspard, and Kim, Jong Wook. "Q-Learning Algorithms: A Comprehensive Classification and Applications". In: *IEEE Access* 7 (2019). Conference Name: IEEE Access, pp. 133653–133667. DOI: 10.1109/ACCESS.2019.2941229 (cited on page 195).

Kalghatgi, Gautam. "Is it really the end of internal combustion engines and petroleum in transport?" In: *Applied Energy* 225 (2018), pp. 965–974. DOI: 10.1016/j.apenergy.2018.05.076 (cited on page 11).

Kareemulla, Thayyil, Delprat, Sebastien, and Czelecz, Loic. "State constrained hybrid vehicle optimal energy management: an interior penalty approach". In: *IFAC-PapersOnLine* 50.1 (2017), pp. 10040–10045. DOI: 10.1016/j.ifacol.2017.08.1774 (cited on page 176).

Kingsford, Carl and Salzberg, Steven L. "What are decision trees?" In: *Nature Biotechnology* 26.9 (2008). Number: 9 Publisher: Nature Publishing Group, pp. 1011–1013. DOI: 10.1038/nbt0908-1011 (cited on page 195).

Kleeberg, Hagen, Tomazic, Daniel, Dohmen, Joerg, Wittek, Karl, and Balazs, Andreas. "Increasing Efficiency in Gasoline Powertrains with a Two-Stage Variable Compression Ratio (VCR) System". In: *SAE Technical Paper.* Issue: 2013-01-0288. SAE International, 2013. DOI: 10.4271/2013-01-0288 (cited on page 37).

Knights, S. *Polymer Electrolyte Membrane and Direct Methanol Fuel Cell Technology: 6 - Operation and durability of low temperature fuel cells*. Publication Title: Volume 1. Woodhead Publishing Limited, 2012. 137–177. DOI: 10.1533/9780857095473.2.137 (cited on page 126).

Konnov, Alexander A. "Yet another kinetic mechanism for hydrogen combustion". In: *Combustion and Flame* 203 (2019), pp. 14–22. DOI: 10.1016/j.combustflame.2019.01.032 (cited on pages 54, 74).

Korean Energy Economics Institute. *Energy focus*. 2019 (cited on page 19).

Landau, L. "On the Theory of Slow Combustion". In: *Dynamics of Curved Fronts*. Ed. by Pierre Pelcé. San Diego: Academic Press, 1988, pp. 403–411. DOI: 10.1016/B978-0-08-092523-3.50044-7 (cited on page 76).

Langmi, Henrietta W., Engelbrecht, Nicolaas, Modisha, Phillimon M., and Bessarabov, Dmitri. "Chapter 13 - Hydrogen storage". In: *Electrochemical Power Sources: Fundamentals, Systems, and Applications*. Ed. by Tom Smolinka and Jurgen Garche. Elsevier, 2022, pp. 455–486. DOI: 10.1016/B978-0-12-819424-9.00006-9 (cited on page 18).

Leitner, Walter, Klankermayer, Jürgen, Pischinger, Stefan, Pitsch, Heinz, and Kohse-Höinghaus, Katharina. "Advanced Biofuels and Beyond: Chemistry Solutions for Propulsion and Production". In: *Angewandte Chemie International Edition* 56.20 (2017). _eprint: https://onlinelibrary.wiley.com/doi/pdf/10.1002/anie.2016072 pp. 5412–5452. DOI: 10.1002/anie.201607257 (cited on page 12).

Li, Huan, Ravey, Alexandre, N'Diaye, Abdoul, and Djerdir, Abdesslem. "A novel equivalent consumption minimization strategy for hybrid electric vehicle powered by fuel cell, battery and supercapacitor". In: *Journal of Power Sources* 395 (2018). Publisher: Elsevier B.V., pp. 262–270. DOI: 10.1016/J.JPOWSOUR.2018.05.078 (cited on page 211).

Li, Huan, Ravey, Alexandre, N'Diaye, Abdoul, and Djerdir, Abdesslem. "Online adaptive equivalent consumption minimization strategy for fuel cell hybrid electric vehicle considering power sources degradation". In: *Energy Conversion and Management* 192 (2019), pp. 133–149. DOI: 10.1016/j.enconman.2019.03.090 (cited on page 203).

Li, W. et al. "A Speedy Reinforcement Learning-Based Energy Management Strategy for Fuel Cell Hybrid Vehicles Considering Fuel Cell System Lifetime". In: *Int. J. Precis. Eng. Manuf. Green Technol.* 9 (2022), pp. 859–872. DOI: 10.1007/s40684-022-00263-4 (cited on page 203).

Li, Xiyun, Wang, Yujie, Yang, Duo, and Chen, Zonghai. "Adaptive energy management strategy for fuel cell/battery hybrid vehicles using Pontryagin's Minimal Principle". In: *Journal of Power Sources* 440 (2019). Publisher: Elsevier B.V. DOI: 10.1016/j.jpowsour.2019.227105 (cited on page 211).

Liao, Zihao, Wei, Lin, Dafalla, Ahmed Mohmed, Suo, Zhenbang, and Jiang, Fangming. "Numerical study of subfreezing temperature cold start of proton exchange membrane fuel cells with zigzag-channeled flow field". In: *International Journal of Heat and Mass Transfer* 165 (2021), p. 120733. DOI: 10.1016/j.ijheatmasstransfer.2020.120733 (cited on page 120).

Lightfoot, M. *Three Steps to Clean up Electric Vehicle Supply Chains*. Publisher: World Economic Forum. 2019. URL: https://www.weforum.org/agenda/2019/09/clean-vehicles-have-a-dirty-secret-and-it-s-time-we-took-action/ (cited on page 152).

Lin, Xinyou, Wu, Jiayun, and Wei, Yimin. "An ensemble learning velocity prediction-based energy management strategy for a plug-in hybrid electric vehicle considering driving pattern adaptive reference SOC". In: *Energy* 234 (2021). Publisher: Elsevier Ltd. DOI: 10.1016/j.energy.2021.121308 (cited on pages 205, 214).

Liu, Y., Li, J., Chen, Z., Qin, D., and Zhang, Y. "Research on a Multi-Objective Hierarchical Prediction Energy Management Strategy for Range Extended Fuel Cell Vehicles". In: *J. Power Sources* 429 (2019), pp. 55–66. DOI: 10.1016/j.jpowsour.2019.04.082 (cited on page 203).

Liu, Yao-Dong, Jia, Ming, Xie, Mao-Zhao, and Pang, Bin. "Development of a New Skeletal Chemical Kinetic Model of Toluene Reference Fuel with Application to Gasoline Surrogate Fuels for Computational Fluid Dynamics Engine Simulation". In: *Energy & Fuels* 27.8 (2013). Publisher: American Chemical Society, pp. 4899–4909. DOI: 10.1021/ef4009955 (cited on page 54).

Livengood, JC and Wu, P. C. "Correlation of Autoignition Phenomena in Internal Combustion Engines and Rapid Compression Machines". In: *Symposium (International) on Combustion* 5.1 (1955), pp. 347–356. DOI: 10.1016/S0082-0784(55)80047-1 (cited on page 53).

Lu, Tianfeng and Law, Chung K. "Toward accommodating realistic fuel chemistry in large scale computations". In: *Progress in Energy and Combustion Science* 35.2 (2009), pp. 195–215. DOI: 10.1016/j.pecs.2008.10.002 (cited on page 53).

Luciani, Sara and Tonoli, Andrea. "Control Strategy Assessment for Improving PEM Fuel Cell System Efficiency in Fuel Cell Hybrid Vehicles". In: *Energies* 15.6 (2022). Publisher: MDPI. DOI: 10.3390/en15062004 (cited on page 218).

Marketing, F. E. V. *Almost CO2-neutral Mobility | FEV Corporate Magazine*. URL: https://magazine.fev.com/en/almost-co2-neutral-mobility/ (visited on 06/08/2023) (cited on page 15).

Marketing, F. E. V. *Carbon-neutral transport – the role of synthetic fuel | FEV Corporate Magazine*. URL: https://magazine.fev.com/en/carbon-neutral-transport-the-role-of-synthetic-fuel/ (visited on 06/08/2023) (cited on page 16).

MATALON, M., CUI, C., and BECHTOLD, J. K. "Hydrodynamic theory of premixed flames: effects of stoichiometry, variable transport coefficients and arbitrary reaction orders". In: *Journal of Fluid Mechanics* 487 (2003). Publisher: Cambridge University Press, pp. 179–210. DOI: 10.1017/S0022112003004683 (cited on page 77).

Matalon, Moshe. "The Darrieus–Landau instability of premixed flames". In: *Fluid Dynamics Research* 50.5 (2018). Publisher: IOP Publishing, p. 051412. DOI: 10.1088/1873-7005/aab510 (cited on page 77).

Matthews, R. D. and Chin, Y. W. "A Fractal-Based SI Engine Model: Comparisons of Predictions with Experimental Data". In: *SAE Technical Paper*. Issue: 910075. 1991. DOI: 10.4271/910079 (cited on page 50).

Mazloomi, Kaveh and Gomes, Chandima. "Hydrogen as an energy carrier: Prospects and challenges". In: *Renewable and Sustainable Energy Reviews* 16.5 (2012), pp. 3024–3033. DOI: 10.1016/j.rser.2012.02.028 (cited on page 20).

Mazumder, S. and Cole, J. V. "Rigorous 3-D Mathematical Modeling of PEM Fuel Cells". In: *Journal of the Electrochemical Society* 150.11 (2003), A1503 (cited on page 119).

Mendiara, T. et al. "Negative CO2 emissions through the use of biofuels in chemical looping technology: A review". In: *Applied Energy* 232 (2018), pp. 657–684. DOI: 10.1016/j.apenergy.2018.09.201 (cited on page 12).

Meneveau, Charles and Poinsot, Thierry. "Stretching and quenching of flamelets in premixed turbulent combustion". In: *Combustion and Flame* 86.4 (1991), pp. 311–332. DOI: 10.1016/0010-2180(91)90126-V (cited on page 47).

Meng, H. "A Three-Dimensional PEM Fuel Cell Model with Consistent Treatment of Water Transport in MEA". In: *Journal of Power Sources* 162 (2006), pp. 426–435 (cited on page 118).

Meng, H. “A Three-Dimensional Mixed-Domain PEM Fuel Cell Model with Fully-Coupled Transport Phenomena”. In: *Journal of Power Sources* 164 (2007), pp. 688–696 (cited on page 118).

Metghalchi, M and Keck, J C. “Burning velocities of mixtures of air with methanol, isooctane, and indolene at high pressure and temperature”. In: *Combustion and flame* 48 (1982), pp. 191–210. DOI: 10.1016/0010-2180(82)90127-4 (cited on page 32).

Miller, John M. *Propulsion Systems for Hybrid Vehicles*. Google-Books-ID: uTiSu1mbBa8C. IET, 2004. 476 pp. (cited on pages 154, 156).

Millo, F. and Ferraro, C. “Knock in S.I. Engines: A Comparison between Different Techniques for Detection and Control”. In: *SAE Technical Paper*. Issue: 982477. 1998. DOI: 10.4271/982477 (cited on page 35).

Millo, Federico, Gullino, Fabrizio, and Rolando, Luciano. “Methodological Approach for 1D Simulation of Port Water Injection for Knock Mitigation in a Turbocharged DISI Engine”. In: *Energies* 13.17 (2020). Number: 17 Publisher: Multidisciplinary Digital Publishing Institute, p. 4297. DOI: 10.3390/en13174297 (cited on page 63).

Mirfarsi, Seyed Hesam, Parnian, Mohammad Javad, and Rowshanzamir, Soosan. “Self-Humidifying Proton Exchange Membranes for Fuel Cell Applications: Advances and Challenges”. In: *Processes* 8.9 (2020). Number: 9 Publisher: Multidisciplinary Digital Publishing Institute, p. 1069. DOI: 10.3390/pr8091069 (cited on page 115).

Molina, S., Novella, R., Pla, B., and Lopez-Juarez, M. “Optimization and sizing of a fuel cell range extender vehicle for passenger car applications in driving cycle conditions”. In: *Applied Energy* 285 (2021). Publisher: Elsevier Ltd. DOI: 10.1016/j.apenergy.2021.116469 (cited on pages 122, 124, 164).

Molina, S., Ruiz, S., Gomez-Soriano, J., and Olcina-Girona, M. “Impact of hydrogen substitution for stable lean operation on spark ignition engines fueled by compressed natural gas”. In: *Results in Engineering* 17 (2023), p. 100799. DOI: 10.1016/j.rineng.2022.100799 (cited on page 72).

Mortimer, M.B. *How Much Does Climate Control Affect EV Range?* 2020 (cited on page 152).

Motoaki, Y., Yi, W., and Salisbury, S. “Empirical Analysis of Electric Vehicle Fast Charging under Cold Temperatures”. In: *Energy Policy* 122 (2018), pp. 162–168. DOI: 10.1016/j.enpol.2018.07.036 (cited on page 153).

Mueller, Christian, Morcinkowski, Britta, Habermann, Klaus, Uhlmann, Thomas, and Schernus, Claus. "Development of a pre-chamber for spark ignition engines in vehicle applications". In: *4th International Conference on Ignition Systems for Gasoline Engines*. 2018 (cited on page 40).

Mukherjee, Partha P., Kang, Qin, and Wang, Chao-Yang. "Pore-scale modeling of two-phase transport in polymer electrolyte fuel cells – Progress and perspective". In: *Energy & Environmental Science* 4.2 (2011), pp. 346–369 (cited on page 120).

Murschenhofer, M., Hacker, V., Bludszuweit, C., et al. "Impact of operating conditions on the performance of polymer electrolyte membrane fuel cells". In: *Journal of Power Sources* 375 (2018). Publisher: Elsevier, pp. 345–352 (cited on page 121).

Musardo, Christian, Rizzoni, Giorgio, Guezennec, Yann, and Staccia, Barbara. "A-ECMS: An Adaptive Algorithm for Hybrid Electric Vehicle Energy Management". In: *European Journal of Control* 11.4 (2013), pp. 509–524. DOI: 10.3166/ejc.11.509-524 (cited on page 177).

Nguyen, T. V. and White, R. E. "A Water and Heat Management Model for Proton-Exchange-Membrane Fuel Cells". In: *Journal of The Electrochemical Society* 140.8 (1993), pp. 2178–2186 (cited on page 119).

Nicholls, J, EI-Messiri, I, and Newhali, H. "Inlet manifold water injection for control of nitrogen oxides-theory and experiment". In: *SAE Technical Paper*. Issue: 690018. 1969 (cited on page 39).

Nielsen, Michael A. "Neural Networks and Deep Learning". In: (2015). Publisher: Determination Press (cited on page 197).

Nishikawa, H., Sasou, H., Kurihara, R., and, et al et. "High fuel utilization operation of pure hydrogen fuel cells". In: *International Journal of Hydrogen Energy* 33 (2008), pp. 6262–6269 (cited on page 114).

North, G. L. and Santavicca, D. A. "The fractal nature of premixed turbulent flames". In: *Combustion Science and Technology* 72.4 (1990), pp. 215–232. DOI: 10.1080/00102209008951648 (cited on page 50).

O'Hayre, Ryan. "Fuel cells for electrochemical energy conversion". In: *EPJ Web of Conferences* 148 (2017), p. 00013. DOI: 10.1051/epjconf/201714800013 (cited on page 105).

Obert, EF. "Detonation and internal coolants". In: *SAE Technical Paper*. Issue: 480173. 1948 (cited on page 39).

OECD.org - OECD. URL: https://www.oecd.org/ (visited on 06/21/2023) (cited on page 1).

Okita, Ryoji. “Mazda SKYACTIV-G Engine with New Boosting Technology”. In: *Advanced Clean Cars Symposium: The Road Ahead*. Sacramento, USA, 2016 (cited on page 40).

Onori, Simona, Serrao, Lorenzo, and Rizzoni, Giorgio. “Adaptive equivalent consumption minimization strategy for hybrid electric vehicles”. In: *ASME 2010 Dynamic Systems and Control Conference, DSCC2010* 1 (2010). ISBN: 9780791844175, pp. 499–505. DOI: 10.1115/DSCC2010-4211 (cited on page 216).

Paganelli, Giovanni, Delprat, Sebastien, Guerra, Thierry M., Rimaux, Jerome, and Santin, Jose J. “Equivalent consumption minimization strategy for parallel hybrid powertrains”. In: *Vehicular Technology Conference IEEE 55th Vehicular Technology Conference VTC Spring 2002*. Vol. 4. 2002, pp. 2076–2081. DOI: 10.1109/VTC.2002.1002989 (cited on page 177).

Pandey, Jayashish Kumar and Kumar, G. N. “Effect of variable compression ratio and equivalence ratio on performance, combustion and emission of hydrogen port injection SI engine”. In: *Energy* 239 (2022), p. 122468. DOI: 10.1016/j.energy.2021.122468 (cited on page 41).

Pardhi, S. et al. “A review of fuel cell powertrains for long-haul heavy-duty vehicles: Technology, hydrogen, energy and thermal management solutions”. In: *Energies* 15.24 (2022). DOI: 10.3390/en15249557 (cited on page 146).

Park, Cheolwoong, Kim, Yongrae, Oh, Sechul, Oh, Junho, and Choi, Young. “Effect of the operation strategy and spark plug conditions on the torque output of a hydrogen port fuel injection engine”. In: *International Journal of Hydrogen Energy* 46.74 (2021), pp. 37063–37070. DOI: 10.1016/j.ijhydene.2021.08.229 (cited on page 42).

Parmar, Aakash, Katariya, Rakesh, and Patel, Vatsal. “A Review on Random Forest: An Ensemble Classifier”. In: *International Conference on Intelligent Data Communication Technologies and Internet of Things (ICICI) 2018*. Ed. by Jude Hemanth, Xavier Fernando, Pavel Lafata, and Zubair Baig. Lecture Notes on Data Engineering and Communications Technologies. Cham: Springer International Publishing, 2019, pp. 758–763. DOI: 10.1007/978-3-030-03146-6_86 (cited on page 195).

Pei, Di and Leamy, Michael J. “Dynamic Programming-Informed Equivalent Cost Minimization Control Strategies for Hybrid-Electric Vehicles”. In: *J. Dyn. Sys., Meas., Control* 135.5 (2013), p. 051013. DOI: 10.1115/1.4024788 (cited on page 177).

Pei, P., Zeng, K., and Zhang, J. "Durability study of a high temperature PEM fuel cell". In: *Journal of Power Sources* 180.2 (2008), pp. 835–842 (cited on pages 124, 126).

Peng, F., Xie, X., Wu, K., Zhao, Y., and Ren, L. "Online hierarchical energy management strategy for fuel cell-based heavy-duty hybrid power systems aiming at collaborative performance enhancement". In: *Energy Conversion and Management* 276 (2023), p. 116501. DOI: 10.1016/j.enconman.2022.116501 (cited on page 145).

Piras, M., De Bellis, V., Malfi, E., Novella, R., and Lopez-Juarez, M. "Adaptive ECMS based on speed forecasting for the control of a heavy-duty fuel cell vehicle for real-world driving". In: *Energy Conversion and Management* 289 (2023), p. 117178. DOI: 10.1016/j.enconman.2023.117178 (cited on pages 122, 123, 206–208, 211–215).

Piras, Marco, Teodosio, Luigi, Tornatore, Cinzia, Marchitto, Luca, and Bozza, Fabio. "Exploring the potentials of water injection to improve fuel consumption and torque in a small displacement PFI spark-ignition engine". In: *Fuel* 327 (2022), p. 125224. DOI: 10.1016/j.fuel.2022.125224 (cited on pages 56, 58–63, 65–70).

Pisner, Derek A. and Schnyer, David M. "Chapter 6 - Support vector machine". In: *Machine Learning*. Ed. by Andrea Mechelli and Sandra Vieira. Academic Press, 2020, pp. 101–121. DOI: 10.1016/B978-0-12-815739-8.00006-7 (cited on page 195).

Poinsot, Thierry and Veynante, Denis. *Theoretical and Numerical Combustion*. 3rd. 2012 (cited on page 47).

Rapp, Valentin, Killingsworth, Nick, and Therkelsen, Peter. *Lean Combustion, 2nd Edition*. Publication Title: Lean-Burn Internal Combustion Engines. Elsevier, 2016. 111-146. DOI: 10.1016/C2013-0-13446-0 (cited on page 40).

Rhodes, D B and Keck, J C. "Laminar burning speed measurements of indolene-air-diluent mixtures at high pressures and temperatures". In: *SAE Technical Paper*. Vol. 850047. 1985. DOI: 10.4271/850047 (cited on page 32).

Richard, Sylvain, Bougrine, Said, Font, Gilles, Lafossas, Florian A., and Berr, Fabien le. "On the Reduction of a 3D CFD Combustion Model to Build a Physical 0D Model for Simulating Heat Release, Knock and Pollutants in SI Engines". In: *Oil Gas Science and Technology - Revue d'IFP Energies nouvelles* 64.3 (2009), pp. 223–242. DOI: 10.2516/ogst/2008055 (cited on page 47).

Richard, Sylvain and Veynante, Denis. “A 0-D flame wrinkling equation to describe the turbulent flame surface evolution in SI engines”. In: *Comptes Rendus Mécanique* 343.3 (2015), pp. 219–231. DOI: 10.1016/j.crme.2014.09.003 (cited on page 47).

Rohit, A et al. “Literature survey of water injection benefits on boosted spark ignited engines”. In: *SAE Technical Paper*. Issue: 2017-01-0658. 2017 (cited on page 39).

Sánchez, Marco, Delprat, Sebastien, and Hofman, Tom. “Energy management of hybrid vehicles with state constraints: A penalty and implicit Hamiltonian minimization approach”. In: *Applied Energy* 260 (2020), p. 114149. DOI: 10.1016/j.apenergy.2019.114149 (cited on page 176).

Sciarretta, Antonio and Guzzella, Lino. “Control of hybrid electric vehicles”. In: *IEEE Control Systems Magazine* 27.2 (2007), pp. 60–70. DOI: 10.1109/MCS.2007.338280 (cited on page 176).

Senecal, Kelly and Leach, Felix. *Racing Toward Zero: The Untold Story of Driving Green*. SAE International, 2021 (cited on page 26).

Sens, Matthias, Binder, Erik, Benz, Andreas, Kramer, Lukas, et al. “Pre-chamber ignition as a Key Technology for Highly Efficient SI Engines-New Approaches and Operating Strategies”. In: *39th International Vienna Motor Symposium*. 2018 (cited on page 40).

Serrano, J.R., Martín, J., Gomez-Soriano, J., and Raggi, R. “Theoretical and experimental evaluation of the spark-ignition premixed oxy-fuel combustion concept for future co2 captive powerplants”. In: *Energy Conversion and Management* 244 (2021), p. 114498 (cited on page 81).

Serrao, Lorenzo, Onori, Simona, and Rizzoni, Giorgio. “A comparative analysis of energy management strategies for hybrid electric vehicles”. In: *J. Dyn. Sys., Meas., Control* 133.3 (2011), p. 031012. DOI: 10.1115/1.4003267 (cited on page 177).

Shankar, R., Marco, J., and Assadian, F. “Design of an Optimized Charge-Blended Energy Management Strategy for a Plugin Hybrid Vehicle”. In: *Proceedings of the 2012 UKACC International Conference on Control, CONTROL 2012*. 2012, pp. 619–624. DOI: 10.1109/CONTROL.2012.6334701 (cited on page 172).

Shen, Jun, Xu, Liang, Chang, Huawei, Tu, Zhengkai, and Chan, Siew Hwa. “Partial flooding and its effect on the performance of a proton exchange membrane fuel cell”. In: *Energy Conversion and Management* 207 (2020), p. 112537. DOI: 10.1016/j.enconman.2020.112537 (cited on page 119).

Shimpalee, S. and Dutta, S. "Numerical prediction of temperature distribution in PEM fuel cells". In: *Numerical Heat Transfer, Part A: Applications* 38.1 (2000), pp. 111–128 (cited on page 119).

Short-Term Energy Outlook - U.S. Energy Information Administration (EIA). URL: https://www.eia.gov/outlooks/steo/data.php (visited on 06/21/2023) (cited on page 4).

Sim, K., Vijayagopal, R., Kim, N., and Rousseau, A. "Optimization of component sizing for a fuel cell-powered truck to minimize ownership cost". In: *Energies* 12.6 (2019). DOI: 10.3390/en12061125 (cited on page 146).

Song, Guang-Hua and Meng, Hua. "Numerical modeling and simulation of PEM fuel cells: Progress and perspective". In: *Acta Mechanica Sinica* 29.3 (2013), pp. 318–334. DOI: 10.1007/s10409-013-0037-y (cited on page 119).

Song, Ke, Huang, Xing, Cai, Zhen, Huang, Pengyu, and Li, Feiqiang. "Research on energy management strategy of fuel-cell vehicles based on nonlinear model predictive control". In: *International Journal of Hydrogen Energy* (2023). DOI: https://doi.org/10.1016/j.ijhydene.2023.07.304 (cited on page 203).

Springer, T.E., Zawodzinski, T.A., and Gottesfeld, S. "Polymer electrolyte fuel cell model". In: *Journal of The Electrochemical Society* 138 (1991). Publisher: The Electrochemical Society, pp. 2334–2342 (cited on pages 118, 121).

Staffell, I. et al. *The role of hydrogen and fuel cells in the future energy systems*. 2017 (cited on page 19).

Stanglmaier, Rudolf and Roberts, Charles. "Homogeneous charge compression ignition (HCCI): benefits, compromises, and future engine applications". In: *SAE transactions* (1999), pp. 2138–2145. DOI: www.jstor.org/stable/44741335 (cited on page 40).

Stevens, Mark. *How an Internal Combustion Engine Works (4-Stroke Gasoline)*. CarTreatments.com. 2016. URL: https://cartreatments.com/how-internal-combustion-engine-works/ (visited on 06/09/2023) (cited on page 26).

Sun, H., Zhang, G. S., Guo, L. J., et al. "A study of dynamic characteristics of PEM fuel cells by measuring local currents". In: *International Journal of Hydrogen Energy* 34.13 (2009), pp. 5529–5536 (cited on page 120).

Sun, Xiaoxiao, Zhou, Yafu, Huang, Lijian, and Lian, Jing. "A real-time PMP energy management strategy for fuel cell hybrid buses based on driving segment feature recognition". In: *International Journal of Hydrogen Energy* 46.80 (2021), pp. 39983–40000. DOI: https://doi.org/10.1016/j.ijhydene.2021.09.204 (cited on page 203).

Tabata, Masayoshi, Yamamoto, Tetsuya, and Fukube, Tatsuya. "Improving NOx and fuel economy for mixture injected SI engine with EGR". In: *SAE transactions* (1995), pp. 1221–1230 (cited on page 37).

Tanaka, S, Ayala, F, and Keck, J C. "A reduced chemical kinetic model for HCCI combustion of primary reference fuels in a rapid compression machine". In: *Combustion and Flame* 133.4 (2003), pp. 467–481. DOI: 10.1016/S0010-2180(03)00057-9 (cited on page 32).

Tawfik, H., Hung, Y., and Mahajan, D. "Metal bipolar plates for PEM fuel cell—A review". In: *Journal of Power Sources*. Selected Papers presented at the FUEL PROCESSING FOR HYDROGEN PRODUCTION SYMPOSIUM at the 230th American Chemical SocietyNational Meeting Washington, DC, USA, 28 August – 1 September 2005 163.2 (2007), pp. 755–767. DOI: 10.1016/j.jpowsour.2006.09.088 (cited on page 115).

Teodosio, Luigi, Marchitto, Luca, Tornatore, Cinzia, Bozza, Fabio, and Valentino, Gerardo. "Effect of Cylinder-by-Cylinder Variation on Performance and Gaseous Emissions of a PFI Spark Ignition Engine: Experimental and 1D Numerical Study". In: *Applied Sciences* 11.13 (2021). Number: 13 Publisher: Multidisciplinary Digital Publishing Institute, p. 6035. DOI: 10.3390/app11136035 (cited on page 55).

The average age of cars on America's roads went up again, report says. CNET. URL: https://www.cnet.com/roadshow/news/average-vehicle-age-increase-america/ (visited on 06/08/2023) (cited on page 12).

The boom of China's automotive aftermarket is imminent. Ipsos. 2016. URL: https://www.ipsos.com/en/boom-chinas-automotive-aftermarket-imminent (visited on 06/08/2023) (cited on page 12).

Tornatore, Cinzia and Sjöberg, Magnus. "Optical Investigation of a Partial Fuel Stratification Strategy to Stabilize Overall Lean Operation of a DISI Engine Fueled with Gasoline and E30". In: *Energies* 14.2 (2021). Number: 2 Publisher: Multidisciplinary Digital Publishing Institute, p. 396. DOI: 10.3390/en14020396 (cited on page 40).

Torregrosa, A. J., Broatch, A., Margot, X., and Gomez-Soriano, J. "Understanding the unsteady pressure field inside combustion chambers of compression-ignited engines using a computational fluid dynamics approach". In: *International Journal of Engine Research* 21.8 (2020), pp. 1273–1285 (cited on page 81).

Tran, D., Cummins, M., Stamos, E., Buelow, J., and Mohrdieck, C. "Development of the Jeep Commander 2 fuel cell hybrid electric vehicle". In: *Society of Automotive Engineers (SAE) Journal* 2001 (2002). Place: Warrendale, PA (cited on page 107).

Tribioli, L. et al. "A Real Time Energy Management Strategy for Plug-in Hybrid Electric Vehicles Based on Optimal Control Theory". In: *Energy Procedia* 45 (2014), pp. 949–958. DOI: 10.1016/J.EGYPRO.2014.01.100 (cited on page 172).

Wang, Chenchen et al. "Experimental study on knock suppression of spark-ignition engine fuelled with kerosene via water injection". In: *Applied Energy* 242 (2019), pp. 248–259. DOI: 10.1016/J.APENERGY.2019.03.123 (cited on page 64).

Wang, Y. and Wang, C. Y. "Two-phase transients of polymer electrolyte fuel cells". In: *Journal of The Electrochemical Society* 154.10 (2007), B636–B643 (cited on page 120).

Wang, Yun and Wang, Chao-Yang. "Transient analysis of polymer electrolyte fuel cells". In: *Electrochimica Acta* 50.6 (2005), pp. 1307–1315. DOI: 10.1016/j.electacta.2004.08.022 (cited on page 118).

Weller, H. G., Tabor, G., Gosman, A. D., and Fureby, C. "Application of a flame-wrinkling LES combustion model to a turbulent mixing layer". In: *Symposium (International) on Combustion* 27.1 (1998), pp. 899–907. DOI: 10.1016/S0082-0784(98)80487-6 (cited on page 47).

Wolter, M., Guercke, H., Isermann, T., and Hofmann, L. "Multi-Agent Based Distributed Power Flow Calculation". In: *Proceedings of the IEEE PES General Meeting*. 2010, pp. 1–6 (cited on page 203).

Worm, Julian, Naber, Jeffrey, Duncan, Jason, Barros, Sergio, and Atkinson, William. "Water Injection as an Enabler for Increased Efficiency at High-Load in a Direct Injected, Boosted, SI Engine". In: *SAE International Journal of Engines* 10 (2017), pp. 951–958. DOI: 10.4271/2017-01-0663 (cited on page 64).

Woschni, G. *A Universally Applicable Equation for the Instantaneous Heat Transfer Coefficient in the Internal Combustion Engine*. SAE Technical Paper 670931. ISSN: 0148-7191, 2688-3627. Warrendale, PA: SAE International, 1967. DOI: 10.4271/670931 (cited on page 54).

Wu, X., Hu, X., Yin, X., Peng, Y., and Pickert, V. "Convex programming improved online power management in a range extended fuel cell electric truck". In: *Journal of Power Sources* 476 (2020), p. 228642. DOI: 10.1016/J.JPOWSOUR.2020.228642 (cited on page 158).

Wu, X. et al. "Convex programming energy management and components sizing of a plug-in fuel cell urban logistics vehicle". In: *Journal of Power Sources* 423 (2019), pp. 358–366. DOI: 10.1016/J.JPOWSOUR.2019.03.044 (cited on page 158).

Xin, G. et al. "Monitoring of hydrogen-fueled engine backfires using dual manifold absolute pressure sensors". In: *International Journal of Hydrogen Energy* 47.26 (2022), pp. 13134–13142 (cited on page 41).

Xing, Lei et al. "Membrane electrode assemblies for PEM fuel cells: A review of functional graded design and optimization". In: *Energy* 177 (2019), pp. 445–464. DOI: 10.1016/j.energy.2019.04.084 (cited on page 120).

Xu, Liangfei et al. "Optimal sizing of plug-in fuel cell electric vehicles using models of vehicle performance and system cost". In: *Applied Energy* 103 (2013), pp. 477–487. DOI: 10.1016/j.apenergy.2012.10.010 (cited on page 145).

Yang, D., Wang, L., Yu, K., and Liang, J. "A reinforcement learning-based energy management strategy for fuel cell hybrid vehicle considering real-time velocity prediction". In: *Energy Conversion and Management* 274 (2022), p. 116453. DOI: 10.1016/J.ENCONMAN.2022.116453 (cited on page 203).

Ye, Q. and Nguyen, T. V. "Three-Dimensional Simulation of Liquid Water Distribution in a PEMFC with Experimentally Measured Capillary Functions". In: *Journal of the Electrochemical Society* 154.12 (2007), B1242–B1251 (cited on page 119).

Yeqin, Wang et al. "Research on energy optimization control strategy of the hybrid electric vehicle based on Pontryagin's minimum principle". In: *Computers & Electrical Engineering* 72 (2018), pp. 203–213. DOI: 10.1016/j.compeleceng.2018.09.018 (cited on page 176).

Yi, J. S. and Nguyen, T. V. "An Along-the-Channel Model for Proton Exchange Membrane Fuel Cells". In: *Journal of The Electrochemical Society* 145.4 (1998), pp. 1149–1159 (cited on page 119).

Yuan, Xiao-Zi, Li, Hui, Zhang, Shengsheng, Martin, Jonathan, and Wang, Haijiang. "A review of polymer electrolyte membrane fuel cell durability test protocols". In: *Journal of Power Sources* 196.22 (2011), pp. 9107–9116. DOI: 10.1016/j.jpowsour.2011.07.082 (cited on page 116).

Zeng, Tao et al. "Optimization-oriented adaptive equivalent consumption minimization strategy based on short-term demand power prediction for fuel cell hybrid vehicle". In: *Energy* 227 (2021). Publisher: Elsevier Ltd. DOI: 10.1016/j.energy.2021.120305 (cited on pages 205, 214).

Zhang, Feilong, Xi, Jianquan, and Langari, Reza. "An adaptive equivalent consumption minimization strategy for parallel hybrid electric vehicle based on Fuzzy PI". In: *Proceeding of 2016 IEEE Intelligent Vehicles Symposium (IV)*. 2016, pp. 460–465. DOI: 10.1109/IVS.2016.7535426 (cited on page 177).

Zhang, Shuan-Hong, Zhao, Yue, Yang, Zhen-Yu, He, Zhe-Feng, and Wu, Hai. "The 1.35Ga diabase sills from the northern North China Craton: Implications for breakup of the Columbia (Nuna) supercontinent". In: *Earth and Planetary Science Letters* 288.3 (2009), pp. 588–600. DOI: 10.1016/j.epsl.2009.10.023 (cited on page 116).

Zhang, Zhendong, He, Hongwen, Guo, Jinquan, and Han, Ruoyan. "Velocity prediction and profile optimization based real-time energy management strategy for Plug-in hybrid electric buses". In: *Applied Energy* 280 (2020). Publisher: Elsevier Ltd. DOI: 10.1016/j.apenergy.2020.116001 (cited on pages 204, 205, 214).

Zheng, W., Zhu, J., and Luo, Q. "Distributed Dispatch of Integrated Electricity-Heat Systems with Variable Mass Flow". In: *IEEE Trans. Smart Grid* (2022). DOI: 10.1109/TSG.2022.3143030 (cited on page 203).

Zhou, Y., Li, H., Ravey, A., and Péra, M.-C. "An integrated predictive energy management for light-duty range-extended plug-in fuel cell electric vehicle". In: *Journal of Power Sources* 451 (2020), p. 227780. DOI: 10.1016/j.jpowsour.2020.227780 (cited on page 231).

Zhou, Yang, Ravey, Alexandre, and Péra, Marie-Cécile. "Multi-objective energy management for fuel cell electric vehicles using online-learning enhanced Markov speed predictor". In: *Energy Conversion and Management* 213 (2020), p. 112821. DOI: 10.1016/j.enconman.2020.112821 (cited on page 203).

Zimont, V. L. "Theory of turbulent combustion of a homogeneous fuel mixture at high Reynolds numbers". In: *Combust. Explos. Shock Waves* 15.3 (1979), pp. 305–311. DOI: 10.1007/BF00785062 (cited on page 46).